SOME ASPECTS OF NONLINEAR LASER PLASMA INTERACTIONS

David A. Johnson

A Thesis Submitted for the Degree of PhD
at the
University of St Andrews

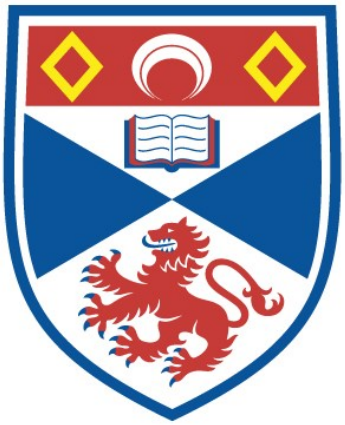

1995

SOME ASPECTS OF NONLINEAR LASER PLASMA INTERACTIONS

DAVID A JOHNSON

THESIS SUBMITTED FOR THE DEGREE OF DOCTOR OF PHILOSOPHY OF THE UNIVERSITY OF ST ANDREWS IN OCTOBER 1994

ProQuest LLC.
789 East Eisenhower Parkway
P.O. Box 1346
Ann Arbor, MI 48106 – 1346

Abstract

Recent advances in the development of high power short pulse laser systems has opened a new regime of laser plasma interactions for study. The thesis is presented in two parts.

In Part I, we consider the implications of these high power laser pulses for the interaction with a uniform underdense plasma, with particular regard to plasma-based accelerators. We present a scheme for the resonant excitation of large electrostatic wakefields in these plasmas using a train of ultra-intense laser pulses. We also present an analysis of the resonant mechanism of this excitation based on consideration of phase space trajectories.

In Part II, we consider the transition from linear Resonance Absorption to non-linear absorption processes in a linear electron density profile as the intensity of the incident radiation increases and the scale length of the density profile decreases. We find that the electron motion excited by an electrostatic field exhibits some extremely complicated dynamics with bifurcations to period doubling and chaotic motion as the strength of the driving field is increased or the density scale length is decreased. We also present some results obtained from particle simulations of these interactions.

Declaration

I declare that the following thesis is a record of the research carried out by me, that the thesis is my own composition, and that it has not previously been submitted in application for a higher degree.

Certificate

I hereby certify that the candidate has fulfilled the conditions of the Resolutions and Regulations appropriate for the degree of Doctor of Philosophy in the University of St Andrews and that the candidate is qualified to submit this thesis in application for that degree.

22/9/94

date

signature of supervisor

Copyright

Postgraduate Career

I was admitted into the University of St. Andrews as a research student under Ordinance General No. 12 in October 1990 to work on the theory of laser-plasma interactions under the supervision of Professor R A Cairns. I was admitted under the above resolution as a candidate for the Degree of Ph. D. in October 1991.

Acknowledgements

My time in St. Andrews has seen many changes in my life and the memories will stay with me forever. I would like, therefore, to thank the following for their contributions.

I would like to thank Dr Robert Bingham of the Rutherford Appleton Laboratory for his enormous enthusiasm, encouragement and financial assistance. The results presented in Part I are the fruits of our collaboration. My thanks also go to my supervisor, Professor Alan Cairns, for his support and guidance. I would also like to thank Dr Graham Bell for his financial support in the fourth year of my studies and for useful discussions on Numerical Analysis. For their help with computational matters, I would like to thank Dr Patricia Heggie, Dr John Ball and Dr John Henderson.

I must also extend my thanks to the Science and Engineering Research Council (now the EPSRC) and the European Commission for their financial support. Also, in connection with my European activities, I would like to thank the plasma physics groups at Imperial College, Darmstadt and Pisa for their collaborative efforts and numerous stimulating discussions.

I would also like to take this opportunity to express my thanks to my parents, whose constant support and encouragement have helped me through my studies more than they realise.

My friends, Nikola and Ester Ruškuc also deserve my most sincere thanks for their support and friendship over the last two years. I hope that my departure from St. Andrews will not weaken our friendship.

Finally, writing a thesis has its share of ups and downs; there have been numerous occasions when I have identified with the writer of Ecclesiastes when he said, 'Of making many books there is no end, and much study wearies the body.' My biggest thanks must therefore go to my girlfriend, Tracy, for keeping me smiling during the 'downs' and her immeasurable help with the production of this thesis.

Contents

Preface

In the course of the last few years significant advances have been made in the field of high power, high intensity laser systems. Ten years ago, a typical tabletop system with a beam size of one centimetre was capable of producing pulses with powers $\sim$ 1GW. The same size system today can produce pulses with a peak power of over a thousand times that amount and may be focused to give an irradiance of the order of $10^{18}\,\mathrm{W/cm^2}$. The increases in peak power and irradiance in that time are due to the development of a technique known as Chirped Pulse Amplification[61, 38]. The major complication that arises in the production of short, high power laser pulses is the emergence of detrimental nonlinear effects as the pulse duration is reduced from the nanosecond regime towards the femtosecond regime. These effects may produce nonlinear phase retardations in the pulse which results in distortion of the wavefront and severe degradation of the beam quality. In the Chirped Pulse Amplification (CPA) scheme, a very short, low energy pulse ($\sim$ 1nJ) is temporally expanded by a factor of up to 10^4. This chirped pulse, with a time-dependent frequency, is then amplified in energy by up to 10 orders of magnitude and temporally recompressed by a factor of 10^4 again to reproduce a diffraction limited pulse of very short duration ($\sim$ 10–100fs) with an extremely high pulse energy. The key stages in the technique are clearly the pulse stretching and compression. Over the last 5 years[39], CPA systems which are based on diffraction grating pairs with positive group velocity dispersions have been developed for use in the stretching stage of the technique. These produce positively chirped pulses, ie the lower frequencies are at the head of the pulse and the

higher frequencies are at the tail. The recompression of these pulses may be performed by a diffraction grating pair with a suitable negative group velocity dispersion to account for the sum of the phase functions introduced by the pulse stretcher and the remainder of the laser system. This all-grating matched stretcher-compressor system was first demonstrated by Pessot et al. [49] when they stretched an 80fs pulse to over 80ps and then recompressed the pulse without introducing any temporal distortion.

The theoretical peak power attainable with the CPA technique may be estimated for various laser systems[48] by considering the ratio of the energy extractable from the laser to the minimum pulse duration. It is estimated that an Nd:glass laser system may produce a pulse of cross section $1.5 \times 10^{-20}\text{cm}^2$ and duration 30fs with a theoretical peak power of the order of 400TW/cm^2.

The availability of ultra-short, ultra-high intensity laser pulses brings a completely new regime of laser-matter interaction within the reach of laboratory experiments and has led to a renewed theoretical interest in this area. At such high laser intensities, the electric and magnetic fields associated with the laser pulse are very large and may be orders of magnitude larger than the Coulomb field that binds atomic electrons. Such a strong field is sufficient to strip the electrons from the atoms within the short duration of the pulse. Furthermore, the free electron quiver velocity in the laser field becomes ultra-relativistic, so that relativistic effects become dominant in laser-plasma interactions and can result in many interesting nonlinear effects.

This thesis is based on the study of this short-pulse, high-intensity laser-plasma interaction regime. The thesis is presented in two parts. In Part I, we investigate the implications of high-intensity lasers for the generation of electrostatic plasma waves in underdense plasmas, with particular application to plasma-based particle accelerators. In Part II, we investigate the effect of the increase in laser intensities available on the absorption of laser energy by a plasma with a linear density gradient. In particular, we investigate the electron dynamics in the intensity regime above that in which linear Resonance Absorption is an effective absorption mechanism.

Part I

Laser Wakefield Acceleration

Chapter 1

Introduction

1.1 Plasma-Based Accelerators

Present day linear electron accelerators can achieve accelerating fields of the order of a few MV/m. This technology requires huge acceleration distances ($\sim$ 100km) to produce particle energies of the order of 1TeV, this being the next energy regime of interest to particle physicists [25, 11, 7]. Lasers can produce extremely intense electric fields which, if they could be utilised in accelerators, would shorten the accelerating length required to produce particles at 1TeV. However, electromagnetic waves in vacuo are purely transverse and cannot therefore be used to impart energy to particles moving with a velocity close to the phase velocity of the wave. We, therefore, require a material medium to change the free space dispersion relations [36]. Four mechanisms have been proposed; the Laser Excited Cavity [46], the Inverse Free-Electron Laser [47], the Inverse Cerenkov Accelerator [30] and the Plasma Based Accelerators [33].

The concept of plasma-based accelerators has received much attention in recent years since plasmas are capable of supporting large electric fields ($\sim$ 100GV/m)[14]. Hence, a plasma-based accelerator would require an acceleration distance of only $\sim$ 10m to produce particles at 1TeV energies. Such an accelerator relies on the generation of large amplitude longitudinal plasma waves with a phase velocity close to the

velocity of light. Several mechanisms have been proposed for generating these waves in a plasma, the Plasma Beat Wave Accelerator (PBWA)[62] the Plasma Wakefield Accelerator (PWFA)[13] and the Laser Wakefield Accelerator (LWFA)[62]. A brief description of each of these is provided, along with an assessment of their relative merits.

1.2 Plasma Beat-Wave Accelerator (PBWA)

1.2.1 Mechanism

In the Beat-Wave scheme, a relativistic plasma wave is generated by the ponderomotive force associated with the beat envelope of two co-propagating laser beams of frequency ω_1 and ω_2 in the plasma. The beat frequency $\omega_2 - \omega_1$ is matched to the plasma frequency, ω_p, to resonantly excite the plasma wave. If the laser frequencies are much higher than the plasma frequency, the phase velocity of the plasmon is very close to the speed of light. Such a high phase velocity is ideal for accelerating particles to high energy. Also, the frequency of the plasma wave is independent of the wavelength so that the group velocity of the wave is zero. Thus, a high field, high phase velocity wave, which does not propagate away once it has formed, may be excited in the plasma.

Figure 1.1 shows a schematic for a modularised Plasma Beat-Wave Accelerator. Two copropagating laser pulses of slightly differing frequencies enter the accelera-

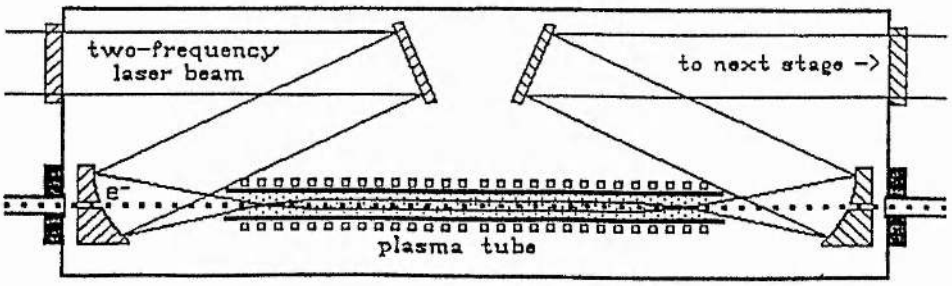

Figure 1.1: Schematic for a Modularised Plasma Beat-Wave Accelerator. After Chen (1990)[13].

tor module and are focused into the plasma tube. Immediately before these mode-matched beams enter the module ($\sim$ 10ns) a fully ionised, highly uniform plasma, with a density such that the plasma frequency resonates with the beat frequency of the laser pulses, is pre-formed in the plasma tube. A number of possible mechanisms

exist for creating the plasma, multiphoton ionisation being the most popular in current experiments. When the laser pulses enter the plasma tube, a large amplitude electrostatic plasma wave is excited in the plasma. Bunches of electrons, synchronised with the laser pulses, are then injected into the plasma tube from an external linac. The electrons which are trapped in the correct phase of the plasma wave are accelerated to higher energy until they outrun the plasmon oscillation and begin to experience a retarding field. It is at this point that the electrons should be extracted from the module. To achieve higher energies, the output electrons from the first module may be injected into a second module to repeat the acceleration process. In this way, a high energy electron beam may be produced.

1.2.2 Theory & Limitations

The fundamental parameters of the Beat-Wave Accelerator are the frequencies and wavenumbers of the laser radiation (ω_1, k_1) and (ω_2, k_2), the plasma frequency $\omega_p = \omega_2 - \omega_1$, plasma wavenumber $\mathrm{k}_p = \mathrm{k}_2 - \mathrm{k}_1$ and the laser pump strengths $\alpha_i = eE_i/m\omega_i c$. The size of the plasma wave generated is measured as the ratio of the density perturbation to the background density $\varepsilon = \delta n/n$. The maximum possible plasma wave electric field occurs when $\varepsilon = 1$ and is given by the cold plasma wave-breaking limit,

$$E_{p(max)} = \frac{mc\omega_p}{e}.$$

An expression can be obtained [13] for the plasma wave amplitude as a function of ε and the plasma density, n_0,

$$|E| = 0.96\varepsilon\sqrt{n_0[\mathrm{cm}^{-3}]}\ \ \mathrm{V/cm} \tag{1.1}$$

where the perturbation parameter ε satisfies,

$$\frac{\partial^2\varepsilon}{\partial t^2} + \omega_p^2\varepsilon = -\frac{1}{2}\, ik_p^2c^2\alpha_1\alpha_2\,. \tag{1.2}$$

This equation may be used to calculate the initial linear growth rate of the plasma wave to give,

$$\varepsilon = \frac{1}{4}\alpha_1\alpha_2\omega_p t\,. \tag{1.3}$$

In the absence of any other effects, the plasma wave would grow with the secular rate of equation(1.3) until $\varepsilon = 1$. This would give a maximum accelerating field, with $n_0 = 10^{18}\mathrm{cm}^{-3}$, of $E_{max} \simeq 1\mathrm{GV/cm}$. However, a number of effects do cause the wave to become saturated at a lower amplitude. The main saturation mechanism is the relativistic resonance detuning which occurs as the electrons in the plasma wave gain energy [51]. In the absence of other effects, relativistic detuning gives a saturation amplitude [51],

$$\varepsilon_{sat} = \left(\frac{16}{3}\alpha_1\alpha_2\right)^{\frac{1}{3}}\,. \tag{1.4}$$

Another saturation mechanism comes from the linear resonance detuning, due to non-uniformity in the plasma density. With the deviation from exact resonance density defined as Δn, the limit on the plasma wave amplitude is [24],

$$\varepsilon_{sat} = \frac{n_0}{\delta n}\alpha_1\alpha_2\,. \tag{1.5}$$

This linear amplitude saturation illustrates the high degree of plasma density uniformity required by the beat-wave mechanism. The plasma density must be uniform to within 0.1% if the linear detuning is not to dominate the relativistic effect. Collisional damping can be neglected when considering plasma wave saturation mechanisms, due to the high electron quiver velocities in the laser and plasmon fields.

Figure 1.2 shows the growth and saturation of a plasma beat-wave including the saturation mechanisms mentioned above.

In addition to the saturation amplitude of the plasmon, the stability of the structure is also of interest if this scheme is to be exploited for particle acceleration. The key to the stability of the plasmon lies, again, in the fact that it is excited resonantly

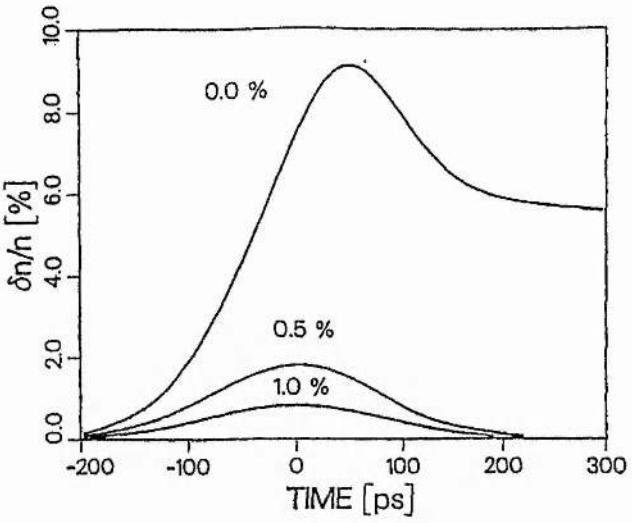

Figure 1.2: Plasma wave amplitude for values of linear detuning $\Delta n/n = 0, 0.5$ and $1.0\lambda_0 = 1.064\mu$m and $\lambda_1 = 1.053\mu$m, with $I_0 = I_1 = 2 \times 10^{14}\,\mathrm{W/cm^2}$ and a pulse FWHM of 200ps. After Dyson(1991)[24]

over a number of plasma periods. On such a timescale, ion dynamics begin to play a significant role in the response of the plasma. The timescale of the ion motion is of the order of ω_{pi}^{-1} and for typical ion densities this is around a few picoseconds. Therefore, in any interaction with a 'long' pulse (> 50ps) of laser radiation, ion effects become important. Stimulated Brillouin Scattering (SBS) is one example of a plasma instability that has a large growth rate in long homogeneous plasmas [28]. SBS excites ion acoustic waves which can destroy the coherence of the beat process and limit the stability of the plasma. It has been shown, [21], that the density ripple caused by ion waves, causes the beat plasmon to couple to other electrostatic modes in the plasma.

1.2.3 Experimental Results

Experiments to verify the BWA scheme have been mainly conducted by three research groups in the United States, the United Kingdom and Japan. Clayton et al [16] working at UCLA were the first to observe the fast beat-wave in 1985. They used a

CO_2 laser system generating the two wavelengths 10.6μm and 9.6μm with around 10J of energy in pulses of 1ns duration. The beat-wave was diagnosed using ruby laser Thomson Scattering and by analysis of the Stokes and anti-Stokes sidebands which developed on the light transmitted through the system. Their results indicated that a 1–3% plasma wave was excited.

More recently, Dangor et al [20] have conducted Beat-Wave experiments using the Vulcan Nd:Glass laser system at RAL. The two laser wavelengths used in this system are 1.053μm (YLF) and 1.064μm (YAG), each beam being of duration 200ps and energy 50J, focused to a spotsize of 200μm. The advantage of using the shorter wavelength radiation lies in the high relativistic $\gamma(=\omega_0/\omega_p)$ associated with the phase velocity of the plasma wave generated. A higher γ factor (and hence a higher phase velocity) being better suited to the acceleration of injected electrons. Using the detection of anti-Stokes sidebands and working with an estimated interaction length of 5mm, a 1% plasmon was inferred. A model with relativistic detuning as the main saturation mechanism, predicts a 9% plasma wave for the pulse parameters used in this experiment [24] which remains stable for a long time.

The experimental observation of the sidebands showed only a 50ps lifetime. The authors attribute the lower saturation amplitude observed in the experiment to the modulational instability[40].

The Japanese group are working with a CO_2 laser system operating on the lines 10.6μm and 9.57μm [34]. The mode-matched laser beams are focused to 1mm to give an intensity $I_{1,2} \geq 2 \times 10^{13}\,\mathrm{W/cm^2}$. This system achieved a 5% plasma beat-wave which corresponds to an electric field of 1.5GV/m at the resonant density $n_0 = 1.1 \times 10^{17}\,\mathrm{cm^{-3}}$. More recently, Clayton et al [17] have reported the first results showing the acceleration of injected electrons by a plasma beat-wave. They used a CO_2 laser system operating on the lines 10.59μm and 10.29μm to give a resonant plasma density $n_0 = 8.6 \times 10^{15}\,\mathrm{cm^{-3}}$. Bunches of 2.1MeV electrons were injected into the plasma from an rf linac in 20ps pulses. The energy detection limit of the

system for the accelerated electrons was 9.1MeV and electrons were detected at this energy, suggesting acceleration had taken place in an 8% plasma beat-wave over the interaction length of 10mm. Independent optical diagnosis of the plasma wave, however, suggested that the actual beat-wave amplitude was $\varepsilon \sim$ 15–30% which suggests that some of the injected electrons may have been accelerated to 20MeV. This experiment proved the principle of the Beat-Wave Accelerator scheme and should lead to an increase in research activity in this area.

1.3 Plasma Wake-Field Accelerator (PWFA)

1.3.1 Mechanism

In the Plasma Wakefield Accelerator scheme, [14, 15], the large amplitude longitudinal plasma wave is excited by a sequence of bunched high energy electrons. The streaming electrons lose energy to the background plasma by exciting a wake plasma wave which may then be utilised to accelerate a trailing beam of lower energy electrons. If the longitudinal spread of each driving electron bunch is small compared to the plasma frequency, the bunch may be considered as a negatively charged macroparticle expelling plasma electrons and leaving an electrostatic charge separation in its wake. The plasma electrons rush in to neutralise this charge imbalance, overshoot and oscillate at the natural frequency of the plasma, ω_p. Since the wave phase velocity must be the same as that of the driving bunch ($\approx c$), the plasma wave has a wavenumber $k_p = \omega_p/c$, as in the beat-wave case.

The injected, accelerated bunch creates its own wakefield in the plasma and if this is adjusted to be as large as the original wake and 180° out of phase with it, the wakes will cancel each other transferring all the original wake energy to the trailing beam.

1.3.2 Theory and Limitations

If we consider a driving electron beam of length d and charge density $\rho(z)$ in a one-dimensional model, the problem is time-independent in the beam frame. In this frame, where the driving electron beam and the wake wave are stationary, the cold plasma streams past the beam with a velocity, u, and is set into oscillation with a velocity, v, and perturbed density, δn.

The model equations of momentum conservation, continuity and Poisson's equation take the form,

$$mu\frac{\partial v}{\partial z} = -eE \tag{1.6}$$

$$n_0\frac{\partial v}{\partial z} + u\frac{\partial(\delta n)}{\partial z} = 0 \tag{1.7}$$

$$\frac{\partial E}{\partial z} = 4\pi\,\rho(z) - 4\pi e\delta n \tag{1.8}$$

where n_0 is the background plasma electron density and E is the wake electric field. Manipulating these equations, we can obtain the solution for E[13],

$$E(z) = 4\pi\int_0^z \rho(z')\cos\left[k_p(z-z')\right]\,\mathrm{d}z' \tag{1.9}$$

where the magnitude of E can be seen to depend on the charge distribution in the driving electron beam.

The energy transfer process from the driving beam to the trailing beam is characterised by the transformer ratio, R. This is defined as

$$R \equiv \frac{E_+}{E_-}, \tag{1.10}$$

where E_- is the peak decelerating field experienced by the driving electron beam and E^+ is the peak accelerating field in the wake. The physical significance of the transformer ratio is that the energy gained by the trailing beam, ΔW, is given by $\Delta W \simeq RW_0$, where W_0 is the energy of the driving beam. It can be shown [2, 12, 54] that for any finite length driving bunch with a uniform charge distribution ρ, the maximum value of the transformer ratio is 2. This poses a limit to the energy gain in the PWFA scheme. However, higher transformer ratios may be obtained by using a beam with a tailored charge distribution [15] or by operating in the nonlinear regime [35]. The variation of the transformer ratio with the charge distribution in the driver bunches gives the maximum R when the charge is distributed such that all particles

in the bunch see the same retarding field [3]. This dependence means that the driving bunch should have a rise time that is long compared to the plasma period and falls off very rapidly. Triangular beam profiles have been suggested and would lead to a limit on the transformer ratio of $2\pi N$, where the rise of the bunch profile is over N plasma periods. Thus the most effective driving bunches are very much longer in the axial direction than in the radial. This, unfortunately, makes the bunch susceptible to nonlinear radial forces and undermines its stability as it propagates through the plasma. These problems may be minimised by operating with an underdense plasma.

1.3.3 Experimental Results

Experiments to investigate the PWFA scheme have been carried out at the Argonne National Laboratory in Illinois, USA. [53, 52] In a typical case, a linac produced a 21MeV driving bunch of electrons of duration 6psecs with a full width of 15psecs. A witness beam at 15MeV was also produced, with a variable path length to the plasma so it could be time delayed by 10nsecs relative to the driving force. This time delay enabled the positioning of the witness beam in the plasma wake produced by the driving bunch. The results from these experiments indicated that an accelerating gradient of a few MeV/m had been excited in the plasma.

A program of research is continuing at the Argonne National Laboratory with the Argonne Wakefield Accelerator (AWA) program. This is a new facility which is currently under construction. It is designed to provide 100 bunches of electrons at 20MeV. Each bunch will have a full width of 20psecs. The witness beam, at 4MeV, will be placed an arbitrary time behind the drive bunch, up to 10nsecs. The initial experiments planned for the AWA facility are intended to experimentally verify an effect called 'plasma blowout'. Unlike the cases studied to date, where coherent plasma waves excited by the drive beam generate an accelerating field, the blowout concept is a transient effect. If the drive pulse is sufficiently intense, electrons are expelled from the volume of the beam. As they rebound they should produce very

strong accelerating fields of the order of 1GV/m or higher. An important feature of this mechanism is its linear focusing.

1.4 Laser Wake-Field Accelerator (LWFA)

1.4.1 Mechanism

In the Laser Wake-Field Accelerator scheme [62, 59, 27], a large amplitude plasma wave is excited by a single, ultra-short (< 1psec), high intensity ($> 10^{18}\mathrm{Wcm}^{-2}$) laser pulse. The pulse duration is shorter than the plasma period so that the ponderomotive force associated with the pulse gives a substantial impulse to the plasma electrons. These electrons then oscillate at their natural frequency to produce the wake plasmon. The physical mechanism of the excitation of a large amplitude plasma wave by an ultra-short laser pulse is shown in Figure 1.3. The short laser pulse provides both

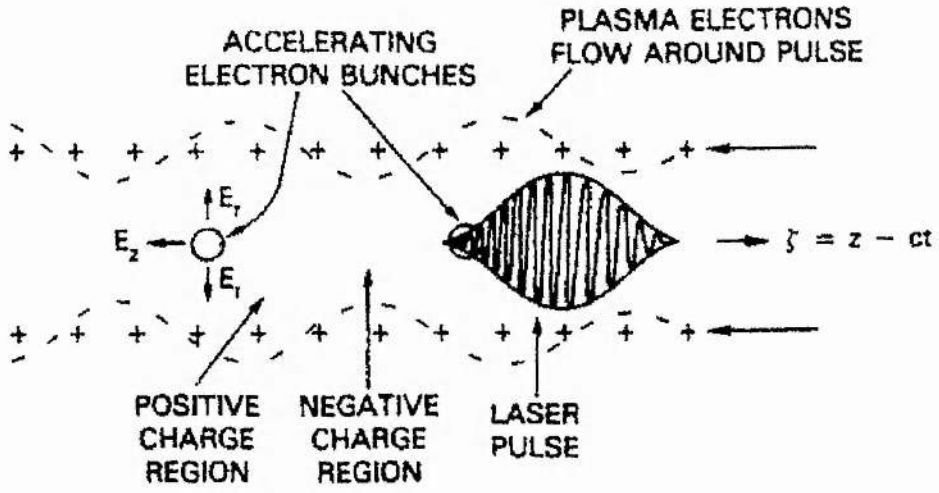

Figure 1.3: Schematic of the Laser Wake-Field Accelerator. After Sprangle (1988) [59]

a radial and an axial ponderomotive force on the plasma electrons and in this sense acts as a negatively charged macroparticle. As the plasma electrons flow around the laser pulse, large amplitude plasma waves are generated. The mechanism is therefore similar to the Plasma Wakefield Accelerator.

1.4.2 Theory & Limitations

The interaction of an ultra-short laser pulse with a plasma may be modelled in a similar way to the interaction of an electron bunch with a plasma in the PWFA scheme. In the case of the LWFA, the laser pulse is represented by a vector potential pulse strength, a_0, which depends on the wavelength and intensity of the laser pulse. For very short laser pulses ($I > 10^{18}\,\mathrm{W/cm^2}$), the value of a_0 is greater than unity which implies that the electron quiver motion in the laser field is highly relativistic and nonlinear. It can be shown [55] that the maximum wakefield amplitude generated by a linearly polarised laser pulse in the 1-D limit is,

$$E_{max}\,[\mathrm{GeV/m}] \simeq 3.8 \times 10^{-8}\,(n_o\,[\mathrm{cm^{-3}}])^{1/2}\frac{a_0^2}{\left(1+\frac{a_0^2}{2}\right)^{1/2}}\,, \tag{1.11}$$

where n_0 is the plasma density in $\mathrm{cm^{-3}}$ and a_0 is the dimensionless pulse strength. This accelerating gradient may then be utilised to accelerate a trailing electron beam. The acceleration distance in the LWFA may be limited by three effects. Firstly, the Rayleigh diffraction length limits the distance the laser pulse can travel in a plasma before it suffers too much diffraction to generate a coherent plasmon. This effect limits the interaction length to $L_d = \pi Z_R$ where Z_R is the vacuum Rayleigh length and is defined by $Z_R = \pi r_0^2/\lambda_0$. Diffraction effects can therefore severely limit the acceleration length for short wavelength / large spotsize laser pulses. Secondly, there exists a phase detuning distance over which the accelerated particles and the plasmon become shifted 90° out of phase. This is due to the difference between the velocity of the electrons and the wakefield phase velocity. The phase detuning distance may be estimated by considering the distance required for an electron to slip from the top to the bottom of the plasma wave potential. If the velocity of the electron is $\approx c$ and the phase velocity of the plasma wave is $v_{ph} = c(1-\frac{\omega_p^2}{\omega^2})^{1/2}$, then the phase detuning distance is approximately [33], $L_{pd} \approx (\frac{\omega^2}{\omega_p^2})\lambda_p$. Finally, the laser depletion length is the propagation distance at which the energy in the plasma wakefield becomes comparable

to the energy in the laser pulse. For a laser pulse with electric field, E_L, and length, l_L, generating a wakefield, E_w, in the plasma, the laser depletion length is given [59] by $L_{ld} = E_L^2 l_L / E_z^2$. Of these three effects, the diffraction length, L_d, poses the most severe restriction on the interaction length for particle acceleration. It has been suggested [56, 57, 58, 59] that relativistic optical guiding may increase the diffraction length of intense laser pulses in a plasma. Optical self-guiding occurs when an intense laser pulse propagating through a plasma modifies the radial plasma density in such a way that the nonlinear refractive index falls off with increasing radial distance from the axis of propagation (ie. $\frac{\partial \eta}{\partial r} < 0$, where η is the refractive index.) This radial focusing of the laser pulse may balance the diffraction effect and hence allow a larger accelerating distance in the LWFA. A constant radius laser beam can be maintained in this way and the matching condition may be written as a condition on the laser power. The critical laser power necessary to achieve a diffraction–focusing matched beam is [60],

$$P_{crit} \simeq 17(\omega/\omega_p)^2 \text{ GW} \tag{1.12}$$

Sprangle et al. [57] have shown that relativistic optical guiding is more effective for longer laser pulses having slow rise times than for short pulses which are only weakly self–guided. However, for short pulses, with a pulse duration comparable to, or shorter than, a plasma period, the plasma has insufficient time to respond to the laser pulse and relativistic self–guiding does not occur. An alternative to relativistic self–guiding of pulses is to preform a radial density channel in the plasma before the pulse enters it [55]. The plasma channel can be formed by propagating a pre–pulse of either a low–intensity laser pulse or a low–current electron beam through the plasma. The pre–pulse expels the plasma from the axis of propagation leaving a density depletion that can guide the wakefield generating, high intensity, laser pulse. A numerical analysis [26] has investigated the possible use of density channel guiding via computer simulations. It was shown that, using this technique, a laser pulse with

a duration comparable to the plasma period could be held reasonably well collimated over distances of the order of ten times the diffraction length.

1.4.3 Experimental Results

The first proof–of–principle experiment for the LWFA scheme was recently performed at the National Laboratory for High Energy Physics in Japan [42]. In their experiment, the Japanese group used a laser system which could produce light at wavelength $\lambda_0 = 1.052\mu$m and power of $\simeq$ 1TW in a pulse of 1psec duration. The pulses were focused to an intensity $I_o \simeq 1 \times 10^{18}$ W/cm^2 and directed into a plasma of density $n_0 = 2.415 \times 10^{15}$cm^{-3}. A 15J, 200psec burst of electrons from a linear accelerator could be passed through a magnetic field to select those electrons at 1MeV. These electrons were then injected into the plasma wakefield generated by the laser pulse and the energy spectrum of the electrons emerging from the plasma was analysed. Some electrons were detected with energies as high as 18MeV, which suggests an accelerating gradient of 1.7GeV/m in the plasmon over the interaction distance of 1cm. A further experiment is now planned using a 10TW table–top laser system to investigate the highly nonlinear regime.

1.5 Summary

We have briefly reviewed the three main schemes for plasma–based accelerators. The PBWA scheme is the most mature, but it is susceptible to a number of plasmon saturation mechanisms. These include relativistic detuning, mode coupling, modulational instability and other laser–plasma instabilities with a growth rate of the order of the plasma frequency.

The PWFA scheme has the advantage that a high–energy electron beam will not degrade as quickly as a laser pulse when it propagates in a plasma. The difficulties with the PWFA scheme are related to beam technology, since shaped driving and injected beams are required to obtain a high transformer ratio. The driving beam is also required to be of a high–energy to drive the plasma wave and may require access to large linear accelerators.

The main advantage of the LWFA is that it uses a single pulse to pump the wake plasmon and therefore avoids the resonance conditions inherent in the PBWA. The drawbacks of the LWFA are again technological ones. The pulse used in the LWFA must be very short, yet still transfer a significant amount of energy to the plasma electrons. This requires very high intensity laser pulses, which are only now becoming available.

In the next Chapter we derive the self–consistent coupled equations describing the interaction of a laser pulse with a homogeneous plasma in 1D geometry.

Chapter 2

Model for Laser Wakefield Generation

2.1 The Model Equations

We now derive the 1-D model equations[22] for the self-consistent propagation of a laser pulse through a uniform cold plasma. In this model, the plasma is treated using one-fluid, cold relativistic hydrodynamics and the laser pulse is represented via Maxwell's equations. The model employs the 'quasi-static'[58] and 'envelope' approximations to obtain a set of two coupled nonlinear equations describing the self-consistent evolution of the vector potential of the laser pulse envelope, a_0, and the scalar potential of the plasma wake-field, Φ. In the following analysis we use the subscript $\perp$ to denote the x-y plane and the subscript z to denote the direction parallel to the z-axis. The laser pulse propagates in the $\hat{z}$ direction with a vector potential $A_\perp$ perpendicular to $\hat{z}$ and the plasma electric field is derived from the scalar potential in the longitudinal direction.

We begin by considering the equation for the momentum of the electron fluid,

$$\left(\frac{\partial}{\partial t} + v_z \frac{\partial}{\partial z}\right) \mathbf{P} = -e\left[\mathbf{E} + \frac{1}{c}\mathbf{v} \times \mathbf{B}\right] \tag{2.1}$$

where $\mathbf{P}$ is the electron momentum, $\mathbf{E}$ is the electric field, $\mathbf{v}$ is the electron fluid velocity and $\mathbf{B}$ is the magnetic field which may be expressed as the curl of the vector potential.

We define,

$$\mathbf{E} = -\frac{1}{c}\frac{\partial \mathbf{A}_\perp}{\partial t} - \hat{z}\frac{\partial \phi}{\partial z}\ ;\ \mathbf{B} = \nabla \times \mathbf{A}_\perp;\ \ \mathbf{A}_\perp = \hat{x}A_x + \hat{y}A_y, \tag{2.2}$$

and recalling that,

$$\mathbf{P} = m_0\gamma\mathbf{v},\ \gamma = \left(1 + P^2/m_0^2c^2\right)^{1/2}, \tag{2.3}$$

we examine the perpendicular component of equation (2.1). If we write the momentum $\mathbf{P} = \mathbf{P}_\perp + \mathbf{P}_z$ the perpendicular component of equation (2.1) gives,

$$\frac{\partial}{\partial t}\left(\frac{P_\perp}{m_0c} - \frac{e}{m_0c^2}A_\perp\right) = 0\,. \tag{2.4}$$

This suggests the normalisation,

$$\frac{e}{m_0c^2}\mathbf{A}_\perp \equiv \mathbf{a}(z,t)\,. \tag{2.5}$$

The first of the 1-D model equations is the parallel component of equation (2.1). We therefore require expressions for v_z, P_z and $(\mathbf{v}\times\mathbf{B})_z$. To find expressions for v_z and P_z, we use the relationships in (2.3) and (2.4) to write,

$$\gamma^2 = 1 + a^2 + \frac{P_z^2}{m_0^2c^2} \tag{2.6}$$

and we write γ as the product of laser and plasma contributions,

$$\gamma = \gamma_a\gamma_z \tag{2.7}$$

where,

$$\gamma_a = \left(1 + \mathbf{a}^2\right)^{1/2}; \quad \gamma_z = \left(1 - \beta^2\right)^{-1/2} \tag{2.8}$$

with $\beta = v_z/c$.

This allows us to write,

$$\gamma_a^2 \gamma_z^2 = \gamma_a^2 + \frac{P_z^2}{m_0^2 c^2} \tag{2.9}$$

$$P_z = m_0 c \gamma_a \sqrt{\gamma_z^2 - 1} \tag{2.10}$$

and from the relationship (2.3),

$$|v_z| = c \left\{ \frac{\sqrt{\gamma_z^2 - 1}}{\gamma_z} \right\}. \tag{2.11}$$

To obtain an expression for $(\mathbf{v} \times \mathbf{B})_z$, we use the relationships (2.2) and (2.5) to obtain,

$$(\mathbf{v} \times \mathbf{B})_z = \frac{m_0 c^3}{2\gamma e} \frac{\partial a^2}{\partial z}. \tag{2.12}$$

Hence, the parallel component of equation (2.1) is,

$$\frac{1}{c}\frac{\partial}{\partial t}\left(\gamma_a \sqrt{\gamma_z^2 - 1}\right) + \frac{\partial}{\partial z}\left(\gamma_a \gamma_z\right) = \frac{\partial \Phi}{\partial z} \tag{2.13}$$

where we have made the normalisation,

$$\frac{e}{m_0 c^2}\phi \equiv \Phi. \tag{2.14}$$

The equation of continuity in density,

$$\frac{\partial n}{\partial t} + \frac{\partial \left(n v_z\right)}{\partial z} = 0 \tag{2.15}$$

gives in this case,

$$\frac{1}{c}\frac{\partial n}{\partial t} + \frac{\partial}{\partial z}\left(\frac{n\sqrt{\gamma_z^2 - 1}}{\gamma_z}\right) = 0 \tag{2.16}$$

where $n = n_0 + \delta n$ is the plasma density.

Poisson's equation for the electric field gives,

$$\frac{\partial^2 \Phi}{\partial z^2} = \frac{\omega_{p0}^2}{c^2}\left(\frac{n}{n_0} - 1\right) \tag{2.17}$$

where $\omega_{p0} = 4\pi\, n_0 e^2/m_0$ and n_0 is the initial plasma density.

To model the laser pulse, we use the transverse electromagnetic wave equation, derived from Maxwell's equations in the standard way to give,

$$\left(c^2\frac{\partial^2}{\partial z^2} - \frac{\partial^2}{\partial t^2}\right)\mathbf{a} = \omega_{p0}^2 \frac{n}{n_0}\frac{\mathbf{a}}{\gamma_a \gamma_z}. \tag{2.18}$$

In order to follow the interaction over many plasma periods, we now make a change of variables to measure the displacement in the frame of the travelling laser pulse. We define the new space and time variables ξ and τ where $\xi = z - v_g t$, τ is a slow time-scale and $v_g = \frac{\partial \omega_0}{\partial k_0}$ is the group velocity of the laser pulse. With this change of variables the parallel component of the momentum equation becomes,

$$\frac{\partial \Phi}{\partial \xi} = \frac{1}{c}\left(\frac{\partial}{\partial \tau} - v_g \frac{\partial}{\partial \xi}\right)\left(\gamma_a \sqrt{\gamma_z^2 - 1}\right) + \frac{\partial}{\partial \xi}\left(\gamma_a \gamma_z\right). \tag{2.19}$$

If we now apply the 'quasi-static' approximation, in which a near steady state is assumed, to equation (2.19) we obtain,

$$\frac{\partial \Phi}{\partial z} = -\beta_0 \frac{\partial}{\partial \xi}\left(\gamma_a \sqrt{\gamma_z^2 - 1}\right) + \frac{\partial}{\partial \xi}\left(\gamma_a \gamma_z\right), \tag{2.20}$$

where we have defined $\beta_0 = v_g/c$.

We may apply the same treatment to equation (2.16) to get,

$$-\beta_0 \frac{\partial n}{\partial \xi} + \frac{\partial}{\partial \xi}\left(\frac{n\sqrt{\gamma_z^2 - 1}}{\gamma_z}\right) = 0. \tag{2.21}$$

Equations (2.20) and (2.21) are integrable to give two constants of the motion. The

initial conditions used in the integration are $a = 0$, $\Phi = 0$ and $n = n_0$. With these conditions, equation (2.20) has the solution,

$$\Phi = \gamma_a \left(\gamma_z - \beta_0 \sqrt{\gamma_z^2 - 1} \right) - 1 , \tag{2.22}$$

and equation (2.21) gives,

$$n \left(\beta_0 \gamma_z - \sqrt{\gamma_z^2 - 1} \right) = n_0 \beta_0 \gamma_z . \tag{2.23}$$

The model may then be reduced to two coupled equations using the relations (2.22) and (2.23). Substituting from these relations, equation (2.17) becomes,

$$\frac{\partial^2 \Phi}{\partial \xi^2} = \frac{\omega_{p0}^2}{c^2} \frac{\sqrt{\gamma_z^2 - 1}}{\beta_0 \gamma_z - \sqrt{\gamma_z^2 - 1}} . \tag{2.24}$$

Finally, in the envelope approximation we assume a laser pulse of the form,

$$\mathbf{a}(z,t) = \frac{1}{2} a_0(\xi, \tau) e^{-i\theta} + c.c. , \tag{2.25}$$

where the amplitude function a_0 is now cast in the frame of the moving laser pulse, $\theta = \omega_0 t - k_0 z$, ω_0 and k_0 being the central frequency and wave-number respectively. Now τ is a slow time-scale such that,

$$a_0^{-1} \frac{\partial^2 a_0}{\partial \tau^2} \ll \omega_0^2 . \tag{2.26}$$

On substituting the form (2.25) into the wave equation, we may perform the differentiation on the fast time-scale exponential part of the pulse and rewrite the derivatives of the slow time-scale amplitude function in terms of the variables ξ and τ. We also use the relationship in equation (2.23) to obtain the final expression of the electro-

magnetic wave equation under the quasi-static and envelope approximations,

$$2i\omega_0 \frac{\partial a_0}{\partial \tau} + 2c\beta_0 \frac{\partial^2 a_0}{\partial \tau \partial \xi} + \frac{c^2 \omega_{p0}^2}{\omega_0^2} \frac{\partial^2 a_0}{\partial \xi^2} = -\omega_{p0}^2 H a_0 \tag{2.27}$$

where,

$$H = 1 - \frac{\beta_0}{\gamma_a \left(\beta_0 \gamma_z - \sqrt{\gamma_z^2 - 1} \right)}. \tag{2.28}$$

The final expression of this model is the coupled set equations (2.24) and (2.27). The model is valid for electromagnetic pulses of arbitrary polarisation and intensities $|a_0|^2 \geq 1$. Equation (2.24) has been solved by Tsintsadze[63] for the limiting case $\beta_0 = 1$ using a given pump. The coupled system, again with $\beta_0 = 1$, has been considered by Bulanov et al.[9]. Our model for the general case has been investigated by a previous worker[1], but with some apparent computational inconsistencies. In the next section, a numerical code for the solution of the set (2.24) and (2.27) is described and an account is given of the development history of this code to date.

2.2 Computer Program for the Numerical Solution of the Model Equations

2.2.1 Description

A computer program for the self-consistent numerical solution of equations (2.24) and (2.27) had been developed by a previous worker [1]. This program uses a simple predictor-corrector pair to integrate Poisson's equation on a numerical grid, working back from the head of the laser pulse where the initial conditions are $\Phi = 0$ and $\partial\Phi/\partial\xi = 0$. At each grid point, the corrector is iterated until convergence is obtained. Equation (2.27) for the pulse envelope is solved using finite differencing techniques. The scheme involves replacing the differential operators in the equation by centered differences and writing the result as two coupled equations for the real and imaginary parts of a_0. These equations are then solved in matrix form by Gaussian Elimination. The centered differences method is an implicit method and is therefore unconditionally stable. The time centering of the equations requires an estimate of Φ at the next time level. The code therefore operates according to the following procedure for each time step. First, the scalar potential Φ is evaluated for the current time, given the form of a_0. This is then used to obtain the first estimate of a_0 at the next time level, which is in turn used to find an estimate of Φ at the next time level. The estimate of Φ may then be used in the time centered equation for a_0.

2.2.2 Numerical Method

As with most numerical work, it is convenient to normalise the space and time variables to some dimensionless quantities. In this case there are a number of possible dimensionless groupings and the chosen normalisation is the one which gives the coefficients in the equation reasonable values. This is to avoid amplification of errors in

the difference relations. We therefore choose the following,

$$\begin{aligned} \frac{\omega_{p0}}{c}\xi &= X \\ \frac{\omega_{p0}^2}{\omega_0}\tau &= T \end{aligned} \tag{2.29}$$

With these normalisations, the envelope equation becomes,

$$\frac{1}{2}\left(\frac{\omega_{p0}}{\omega_0}\right)^2 \frac{\partial^2 a_0}{\partial X^2} + \beta_0 \frac{\omega_{p0}}{\omega_0}\frac{\partial^2 a_0}{\partial X \partial T} + i\frac{\partial a_0}{\partial T} = -\frac{1}{2}H a_0 \tag{2.30}$$

The centered difference scheme may be written in terms of the difference variable $a_j^n \approx a_0(X,T)$ where $X = j\,\Delta X$ and $T = n\,\Delta T$ as,

$$\begin{aligned} \frac{\partial a_j^n}{\partial T} &= \frac{a_j^{n+1} - a_j^n}{\Delta T} \\ \frac{\partial^2 a_j^n}{\partial X \partial T} &= \frac{1}{2\Delta X \Delta T}\left(a_{j+1}^{n+1} - a_{j-1}^{n+1} - a_{j+1}^n + a_{j-1}^n\right) \\ \frac{\partial^2 a_j^n}{\partial X^2} &= \frac{1}{2(\Delta X)^2}\left(a_{j+1}^{n+1} + a_{j-1}^{n+1} - 2a_j^{n+1} + a_{j+1}^n + a_{j-1}^n - 2a_j^n\right) \end{aligned} \tag{2.31}$$

These relations may now be substituted into equation (2.30) to give an equation in the difference variable which is complex. To verify the stability of this scheme, we may perform a Von Neumann analysis [45], which is based on a Fourier series equation. We substitute,

$$a_j^n = A\,\exp\left(imj\Delta X\right)\zeta^n \tag{2.32}$$

where A, ζ and m are constants and m is an integer.

This allows the growth of the m^{th} harmonic in the solution to be analysed, where $\zeta(m)$ is the growth factor. For stability, we require that the growth factor does not exceed unity for any of the modes in the solution. In the case of the envelope equation, the growth factor as a function of mode number is,

$$\zeta(m) = \frac{2N2\sin m\Delta X + N3 - 2N1\left(\cos m\Delta X - 1\right) - \frac{1}{4}H^n}{2N1\left(\cos m\Delta X - 1\right) + 2N2\sin m\Delta X + N3 + \frac{1}{4}H^{n+1}} \tag{2.33}$$

where,

$$\begin{aligned} N1 &= \frac{1}{2}\left(\frac{\omega_{p0}}{\omega_0}\right)^2 \frac{1}{2\left(\Delta X\right)^2}, \\ N2 &= \beta_0 \frac{\omega_{p0}}{\omega_0} \frac{1}{2\Delta X \Delta T}, \\ N3 &= \frac{1}{\Delta T} i. \end{aligned}$$

We can see from equation (2.33) that the numerator is always slightly smaller than the denominator and therefore the difference scheme is unconditionally stable.

The numerical solution of Poisson's equation begins by writing the second order differential equation as a system of two first order equations,

$$\begin{aligned} u' &= v \\ v' &= \left(\frac{\omega_{p0}}{c}\right)^2 G \end{aligned} \tag{2.34}$$

where $u = \Phi$, and $v = \frac{du}{d\xi}$ and

$$G = \frac{\sqrt{\gamma_z^2 - 1}}{\beta_0 \gamma_z - \sqrt{\gamma_z^2 - 1}}. \tag{2.35}$$

We use predictor equations of the form,

$$y_{j+1} = y_j + \frac{h}{2}(3f_j - f_{j-1}) \tag{2.36}$$

and the corrector form,

$$y_{j+1} = y_j + \frac{h}{2}(f_{j+1} + f_j) \tag{2.37}$$

for each of the equations (2.35).

2.2.3 Code Development

Porting to Sun Workstations

The first task for the current author was to port the code that existed at the Rutherford Appleton Laboratory (RAL), running on VMS/VAX operating system, to the Sun Workstations at the University of St. Andrews. The FORTRAN source code was supplied by RAL and proved to be largely compatible with the Sun FORTRAN compiler. However, difficulties arose with some parts of the transfer process. The main incompatibility arose with the graphical output routines. These make use of the Numerical Algorithms Group (NAG) Graphical Library and originally used a single precision implementation of the library. Since the code was last compiled at RAL, the NAG Graphics Library at both RAL and St. Andrews had been upgraded to a double precision implimentation. The code was therefore modified to work explicitly in double numerical precision in order to communicate properly with the new graphics routines. Figure 2.2 shows the output from this double precision version of the program for a typical symmetric Gaussian pulse. This is one of a series of tests that were performed on the code to verify that the results obtained using it agreed with the results of the original version held at RAL.

Confidence Checks

The final batch of confidence tests performed on the code were designed to reproduce the results of the previous worker [1],which demonstrate the effect of the Gaussian pulse shape on the excited wakefield. These tests demonstrated that, whilst the results for symmetric laser pulses showed the expected behaviour for short times, the results at longer times showed modulation of the trailing edge of the pulse envelope with the imaginary part of the solution exhibiting secular growth. The growth of the imaginary part of the solution of a_0 causes an anomalous increase in the magnitude of a_0 and an unrepresentative wake structure in the simulation. Figure 2.3 shows the output for a symmetric pulse at times $2T_p$ and $54T_p$. The result at time $2T_p$ is as expected [1]. However the result at the later time shows the growth of the imaginary part of a_0 and the effect that this has on the pulse envelope. The results for asymmetric pulses show a catastrophic failure in the solver for a_0. Figure 2.4 shows the output for a shaped Gaussian pulse with a sharp rise and a slower decay. The short time behaviour is again as expected with the pulse generating a nonlinear wake in the plasma. However, the result after 40 plasma periods shows that the output has been totally swamped by a blow–up in the imaginary part of the solution for the laser pulse envelope.

The time and space centered routines for the pulse envelope solver were checked in an extended debugging process. First the equations for the pulse and the plasma potential were decoupled by setting $H = 0$ on the right hand side of equation (2.27). The code was then retested with a symmetric Gaussian pulse at shorter time intervals. The results in Figure 2.5 show that these tests verified that the short time behaviour was correctly reproduced in the original tests. With this information, and the original test output, the error was deduced to lie in the imaginary part of the solution. This is because initially the imaginary part is zero and it only evolves after some interaction time. Therefore, the relevant lines of the program were scrutinised for possible sources of error.

A programming error was located in the code of the Gaussian Elimination routine

and was corrected. Initial results with the corrected code showed a slight improvement, but the imaginary part of the solution for a_0 continued to grow in a secular way and eventually swamped the output. After further scrutiny of the code, a second programming error was discovered in the same Elimination routine. When this error was corrected, the difficulty with the imaginary component of a_0 disappeared. Figure 2.6 shows the output from the corrected code for a symmetric laser pulse profile. The behaviour at time $t = 2T_P$ is similar to that in the results given by the original version of the program. However, after 54 plasma periods the overall maximum pulse amplitude remains at its initial value and, unlike the previous results, the pulse profile is also largely unchanged. This remains the case even after 200 plasma periods, showing this version of the code gives time stable results. Tests with asymmetric pulses using the corrected code also show good agreement with the results previously published [1]. Figure 2.7 shows the output for a pulse with a sharp rise and slower decay. At time $t = 0.4T_p$ the results are the same as those generated by the previous versions of the code. However, after 40 plasma periods the solution is no longer swamped by the imaginary part of a_0. The output shows the expected behaviour as described in previous work [1]. The laser pulse generates a nonlinear plasma wakefield and, inside the pulse, this field reacts back on the tail of the pulse to modulate the pulse profile.

The results from the corrected code appear to show all the behaviour expected from previous work. A final confidence check of the elimination routine in the code, involved using a 'black–box' routine from the lapack FORTRAN library available freely via netlib [44]. This version of the program uses a routine from the lapack library to perform the matrix inversion in the elimination subroutine. The lapack version was compiled and executed for some test cases to verify the correct operation of the code. The results show absolute agreement with the previous corrected version of the program. Figure 2.8 shows the output for a test case which reproduces exactly the pulse profile distortion observed in results published previously [1].

Re-evaluation of the Difference Scheme

Although the simulation code, now referred to as Sunfad, has been fully debugged and produces consistent results in the above comparative tests, some numerical error is still detectable in the output. At this stage, a re–evaluation of the finite difference scheme used in the code was conducted [29]. Figure 2.9 shows the typical variation of the mixed derivative term in equation (2.27) across the computational mesh. This spiky behaviour precludes any explicit finite difference scheme since, in order to satisfy the Courant condition for stability [18], the time step would be prohibitively small. We therefore confine this evaluation to schemes which are implicit and unconditionally stable. The Crank Nicholson [19] type scheme used in the code is second order accurate in both space and time and is the most accurate representation using only adjacent mesh points. However, in tests of advection, it has been observed that 'donor cell' or upstream differencing may give a more faithful result than even the Crank Nicholson scheme. Therefore a time centered, upstream spatial difference scheme was investigated for the solution of equation (2.27). Figure 2.1 illustrates this difference scheme on the computational mesh.

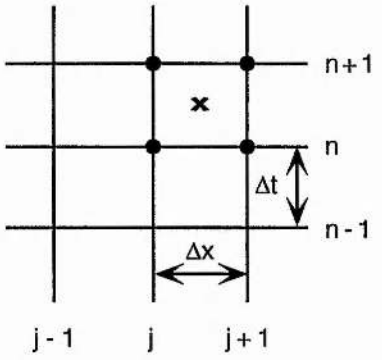

Figure 2.1: The upstream finite difference scheme

Upstream differencing also incorporates a diffusive smoothing of the profile which is not a cause for concern with symmetric Gaussian pulses, but may cause steep sided asymmetric pulses to be smoothed. Figure 2.10 shows the output from the

upstream version of the code for both symmetric and asymmetric pulses. For the symmetric pulse we see the same results as those generated by the Sunfad code, with the exception that the maximum pulse amplitude remains closer to its initial value throughout the simulation. In the case of the asymmetric pulse, we see that again the pulse maximum remains closer to its initial value and there are some differences in the fine detail from the corresponding results obtained with the Sunfad code. In particular, the head of the pulse shows no noticeable increase in amplitude and the detail around the spike in the tail of the pulse envelope is slightly different. Overall, however, the results show excellent agreement with those generated by Sunfad, with minor differences being attributable to the different numerical schemes.

2.3 Summary

In this chapter, we have presented a 1–D, cold, relativistic, fluid model for the laser–plasma interactions which lead to the generation of a wake plasmon. We have also described a numerical computer code, Sunfad, for the solution of the model equations and given an account of the program's development through the debugging and testing stages. The present code solves the model equations with an acceptable degree of stability and accuracy and faithfully reproduces results published previously [1]. These results show that the pulse envelope of long ($> c/\omega_p$) laser pulses is modified by the reaction of the wakefield. The distortion occurs around the wake-potential minimum, which is also a local maximum of the density perturbation δn. This behaviour is explained physically by the variation of the local group velocity within the pulse as the local density changes. The linear group velocity decreases as the density increases, and increases as the density decreases. Therefore, the light wave is locally slowed-down as it propagates up a density gradient and speeds up as it propagates down the density gradient. This causes photons to accumulate on one side of the gradient and modifies the pulse envelope accordingly. Recent work by Decker and Mori[23] has investigated the group velocity of large amplitude electromagnetic waves in a plasma. They show that for short pulses ($\leq c/\omega_p$) the group velocity of the laser pulse approaches the linear group velocity, $v_g = c\sqrt{\left(1 - \omega_p^2/\omega^2\right)}$. However, for longer pulses they find that the group velocity is subject to local modifications as parts of the pulse coincide with density maxima and minima. This is in excellent agreement with the behaviour in the results obtained with Sunfad and confirms the explanation offered by the previous worker[1]. Decker & Mori have also used their particle-in-cell simulation code to investigate the common assumption in Laser Wakefield Accelerator theoretical work that the phase velocity of the wakefield is equal to the group velocity of the laser pulse. They find that the assumption is true only for symmetric pulses with linear laser strengths ($|a_o| \leq 1$). Furthermore,

the pulse shape has a significant effect on the phase velocity of the wakefield. Pulses with a relatively long rise time and short fall give rise to wake velocities higher than the group velocity of the laser pulse, whereas pulses with a sharp rise and slower fall give wake phase velocities lower than the group velocity of the laser pulse. These results[23] cast a new light on the results reproduced by the Sunfad code. Since the energy gain in an accelerator is proportional to both the accelerating field strength and the acceleration distance, de-phasing between the particles and the wakefield poses a serious limitation to the energy gain available in any wakefield accelerator. For a given laser strength, it may be preferable to use a pulse profile which generates a lower-amplitude wakefield with a phase velocity closer to the light speed, rather than one which generates a larger-amplitude wake but with a lower phase velocity, and hence a shorter de-phasing distance.

The reaction of the plasma wakefield on the tail of long asymmetric pulses, as observed in simulations using Sunfad, suggests that some interesting behaviour may be found if two or more laser pulses are used instead of a single pulse. In the next chapter, we describe an extension to the theory of single pulse wakefield generation to include a train of several laser pulses. We also present some simulation results from the multiple pulse version of the Sunfad computer code.

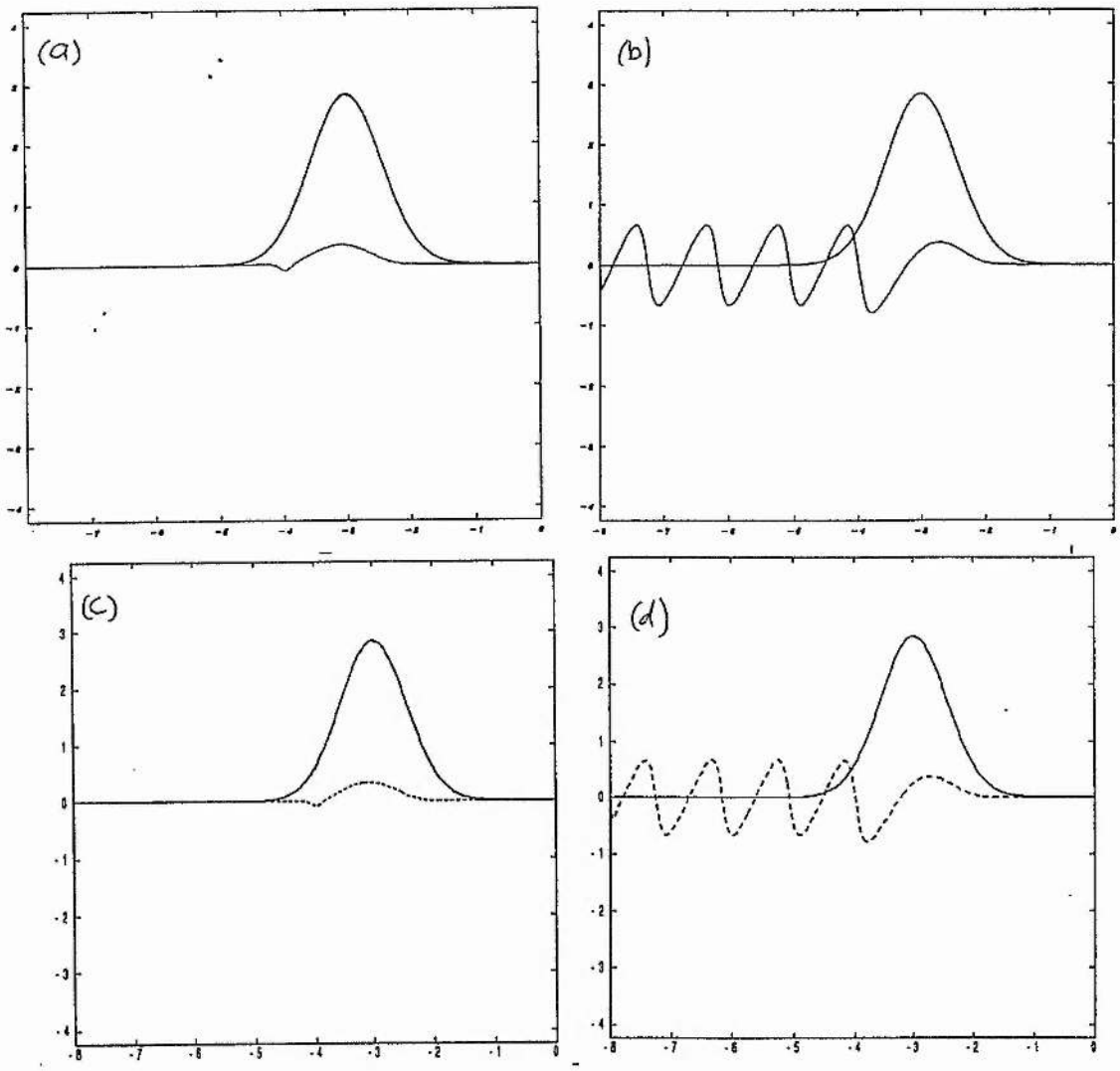

Figure 2.2: Simulation results showing the interaction of a symmetric Gaussian pulse with underdense plasma for the parameters $|a_o^{in}| = \sqrt{8}$, $\omega_{po}/\omega_o = 0.05$, Gaussian rise coefficient $\sigma_r = 5 \times c/\omega_{po} = 0.795$ and Gaussian fall coefficient $\sigma_f = 0.795\lambda_p$ at time $t = 6T_p$. (a) & (c) show the magnitude of the normalised vector potential $|a_o|$ (solid line) and the real and imaginary parts of $|a_o|$ (dashed lines). (b) & (d) show the magnitude of $|a_o|$ (solid line) and the wake-electric field E_w (dashed curve). The spatial coordinate is $\xi = z - v_g t$ normalised to the plasma wavelength, λ_p. (a) & (b) are from the original code at RAL and (c) & (d) are from the initial port to St. Andrews.

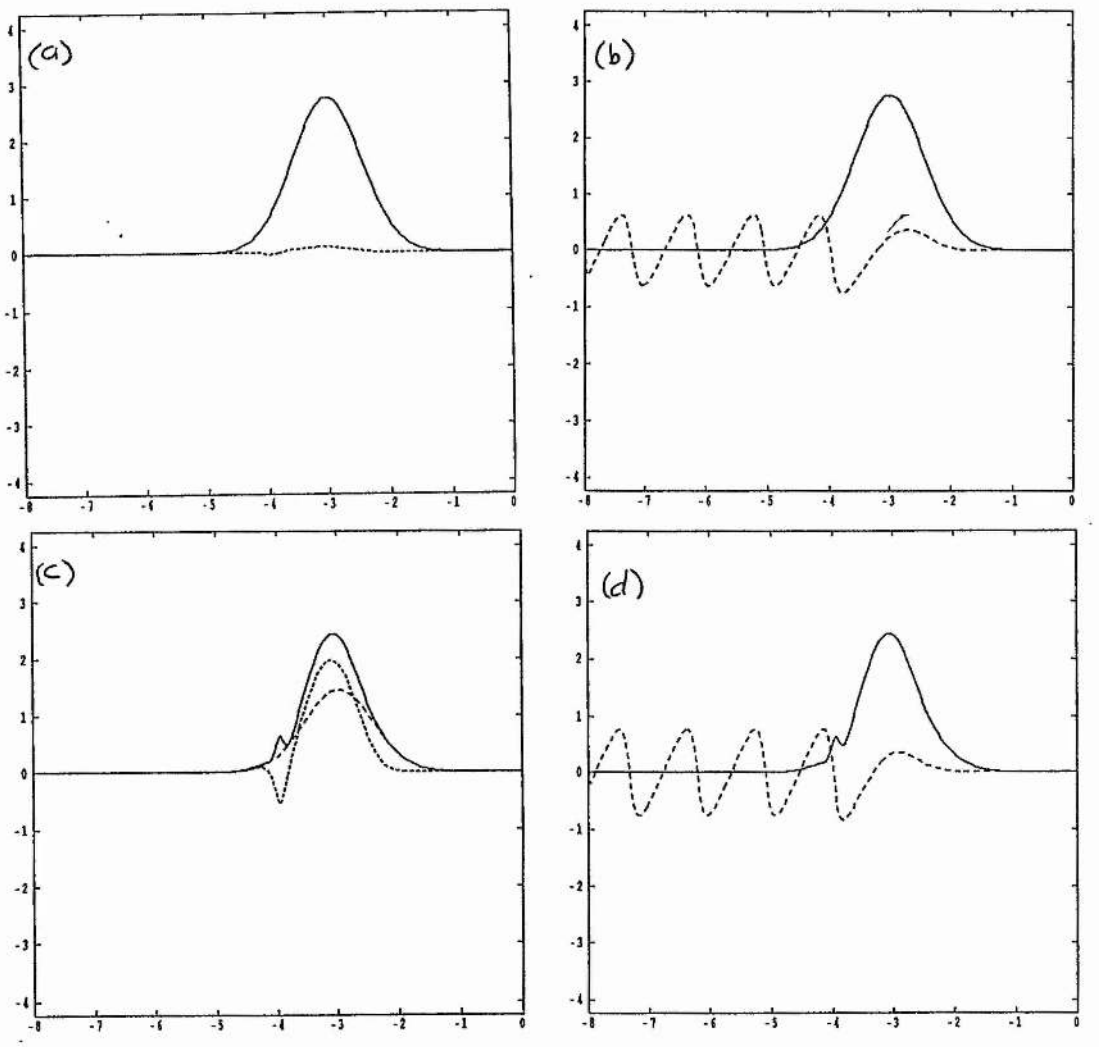

Figure 2.3: The values of the magnitude of the normalised vector potential $|a_o|$ (solid line) and the real and imaginary parts of a_o (dashed lines) with position ξ. Parameter values are $|a_o^{in}| = \sqrt{8}$, $\omega_{po}/\omega_o = 0.05$, $\sigma_r = \sigma_f = 0.795\lambda_p$ Curves (a) & (b) are for time $t = 2T_p$ and curves (c) & (d) are for time $t = 54T_p$.

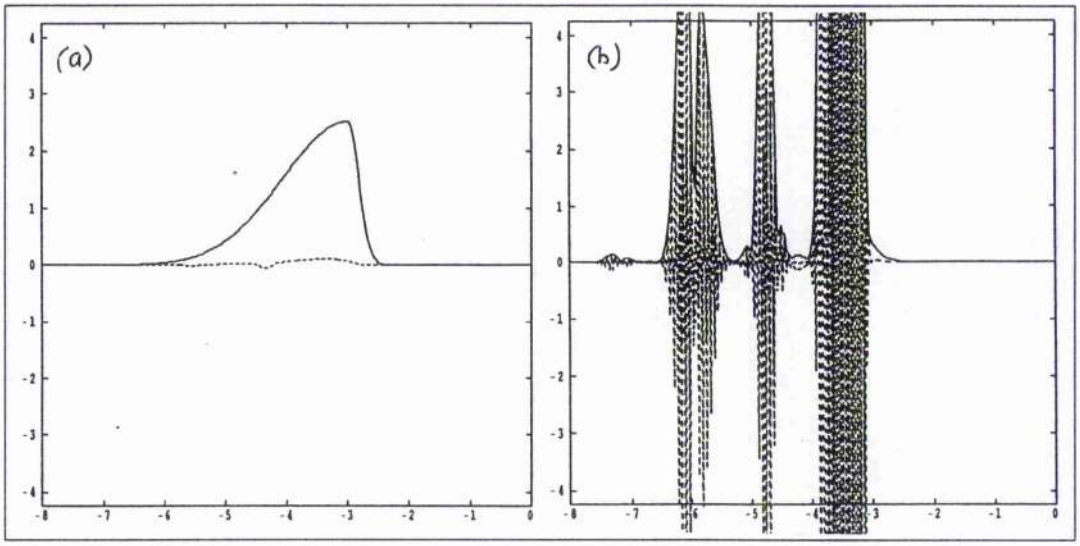

Figure 2.4: Test output showing the magnitude of $|a_o|$ (solid line) and the real and imaginary parts of a_o (dashed lines) for an asymmetric pulse with rise coefficient $\sigma_r = 0.25\lambda_p$ and fall coefficient $\sigma_f = 1.5\lambda_p$. (a) is at time $t = 0.4T_p$ and (b) at time $t = 40T_p$.

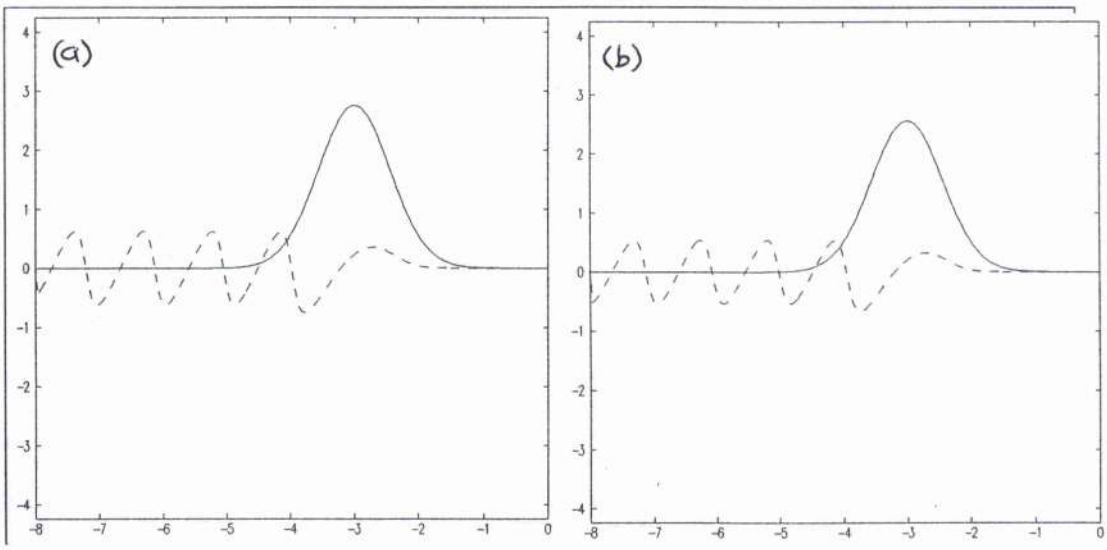

Figure 2.5: Results with $H = 0$ to decouple the pulse and wake potential equations. The magnitude of $|a_o|$ (solid line) and the plasma wakefield E_w (dashed line) are plotted against the position in the pulse frame, ξ. Simulation parameters are $|a_o^{in}| = \sqrt{8}$, $\omega_{po}/\omega_o = 0.05$, $\sigma_r = \sigma_f = 0.795\lambda_p$ for (a) time $t = 2T_p$ and (b) time $t = 8T_p$.

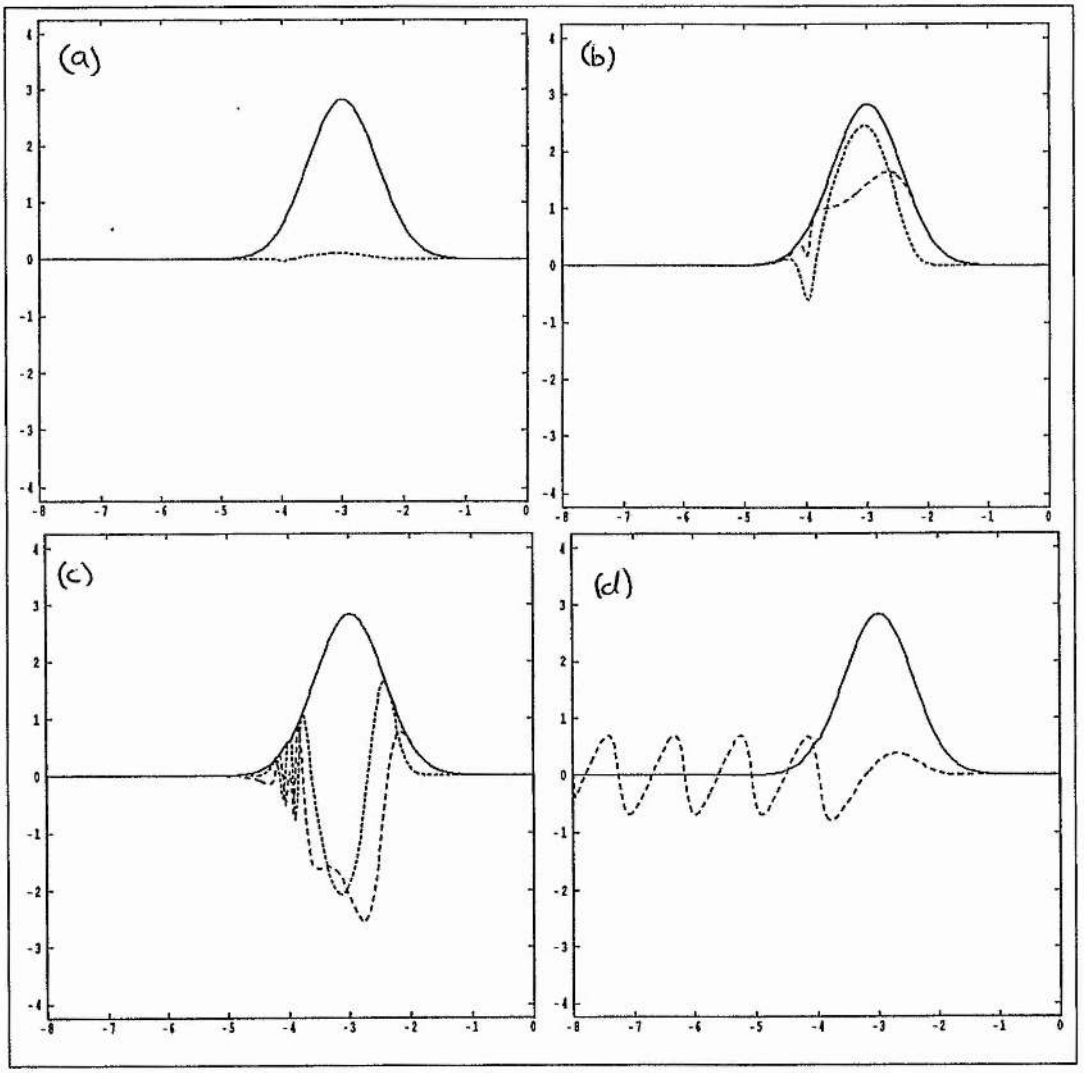

Figure 2.6: The magnitude of $|a_o|$ (solid line) and the real and imaginary parts of a_o (dashed lines) for a symmetric pulse at times (a) $t = 2T_p$, (b) $t = 54T_p$ and $t = 200T_p$. (d) shows the magnitude of $|a_o|$ and the wakefield E_w at time $t = 200T_p$. Parameter values are $|a_o^{in}| = \sqrt{8}$, $\omega_{po}/\omega_o = 0.05$, $\sigma_r = \sigma_f = 0.795\lambda_p$

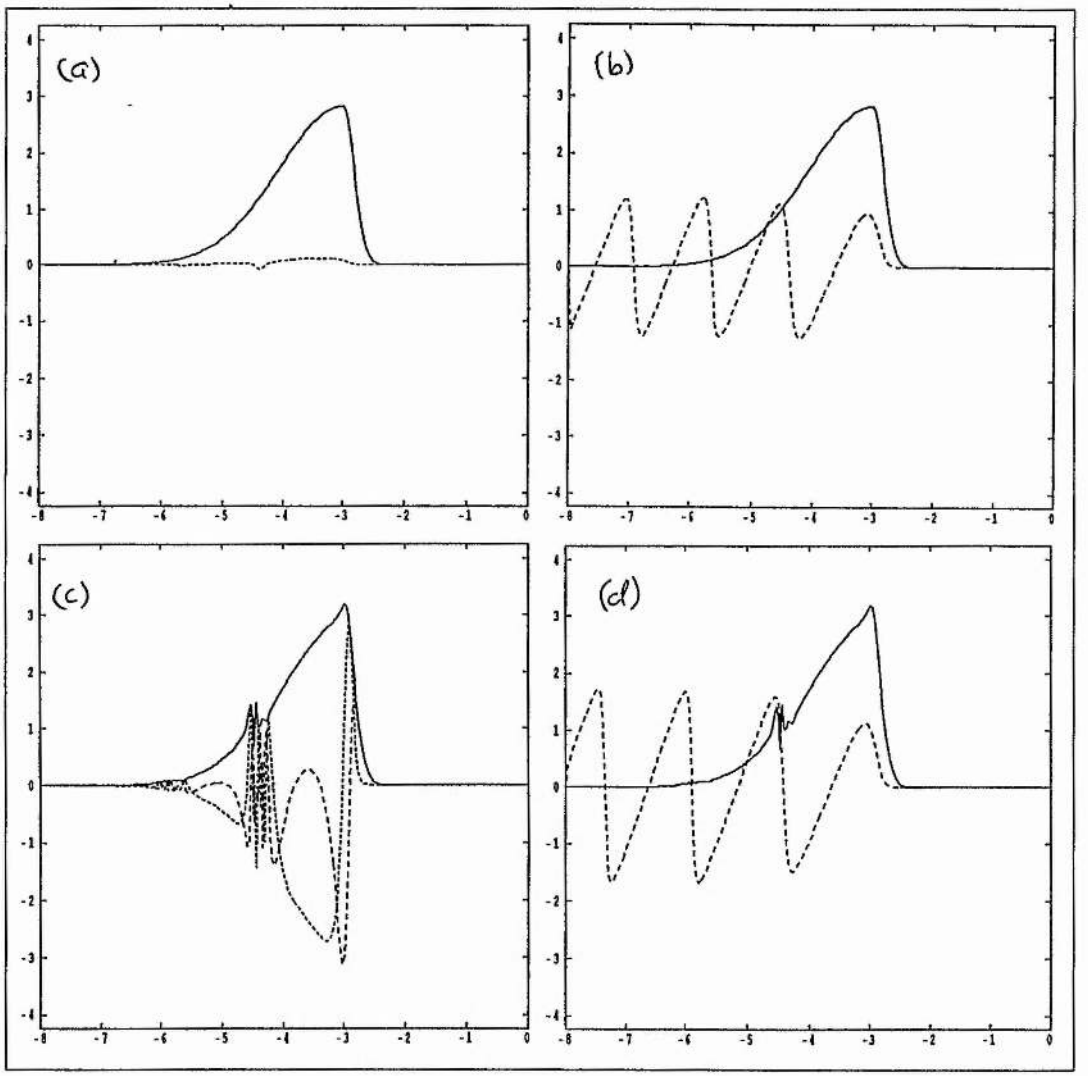

Figure 2.7: Results for an asymmetric pulse with $\sigma_r = 0.25\lambda_p$ and $\sigma_f = 1.5\lambda_p$. (a) & (c) show the magnitude of $|a_o|$ (solid line) and the real and imaginary parts of a_o (dashed lines). (b) & (d) show the magnitude of $|a_o|$ and the wakefield, E_w. (a) & (b) are at time $t = 0.4T_p$ and (c) & (d) are at time $t = 40T_p$.

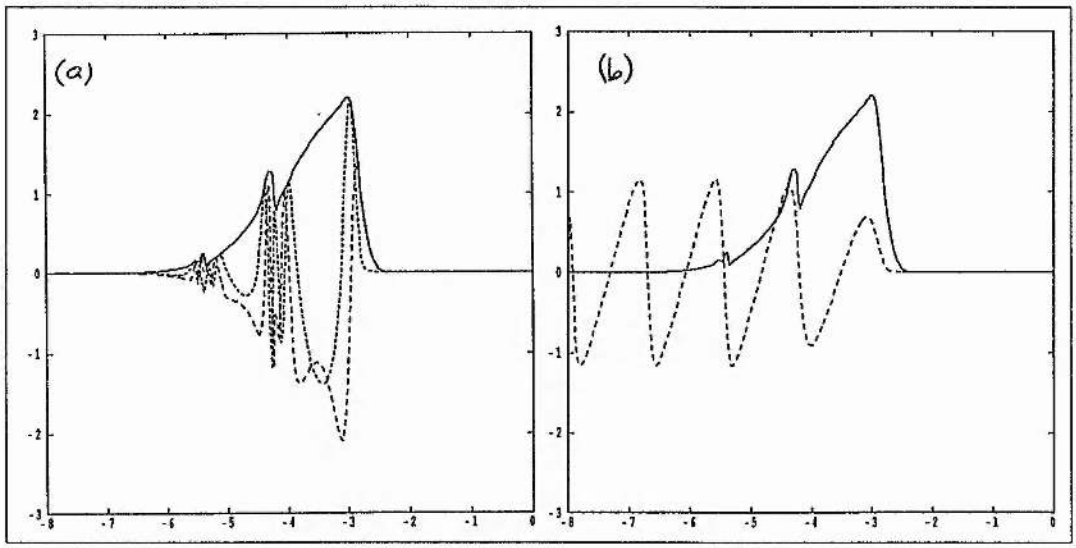

Figure 2.8: The values of the magnitude of the normalised vector potential $|a_o|$ (solid line) and (a) the real and imaginary parts of a_o and also (b)(dashed lines) the wakefield, E_w with position at time $t = 40T_p$. Parameter values are $|a_o^{in}| = 2.0$, $\omega_{po}/\omega_o = 0.05$, $\sigma_r = 0.25\lambda_p$ and $\sigma_f = 1.5\lambda_p$

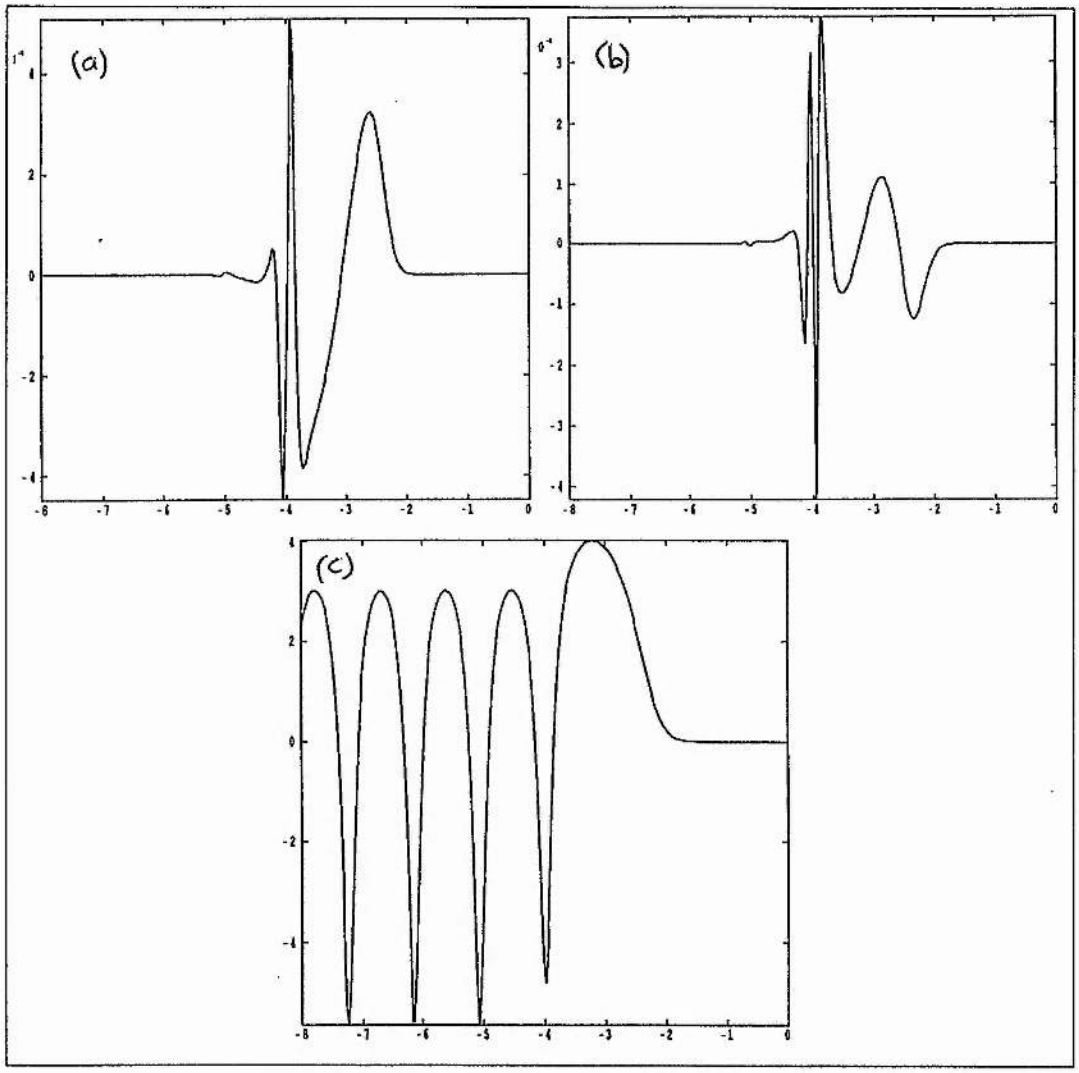

Figure 2.9: Illustration of the typical variation of the mixed derivative and H terms in equation (2.27). (a) shows the mixed derivative of the real part of a_o , (b) shows the mixed derivative of the imaginary part of a_o and (c) shows the variation of H across the computational mesh.

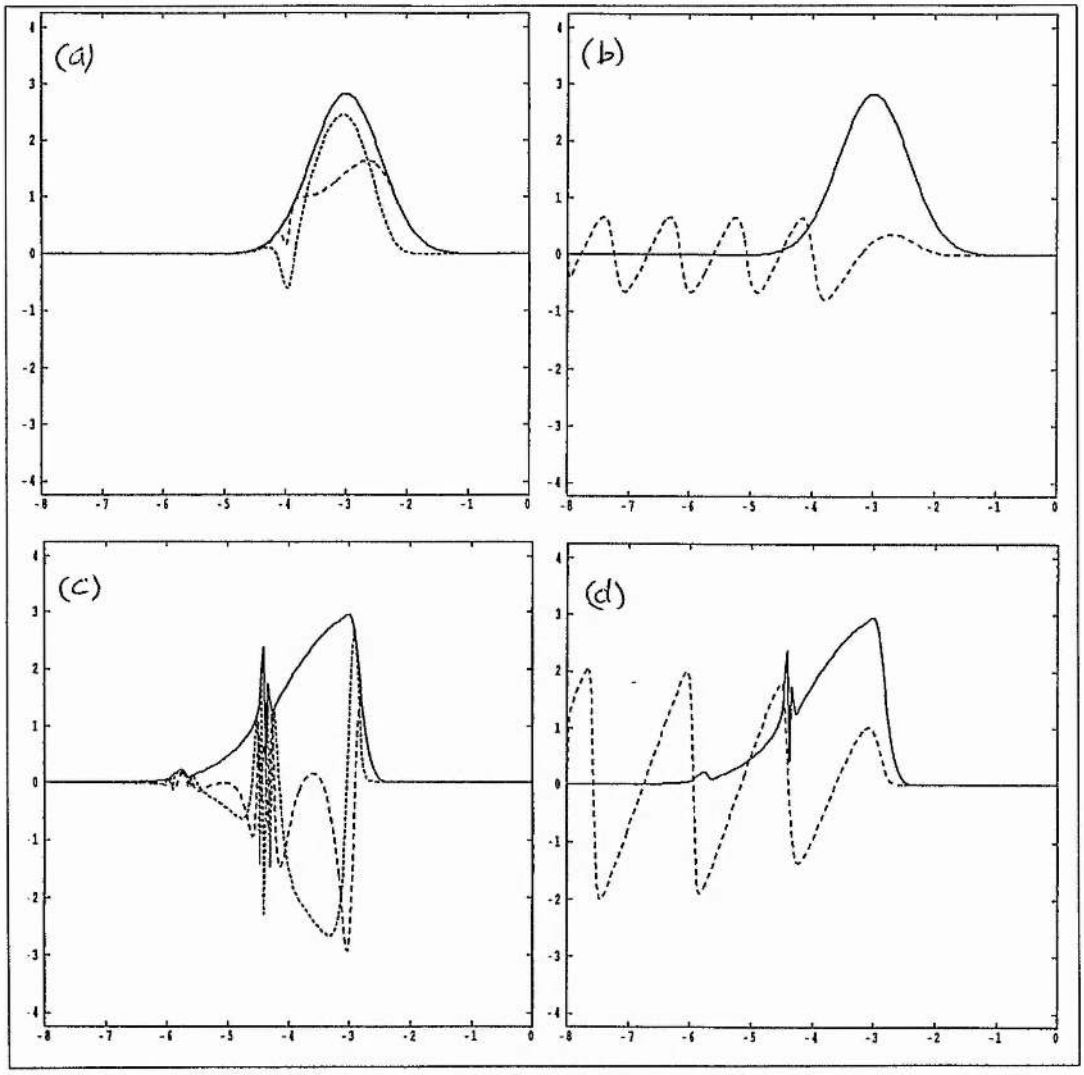

Figure 2.10: Output from the code using upstream differencing. (a) & (b) show the magnitude of $|a_o|$ (solid line) and the real and imaginary parts of a_o and also E_w for a symmetric pulse with $\sigma_r = \sigma_f = 0.795\lambda_p$. (c) & (d) show the same quantities for an asymmetric pulse with $\sigma_r = 0.25\lambda_p$ and $\sigma_f = 1.5\lambda_p$. Common parameters are $|a_o^{in}| = \sqrt{8}$, $\omega_{po}/\omega_o = 0.05$ and time $t = 54T_p$.

Chapter 3

Multiple Pulse Laser Wakefield Accelerator

In this chapter, we extend the theory presented in the previous chapter to investigate the effect of successive laser pulses on the plasma wakefield. In particular, we look for a nonlinear enhancement of the wakefield amplitude. Such an enhancement would suggest that greater efficiency could be achieved in the excitation of the plasmon in the LWFA scheme if multiple laser pulses are employed.

3.1 The Theory of Multiple Pulses

We build our multiple pulse model on the single pulse model presented in the previous chapter. To simplify the theory, we use the approximation that the group velocity of the electromagnetic wave, v_g, is equal to the light speed, c. In this case, the electrostatic plasma potential is generated according to the equation,

$$\frac{d^2\Phi}{d\xi^2} = \frac{1}{2}\frac{\omega_p^2}{c^2}\left\{\frac{\gamma_a^2}{(1+\Phi)^2} - 1\right\}. \tag{3.1}$$

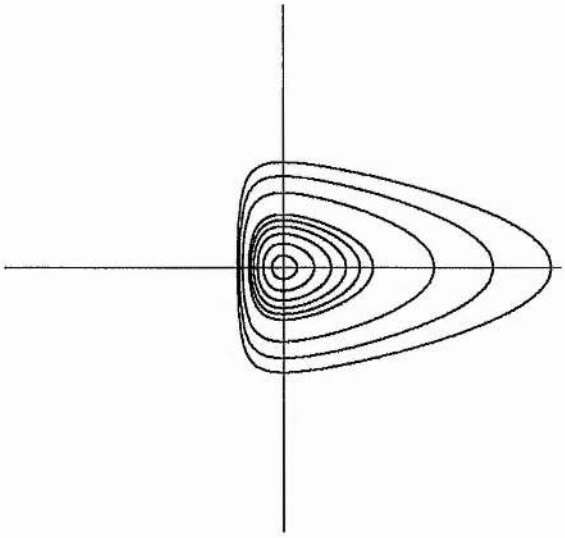

Figure 3.1: The trajectories in (u, Φ) phase space generated by equation (3.2) for varying values of the constant K. When $K = 1$, the trajectory is a fixed point at the origin and as the value of K increases, the trajectories become increasingly distorted from the linear circular orbits. Notice the bunching of the trajectories as the minimum value of Φ is approached.

In the absence of a laser pulse (ie. $|a_0| = 0$), $\gamma_a = 1$ and a first integral of equation (3.1) may be obtained,

$$u^2 + \frac{1}{1+\Phi} + \Phi = K\,, \tag{3.2}$$

where K is a constant and

$$u = \frac{c}{\omega_p}\frac{d\Phi}{d\xi}\,. \tag{3.3}$$

We see from equation (3.2) that the constant, K, has the value 1 for the initial equilibrium state $u = \Phi = 0$. The curves generated by equation (3.2) in the (u, Φ) phase space are illustrated in figure 3.1.

Next we suppose that we can approximate a short pulse by a δ-function so that,

$$\gamma_a^2 = 1 + 2A\,\delta\left(\xi - \xi_o\right)\,, \tag{3.4}$$

where A is a positive constant. The effect of such a pulse in the plasma is to produce

an impulsive change in u of magnitude,

$$\Delta u = \frac{A}{(1+\Phi)^2}. \tag{3.5}$$

When we apply such a δ-function pulse to the initial equilibrium state plasma, we excite an oscillation which is represented by a closed orbit in the (u, Φ) phase space. This new trajectory is characterised by the value of the constant, K. To find the value of K after the impulse is applied in u, we substitute the form in equation (3.5) into equation (3.2) to get,

$$K = 1 + A^2. \tag{3.6}$$

We notice that the maximum value of Φ is approximately A^2 if $A \gg 1$.

If, instead of a single pulse, we use a series of pulses we can exploit the Φ dependence of the impulses given by equation (3.5) and drive the system each time it passes through a minimum value of Φ. This approach has the advantage that each individual pulse has a rather smaller value of A than the single pulse. In this way each successive pulse produces a larger jump in u and there is a rapid increase in the maximum value of Φ and the amplitude of the wakefield.

To show just how strong this effect can be, we note that for large K the maximum and minimum values of Φ are, approximately,

$$\begin{aligned} \Phi_{\max} &= K \\ \Phi_{\min} &= -1 + 1/K \end{aligned} \tag{3.7}$$

If we apply the impulse when the wave is passing through $\Phi_{\min}$, we get

$$\Delta u = AK^2 \tag{3.8}$$

and the new value of K is

$$\begin{aligned} K_1 &= A^2K^4 + K - 1 + \frac{1}{K} \\ &\approx A^2K^4 \end{aligned} \tag{3.9}$$

if A is of order 1 and K is large. Thus, once we get into the large K regime, there is the potential for extremely rapid growth of the electrostatic wave amplitude with successive pulses.

These simple considerations indicate how the nonlinearity, of the behaviour of the electrostatic potential, may be exploited by using short pulses to drive up the wave amplitude at a point in its cycle where they are very effective in increasing the amplitude.

3.2 Computational Considerations

In order to use the Sunfad single pulse code to study the interaction of multiple pulses with the plasma, a few changes are necessary. The main alteration to allow multiple pulse trains involves introducing new variables to define the pulse characteristics and the spacing between the trailing pulses in the moving frame. These new variables are then used to define the initial value of the 'envelope', a_0, across the computational mesh. To analyse the interaction of the pulses, the code is also modified slightly to produce numerical plots of the phase space (u, Φ) in the output graphics. This allows us to see the exact phase of the plasma wave at which subsequent impulses from the trailing pulses are applied.

The nonlinear modification to the plasma wavelength induced by intense laser pulses makes it difficult to accurately predict where the minima in Φ will occur for a given leading pulse laser strength. To position multiple pulse trains around the minima in Φ, we therefore require some aid in predicting the structure of the wakefield with which the pulse will interact. One way to obtain this information is to run the full simulation code for the leading pulse alone and analyse the structure of the resulting wakefield. However, this may take some time to do and involves much editing of the input files for Sunfad. To save time in the positioning of the pulses in the simulation, a simple solver program, running on an Apple Macintosh computer, is used instead. This program calculates the numerical solution of equation (3.1) for the wake potential excited by the leading pulse, assuming that the laser pulse is 'hard', ie. that it is not modified by the reaction of the plasma. This assumption is, strictly, only correct for circularly polarised pulses. Since we use the results from this program to place the pulses initially on the simulation mesh, we may also legitimately neglect the plasma reaction, which would take a certain amount of time to modify the pulse envelope, for pulses with linear polarisation. In the 'macwaket' program, we define

the single laser pulse by,

$$A_0 = a_0 \exp\left\{-\left(\frac{(\xi-\xi_0)}{\sigma}\right)^2\right\},$$

and write $\gamma_a^2 = 1 + 1/2\,|A_0|^2$ for linear polarisation. We now write equation (3.1) as the first order system,

$$\begin{aligned} \dot{y_1} &= y_2 \\ \dot{y_2} &= \frac{1}{2}\left\{\frac{\gamma_a^2}{(1+\Phi)^2} - 1\right\}, \end{aligned} \tag{3.10}$$

where $y_1 = \Phi$ and $y_2 = \frac{d\Phi}{d\xi}$. We solve the system (3.11) on the interval $0 \leq \xi \leq 4$, where ξ is in units c/ω_p, subject to the initial conditions $\Phi = 0$ and $\frac{d\Phi}{d\xi} = 0$ at $\xi = 0$. The program takes the laser parameters a_0 and σ as input, together with the number of intervals to be used on the computational mesh and an error tolerance for locating the minima of Φ. It then solves the system (3.10) with the pulse centred on $\xi = 1$. At each step, the program analyses y_2 for a sign change from negative to positive as this would indicate that the two most recent mesh points straddle a local minimum value of Φ. If the correct sign change is found, the program returns to the previous mesh point (negative gradient in Φ) and divides the step size by two. The program then integrates the equations with this step size until the value of y_2 becomes positive again. If the positive value of y_2 lies between zero and the tolerance value specified by the user, the program prints the position and the gradient to the screen output as the location of a local minimum of Φ. If, on the other hand, the value of y_2 lies outside the tolerance range, the process of halving the step size and regressing to the previous mesh point is repeated. In this way, the program 'homes-in' on the turning point. Behind the local minimum the integration of the system continues with the original step size until the integration point straddles the next minimum in the plasma

potential. At the end of the integration, the program writes the data representing the laser pulse and the solution for the plasma potential to a file. This data may then be imported into a graphing application to produce a graphical output.

The 'macwaket' program was used extensively to aid the phasing of the two-pulse laser trains in the next section. It proved to be very accurate and speeded the Sunfad simulations by eliminating the uncertainty in the wake structure excited by the leading pulse. We now present some sample output from the 'macwaket' program. Figure 3.2 shows the pulse profile and wake potential for the parameter values $a_0 = 2$ and $\sigma = 0.25$. If we split the energy of a single pulse with $|a_0| = 4.24$ and $\sigma_{r,f} = 0.05$

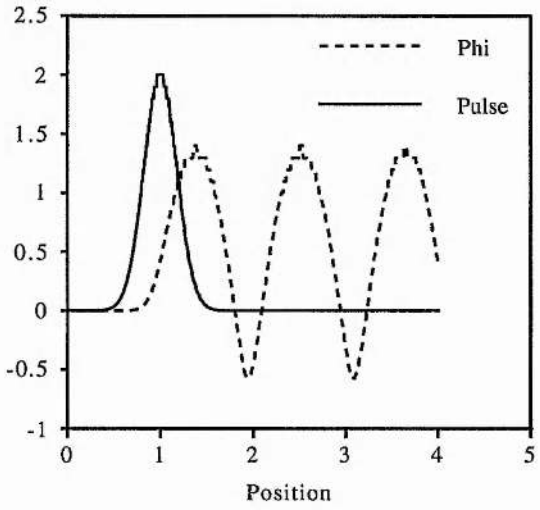

Figure 3.2: The pulse profile with $a_0 = 2$ and $\sigma = 0.25$ and the calculated wake potential,Φ, plotted against position ξ in the pulse frame.

equally beteen two pulses, then each pulse has a laser strength $|a| = 3.0$ and the same Gaussian coefficients as the single pulse. Figure 3.3 shows the output from the 'macwaket' program for such a leading pulse. The screen output from the program gives the location of the two minima in Φ as $\xi = 1.95$ and $\xi = 3.05$ where the gradient in Φ is 0.008 and 0.009 respectively. This information is used in the next section to position the pulses in the Sunfad simulation.

The listing of the 'macwaket' program is given in Appendix A.

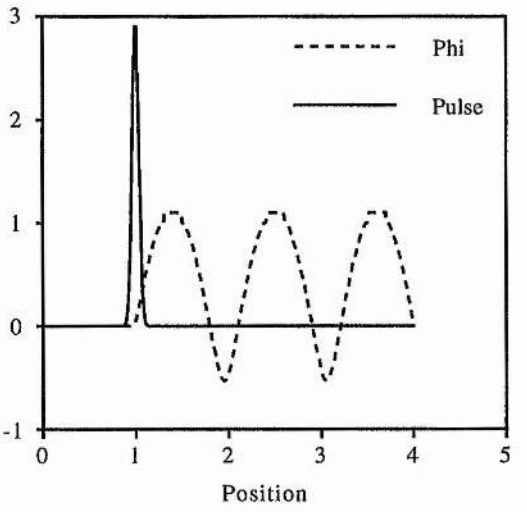

Figure 3.3: The pulse profile with $a_0 = 3$ and $\sigma = 0.05$ and the calculated wake potential,Φ, plotted against position ξ in the pulse frame.

3.3 Results

We now set out to investigate the interactions of multiple laser pulses armed with the theory described earlier and the modified simulation code. We begin by confirming the expectations of linear theory for pulse strengths $|a_0| \leq 1.0$ We then increase the strength of the laser pulses to investigate the modifications to the linear behaviour in this parameter regime. Once we have demonstrated the nonlinear effects for two-pulse trains, we present some results for pulse trains consisting of three and even five pulses. We will then present some interesting results arising from the phase sensitivity of the interaction between the pulses and the plasma wake structure. We show that it is possible to 'accelerate' the final pulse in the train, by phasing it to lie in the accelerating region of the wakefield, and reduce the wake oscillation to a negligible level. Finally, we will consider some theory and simulations to investigate the optimum way in which to split the energy of a single pulse between two pulses to excite the largest possible wake field structure.

We begin, then, with the linear parameter regime.

3.3.1 Linear Parameter Regime

In this parameter regime, a linear plasma wave is excited and therefore the orbits in the (u, Φ) phase space are circular. To investigate the linear regime, we consider a single pulse with laser strength $|a_0| = 1$ and then split the energy in this pulse between two pulses. We use symmetric Gaussian pulses with rise and fall coefficients $\sigma_{r,f} = 0.25$ and a frequency ratio $\omega_p/\omega_0 = 1/20$. These parameters would correspond, say, to a single 30fs pulse from an Nd:Glass laser system focused to an intensity $I_0 \simeq 1 \times 10^{18} W/cm^2$ in a plasma of density $n_0 \simeq 2 \times 10^{18} cm^{-3}$. Figure 3.7 shows the simulation output for a single pulse with these parameter values at time $t = 6T_p$. We see that a linear wakefield is excited with amplitude $E_w \simeq 0.3$ which corresponds to $E_z = 4.7 \times 10^{10}$ V/m which is two orders of magnitude below the cold plasma

wavebreaking limit for our sample density. The phase trajectories in Figure 3.7 show that the plasma wave is linear since the excited orbit is almost circular. We now consider the case where the energy in this single pulse is split between two pulses. The energy in a pulse is proportional to the integral of the square of the potential, ie.

$$\text{Pulse Energy} \propto \int_{-\infty}^{\infty} |a_0^2|\, d\xi \tag{3.11}$$

where for a Gaussian pulse we have,

$$a_0 = A_0 \exp\left\{-\left(\frac{\xi - \xi_0}{\sigma}\right)^2\right\}. \tag{3.12}$$

To balance the energy in the single pulse with the two symmetric pulses with Gaussian coefficients σ_1 and σ_2 and maximum amplitudes A_1 and A_2, we require

$$\sigma_0 A_0^2 \;=\; \sigma_1 A_1^2 + \sigma_2 A_2^2. \tag{3.13}$$

For simplicity we take $\sigma_0 = \sigma_1 = \sigma_2$ and consider 4 of the possible energy splits between the two pulses. First, we consider the case where the energy is split equally between the two pulses so that $A_1 = A_2 = 1/\sqrt{2}$. Figure 3.8 shows the simulation output for this case at time $t = 6T_p$. We see that the wakefield excited by this train of two pulses has a maximum amplitude $E_w = 3.0$ which is very nearly identical to that excited by the single pulse. The phase trajectories in Figure 3.8 show that the impulse from the second laser pulse is centred around the point in the cycle when the wake potential is zero and the wake electric field has a local maximum. Next, we consider the case where 2/3 of the total energy is carried in the leading pulse. This requires $A_1 = \sqrt{2/3}$ and $A_2 = \sqrt{1/3}$. Figure 3.9 shows the simulation output for this case at time $t = 6T_p$. Again, we see that the wakefield excited by this pulse train has a maximum amplitude $E_w = 0.3$ and the impulse from the second pulse is centred on the point where $\Phi = 0$ and E_w has a local maximum. Figures 3.10 and 3.11 show the

output for two further cases. In Figure 3.10 the energy is split in the ratio 4:1. These results show the same behaviour as the previous two-pulse cases in this linear regime. The maximum wakefield is the same as that generated by a single pulse with $|a_0| = 1$ and the second pulse should be phased to coincide with the zero in Φ and the local maximum in E_w. This is as expected from the linear theory with a linear addition of wake amplitudes. The K values for the orbits excited in these linear two-pulse cases are of the order 1.1 and we are therefore not in the $K \gg 1$ regime for the nonlinear theory of Section 3.1. A final illustration of the pulse phasing in the linear regime is given in Figure 3.12 where the relative plasma density has been reduced by a factor of $\sqrt{5}$ to make the pulses shorter on the spatial scale of the simulation. In Figure 3.12a the second pulse is coincident with the point in the cycle where Φ has a local minimum according to the nonlinear theory. The results show that this results in no amplification of the wakefield excited by the leading pulse. In Figure 3.12b the second pulse is coincident at $\Phi = 0$, and the wakefield is amplified.

In this section, we have demonstrated that in the linear parameter regime we get the expected behaviour so that the best wake enhancement is achieved when the trailing pulse adds to the field at its maximum value (ie. $\Phi = 0$).

3.3.2 Nonlinear Wakefield Enhancement Using Two Laser Pulses

Having verified the linear behaviour, we now investigate the response to more intense pulses ($|a_0| > 1$) and look for the nonlinear wake enhancement predicted in Section 3.1. We begin by considering a single pulse with $|a_0| = 2$ which corresponds to a fourfold increase in intensity over the linear case. Figure 3.13 shows the wake structure excited by a single pulse with $|a_0| = 2$. The maximum amplitude of the wakefield is $E_w \simeq 0.85$ and the nonlinearity of the wake is evident from the steepening of the front of the field gradient and the slight apparent lengthening of the oscillation wavelength. The nonlinear nature of the wake oscillation is also represented by the distortion of

the orbits in the (u, Φ) phase plane away from the circular form. We compare this interaction with the case where the energy of this single pulse is split equally between two pulses with the same profile. In this case, we have $A_1 = A_2 = \sqrt{2}$. Figure 3.14 shows the simulation output for two such pulses. Now, the wakefield is significantly enhanced by the interaction of the two laser pulses over the wakefield excited by the single pulse. The maximum wakefield amplitude excited is now $E_w \simeq 1$, which is 18% higher than that excited by the single pulse. The phase space trajectories show that the impulse from the second laser pulse is applied very close to the local minimum of the electrostatic plasma potential. The enhanced efficiency of the energy transfer to the wake plasmon is due to the bunching of the phase trajectories at the minimum of the potential, Φ. This allows a given impulse to push the system onto a larger orbit at this point. The wake structure excited by the two pulses in Figure 3.14 shows a 15% nonlinear increase in the wavelength of the oscillation and a marked steepening of the field gradient. Figure 3.14 also shows the marked nonlinearity in the wake potential. This result demonstrates that two pulses can indeed be more effective than a single pulse in generating a wake plasmon if they are phased correctly. The theory of Section 3.1 uses δ-function pulses to analyse this enhancement. We therefore now consider pulses with Gaussian coefficients $\sigma_{r,f} = 0.05$. In our example of a pulse with wavelength $\lambda_0 = 1.06\mu$m the frequency ratio $\omega_p/\omega_0 = 0.05$, these Gaussian coefficients represent a pulse of duration 6fs. We use this in the simulation code to approximate a δ-function pulse as 6fs represents two cycles of the laser radiation. We consider first the energy of our single pulse with $|a_0| = 2$ split equally between a pulse with Gaussian coefficients $\sigma_{r,f} = 0.25$ and one with $\sigma_{r,f} = 0.05$. In this way, the leading pulse excites a wake oscillation which is sufficiently nonlinear for the more localised impulse from the second laser to be more effective. Figure 3.15 shows the simulation output for this system at time $t = 6T_p$. With this configuration, we see a further improvement in the efficiency of the energy transfer. The maximum amplitude of the wakefield is now of the order $E_w \simeq 2$ and the wake structure is more strongly

nonlinear. Again, the phasing of the two pulses is critical in exciting the maximal wakefield and Figure 3.15 shows that the second pulse interacts with the plasma at a local minimum of the electrostatic potential. However, a larger wakefield amplitude can be excited if we split the energy of the original pulse between two pulses each with $\sigma_{r,f} = 0.05$. This system comes closer to the δ-function theory of Section 3.1 and Figure 3.16 shows the simulation output at time $t = 6T_p$ for two such pulses. In order to preserve the pulse energy, we require $A_1 = A_2 = \sqrt{10}$ with $\sigma_{r,f} = 0.05$. This increase in laser strength corresponds to a 2.5 times increase in the intensity of the pulses compared to the single pulse with $|a_0| = 2$. For a pulse from an Nd:Glass laser system, A_1 and A_2 correspond to $I_0 \simeq 1.25 \times 10^{19}\mathrm{W/cm}^2$. The results in Figure 3.16 show that a final wake amplitude $E_w \simeq 2.5$ ($E_z \simeq 380\mathrm{GV/m}$ for $\lambda_0 = 1.06\mu\mathrm{m}$) is excited by the pulses and, again, they are phased so that the second pulse interacts at a local minimum of the plasma electrostatic potential generated by the leading pulse. We recall that the single pulse with the same total energy excites a wakefield with $E_w \simeq 0.85$. Therefore, by using shorter pulses and exploiting the nonlinearity of the plasma response, we can achieve a three fold increase in the amplitude of the wake plasma electric field. The theory of Section 3.1 predicts that this effect will increase as the excited wakefield becomes more nonlinear. In terms of the modified Sunfad code, however, the placement of the pulses in accordance with the theory becomes more difficult. This is because the nonlinear steepening of the wake wave field reduces the spatial separation between the minima and zeros of the potential, Φ. Since the Sunfad code works with a spatial scale normalised to the linear plasma wavelength, we have two alternatives for dealing with this difficulty. First, we could decrease the frequency ratio ω_p/ω_0. This would imply a lower relative plasma density and a longer plasma wavelength, allowing the same pulse to be represented with smaller Gaussian coefficients. This has the advantage that we may model pulses of the same length as previous cases, but the reduction in the plasma frequency leads to a reduction in the amplitude of the wakefield. Alternatively, we may simply reduce the pulse length

by decreasing the Gaussian coefficients whilst holding the frequency ratio fixed. In this case, we move closer to the δ-function pulse of the theory presented above and remain in the relatively high plasma density/short-pulse high intensity regime that leads to the largest wakefields. Figure 3.17 shows a sample run for the first alternative considered above, where the frequency ratio and the Gaussian coefficients are reduced.

We see the wakefield generated by a single pulse with $|a_0| = 3$ in this parameter regime has a maximum amplitude $E_w \simeq 0.75$. If we split this energy equally between two pulses we may now position the pulses more accurately on the simulation mesh. Figure 3.18 shows the result of phasing the second pulse to coincide with a local maximum of the wakefield in accordance with the linear theory. In this case we see that the maximum wakefield amplitude is again $E_w \simeq 0.75$ and there is no apparent advantage, in terms of wakefield generation, to using two pulses. However, in Figure 3.19 we see the output for the same pulses phased this time so that the second pulse interacts close to the local minimum of Φ. The maximum wakefield amplitude is now $E_w \simeq 0.95$, which represents a 26% increase in the amplitude over the single pulse case. Finally in this section we look at a sample case for the second alternative above; using ultra-short pulses of ultra-high intensity radiation in more dense plasma. In this example we consider the energy in a single pulse with $|a_0| = 4.24$ and Gaussian coefficients $\sigma_{r,f} = 0.05$ at the frequency ratio $\omega_p/\omega_0 = 0.05$. For $\lambda_0 = 1.06\mu$m this case models a pulse of intensity $I_0 \simeq 2 \times 10^{19}\mathrm{W/cm}^2$ and duration $t_l = 6fs$. Figure 3.20 shows that such a pulse excites a highly nonlinear wakefield, with a maximum amplitude $E_w \simeq 1.35$.

We notice the significant nonlinear steepening of the wakefield which leads to the phasing difficulties associated with longer laser pulses in the multiple pulse scheme. If we split the energy in this single pulse equally between two pulses, we require $|a_1| = |a_2| \simeq 3.0$. As with the previous case, we find that when the pulses are phased according to the expectations of linear theory we see a similar value amplitude to that

excited by the single pulse. As we alter the phasing of the pulses to bring the second pulse closer to the local minimum in Φ, the amplitude of the final wake structure increases. Figure 3.21 shows the output for these two pulses with the second pulse lying between the maximum in E and the minimum in Φ. We see that in this case the wake amplitude is increased to $E_w \simeq 1.7$ and the maximum value of the pulse electrostatic potential is $\Phi_{\max} \simeq 3.8$. As the second pulse is moved in the simulation frame to bring it closer to $\Phi_{\min}$, the phase trajectories in the (u, Φ) space become very large. Indeed, the oscillation in Φ becomes so large that the solver routine in Sunfad is unable to cope and breaks just behind the second pulse. We are, however, still able to track the maximum values of Φ as the relative position of the trailing pulse is altered until the value exceeds 1,000. This occurs very close to the minimum in Φ.

In this section we have demonstrated that nonlinear wake enhancement is possible using two pulses in the LWFA scheme.

3.3.3 Multiple Pulse Trains

The natural extension to wakefield excitation using two laser pulses is to consider the interaction of a train of several pulses with the wake plasma. We now consider briefly the cases with 3 and 5 pulses in the train. Figure 3.22 illustrates a simulation using a 3-pulse configuration.

Each pulse has $|a| = 2/\sqrt{3}$ and $\sigma = 0.25$ so that the total energy carried in the three pulses is the same as that in a single pulse of strength $|a_0| = 2$, as shown in Figure 3.13. We see in Figure 3.22 that the leading pulse excites a weakly-nonlinear wake structure and each of the subsequent pulses interacts with the plasma between the local maximum of the wakefield and the local minimum of the wake potential. As in the two-pulse case, the optimum point for wakefield excitation moves from the local maximum of E towards the local minimum of Φ as the wake structure becomes more nonlinear. We see that in this case we again achieve a wake amplitude enhancement

of the order of 25% over the single pulse case. As a second example with a three-pulse train we consider the case where each pulse has $|a_0| = 2$ and $\sigma_{r,f} = 0.05$. Now each pulse provides a localised impulse to the plasma electrons. Figure 3.23 shows the simulation output at time $t = 6T_p$.

We see that the trailing pulses in the train are phased to coincide with the local minimum in Φ and the wake structure has a maximum amplitude $E_w \simeq 1.0$. The phase plane trajectories again illustrate the bunching of neighbouring trajectories near the minimum of Φ. Finally in this section, we consider a train of five pulses with $|a| = 2$ and $\sigma_{r,f} = 0.05$. The total energy in this train is then equivalent to that in a single pulse with $|a_0| = 2$ and $\sigma = 0.25$. Figure 3.24 shows the simulation output for this case at time $t = 0.4T_p$.

We see that the trailing pulses are phased to coincide with successive minima in Φ. The wake structure now has a maximum amplitude $E_w \simeq 2.3$, which is a significant improvement on the single pulse case. However, as this train of pulses propagates through the plasma, each pulse experiences a different local density. This causes the pulses to propagate at slightly different group velocities and to drift out of phase with the wake structure. This phase de-tuning is a severe limitation on the use of multiple pulse trains to excite large plasma wakefields over distances greater than a few plasma wavelengths. To illustrate this phase slippage, Figure 3.25 shows the phase trajectories and the density perturbation for the same simulation parameters as Figure 3.24 at time $t = 10T_p$.

We see that this slippage has reduced the effectiveness of the pulses so that the maximum amplitude of the wake structure is now $E_w \simeq 1.7$ The plot of the normalised density perturbation shows that each of the trailing pulses are initially propagating at local density maxima and these densities differ by a factor of 4 after $10T_p$. The effect of the density perturbation on the group velocities of the pulses may be reduced by reducing the initial plasma density. However, this is detrimental to the maximum possible wakefield amplitude that the plasma may support because it lowers the cold

plasma wavebreaking limit and the plasma frequency. Pulse trains consisting of more than two pulses are therefore unlikely to be very successful in practical applications as the phasing of the pulses has to be precise to attain the wake enhancement. The most likely scheme for a practical application is a two-pulse train with the first pulse sufficiently large to excite a nonlinear wake structure and the second as short as possible to give a localised impulse at the optimum phase in the wake oscillation. As a final example of multiple-pulse wake excitation in this section, we take such a configuration with the leading pulse having $|a| = 2.0$ and $\sigma_{r,f} = 0.25$. Figure 3.26 shows the output from this system at time $t = 0.4T_p$. We see that the ultra-short trailing pulse is spatially coincident with the local minimum in Φ and a highly nonlinear wake structure is generated in the plasma with $E_w \simeq 1.5$. The density maximum associated with the minimum in Φ again leads to some phase slippage between the pulses and a degradation of the wakefield over time. However, simulation results from the Sunfad code indicate that a significant wake structure persists until $t \sim 10T_p$.

In this section, then, we have demonstrated that wake structures may be excited using multiple-pulse trains, but that the problems associated with a two-pulse scheme are magnified as the number of pulses is increased. That is, the phase slippage between the trailing pulses and the wake plasmon has a more dramatic effect at earlier simulation times. In the next section we look at a different application for multiple laser pulses.

3.3.4 Photon Acceleration

We have presented some results to show that a correctly phased trailing pulse or train of pulses may interact with the wake structure excited by a lead pulse to amplify the wake oscillation. In a particle accelerator scheme we then inject a trailing bunch of electrons into the accelerating phase of the plasma wave, so that the energy in the wake may be transferred to the trailing electrons. If, however, instead of a trailing electron beam, we use a further pulse of laser radiation, the energy in

the wakefield may be transferred to this final pulse. In this case the frequency of the trailing pulse is continuously amplified as it is accelerated and the process is known as 'Photon Acceleration'[65]. The concept of PhotonAcceleration has been the subject of a recent numerical study [64, 65]. With the multiple-pulse version of the Sunfad code we are able to position a laser pulse exactly in the accelerating phase of the wake plasma wave and hence observe Photon Acceleration. Figure 3.27 shows the output from a simulation in which a single pulse with $|a_0| = \sqrt{10}$ excites a wake plasmon and an identical trailing pulse is positioned in the accelerating phase of the wave to leave almost no plasma oscillation in its wake.

In terms of the phase plane trajectories, the leading pulse excites an oscillation and the trailing pulse provides a kick at the appropriate place in the oscillation to push the system back to a linear trajectory with almost zero amplitude. Since our code works in the envelope approximation, the frequency spread within each pulse cannot be illustrated. However, our interpretation of this result is that the energy of the plasma oscillation is transferred to the trailing pulse in the form of an up-shifting of the frequency spread. Phase slippage between the plasma wave and the accelerated pulse again limits the useful accelerating length. In the case considered above the phase de-tuning as the pulse gains on the plasma wave results in less energy being transferred to the trailing pulse and a larger residual wakefield. After 40 plasma periods, Figure 3.28, the amplitude of the residual wakefield is approximately half that of the wake structure excited by the leading pulse. At lower relative plasma densities, the effects of phase-slippage take longer to occur.

Figure 3.29 shows the case for a frequency ratio $\omega_p/\omega_0 = 0.01$ at times $t = 2T_p$ and $100T_p$.

The plots of $|a|$ and E_w vs ξ show that the trailing pulse remains positioned in the accelerating phase of the plasma wave throughout the simulation. Figure 3.29 also shows that the trailing pulse is initially positioned slightly behind the optimum accelerating phase and the slight slippage it experiences during the simulation

brings it forward into a better phase. This is a well-known method for increasing the wake/particle de-phasing distance in wakefield particle accelerator schemes. Finally, we look at Photon Acceleration using a multiple-pulse train to excite the wake structure. Figure 3.30 shows such a scheme.

Three, identical, symmetric Gaussian pulses, placed in accordance with the nonlinear theory of Section 3.1, excite a wake structure of amplitude $E_w \simeq 1.1$ and a fourth pulse, phased to lie in the accelerating region of the wakefield, is accelerated by absorbing the energy in the wake structure. The plot of the (u, Φ) phase space trajectories illustrates the impulses given to the plasma electrons by each of the laser pulses. We see that the final pulse in the train 'kicks' the system back in towards the origin and a zero wakefield.

In this section, we have briefly presented some results which we believe demonstrate the effect known as 'Photon Acceleration'. In the next section we return to the problem of exciting the largest possible wakefield with two laser pulses, by examining the energy fraction carried by each pulse.

3.3.5 Optimal Energy Splitting

Thus far in our investigations, we have taken the energy of a single pulse and split it equally between the pulses in a multiple-pulse train. However, there is no specific reason for splitting the energy in this way and the question now arises as to whether some other ratio may be more efficient in exciting a wake structure in the plasma.

Given the structure of the phase space trajectories for the plasma oscillation, one may anticipate that a more energetic leading pulse may be more effective as it excites a more strongly nonlinear oscillation which the second pulse may exploit. On the other hand, the trailing pulse should still contain a significant proportion of the energy. We now present an analysis of the theory of Section 3.1 to investigate this question. Since the theory deals with δ-function pulses and high K values, we require that the leading pulse be sufficiently energetic to excite a nonlinear plasma oscillation.

We consider splitting the energy in a single δ-function pulse, with laser strength A_0, between two δ-function pulses with a fraction, η, of the energy in the leading pulse and $(1-\eta)$ in the trailing pulse, ie.

$$A_0^2 = A_1^2 + A_2^2 \tag{3.14}$$

and

$$A_1 = \sqrt{\eta} A_0 \ , \ A_2 = \sqrt{1-\eta} A_0 . \tag{3.15}$$

We assume that the leading pulse is large enough to excite a nonlinear wake structure and apply the theory of Section 3.1. Equation (3.6) gives the value of K excited by this lead pulse as,

$$K = 1 + \eta A_0^2 \tag{3.16}$$

This orbit has a minimum Φ value of $-1 + 1/K \simeq -1 + 1/\eta A_0^2$ since $A_0 \gg 1$. The equation determining the phase trajectories now dictates that the trailing pulse, with $A_2 = \sqrt{1-\eta} A_0$, will give an impulse,

$$\Delta u = \sqrt{1-\eta}\, A_0 K^2 , \tag{3.17}$$

when it is applied at the local minimum of Φ in the plasma. The new orbit excited is characterised by the new constant K_1,

$$K_1 = (1-\eta) A_0^2 K^4 + K - 1 + \frac{1}{K} , \tag{3.18}$$

and we now substitute the value of K in terms of the leading pulse parameters to get,

$$K_1 = A_0^2 \left\{ (1-\eta) \left(1 + \eta A_0^2 \right)^4 + \eta \right\} + \frac{1}{1+\eta A_0^2} \tag{3.19}$$

To determine the optimal energy split between the two pulses we now seek to maximise

the value of K_1 in equation (3.19) as a function of η. To find the extrema of K_1 in η we require the first derivative of K_1,

$$\frac{dK_1}{d\eta} = A_0^2 \left\{ -\left(1+\eta A_0^2\right)^4 + 4A_0^2(1-\eta)\left(1+\eta A_0^2\right)^3 + 1 - \left(1+\eta A_0^2\right)^{-2} \right\} \quad (3.20)$$

Since the above is valid for $A_0 \gg 1$, we may perform an asymptotic analysis on equation (3.20) for large A_0. We therefore set the coefficient of the highest power of A_0 on the right hand side of equation (3.20) equal to zero to obtain the value of η at the extremum of K_1 as A_0 tends to infinity. We obtain the value $\eta = 0.8$ from this analysis. So, as the laser strength A_0 increases, we expect the energy fraction in the leading pulse to tend to 80% to generate the maximum wakefield amplitude. To gain an estimate of the optimal energy splitting for a particular laser strength we obtain the numerical solution of equation (3.19). Figure 3.4 shows the relative magnitude of the wake structure vs η for values of A_0 between 2 and 3. We see that the energy splitting has a marked effect on the magnitude of the wakefield and the optimal splitting fraction increases, tending to $\eta_{opt} = 0.8$, with increasing A_0. Figure 3.5 shows a similar plot of wakefield size vs energy splitting fraction for a higher range of laser strengths. We may take the information in Figures 3.4 and 3.5 and plot the optimal splitting fraction, η_{opt}, vs laser strength as shown in Figure 3.6. This again illustrates the asymptotic behaviour of η_{opt} and may be used to interpolate the value of η_{opt} for a given value of A_0 in the range. We now illustrate this theory with an example. We consider a single pulse with laser strength $|A_0| = 3.0$ and Gaussian coefficients $\sigma_{r,f} = 0.05$ to approximate a δ-function pulse. Figure 3.31 shows the wake structure excited by this single pulse at time $t = 6T_p$. Equation (3.20) gives $\eta_{opt} = 0.79$ for $|A_0| = 4.0$ and this translates into laser strengths $A_1 = 3.58$ and $A_2 = 1.52$ for the leading and trailing pulses respectively. Figure 3.32 shows the simulation output for the two-pulse train with these laser strengths phased according to the theory of Section 3.1. We see that the wakefield has a maximum amplitude

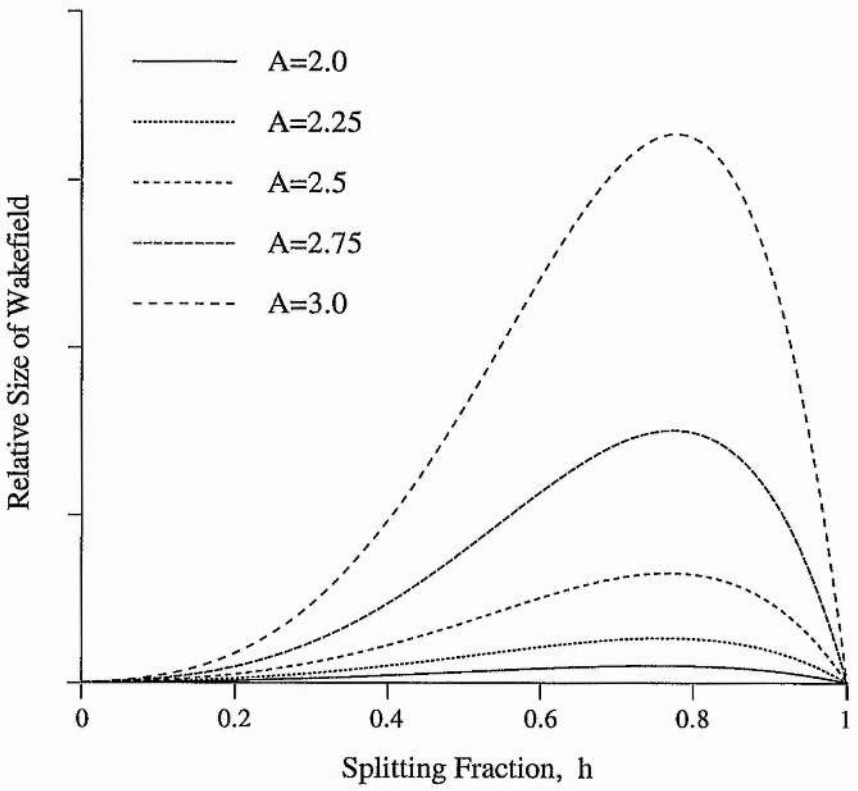

Figure 3.4: The relative wakefield magintude vs η for values of the laser strength of the single pulse $|a_0|$ between 2 and 3.

$E_w \simeq 1.68$. This represents a large improvement over the single pulse which excites a wake amplitude $E_w \simeq 1.25$, but is this the maximum possible with this energy? Table 3.1 shows the variation in the amplitude of the plasma wakefield with the energy splitting between the two pulses in our example. We see from Table 3.1 that $\eta \simeq 0.8$ does indeed give the largest wake amplitude, although the differential between the values is not as large as predicted by the theory. This is almost certainly due to the fact that the theory uses δ-function pulses which impart their impulse to the system instantaneously, whereas we have to use finite length pulses in the simulation. To attempt to get closer to the theory, we increase the frequency ratio ω_p/ω_0 to the value 0.1. This increases the plasma frequency relative to the laser frequency and shortens the spatial scale in the simulation. This allows the pulses with $\sigma_{r,f} = 0.05$

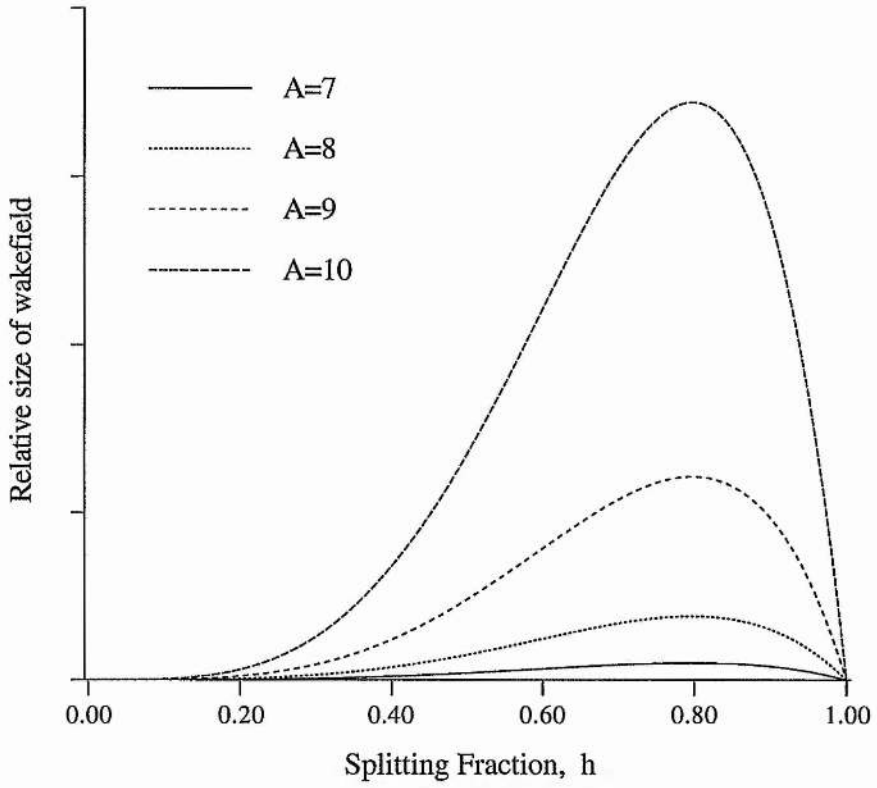

Figure 3.5: The relative wakefield magintude vs η for values of the laser strength of the single pulse $|a_0|$ between 7 and 10.

to represent even shorter pulses (T_l = 3fs for Nd:YAG radiation). Figure 3.33 shows the simulation output obtained with this new frequency ratio for the optimally split pulses. In this case, we see the wakefield that the pulses excite, is more nonlinear than in the previous case. Table 3.2 gives the variation of wake amplitude with energy fraction in the leading pulse obtained from Sunfad simulations. Table 3.2 again shows that the wakefield amplitude shows the expected dependance on the energy fraction in the leading pulse, but the differential between the values is not as large as predicted. We conclude that, for any non δ-function pulses, there does exist an optimum energy balance between the leading and trailing pulses, but that the advantage to be gained over, say, a straightforward equal split may not be large in terms of the wakefield amplitude.

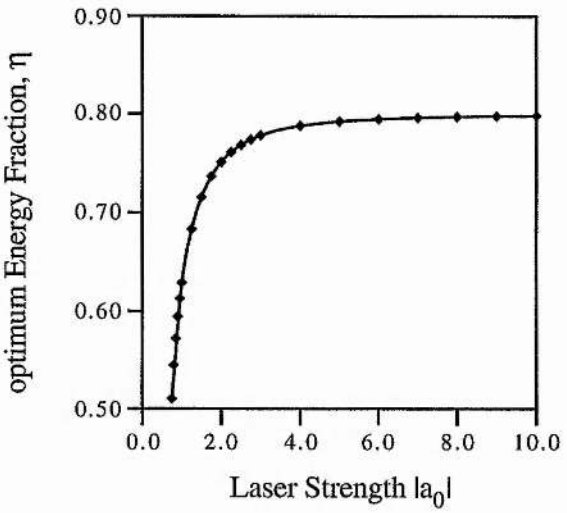

Figure 3.6: A plot of the optimum energy fraction in the leading pulse of a two-pulse train vs the laser strength,$|a_0|$. This shows that η_{opt} tends asymptotically to the value 0.8 with increasing laser strength.

Energy Fraction η	Wakefield Amplitude E_w
0.4	1.46
0.5	1.50
0.6	1.55
0.8	1.68
0.9	1.42

Table 3.1: Values of the maximum wake amplitude excited with the given energy fraction for a single pulse with $|a_0| = 4$.

Energy Fraction η	Wakefield Amplitude E_w
0.4	1.46
0.5	1.58
0.8	1.75
0.9	1.58

Table 3.2: Values of the maximum wake amplitude excited with the given energy fraction of a single pulse with $|a_0| = 4$ and $\omega_p/\omega_0 = 0.1$.

3.4 Summary

In this chapter we have presented the theory and some results for a multiple-pulse wakefield enhancement scheme. The results indicate that the enhancement is a non-linear effect which increases with the laser strength and the frequency ratio. The maximum wakefield is obtained when ultra-short, ultra-high intensity pulses are phased in such a way that they interact with the plasma electrons near the local minimum of the electrostatic plasma potential. The optimum point for the interaction moves from the linear position ($E_w = E_{w\max}$) towards the local minimum in Φ as the laser strength of the leading pulse is increased. We have also observed some phase slippage between the laser pulses and the wake plasmon. This leads to a degradation of the wakefield with time. The effect of phase slippage becomes more acute for multiple-pulse trains and at higher plasma densities. We have also shown that 'Photon Acceleration' takes place when the trailing pulse enters the accelerating phase of the wakefield.

It has been suggested previously [14, 50, 41] that multiple pulses might be used and some analysis has been carried out [4]. However, the novel phase plane analysis presented here shows, more clearly than earlier work, just how the nonlinear structure of the equations is such as to make excitation by a series of correctly placed pulses a very effective way of generating a high amplitude wakefield.

We have seen in this chapter that phase-slippage between the laser pulses and the plasma wave limits the effective length over which the wakefield can be maintained. Phase slippage between the plasma wave and an injected bunch of electrons also limits the acceleration length in the acclerator schemes. In the next chapter we look at one of the methods proposed to lessen the effect of phase slippage by varying the density of the background plasma.

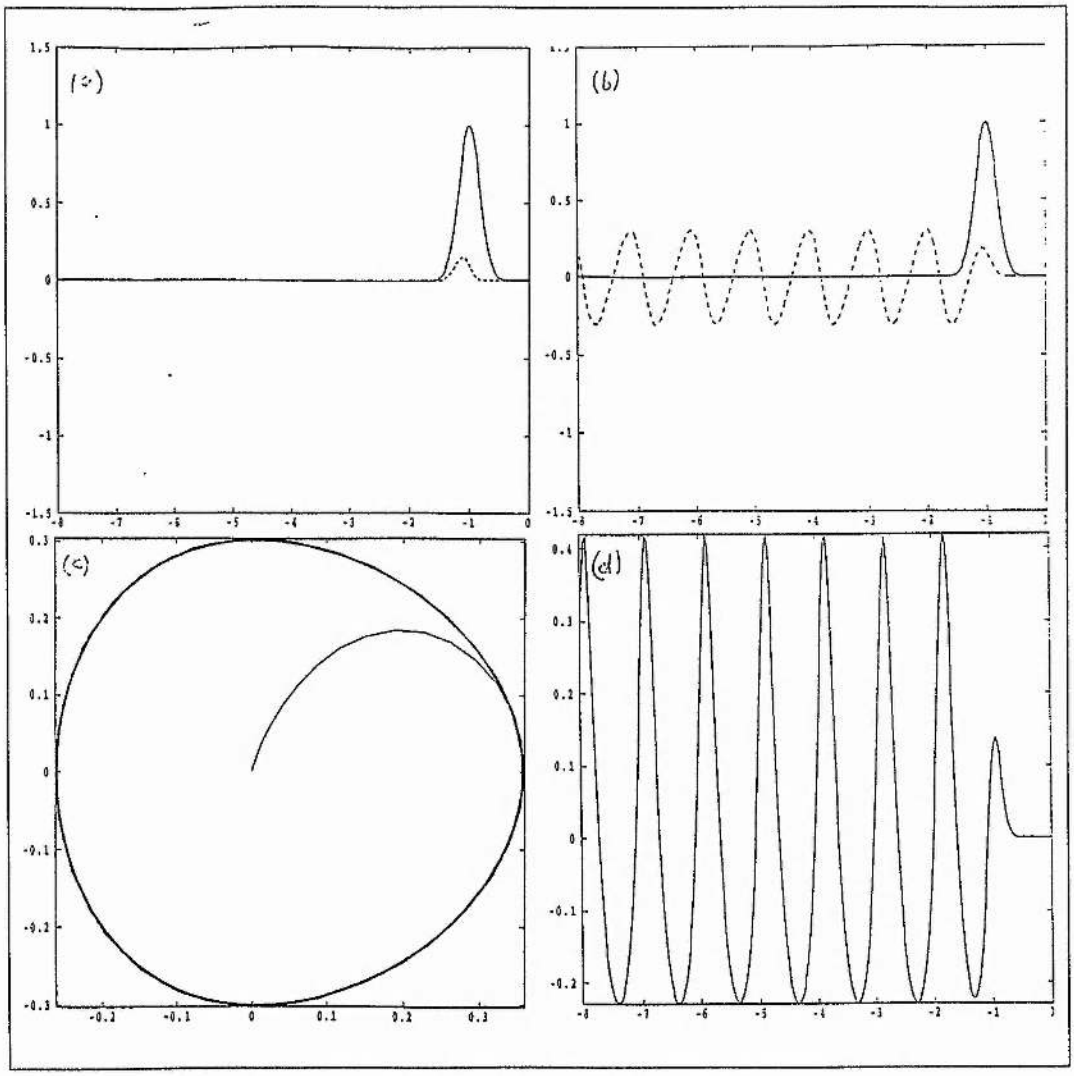

Figure 3.7: The simulation output for a single pulse with parameters $|a_o| = 1$ and $\sigma_r = \sigma f = 0.25$ and a frequency ratio $\omega_{po}/\omega_o = 0.05$ at time $t = 6T_p$. (a) shows the magnitude of $|a_o|$ (solid line) and the real and imaginary parts of a_o (dashed lines); (b) shows the magnitude of $|a_o|$ and the wake electric field, E_w (dashed line); (c) shows the phase trajectories in (u, Φ) space and (d) shows the normalised electron density perturbation across the simulation grid.

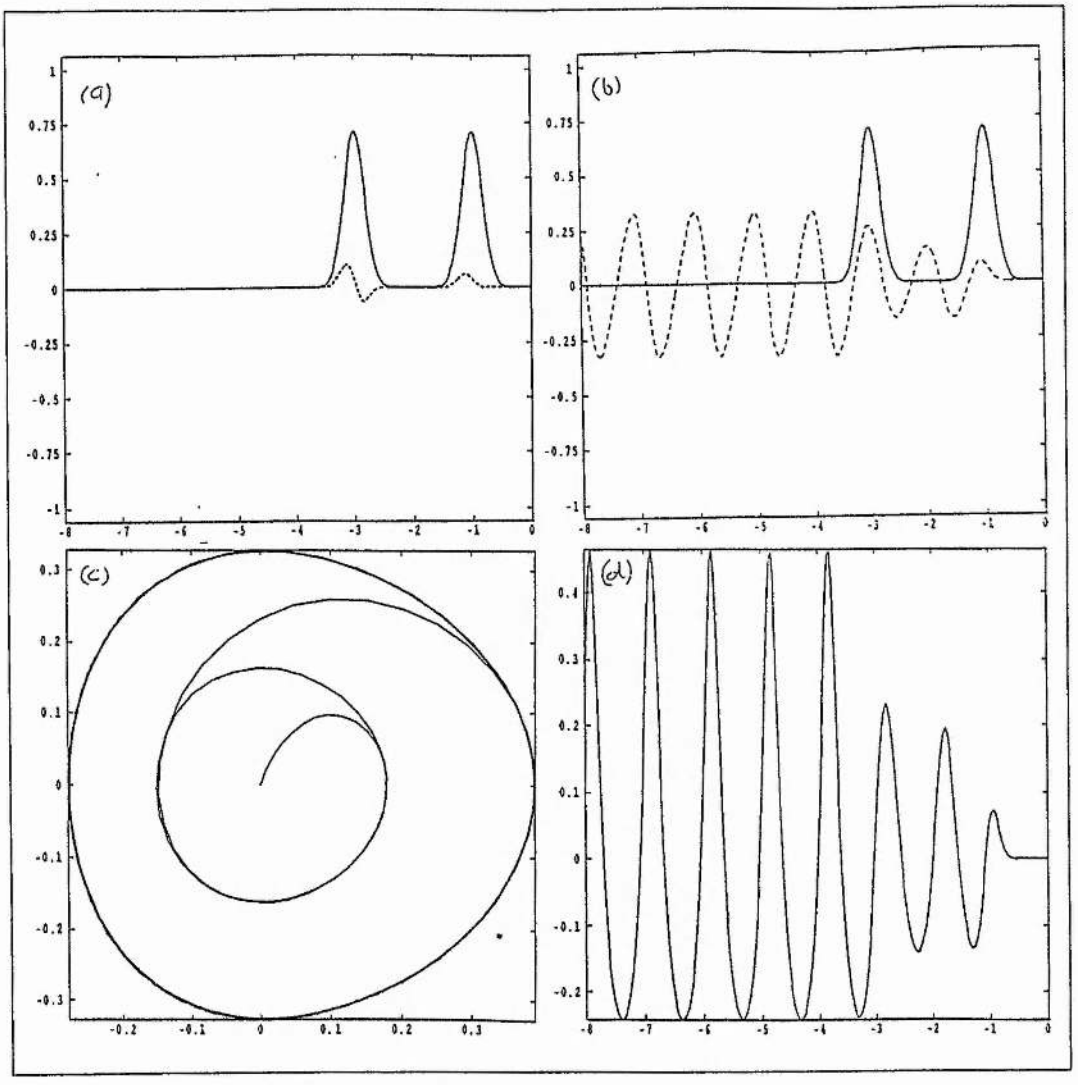

Figure 3.8: The simulation output for a train of two laser pulses with parameters $A_1 = A_2 = \frac{1}{\sqrt{2}}$ and $\sigma_r = \sigma f = 0.25$ and a frequency ratio $\omega_{po}/\omega_o = 0.05$ at time $t = 6T_p$. (a) shows the magnitude of $|a_o|$ (solid line) and the real and imaginary parts of a_o (dashed lines); (b) shows the magnitude of $|a_o|$ and the wake electric field, E_w (dashed line); (c) shows the phase trajectories in (u, Φ) space and (d) shows the normalised electron density perturbation across the simulation grid.

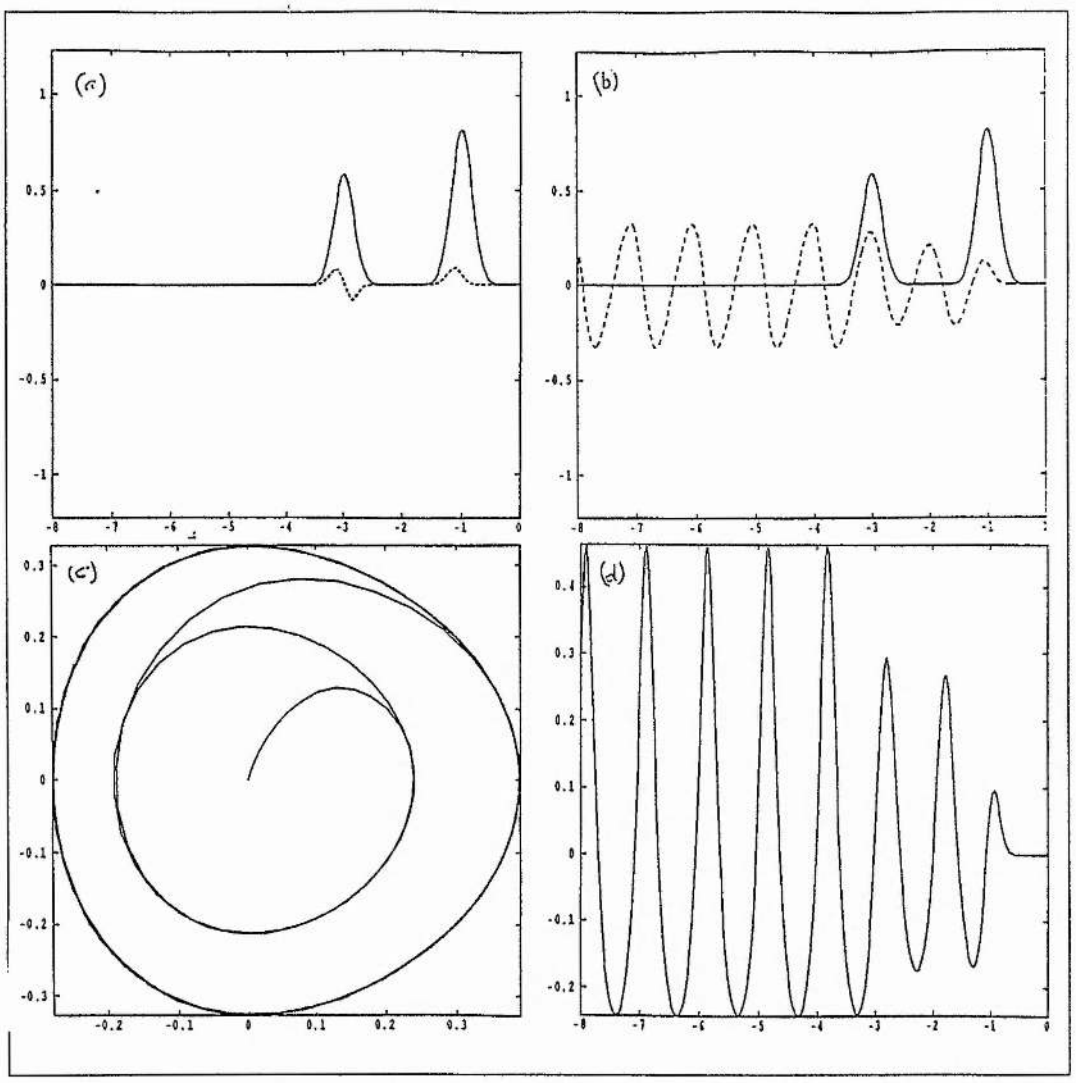

Figure 3.9: The simulation output for a train of two laser pulses with parameters $A_1 = \sqrt{\frac{2}{3}}, A_2 = \frac{1}{\sqrt{3}}$ and $\sigma_r = \sigma f = 0.25$ and a frequency ratio $\omega_{po}/\omega_o = 0.05$ at time $t = 6T_p$. (a) shows the magnitude of $|a_o|$ (solid line) and the real and imaginary parts of a_o (dashed lines); (b) shows the magnitude of $|a_o|$ and the wake electric field, E_w (dashed line); (c) shows the phase trajectories in (u, Φ) space and (d) shows the normalised electron density perturbation across the simulation grid.

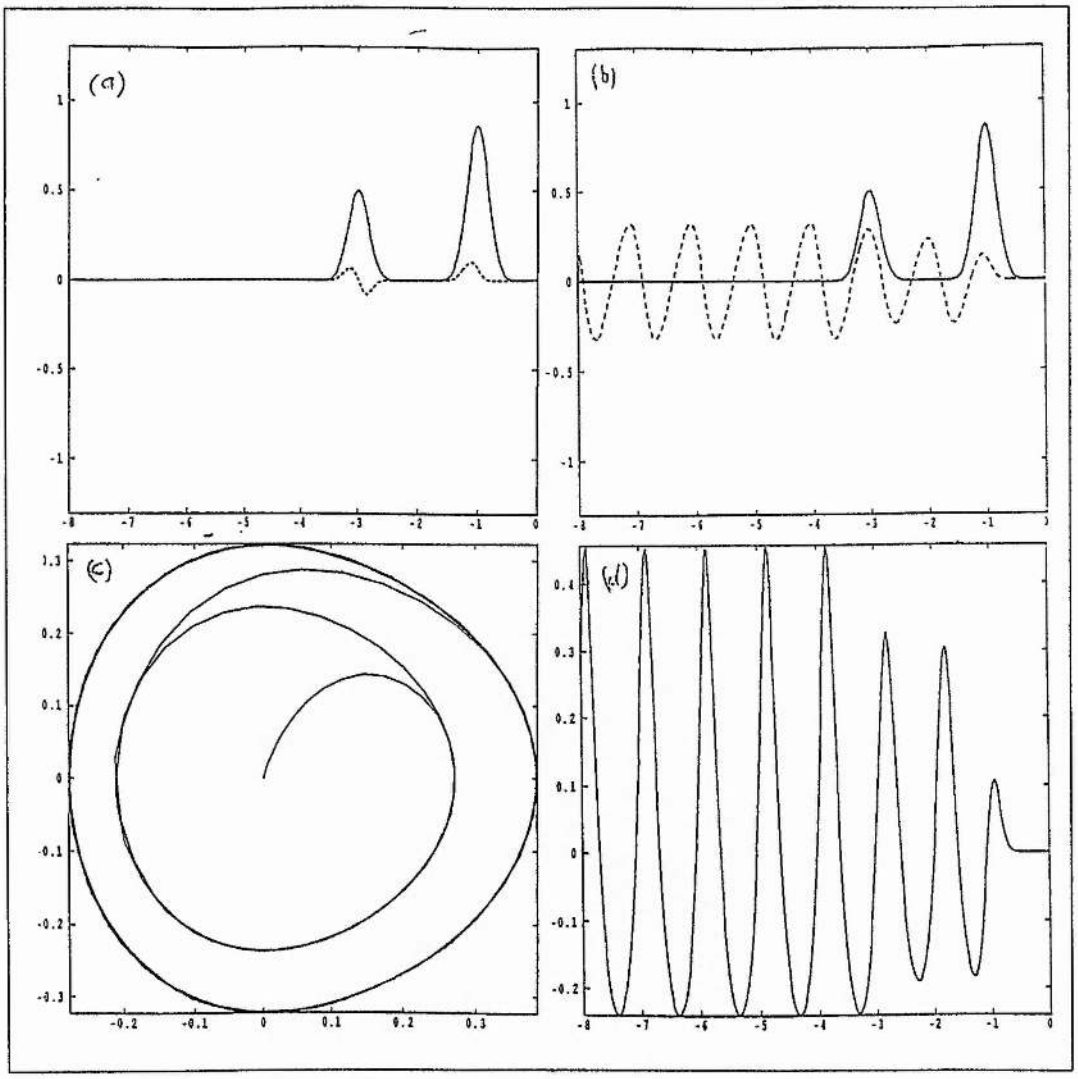

Figure 3.10: The simulation output for a train of two laser pulses with parameters $A_1 = \frac{\sqrt{3}}{2}, A_2 = \frac{1}{2}$ and $\sigma_r = \sigma f = 0.25$ and a frequency ratio $\omega_{po}/\omega_o = 0.05$ at time $t = 6T_p$. (a) shows the magnitude of $|a_o|$ (solid line) and the real and imaginary parts of a_o (dashed lines); (b) shows the magnitude of $|a_o|$ and the wake electric field, E_w (dashed line); (c) shows the phase trajectories in (u, Φ) space and (d) shows the normalised electron density perturbation across the simulation grid.

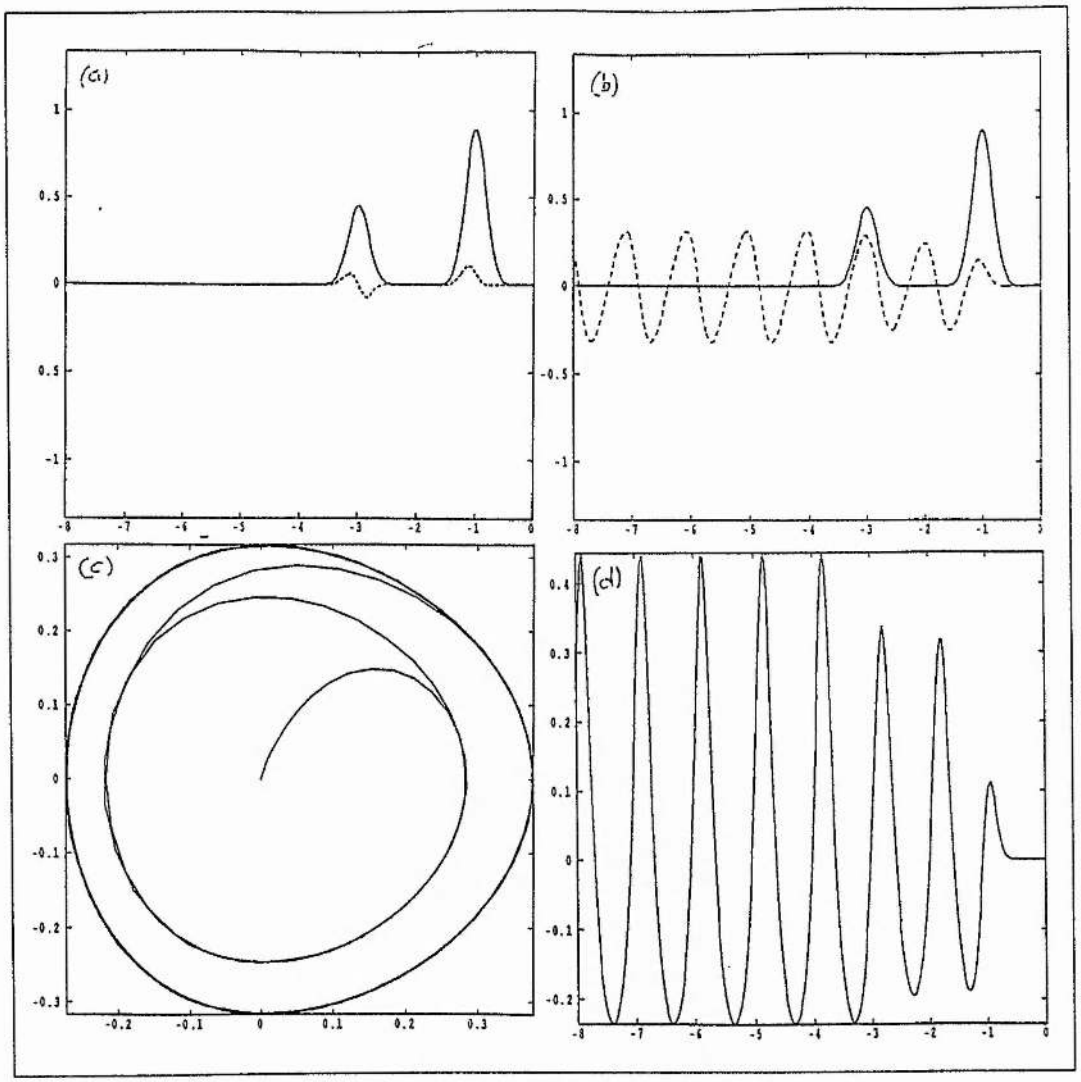

Figure 3.11: The simulation output for a train of two laser pulses with parameters $A_1 = \frac{2}{\sqrt{5}}$, $A_2 = \frac{1}{\sqrt{5}}$ and $\sigma_r = \sigma f = 0.25$ and a frequency ratio $\omega_{po}/\omega_o = 0.05$ at time $t = 6T_p$. (a) shows the magnitude of $|a_o|$ (solid line) and the real and imaginary parts of a_o (dashed lines); (b) shows the magnitude of $|a_o|$ and the wake electric field, E_w (dashed line); (c) shows the phase trajectories in (u, Φ) space and (d) shows the normalised electron density perturbation across the simulation grid.

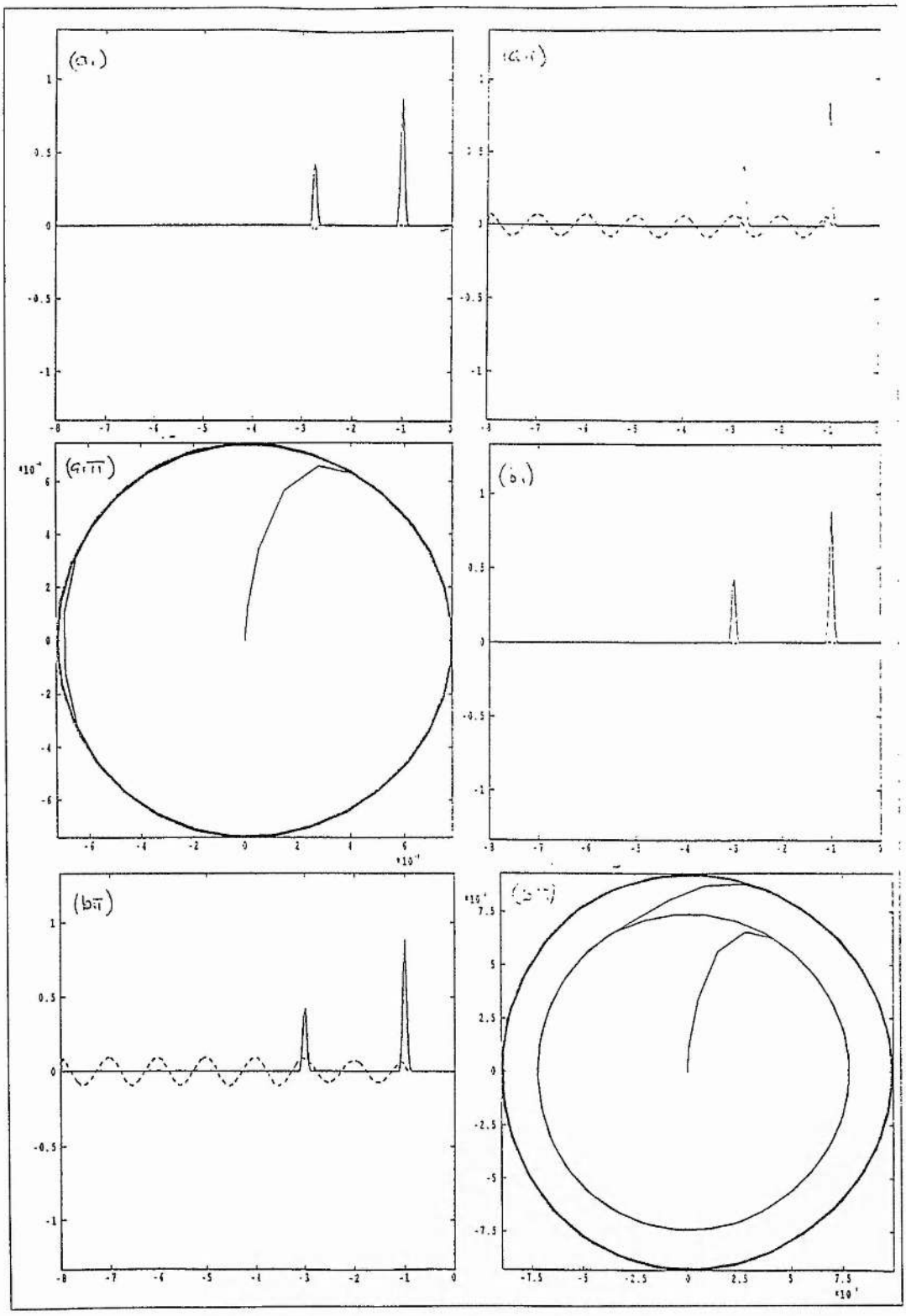

Figure 3.12: Simulation output for a train of two laser pulses with parameter values $A_1 = \frac{2}{\sqrt{5}}$, $A_2 = \frac{1}{\sqrt{5}}$, $\sigma_{\mathrm{r,f}} = 0.05$ and $\frac{\omega_p}{\omega} = 0.01$ at time $t = 30T_p$ In case (a) the spacing between the two pulses gives no amplification in the wakefield. The pulse spacing in case (b) gives a small amplification. In each case, (i) shows the magnitude of the laser pulses and their real and imaginary parts ; (ii) shows the magnitude of the pulses and the wake electric field, E_w, and (iii) shows the phase trajectories in (u, Φ) space.

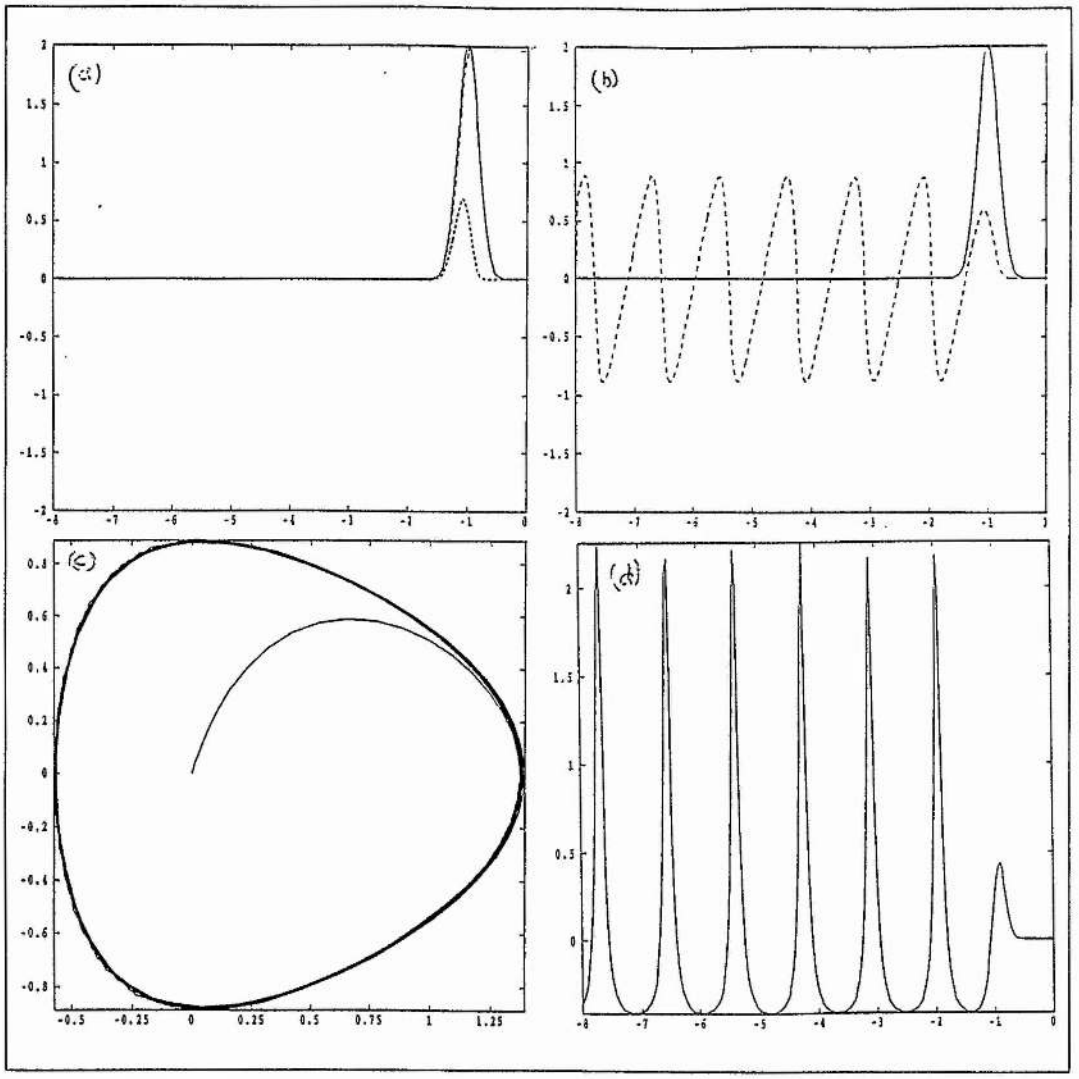

Figure 3.13: The simulation output for a single pulse with parameters $|a_o| = 2$ and $\sigma_r = \sigma f = 0.25$ and a frequency ratio $\omega_{po}/\omega_o = 0.05$ at time $t = 6T_p$. (a) shows the magnitude of $|a_o|$ (solid line) and the real and imaginary parts of a_o (dashed lines); (b) shows the magnitude of $|a_o|$ and the wake electric field, E_w (dashed line); (c) shows the phase trajectories in (u, Φ) space and (d) shows the normalised electron density perturbation across the simulation grid.

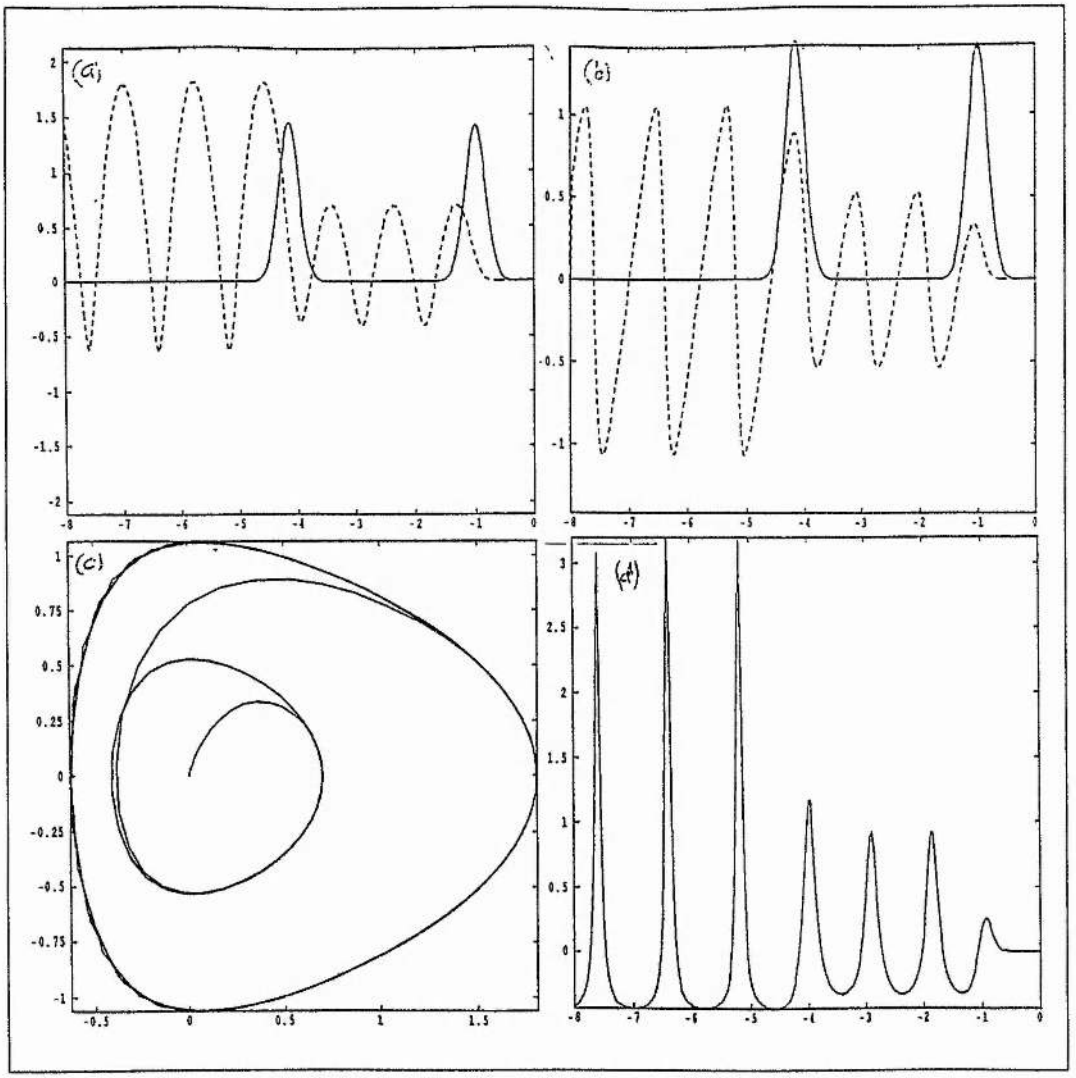

Figure 3.14: The simulation output for a train of two laser pulses with parameters $A_1 = A_2 = \sqrt{2}$ and $\sigma_r = \sigma f = 0.25$ and a frequency ratio $\omega_{po}/\omega_o = 0.05$ at time $t = 6T_p$. (a) shows the magnitude of $|a_o|$ (solid line) and the real and imaginary parts of a_o (dashed lines); (b) shows the magnitude of $|a_o|$ and the wake electric field, E_w (dashed line); (c) shows the phase trajectories in (u, Φ) space and (d) shows the normalised electron density perturbation across the simulation grid.

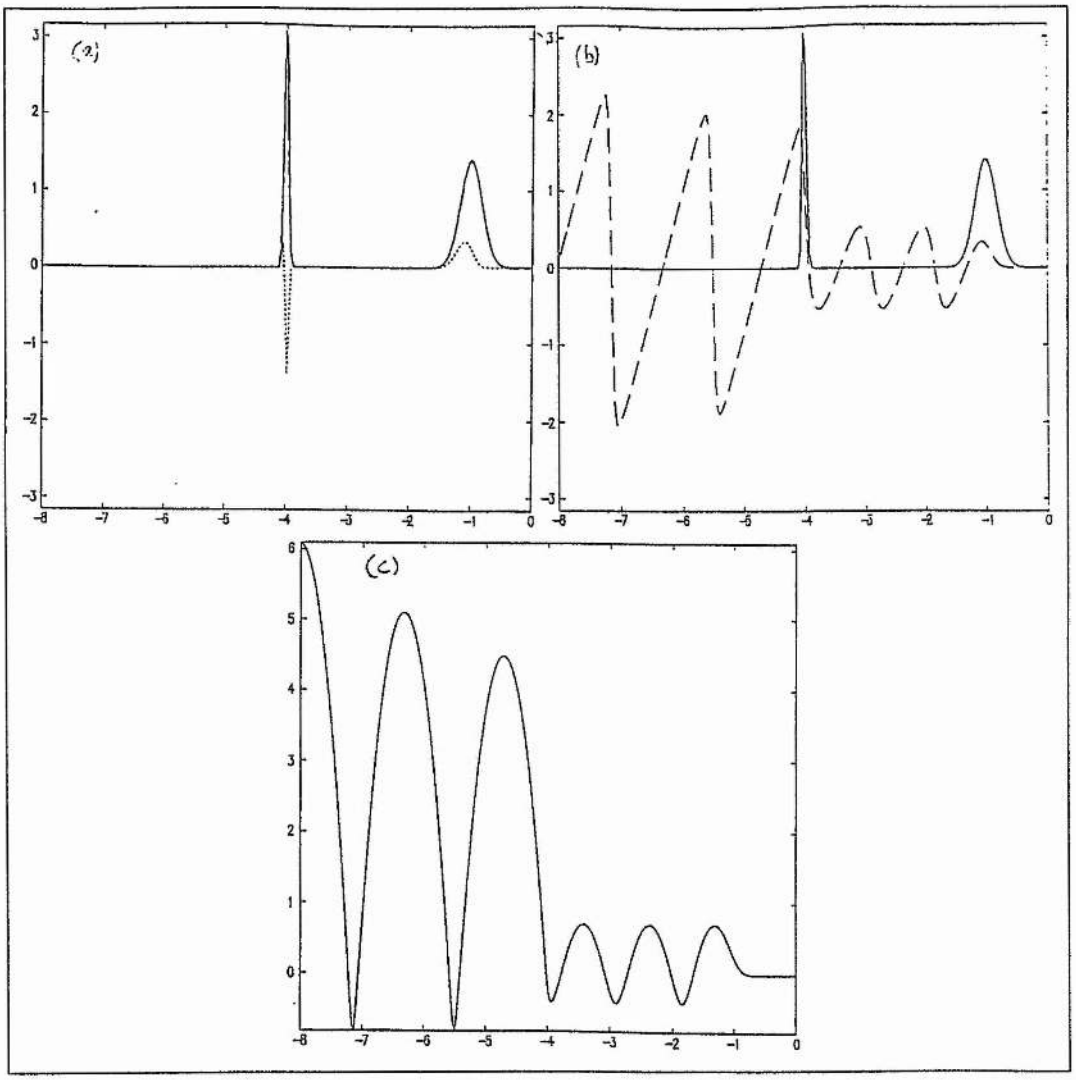

Figure 3.15: Simulation output for a train of two laser pulses at time $t = 6T_p$ for the parameter values $A_1 = \sqrt{2}, A_2 = \sqrt{10}, \sigma_{\mathrm{r,f}} = 0.25$ for the lead pulse and $\sigma_{\mathrm{r,f}} = 0.05$ for the trailing pulse and $\frac{\omega_p}{\omega} = 0.05$ (a) shows the magnitude of the pulse amplitudes (solid line) and their real and imaginary parts (dashed lines); (b) shows the magnitude of the pulses and the wake electric field (dashed line) and (c) shows the electrostatic potential, Φ.

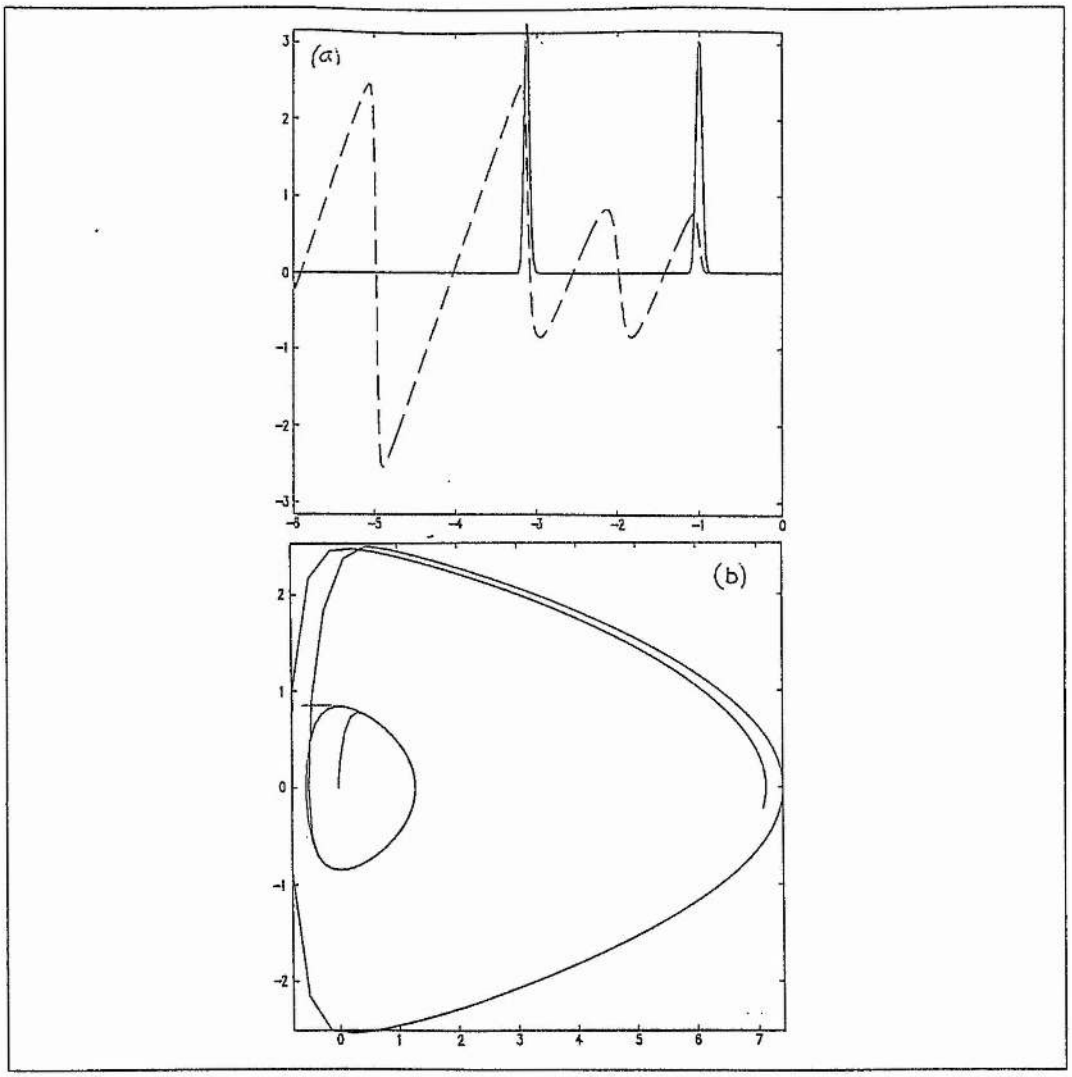

Figure 3.16: Simulation output for a train of two laser pulses at time $t = 6T_p$ for the parameter values $A_1 = A_2 = \sqrt{10}, \sigma_{\mathrm{r,f}} = 0.05$ for the lead pulse and $\sigma_{\mathrm{r,f}} = 0.05$ for the trailing pulse and $\frac{\omega_p}{\omega} = 0.05$ (a) shows the magnitude of the laser pulses (solid line) and the electric wakefield (dashed lines) and (b) shows the phase trajectories in (u, Φ) space.

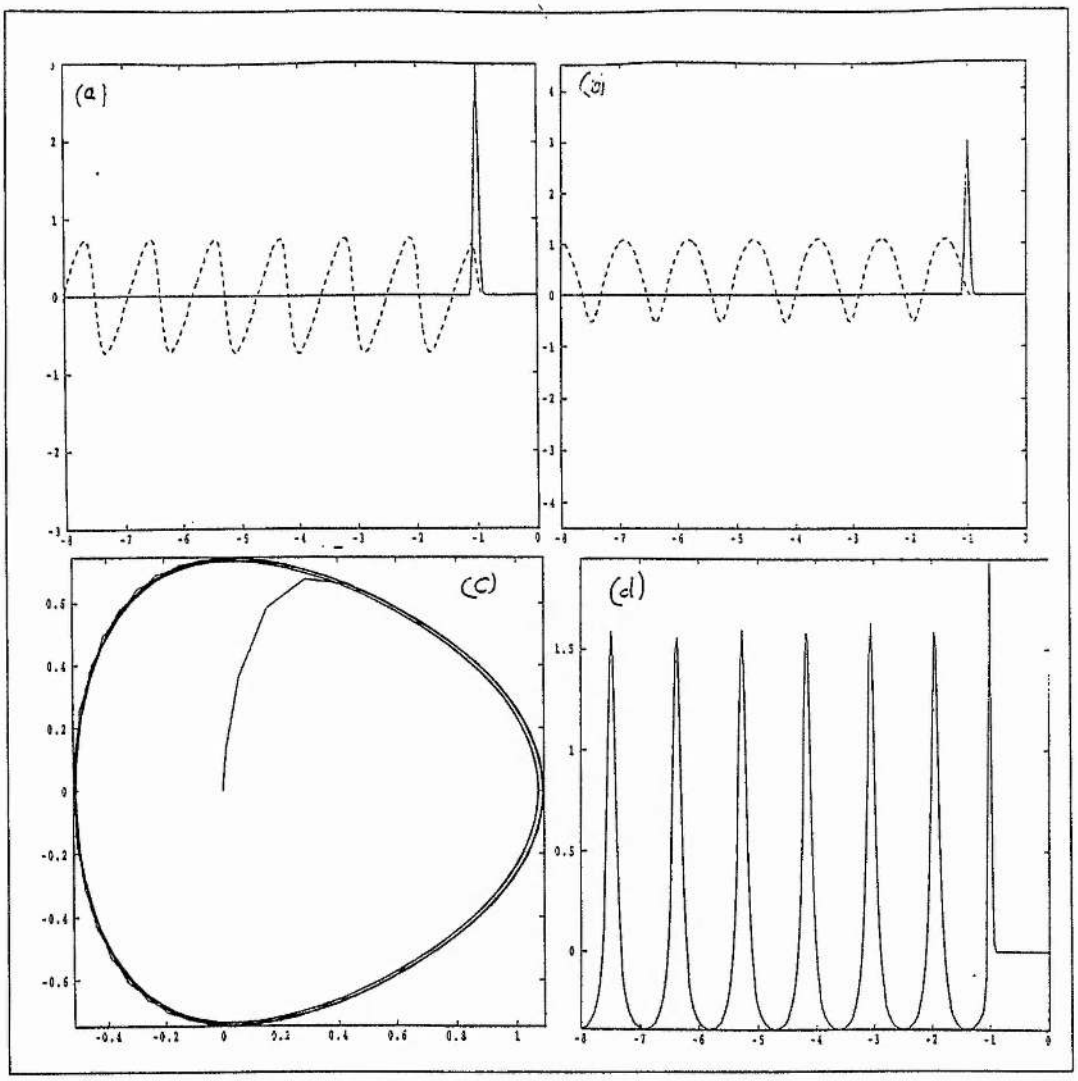

Figure 3.17: Simulation output for a single pulse at time $t = 6T_p$ for the parameter values $a_0 = 3\,, \sigma_{r,f} = 0.05$ and $\frac{\omega_p}{\omega} = 0.01$. (a) shows the magnitude of the pulse (solid line) and the electric wakefield (dashed lines); (b) shows the magnitude of the pulse and the electrostatic potential, Φ,(dashed line); (c) shows the phase trajectories in (u, Φ) space and (d) shows the normalised electron perturbation.

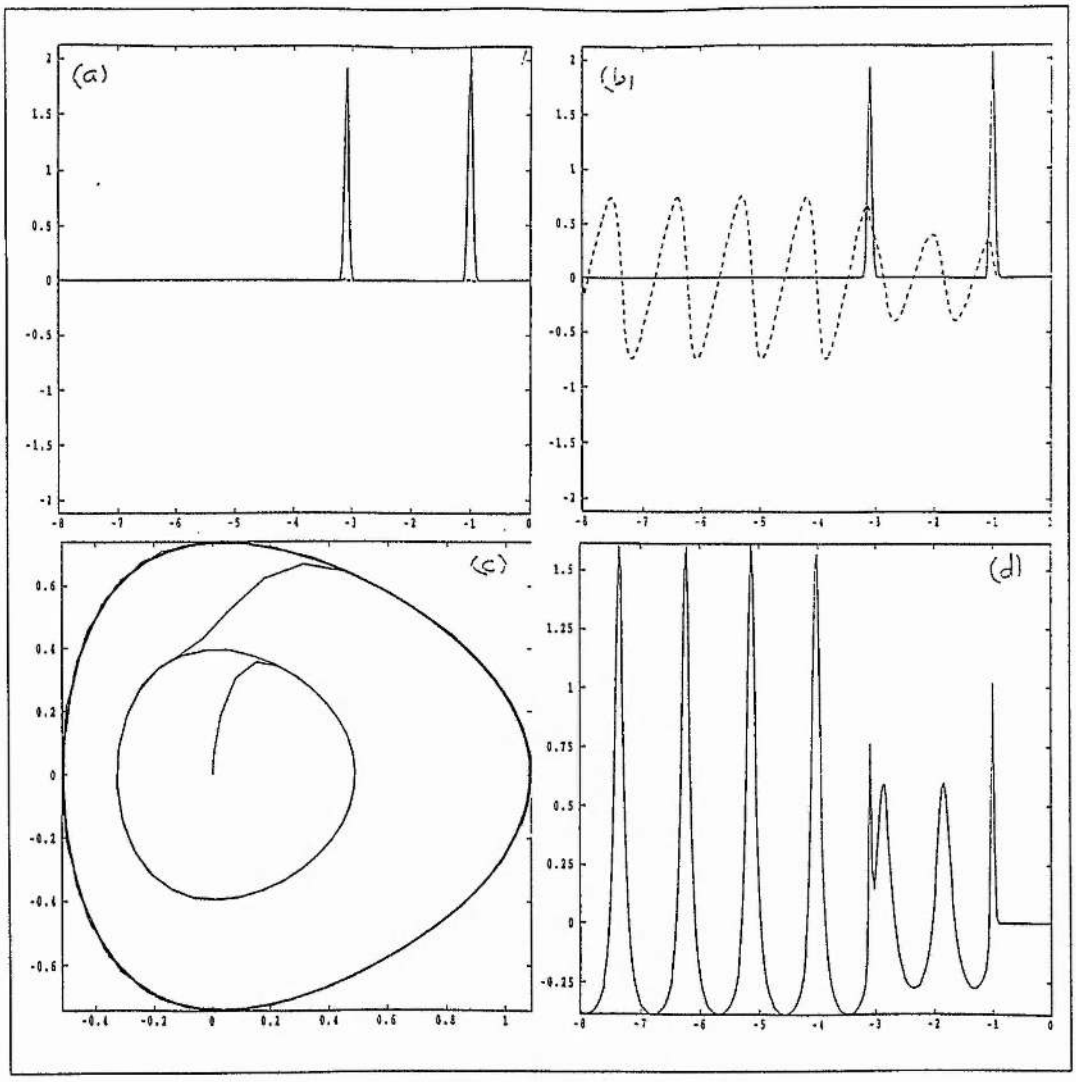

Figure 3.18: The simulation output for a train of two laser pulses with parameters $A_1 = A_2 = 2.12$ and $\sigma_\tau = \sigma f = 0.05$ and a frequency ratio $\omega_{po}/\omega_o = 0.01$ at time $t = 30T_p$. The second pulse is phased to coincide with a local maximum of the wakefield. (a) shows the magnitude of $|a_o|$ (solid line) and the real and imaginary parts of a_o (dashed lines); (b) shows the magnitude of $|a_o|$ and the wake electric field, E_w (dashed line); (c) shows the phase trajectories in (u, Φ) space and (d) shows the normalised electron density perturbation across the simulation grid.

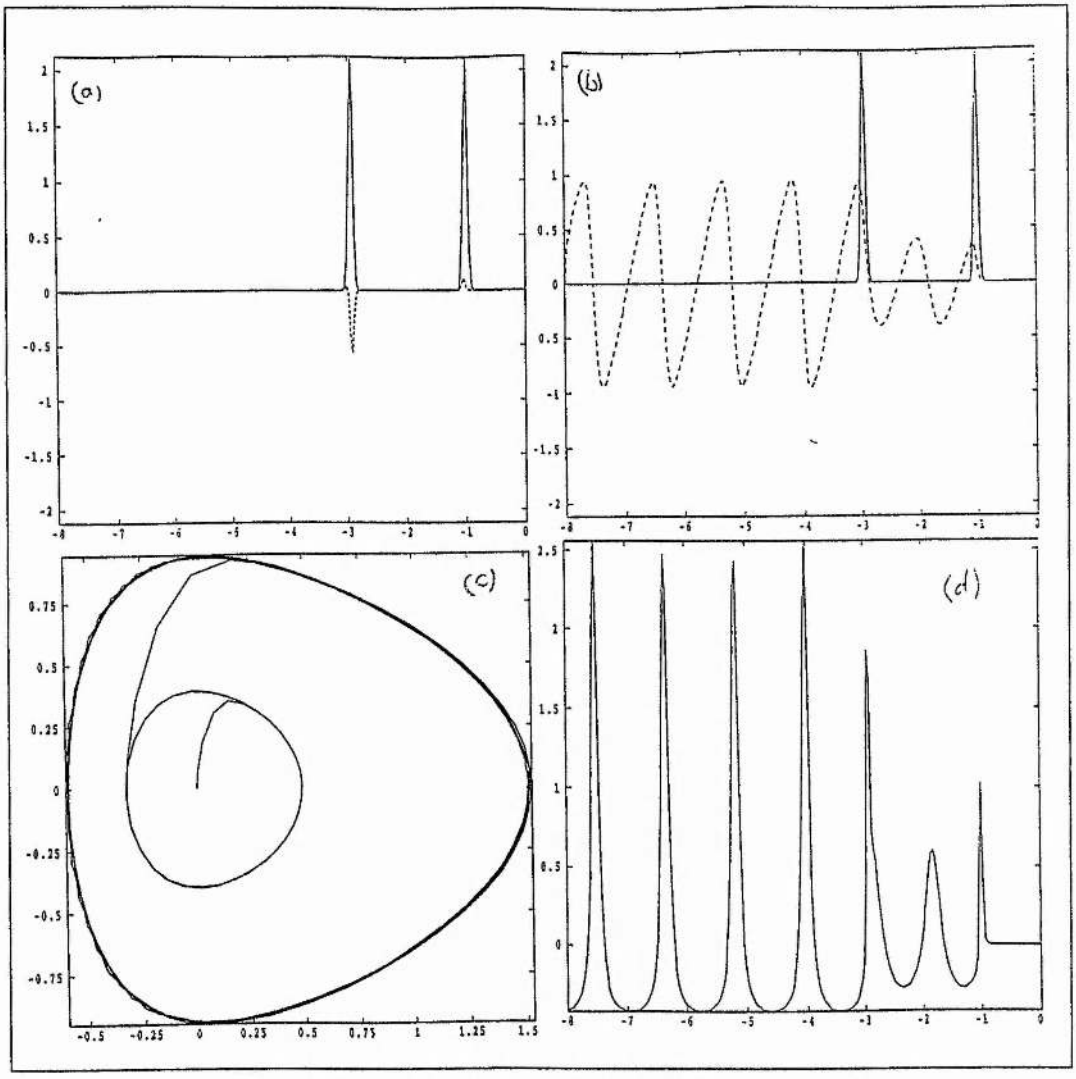

Figure 3.19: The simulation output for a train of two laser pulses with parameters $A_1 = A_2 = 2.12$ and $\sigma_r = \sigma f = 0.05$ and a frequency ratio $\omega_{po}/\omega_o = 0.01$ at time $t = 30T_p$. The second pulse is phased to interact close to the local minimum of the wake potential. (a) shows the magnitude of $|a_o|$ (solid line) and the real and imaginary parts of a_o (dashed lines); (b) shows the magnitude of $|a_o|$ and the wake electric field, E_w (dashed line); (c) shows the phase trajectories in (u, Φ) space and (d) shows the normalised electron density perturbation across the simulation grid.

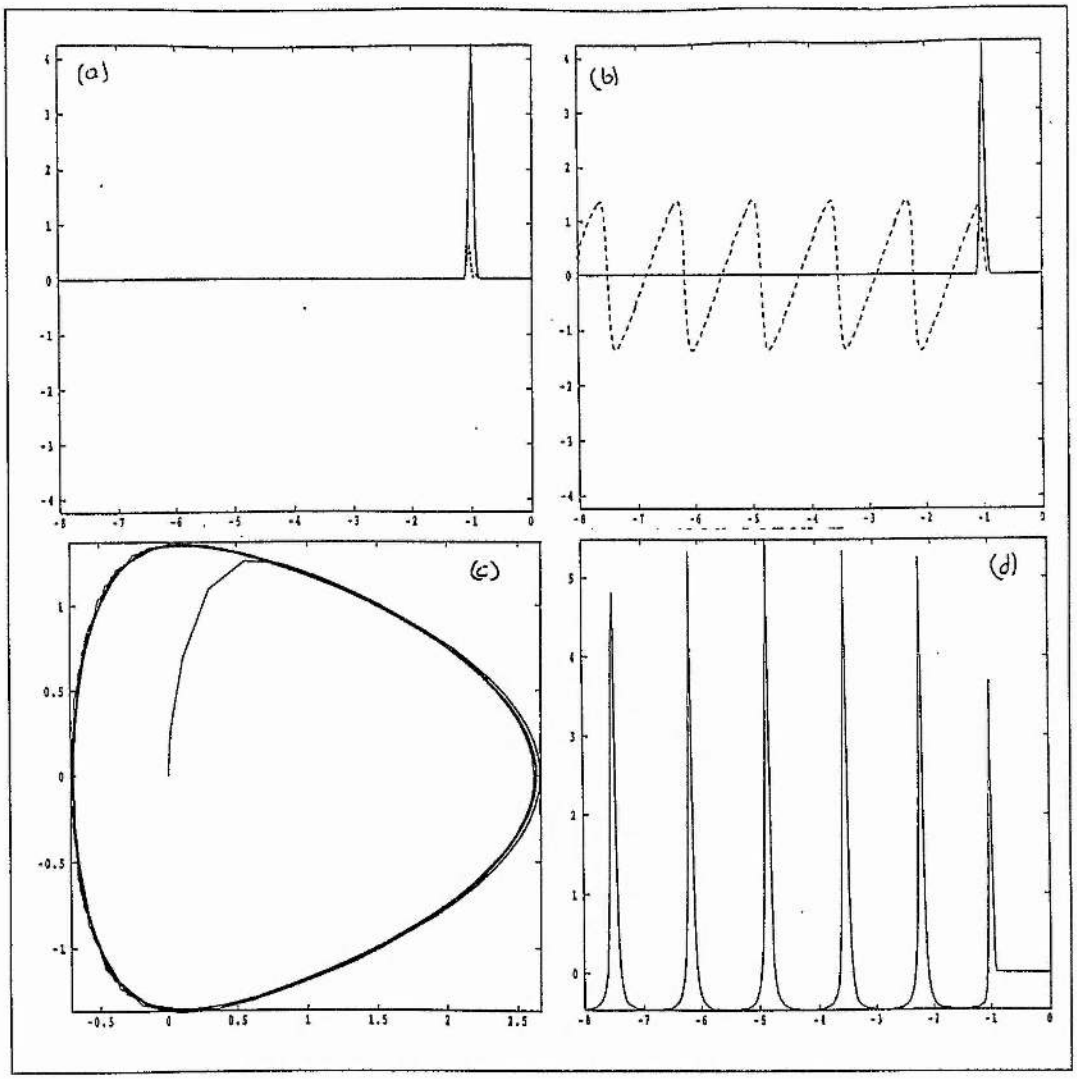

Figure 3.20: The simulation output for a single pulse with parameters $|a_o| = 4.24$ and $\sigma_r = \sigma f = 0.05$ and a frequency ratio $\omega_{po}/\omega_o = 0.05$ at time $t = 6T_p$. (a) shows the magnitude of $|a_o|$ (solid line) and the real and imaginary parts of a_o (dashed lines); (b) shows the magnitude of $|a_o|$ and the wake electric field, E_w (dashed line); (c) shows the phase trajectories in (u, Φ) space and (d) shows the normalised electron density perturbation across the simulation grid.

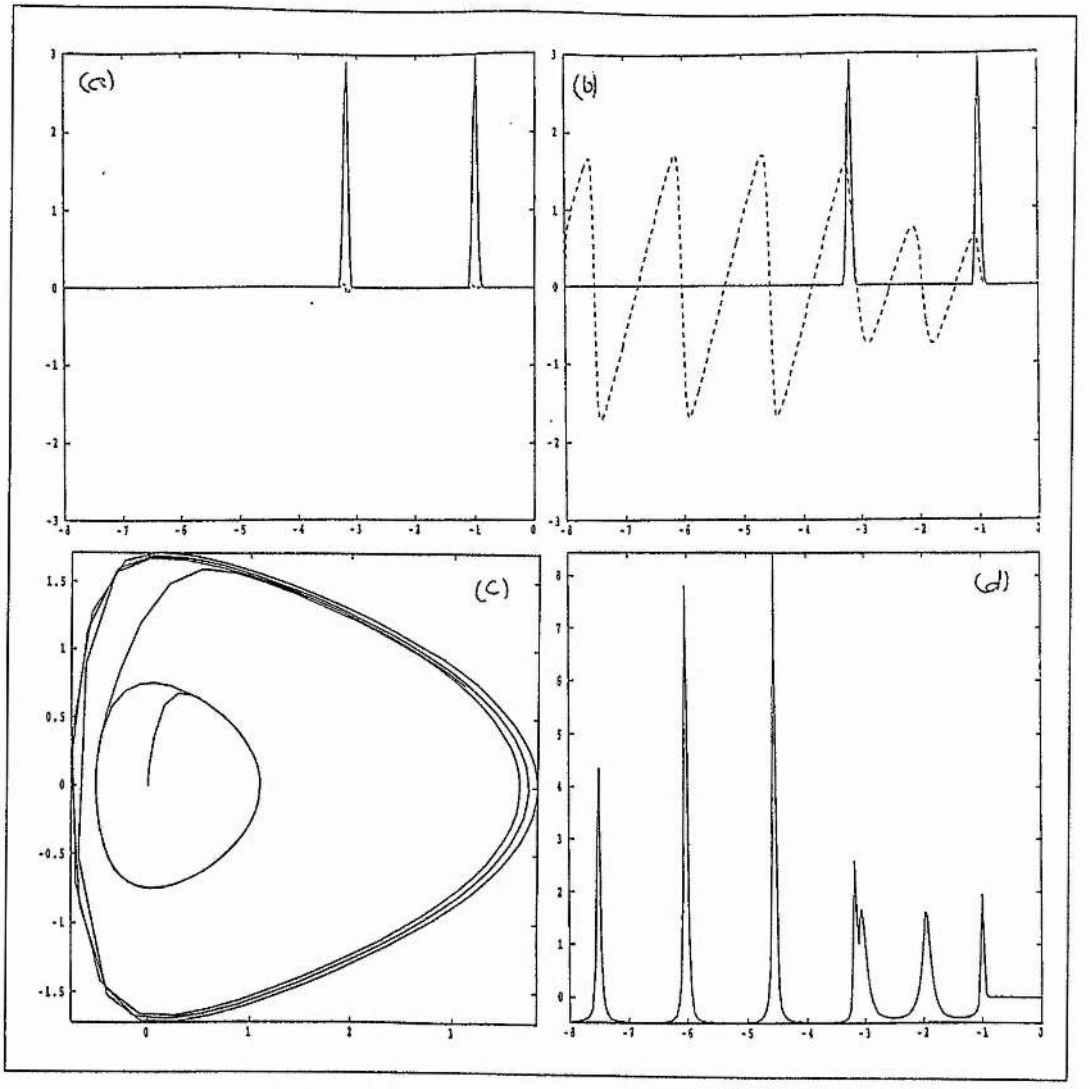

Figure 3.21: The simulation output for a train of two laser pulses with parameters $A_1 = A_2 = 3$ and $\sigma_r = \sigma f = 0.05$ and a frequency ratio $\omega_{po}/\omega_o = 0.05$ at time $t = 1T_p$. (a) shows the magnitude of $|a_o|$ (solid line) and the real and imaginary parts of a_o (dashed lines); (b) shows the magnitude of $|a_o|$ and the wake electric field, E_w (dashed line); (c) shows the phase trajectories in (u, Φ) space and (d) shows the normalised electron density perturbation across the simulation grid.

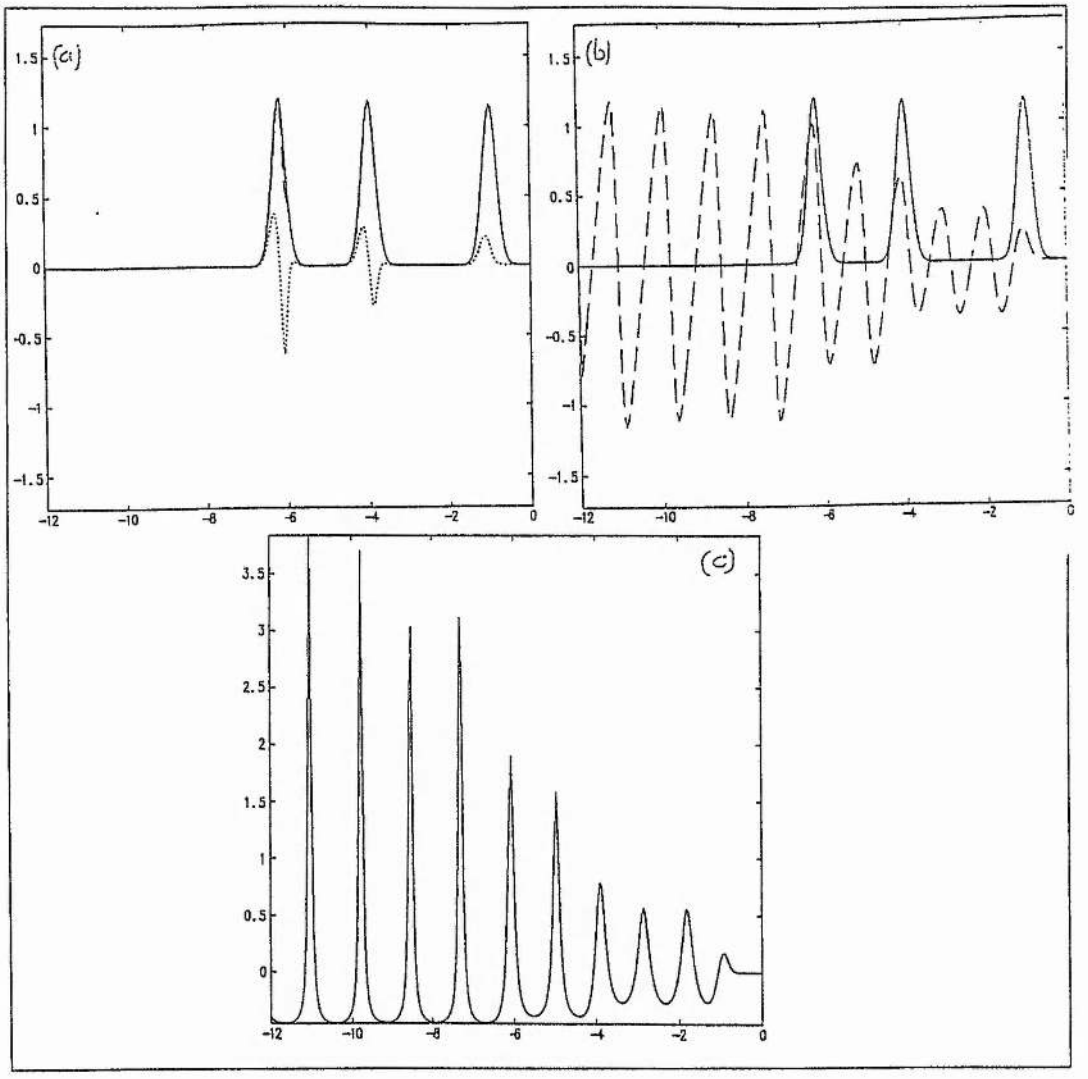

Figure 3.22: Simulation output for a train of three laser pulses with parameter values $A_1 = A_2 = A_3 = \frac{2}{\sqrt{3}}, \sigma_{r,f} = 0.25$ and $\frac{\omega_p}{\omega} = 0.05$ at time $t = 6T_p$. (a) shows the magnitude of the laser pulses (solid line) and their real and imaginary parts (dashed lines); (b) shows the magnitude of the laser pulses and the wake electric field (dashed line) and (c) shows the normalised electron density perturbation.

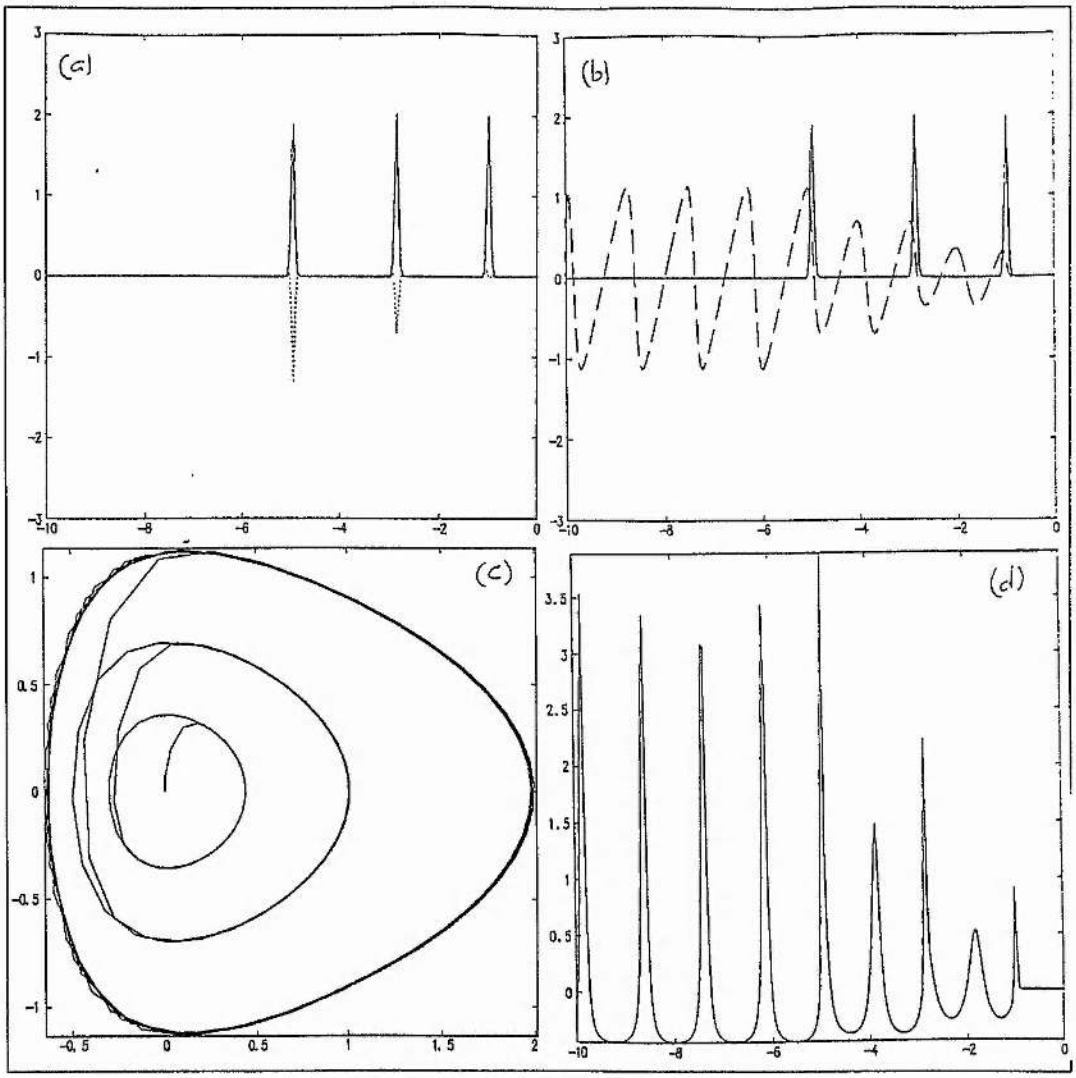

Figure 3.23: Simulation output for a train of three laser pulses at time $t = 6T_p$ for the parameter values $A_1 = A_2 = A_3 = 2, \sigma_{r,f} = 0.05$ and $\frac{\omega_p}{\omega} = 0.05$. (a) shows the magnitude of $|a_o|$ (solid line) and the real and imaginary parts of a_o (dashed lines); (b) shows the magnitude of $|a_o|$ and the wake electric field, E_w (dashed line); (c) shows the phase trajectories in (u, Φ) space and (d) shows the normalised electron density perturbation across the simulation grid.

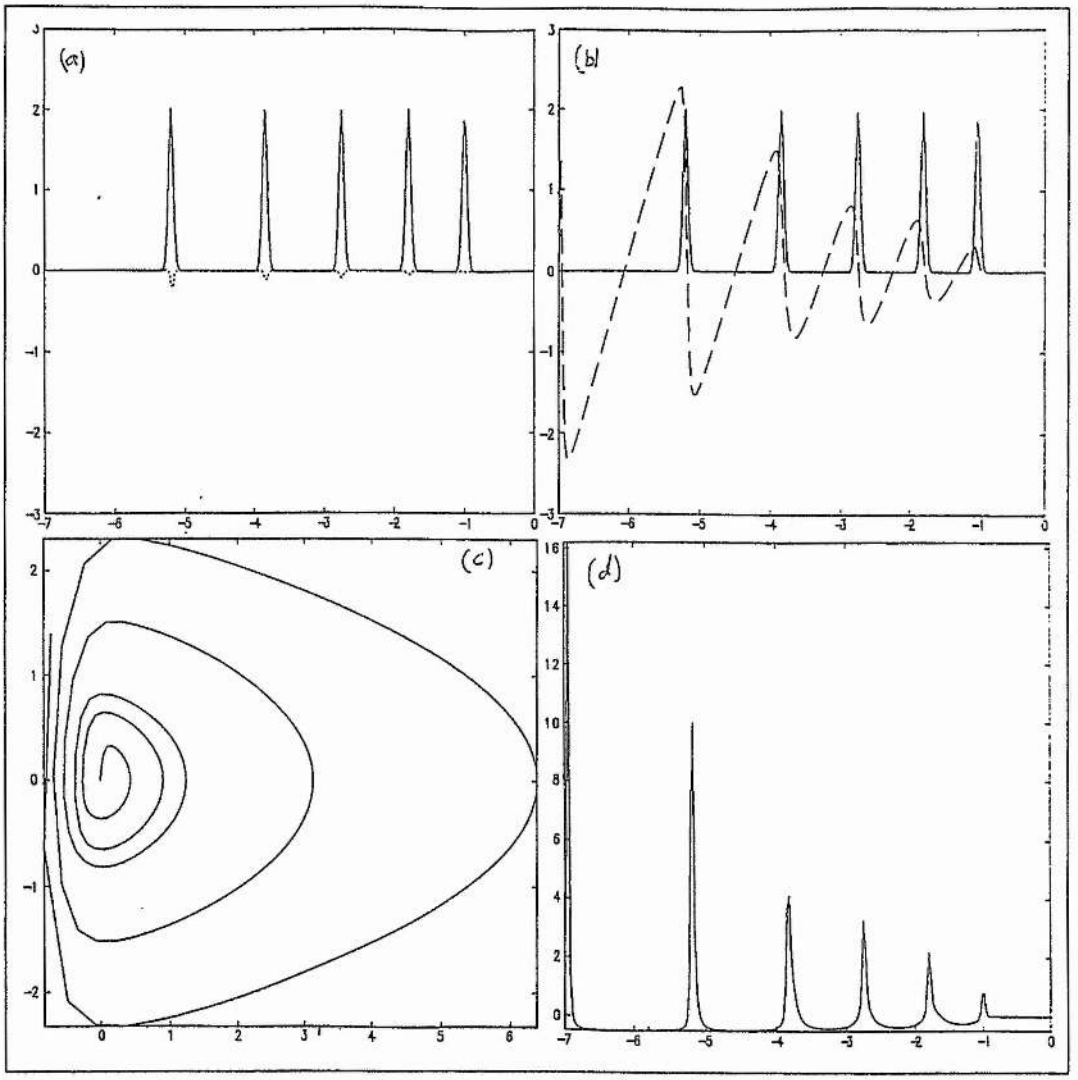

Figure 3.24: Simulation output for a train of five laser pulses at time $t = 0.4T_p$ for the parameter values $|a| = 2\,, \sigma_{\mathrm{r,f}} = 0.05$ and $\frac{\omega_p}{\omega} = 0.05$. (a) shows the magnitude of $|a_o|$ (solid line) and the real and imaginary parts of a_o (dashed lines); (b) shows the magnitude of $|a_o|$ and the wake electric field, E_w (dashed line); (c) shows the phase trajectories in (u, Φ) space and (d) shows the normalised electron density perturbation across the simulation grid.

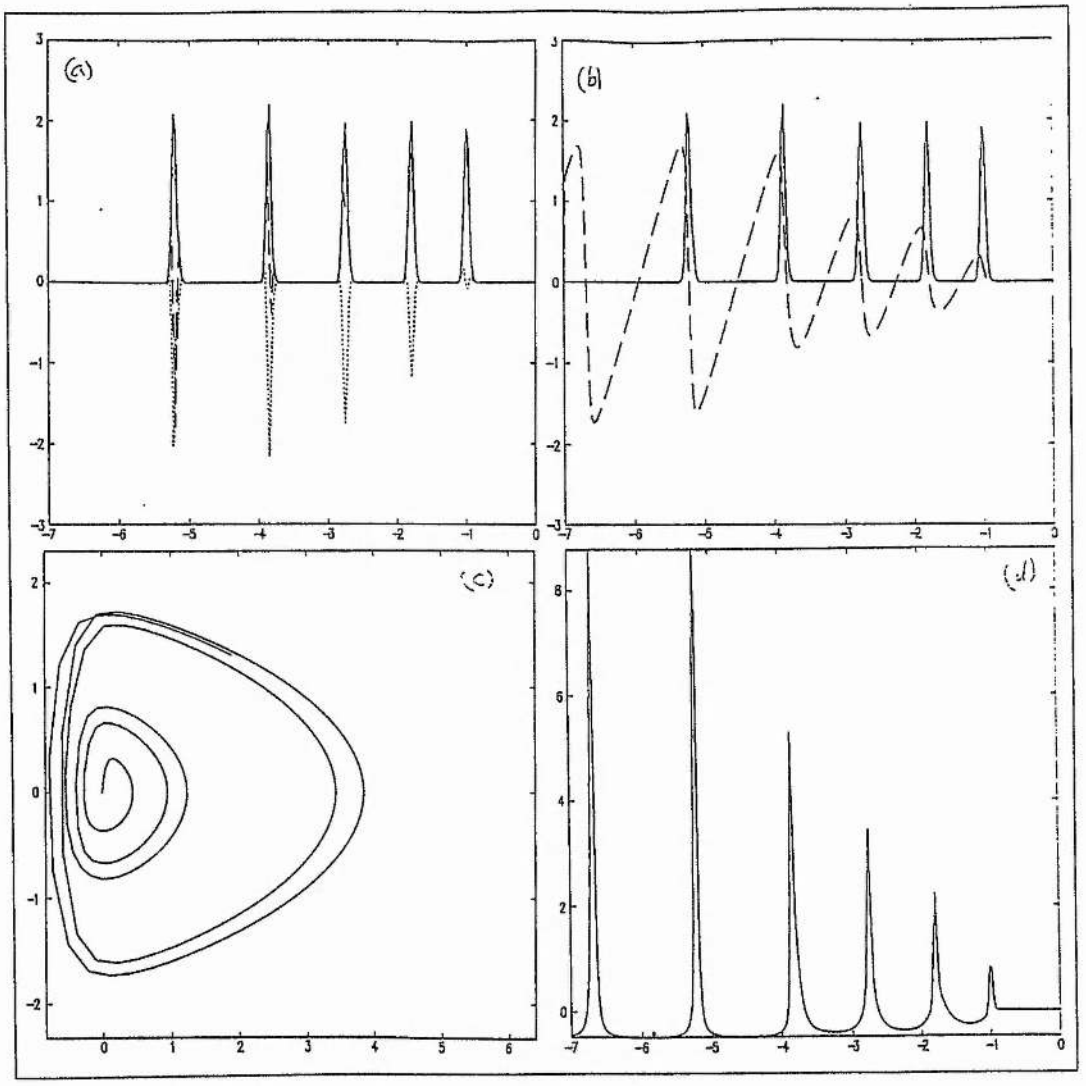

Figure 3.25: Simulation output for a train of five laser pulses at time $t = 10T_p$ for the parameter values $|a| = 2\,, \sigma_{\mathrm{r,f}} = 0.05$ and $\frac{\omega_p}{\omega} = 0.05$. (a) shows the magnitude of $|a_o|$ (solid line) and the real and imaginary parts of a_o (dashed lines); (b) shows the magnitude of $|a_o|$ and the wake electric field, E_w (dashed line); (c) shows the phase trajectories in (u, Φ) space and (d) shows the normalised electron density perturbation across the simulation grid.

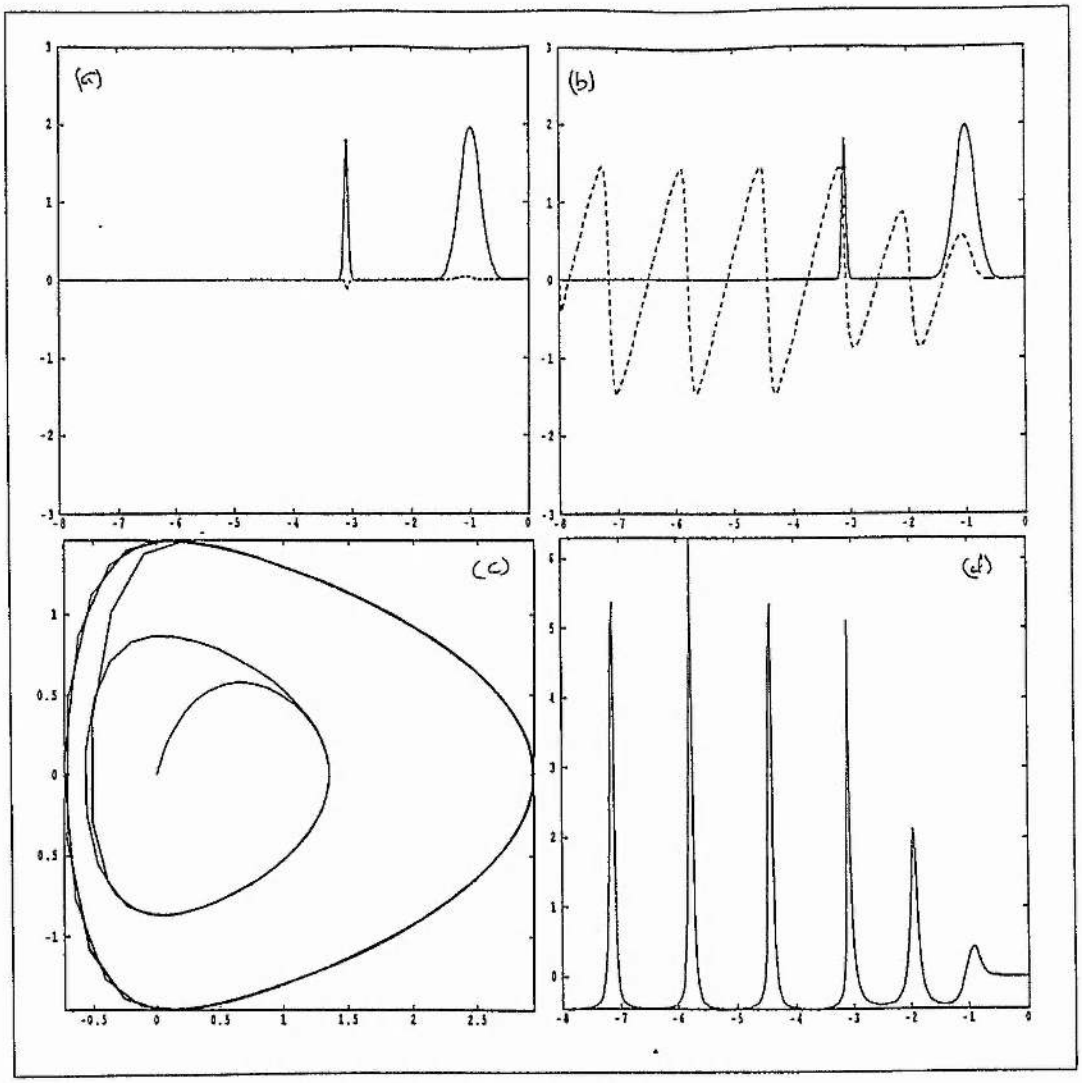

Figure 3.26: Simulation output for a train of two laser pulses at time $t = 0.4T_p$ for the parameter values $A_1 = A_2 = 2, \sigma_{\mathrm{r,f}} = 0.25$ for the leading pulse, $\sigma_{\mathrm{r,f}} = 0.05$ for the trailing pulse and $\frac{\omega_p}{\omega} = 0.05$. (a) shows the magnitude of $|a_o|$ (solid line) and the real and imaginary parts of a_o (dashed lines); (b) shows the magnitude of $|a_o|$ and the wake electric field, E_w (dashed line); (c) shows the phase trajectories in (u, Φ) space and (d) shows the normalised electron density perturbation across the simulation grid.

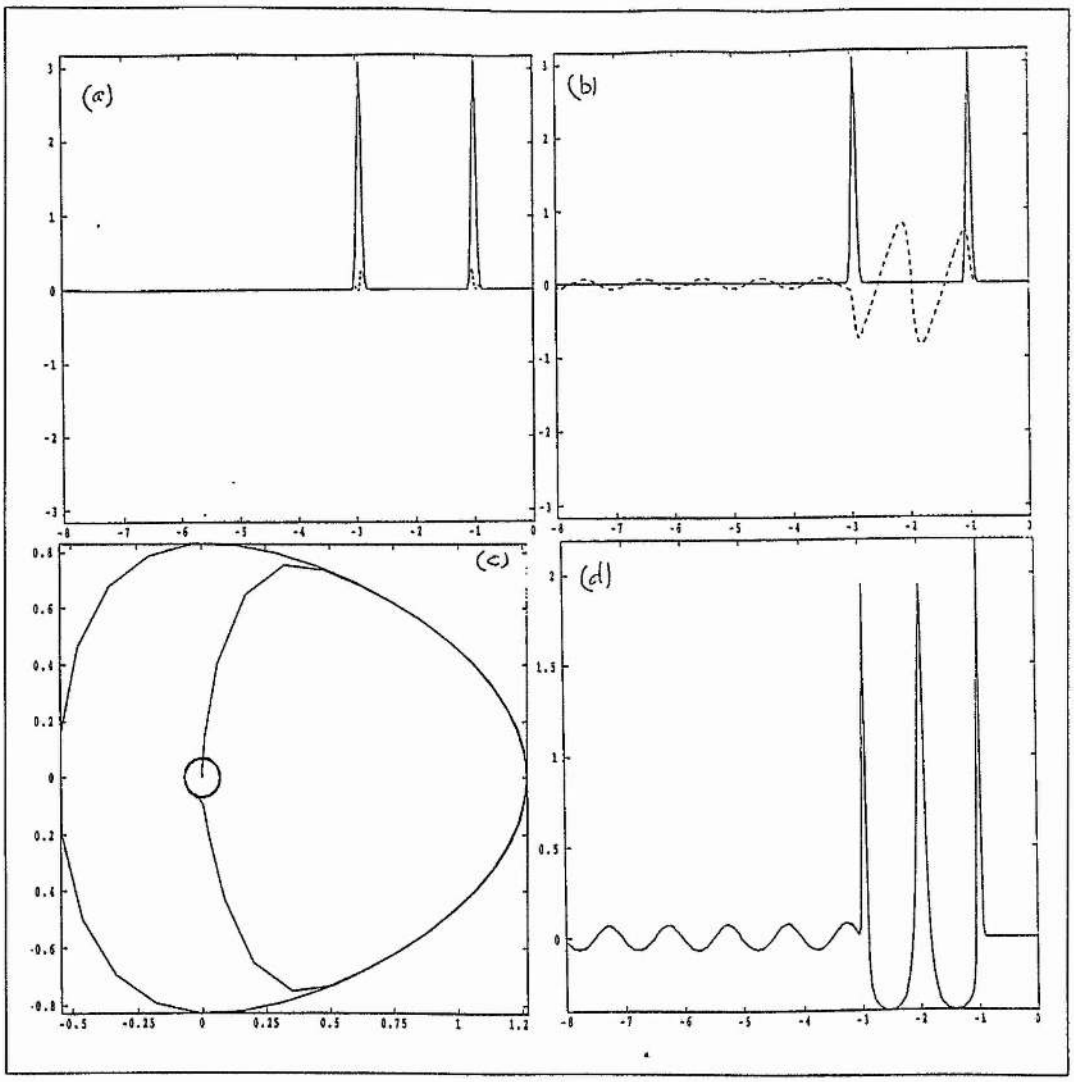

Figure 3.27: Simulation output for a train of two laser pulses at time $t = 6T_p$ for the parameter values $A_1 = A_2 = \sqrt{10}\,, \sigma_{\mathrm{r,f}} = 0.05$ and $\frac{\omega_p}{\omega} = 0.05$. The pulses are phased such that the trailing pulse is in the accelerating phase of the plasma wave. (a) shows the magnitude of $|a_o|$ (solid line) and the real and imaginary parts of a_o (dashed lines); (b) shows the magnitude of $|a_o|$ and the wake electric field, E_w (dashed line); (c) shows the phase trajectories in (u, Φ) space and (d) shows the normalised electron density perturbation across the simulation grid.

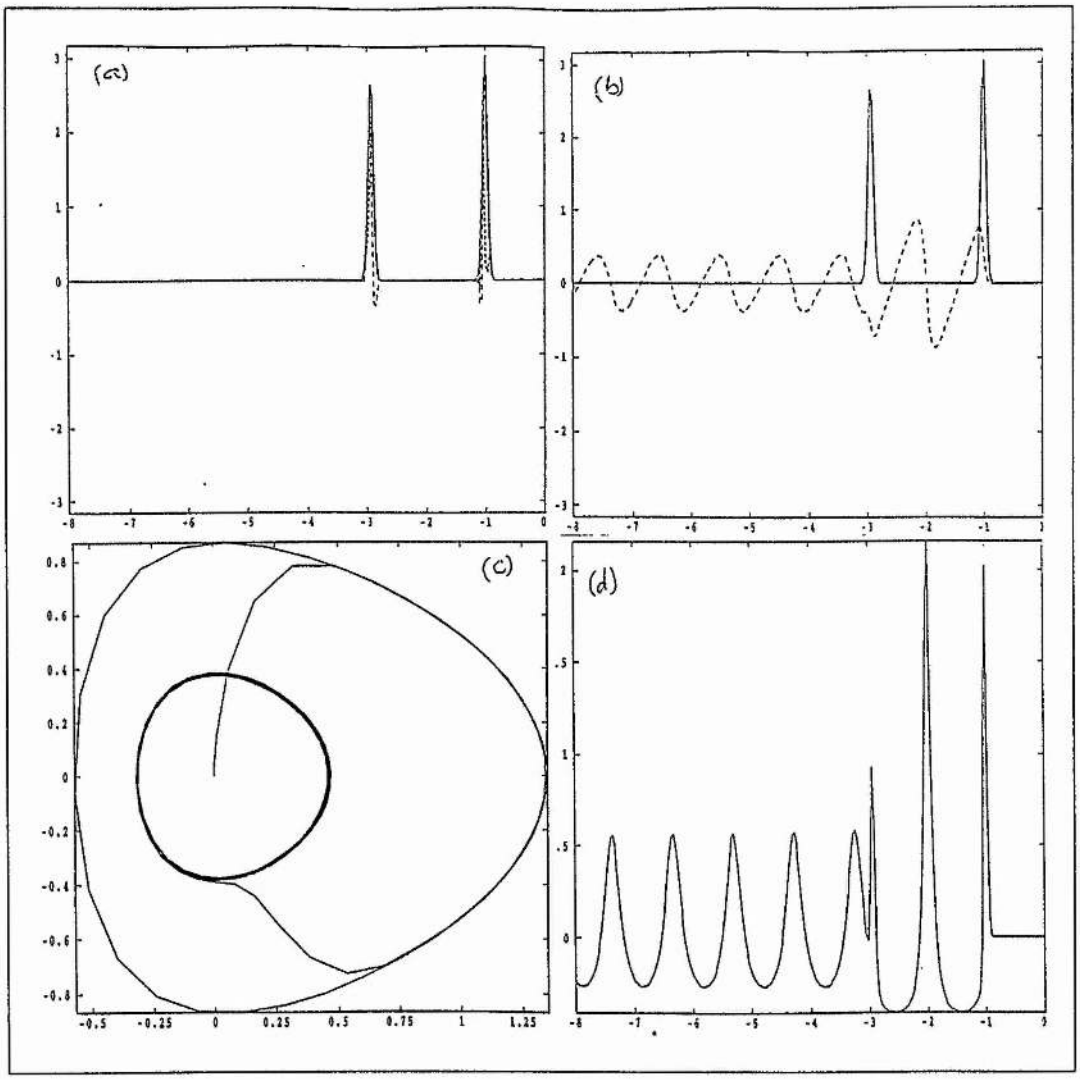

Figure 3.28: Simulation output for a train of two laser pulses at time $t = 40T_p$ for the parameter values $A_1 = A_2 = \sqrt{10}, \sigma_{r,f} = 0.05$ and $\frac{\omega_p}{\omega} = 0.05$. (a) shows the magnitude of $|a_o|$ (solid line) and the real and imaginary parts of a_o (dashed lines); (b) shows the magnitude of $|a_o|$ and the wake electric field, E_w (dashed line); (c) shows the phase trajectories in (u, Φ) space and (d) shows the normalised electron density perturbation across the simulation grid.

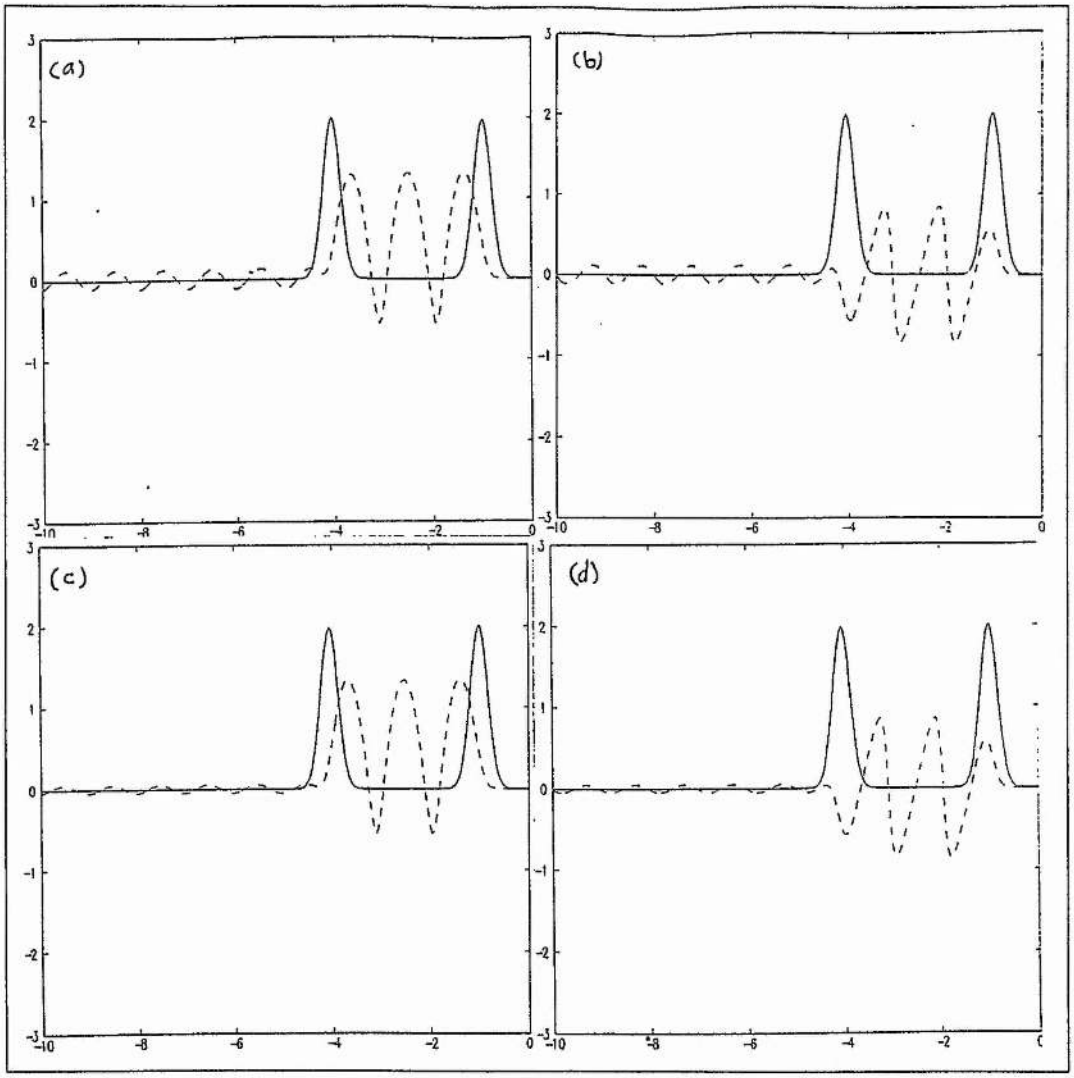

Figure 3.29: Simulation output for a train of two laser pulses for the parameter values $A_1 = A_2 = 2\,, \sigma_{r,f} = 0.25$ and $\frac{\omega_p}{\omega} = 0.01$ at times $t = 2T_p$ and $100T_p$. (a) and (c) show the magnitudes of the laser pulses (solid line) and the plasma electrostatic potential (dashed line); (b) and (d) show the magnitudes of the laser pulses (solid line) and the wake electric field, E_w. (a) and (b) is the output at time $t = 2T_p$; (c) and (d) are at time $t = 100T_p$.

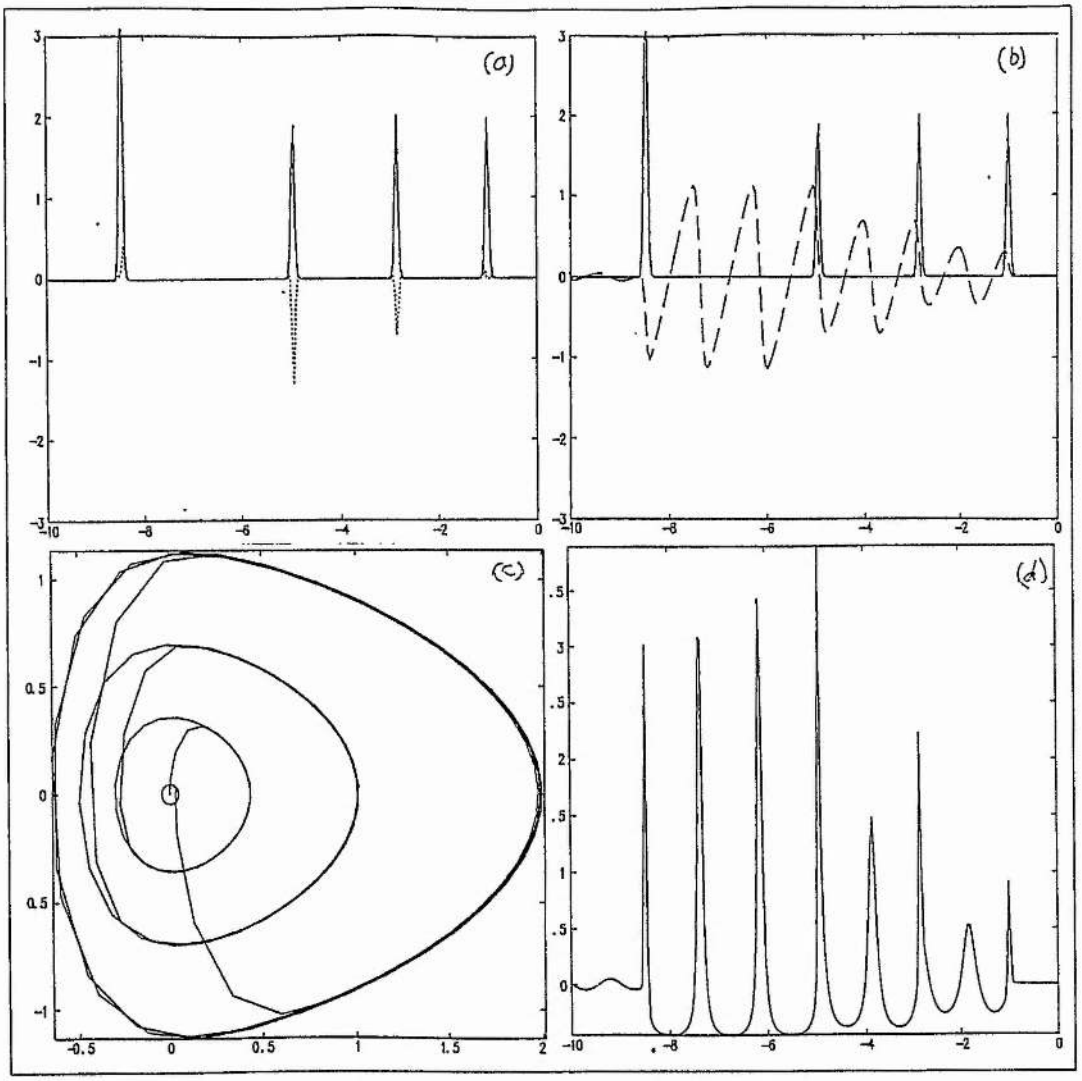

Figure 3.30: Simulation output for a four pulse laser train at time $t = 6T_p$. The three leading pulses each have the parameter values $|a| = 2\,, \sigma_{r,f} = 0.05$ and $\frac{\omega_p}{\omega} = 0.05$. The trailing pulse has $|a| = 2$. (a) shows the magnitude of $|a_o|$ (solid line) and the real and imaginary parts of a_o (dashed lines); (b) shows the magnitude of $|a_o|$ and the wake electric field, E_w (dashed line); (c) shows the phase trajectories in (u, Φ) space and (d) shows the normalised electron density perturbation across the simulation grid.

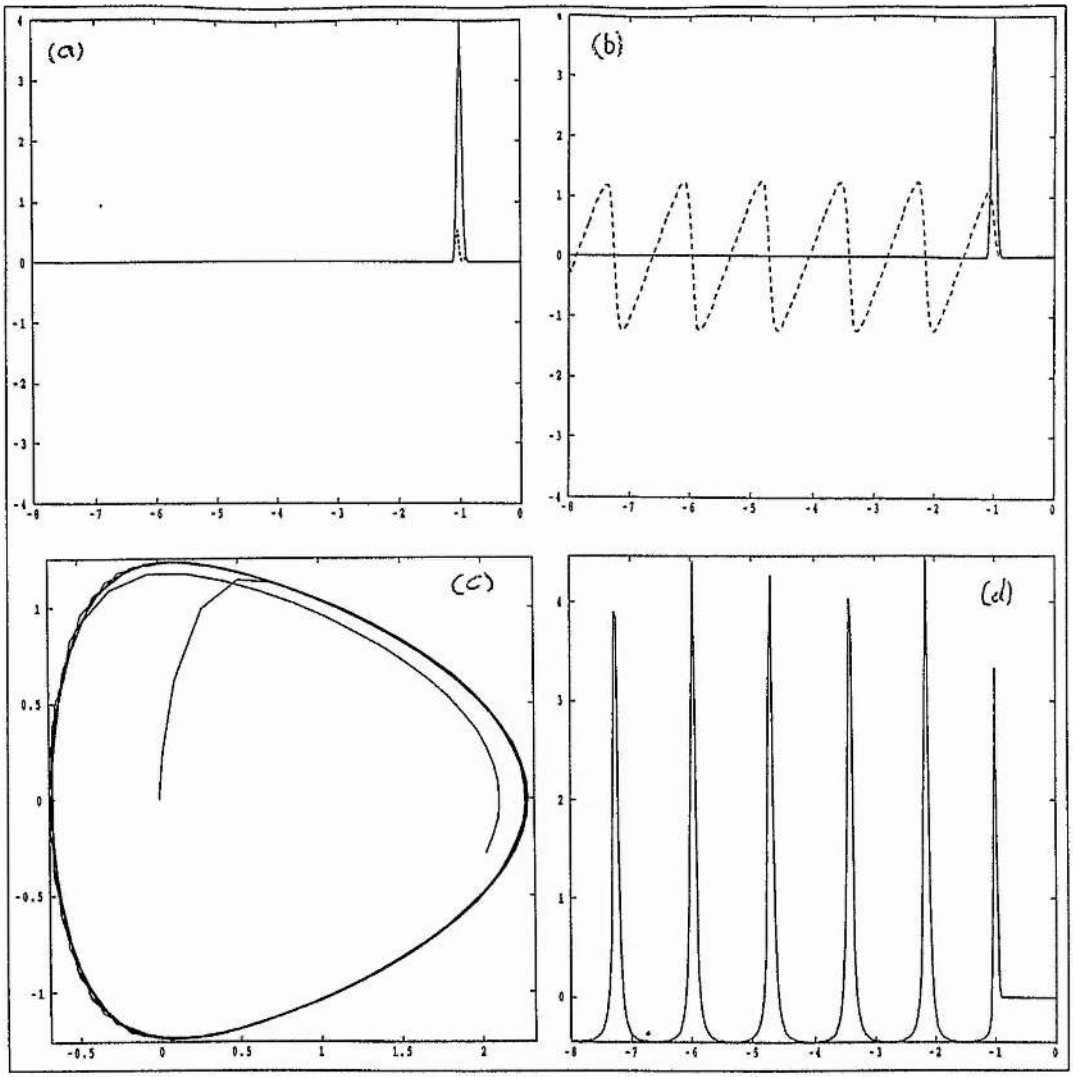

Figure 3.31: Simulation output for a single pulse at time $t = 6T_p$ for the parameter values $a_0 = 4$, $\sigma_{\mathrm{r,f}} = 0.05$ and $\frac{\omega_p}{\omega} = 0.05$. (a) shows the magnitude of $|a_o|$ (solid line) and the real and imaginary parts of a_o (dashed lines); (b) shows the magnitude of $|a_o|$ and the wake electric field, E_w (dashed line); (c) shows the phase trajectories in (u, Φ) space and (d) shows the normalised electron density perturbation across the simulation grid.

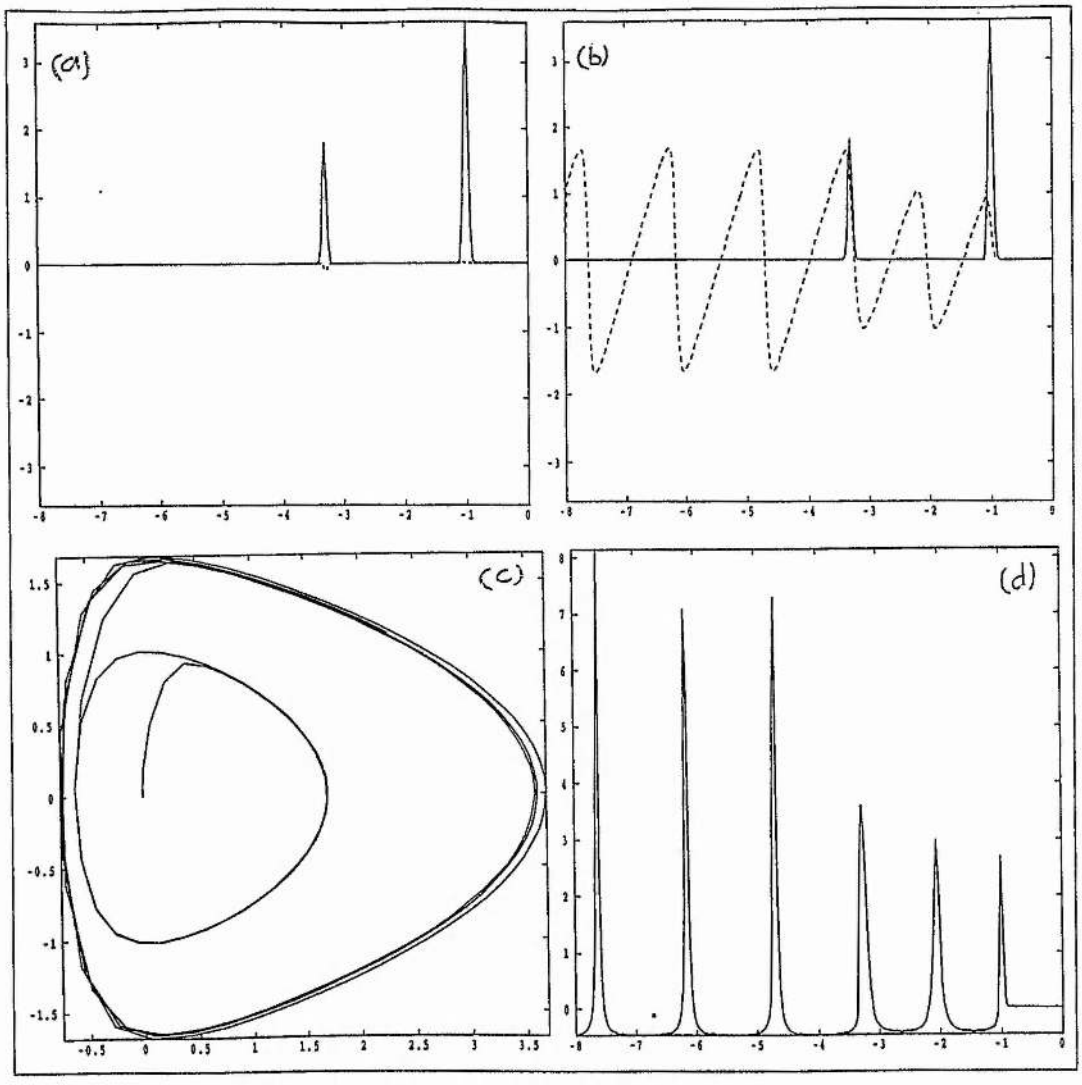

Figure 3.32: Simulation output for a train of two laser pulses at time $t = 0.4T_p$ for the parameter values $A_1 = 3.580\,, A_2 = 1.790\,, \sigma_{\mathrm{r,f}} = 0.05$ and $\frac{\omega_p}{\omega} = 0.05$. (a) shows the magnitude of $|a_o|$ (solid line) and the real and imaginary parts of a_o (dashed lines); (b) shows the magnitude of $|a_o|$ and the wake electric field, E_w (dashed line); (c) shows the phase trajectories in (u, Φ) space and (d) shows the normalised electron density perturbation across the simulation grid.

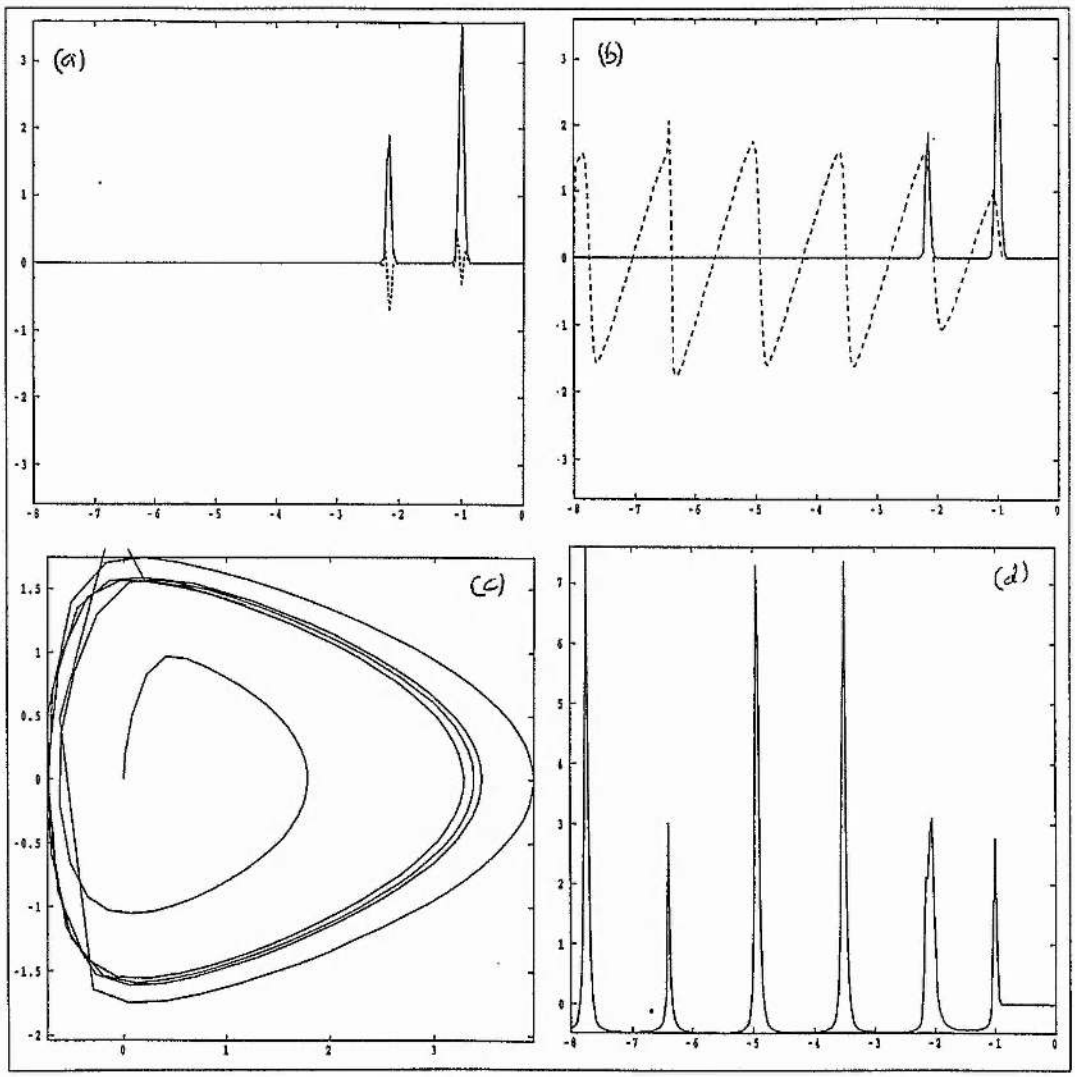

Figure 3.33: Simulation output for a train of two laser pulses at time $t = 2T_p$ for the parameter values $A_1 = 3.580\,, A_2 = 1.790\,, \sigma_{\mathrm{r,f}} = 0.05$ and $\frac{\omega_p}{\omega} = 0.1$. (a) shows the magnitude of $|a_o|$ (solid line) and the real and imaginary parts of a_o (dashed lines); (b) shows the magnitude of $|a_o|$ and the wake electric field, E_w (dashed line); (c) shows the phase trajectories in (u, Φ) space and (d) shows the normalised electron density perturbation across the simulation grid.

Chapter 4

Inhomogeneous Plasma Wakefield Generation

One of the main limitations on the acceleration length in particle accelerators based on using a relativistic electron plasma wave is the de-phasing distance between the plasma wave and the injected particles. The same effect also limits the amount of frequency up-shift in the Photon Accelerator scheme, where the injected electron bunch is replaced by a short ($\leq \frac{1}{2}\lambda_p$) pulse of laser radiation. One possible solution to both of these de-phasing problems is to continuously change the phase velocity of the plasma wave as the electrons/photons are accelerated, so that they remain in the accelerating phase of the plasma wave. In the Laser Wakefield Accelerator scheme, the phase velocity of the plasma wave is closely matched to the group velocity of the laser pulse. If the laser pulse is sufficiently short compared to the background plasma wavelength, its group velocity is the linear group velocity $v_g = c\sqrt{1 - \frac{\omega_p^2}{\omega_0^2}}$. We may, therefore, modify the group velocity of the pulse through the local plasma density. This suggests that a ramped plasma density can provide the desired change in the phase velocity of the plasma wave and consequently increase the de-phasing distance for acceleration.

In this chapter, we present two formulations of a 1-D model for laser wakefield

generation in an inhomogeneous plasma, where the local background plasma density is a linear function of the propagation distance in the plasma. As before, we describe the plasma quantities using the cold, relativistic fluid equations and the laser pulse via Maxwell's equations. We also present an account of two numerical approaches to the solution of these new model equations and the difficulties associated with the implementation of each scheme. Finally, we present some preliminary results from the computer programs written to execute the numerical solution of the model equations.

We begin by considering the effect of the density gradient on the model equations of Chapter 2.

4.1 First Model for Inhomogeneous Plasma

We take the model of Chapter 2 and introduce a positive density gradient in the plasma with scale length L, so that the background electron density, n_0, is given by,

$$n_0 = N_0 \left(1 + \frac{z}{L}\right) , \tag{4.1}$$

where N_0 is the density at the start of the ramp and z is the propagation distance in the $\hat{z}$ direction. This density ramp makes the local plasma frequency,

$$\omega_p^2 = \omega_{p0}^2 \left(1 + \frac{z}{L}\right) , \tag{4.2}$$

where ω_{p0} is the plasma frequency at the density N_0. The effect on the model equations of Chapter 2 is explicit in the mass conservation and Poisson equations and implicit in the Maxwell's equation for the laser pulse via the coupling to the normalised plasma potential Φ. The first equation of the 'gradient' model is, again, the parallel component of the momentum equation for the electron plasma fluid,

$$\frac{1}{c}\frac{\partial}{\partial t}\left(\gamma_a \sqrt{\gamma_z^2 - 1}\right) + \frac{\partial}{\partial z}\left(\gamma_a \gamma_z\right) = \frac{\partial \Phi}{\partial z} \tag{4.3}$$

where we use the same notation and normalisation as in Chapter 2. The mass conservation equation for the electron fluid gives,

$$\frac{1}{c}\frac{\partial n\left(z\right)}{\partial t} + \frac{\partial}{\partial z}\left(\frac{n\left(z\right)\sqrt{\gamma_z^2 - 1}}{\gamma_z}\right) = 0 \tag{4.4}$$

where $n = n_0 + \delta n$ and δn is the density perturbation caused by the laser pulse. Poisson's equation takes the same form as in Chapter 2 ie.

$$\frac{\partial^2 \Phi}{\partial z^2} = \frac{\omega_p^2}{c^2}\left(\frac{n}{n_0\left(z\right)} - 1\right) \tag{4.5}$$

with the position dependent forms of the plasma frequency and the background plasma density.

The equation for the laser pulse may, similarly, be written down in terms of the new quantities,

$$\left(c^2\frac{\partial^2}{\partial z^2}-\frac{\partial^2}{\partial t^2}\right)\mathbf{a}=\omega_p^2(z)\frac{n}{n_0(z)}\frac{\mathbf{a}}{\gamma_a\gamma_z} \tag{4.6}$$

where **a** is the vector potential for the laser pulse normalised as before. In the homogeneous plasma model of Chapter 2 we use some approximations and first integrals to reduce this basic set of equations to the two coupled equations that comprise that model. We now take each of the approximations and consider their validity for the current case. First, we consider the change to the pulse frame, an inertial frame moving with the linear group velocity of the laser pulse. In the inhomogeneous plasma the group velocity of the pulse is not constant, but if the scale length of the density gradient is long, then the group velocity may only change by a few percent during the simulation. We therefore make a change of variables to the 'initial pulse frame' moving with velocity, $v_{g0}=c\sqrt{1-\frac{\omega_{p0}^2}{\omega_0^2}}$. In this way we expect the pulses to slowly slip backwards in the frame as the simulation progresses and the pulse propagates up the density gradient. In a similar way to the previous model, it is convenient to define the parameter $\beta_0=\frac{v_{g0}}{c}$. Next, we consider the envelope approximation. This remains a valid description of the laser pulse in this model and we write,

$$\mathbf{a}(z,t)=\frac{1}{2}\mathbf{a}_0(\xi,\tau)e^{-i\theta}+c.c., \tag{4.7}$$

in the same way as before. Finally, we consider the 'quasi-static' approximation [58]. This assumes that the laser pulse is sufficiently short so that the vector and scalar potentials hardly change during the transit time of the plasma through the pulse. For the long scale length density variation considered here, the transit time of the plasma through the pulse is hardly altered and the wake structure may be considered static in the region of the laser pulse so that the quasi-static approximation remains valid

for the electron fluid momentum equation. However, since the wake extends over a long distance behind the pulse and consequently is affected by the density gradient, the quasi-static approximation may not be applied to the mass continuity equation. We consider the application of the quasi-static approximation to this model by setting the time derivative in the momentum equation to zero. If we transform to the moving frame and apply the quasi-static approximation we obtain,

$$\frac{\partial}{\partial \xi}\left(\gamma_a \gamma_z - \beta_0 \gamma_a \sqrt{\gamma_z^2 - 1} - \Phi\right) = 0\,. \tag{4.8}$$

As in the previous model, we may integrate this to obtain a constant of the motion. We use the initial conditions $\mathbf{a} = \mathbf{0}$, $\Phi = 0$ to find,

$$\gamma_a\left(\gamma_z - \beta_0\sqrt{\gamma_z^2 - 1}\right) - \Phi = 1\,. \tag{4.9}$$

In contrast to the homogeneous case, we cannot now apply the quasi-static approximation to the mass continuity equation and derive a second integral of the motion. We therefore retain the statement of mass continuity in the moving frame as given in equation (4.4).

We use the information from equation (4.9) to substitute in Poisson's equation. The model is now expressed by the three coupled equations for a_0, n and Φ as given below,

$$\frac{\partial^2}{\partial \xi^2}\left\{\gamma_a\left(\gamma_z - \beta_0\sqrt{\gamma_z^2 - 1}\right)\right\} = \frac{\omega_p^2}{c}\left(\frac{n}{n_0} - 1\right) \tag{4.10}$$

$$\frac{1}{c}\frac{\partial n}{\partial \tau} + \frac{\partial}{\partial \xi}\left\{n\,\frac{\left(\sqrt{\gamma_z^2 - 1} - \beta_0\gamma_z\right)}{\gamma_z}\right\} = 0 \tag{4.11}$$

$$2\frac{\partial}{\partial \tau}\left(v_{g0}\frac{\partial a_0}{\partial \xi} + i\omega_0 a_0\right) + c^2\,\frac{\omega_p^2}{\omega_0^2}\,\frac{\partial^2 a_0}{\partial \xi^2} + \omega_p^2 a_0 = \omega_p^2\,\frac{n}{n_0}\,\frac{a_0}{\gamma_a\gamma_z} \tag{4.12}$$

These equations are to be solved simultaneously, using a suitable numerical scheme,

with the relevant initial and boundary conditions.

4.1.1 Numerical Scheme

We propose to solve the above model equations using the following time and space centered procedure at each timestep:

1. Calculate the background density across the computational mesh.
2. Solve equation (4.10) for Φ using the current values of γ_a and n/N_0.
3. Solve equation (4.11) to get a first estimate of n/N_0 at the new time.
4. Solve equation (4.12) to get a first estimate of a_0 at the new time.
5. Solve equation (4.10) to obtain an estimate of Φ at the new time.
6. Solve equation (4.11) using the estimates of the other quantities to time-centre the calculation for n/N_0.
7. Solve equation (4.12) using the estimates of the other quantities to time-centre the calculation for a_0.
8. Advance the value of the time variable by 1 step.

We briefly lay out the manipulation of the model equations to get them in a form suitable for numerical computation. We normalise the equations to the spatial scale $\frac{c}{\omega_{p0}}$. Taking equation (4.10) we apply the scaling $P = \frac{\omega_{p0}}{c}\xi$ and $T = \frac{\omega_0}{\omega_{p0}^2}t$ to obtain,

$$\frac{\partial^2(\Phi+1)}{\partial P^2} = D(P,T)\left(\frac{N(P,T)}{D(P,T)} - 1\right), \tag{4.13}$$

where $D = \left(1 + \frac{1}{l}\left(P + \beta_0\frac{\omega_0}{\omega_{p0}}T\right)\right)$, $N = \frac{n}{N_0}$ and l is the scale length of the density gradient in units of $\frac{c}{\omega_{p0}}$. This equation is solved using the predictor-corrector pair of the Sunfad program.

Equation (4.11) is scaled in the same way to leave the equation,

$$\frac{\omega_{p0}}{\omega_0}\frac{\partial N}{\partial T} + \frac{\partial}{\partial P}\left(N\frac{\sqrt{\gamma_z^2 - 1} - \beta_0\gamma_z}{\gamma_z}\right) = 0. \tag{4.14}$$

This equation is solved using time and space-centered finite difference approximations with the time-dependent boundary condition,

$$D = 1 + \frac{1}{l}\left(\beta_0 \frac{\omega_0}{\omega_{p0}} T\right), \tag{4.15}$$

at the right hand edge of the computational grid. Finally, equation (4.12) transforms to give the equation,

$$\frac{\omega_{p0}}{\omega_0}\beta_0 \frac{\partial^2 a_0}{\partial T \partial P} + i\frac{\partial a_0}{\partial T} + \frac{1}{2}\frac{\omega_p^2}{\omega_0^2}\frac{\partial^2 a_0}{\partial P^2} = -\frac{1}{2}\left(\frac{\omega_p}{\omega_{p0}}\right)^2 K\, a_0, \tag{4.16}$$

where we define,

$$K = 1 - \frac{N}{D}\frac{1}{\gamma_a \gamma_z}, \tag{4.17}$$

and this term is centered in the numerical scheme.

A computer program based on the above scheme was developed and some preliminary debugging work was performed. Figure 4.2 shows the test output from the new code showing the convection of the density ramp across the computational mesh in the absence of a laser pulse. The density plots are normalised to the initial density, N_0. As the simulation progresses, we see that the correct number of electrons are injected at the right hand edge of the grid, since the density perturbation, and hence the field, is zero at each end of the cell. However, the electrons do not appear to be convecting across the grid in the correct manner. Indeed we see that there is a bunching of electrons in the right hand half of the mesh. In an attempt to diagnose this bug in the program, a test switch was implemented which forces the right hand side of equation (4.13) to remain at zero through the simulation. This effectively decouples the calculation of Φ and the normalised density $\frac{n}{N_0}$. Figure 4.3 illustrates the evolution of $\frac{n}{N_0}$ when this test switch is envoked. We see that the leading edge of the density gradient suffers from a high degree of numerical diffusive error. The gradient at the right hand edge of the cell is linear as expected, but as the solution for $\frac{n}{N_0}$ is integrated

back across the cell the diffusive effect builds up and distorts the linear ramp. We can confirm, however, that the background density across the cell held in the array D is correctly stored. Figure 4.4 shows the evolution of this array in time. We see that the density ramp is accurately represented in this array as a linear profile convecting across the computational mesh at the correct velocity. The source of the error in this program lies in the numerical solution of equation (4.14) where the solution appears to suffer from a numerical diffusive effect. Due to the lack of time, no further investigation of this model has been undertaken. Instead, some consideration has been given to an alternative model for inhomogeneous plasma wakefield generation. The alternative model does not rely on the quasi-static approximation, which is not as applicable in the inhomogeneous plasma case as it is in the homogenous case.In the next, section, we give a brief account of this second model which is based on a Lagrangian approach to the problem.

4.2 A Lagrangian Model Formulation

The model explored in Section 4.1 is severely limited by the long density scale length required for the 'quasi-static' approximation to remain valid for equation (4.3). In this section we present an outline of a different approach to the modelling of inhomogeneous plasma wakefield generation. In this formulation, we retain the description of the laser pulse from the previous model, but solve the equations for the plasma quantities in the rest frame of the plasma. This Lagrangian approach requires the solution of equations in the two different frames with laser and plasma quantities interpolated between the frames.

We begin our derivation with the momentum equation for the plasma electrons. Consideration of the parallel component of this equation gives the well-known form as given in equation (4.3). In this formulation, however, we adopt the Lagrangian description and consider equation (4.3) in the frame moving with the plasma electron fluid. That is, we define the convective derivative,

$$\frac{d}{dt} = \frac{\partial}{\partial t} + c\left\{\frac{\sqrt{\gamma_z^2 - 1}}{\gamma_z}\right\}\frac{\partial}{\partial z}. \tag{4.18}$$

For convenience, we also define,

$$\chi = \gamma_a\sqrt{\gamma_z^2 - 1}\,, \tag{4.19}$$

so that the momentum equation becomes,

$$\frac{d\chi}{dt} = -\frac{e}{m_0 c}E_z - \frac{c}{2\gamma_a\gamma_z}\frac{\partial}{\partial z}\left(a^2\right). \tag{4.20}$$

where E_z is the electrostatic field in the plasma.

Once we define a convective derivative, we may obtain an expression for the variation of ξ, the pulse frame position variable, in the plasma frame. We have $\xi = z - v_l t$,

where v_l is the velocity of the laser pulse frame. So,

$$\frac{d\xi}{dt} = c\sqrt{1 - \frac{1}{\gamma_z^2}} - v_l \tag{4.21}$$

where the first term on the right hand side above is the velocity of the plasma fluid in the $\hat{z}$ direction.

Next, we employ Gauss' law to give an equation for the longitudinal plasma field E_z. This requires,

$$\frac{dE_z}{dz} = 4\pi\rho\,, \tag{4.22}$$

where $\rho = e(n_i - n_e)$ and $E_z = 0$ on the right-hand boundary.

Finally, we carry-over the description of the laser pulse from the previous models to complete this Lagrangian formulation,

$$\left(c^2\frac{\partial^2}{\partial z^2} - \frac{\partial^2}{\partial t^2}\right)\mathbf{a} = \omega_p^2\frac{\mathbf{a}}{\gamma}\,. \tag{4.23}$$

The equations (4.20–4.23) form the basic set for the model. To obtain the final expression of the model equations in a form amenable to numerical solution, we perform some further manipulations. The equations in the plasma frame are simply scaled in space and time by the factors $S = \frac{\omega_{p0}}{c}z$ and $T = \omega_{p0}\,t$, where ω_{p0} is the plasma frequency at the top of the density gradient. In addition, we introduce a normalised plasma electric field via $E = \frac{e}{m_0 c\omega_{p0}}E_z$. The equation for the laser pulse is treated in the same manner as in previous models – we employ the envelope approximation and cast the equation in the moving pulse frame.

With these manipulations, the final model equations are,

$$\frac{d\chi}{dT} = -E - \frac{1}{\gamma_z}\frac{\partial \gamma_a}{\partial S} \tag{4.24}$$

$$\frac{dS}{dT} = \frac{\sqrt{\gamma_z^2 - 1}}{\gamma_z} \tag{4.25}$$

$$\frac{dE}{dS} = -\left(\frac{n_e}{N_0} - \frac{S}{L}\right) \tag{4.26}$$

$$\left(1 - V^2\right)\frac{\partial^2 a_0}{\partial \xi^2} + 2i\left(\frac{ck_0}{\omega_{p0}} - \frac{\omega_0}{\omega_{p0}}V\right)\frac{\partial a_0}{\partial \xi} + 2V\frac{\partial^2 a_0}{\partial \xi \partial \tau} + 2i\frac{\omega_0}{\omega_{p0}}\frac{\partial a_0}{\partial \tau} = -\frac{\omega_p^2}{\omega_{p0}^2}\left(1 - \frac{1}{\gamma_a \gamma_z}\right)a_0 \tag{4.27}$$

In the above equations we have assumed a linear background density gradient function $n_0 = N_0\frac{S}{L}$ where L is the ramp scale length in units $\frac{c}{\omega_{p0}}$ and N_0 is the electron density at $S = L$. The total electron density n_e is the background density plus the perturbation due to the laser pulse, ie. $n_e = n_0 + \delta n_e$. If we scale the density to N_0, the density perturbation $\frac{\delta n_e}{N_0}$ may be written,

$$\frac{\delta n_e}{N_0} = \frac{n_e}{N_0} - \frac{S}{L}, \tag{4.28}$$

as used in equation (4.26).

The model equations (4.24–4.27) may now be solved in the following manner. We begin by considering a density gradient, yet to enter the 'pulse frame', defined by a number of density elements with uniform spacing. Next, we define the envelope of the laser pulse in the pulse frame and begin the numerical procedure. At each timestep in the simulation, we inject a particle bunch at the right-hand edge of the pulse frame. Then we solve equation (4.24) to find χ for each of the density elements currently in the pulse frame, interpolating the pulse frame quantities onto the plasma frame. From equation (4.25) we see that we can calculate the value of γ_z for each element

via the relationship,

$$\gamma_z = \left(\frac{\chi^2}{\gamma_a^2} + 1\right)^{\frac{1}{2}} . \tag{4.29}$$

We, therefore, calculate the values of γ_z for each density element and interpolate these values back onto the pulse frame. Next, we use the γ_z values of each density element in the plasma frame to find the plasma velocity of each element and hence the new position of all the elements in the pulse frame window. We then interpolate the new positions of the density elements onto the pulse frame to give a density value at each mesh point in the pulse frame. The scheme for this interpolation is illustrated in Figure 4.1 where the pulse frame grid point $\xi(i)$ is straddled by two plasma density elements. The density value at the grid point is calculated from,

$$\text{den(i)} = \left(\frac{\text{denp}(j)\,[\xi(i) - \xi_p(j)] + \text{denp}(j+1)\,[\xi_p(j+1) - \xi(i)]}{\xi_p(j+1) - \xi_p(j)}\right) \tag{4.30}$$

where denp(j) and denp($j+1$) are the densities associated with elements j and $j+1$ respectively. Once we have the density on the pulse mesh, we solve equation (4.26)

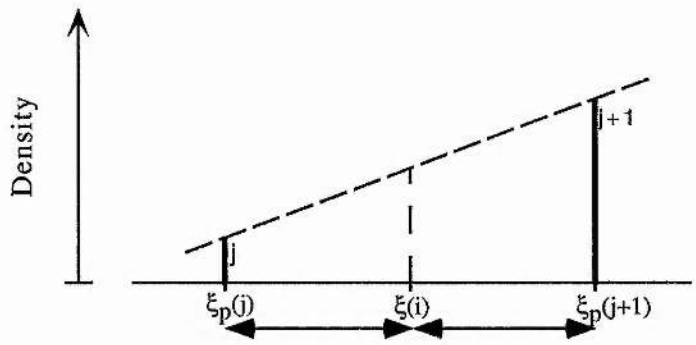

Figure 4.1: Illustration of the interpolation of the plasma density onto the pulse frame mesh. Here, the density elements j and $j+1$ are located at $\xi_p(j)$ and $\xi_p(j+1)$ and straddle the grid point $\xi(i)$ in the pulse frame.

to find the electric field on the pulse grid and interpolate this back to find E at the position of each of the density elements. From E we calculate the plasma potential, Φ, on the pulse grid. Finally, we solve equation (4.27), using the quantities calculated

on the pulse grid, to give the form of the envelope of the laser pulse.

A preliminary computer program has been written to implement the above procedure using space and time-centred finite difference approximations to obtain the solutions of each of the equations. This centred-differences scheme requires that the procedure outlined above be executed twice for each timestep. The first solution of each equation provides an estimate of the values at the desired time and these 'estimates' are then used in the second pass to time-centre the equations.

The computer code, called GradFad, consists of many self-contained subroutines to perform the various functions in the numerical scheme. The subroutines for the interpolation of quantities between the pulse and the plasma frames are crucial to the success of the numerical scheme and have received the most attention in the limited de-bugging time available to the present author. Unfortunately, due once again to lack of time, the program has not yet progressed beyond the de-bugging stage of its development. The de-bugging test conducted so far show that the program is capable of convecting the density gradient across the pulse frame mesh in the absence of a laser pulse and the interpolation routines between the two frames appear to work correctly. However, further tests are required to analyse the handling of the laser pulse by the program and identify any further bugs.

4.3 Summary

In this Chapter we have considered the possibilities for constructing a 1-D model for Laser Wakefield Generation in an Inhomogeneous plasma. In our first formulation of such a model, we extended the model of Chapter 2 to include a long scale-length gradient in the plasma density. This model allows only a very slight gradient in the plasma density in order to maintain the validity of the Quasi-Static approximation. This approximation is invalid if the density gradient is sufficient to change the wake structure behind the laser pulse as it propagates through the plasma. This model is, in some respects, self-defeating since the area of interest – the limitation of particle/wake de-phasing – requires that the gradient should be sufficient to modify the wake structure.

In the second formulation presented in this Chapter, we discard the quasi-static approximation and adopt a Lagrangian approach to the solution of the remaining model equations. This model *is* valid in the parameter regime of interest and we propose a numerical scheme for the solution of the model equations. Some progress has also been made in implementing this scheme in a computer program, although the program remains in a partially de-bugged state only. The completion of the de-bugging process is left to a future worker in the hope that this scheme may yield some interesting results and provide an insight into the limitation of particle/wake de-phasing in the Laser Wakefield Accelerator scheme.

In the next Chapter we present a brief summary of Part I of this thesis and outline some areas for future investigation arising from this work.

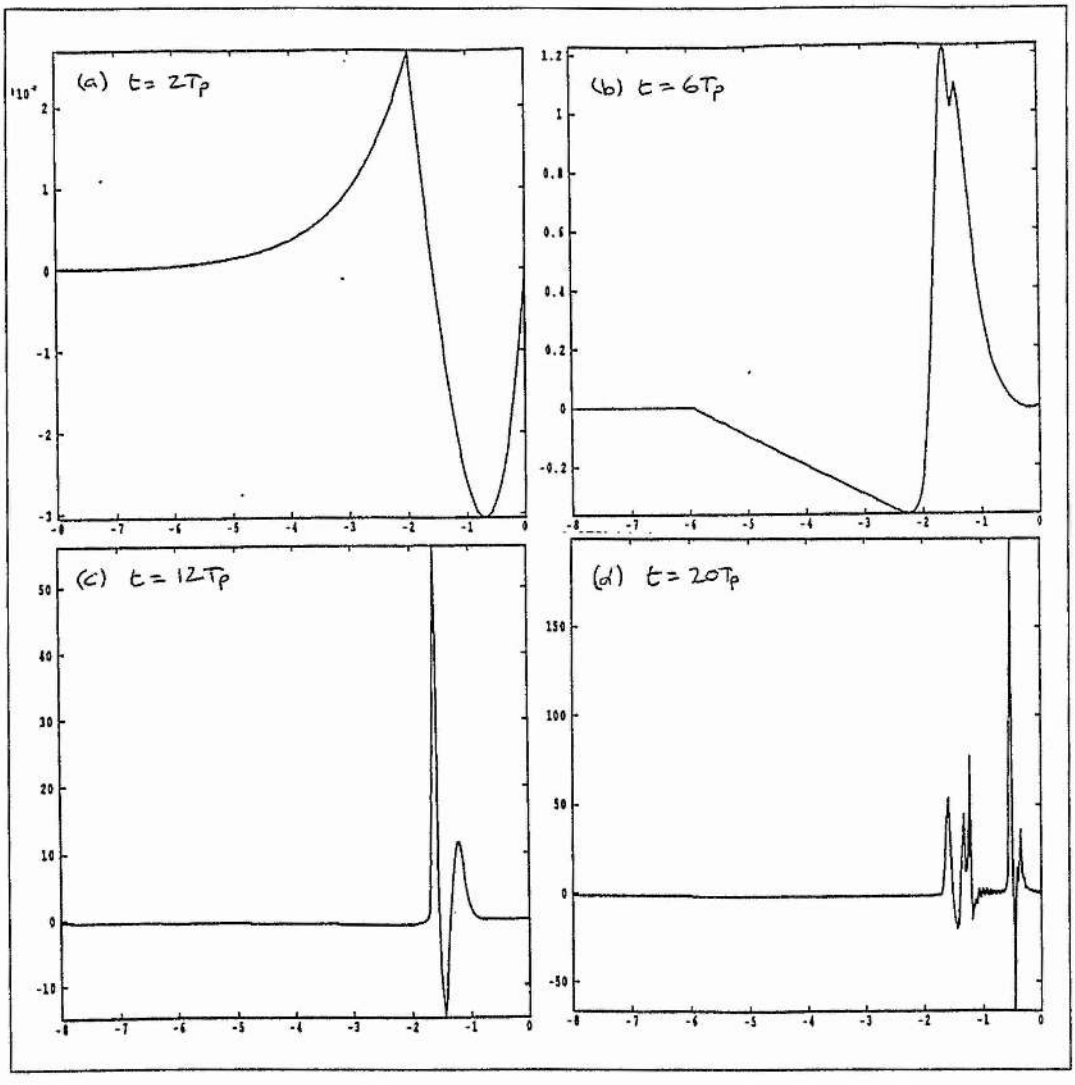

Figure 4.2: Test output showing the convection of the density ramp across the computational mesh in the absence of a laser pulse.

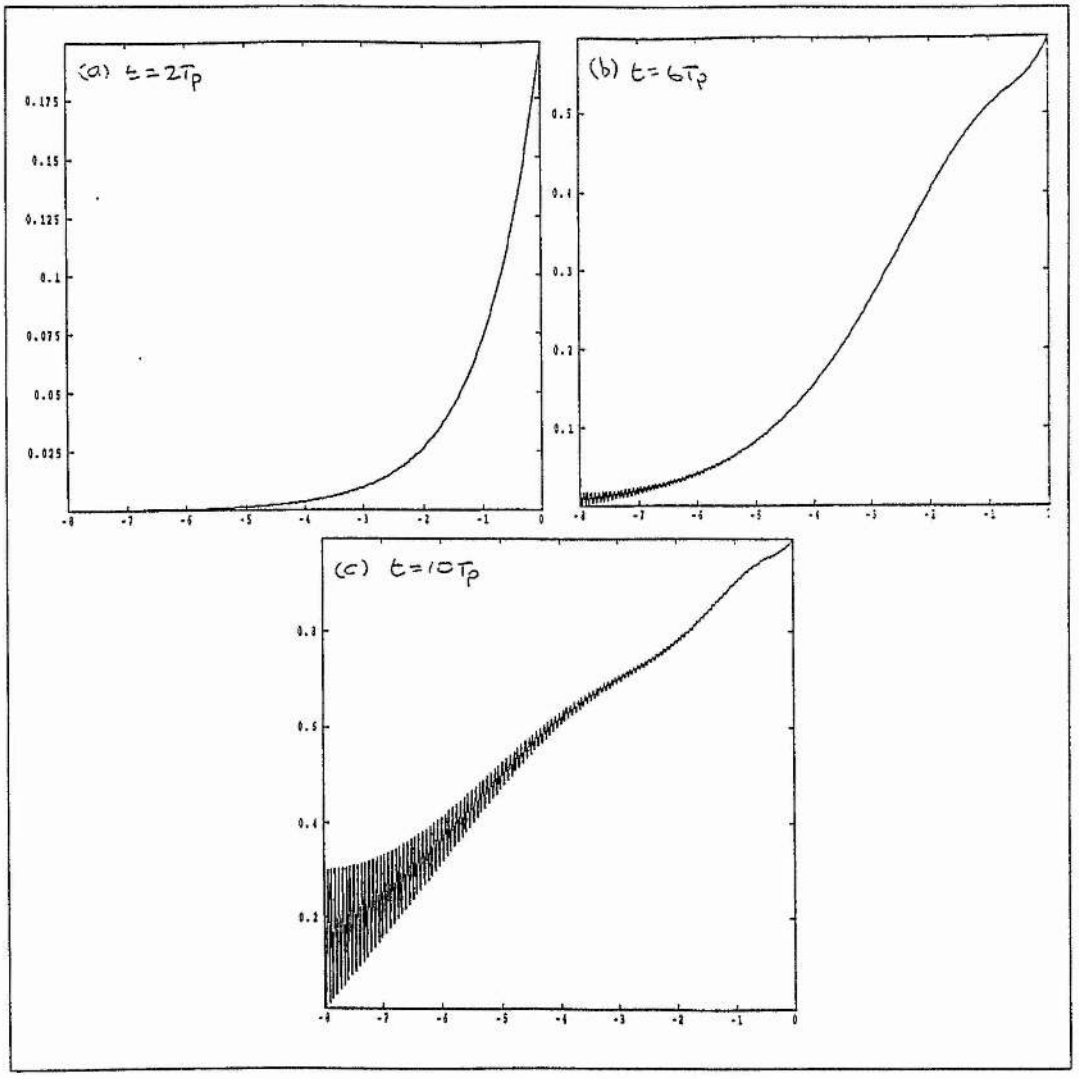

Figure 4.3: The evolution of $\frac{n}{N_0}$ for the decoupled calculation.

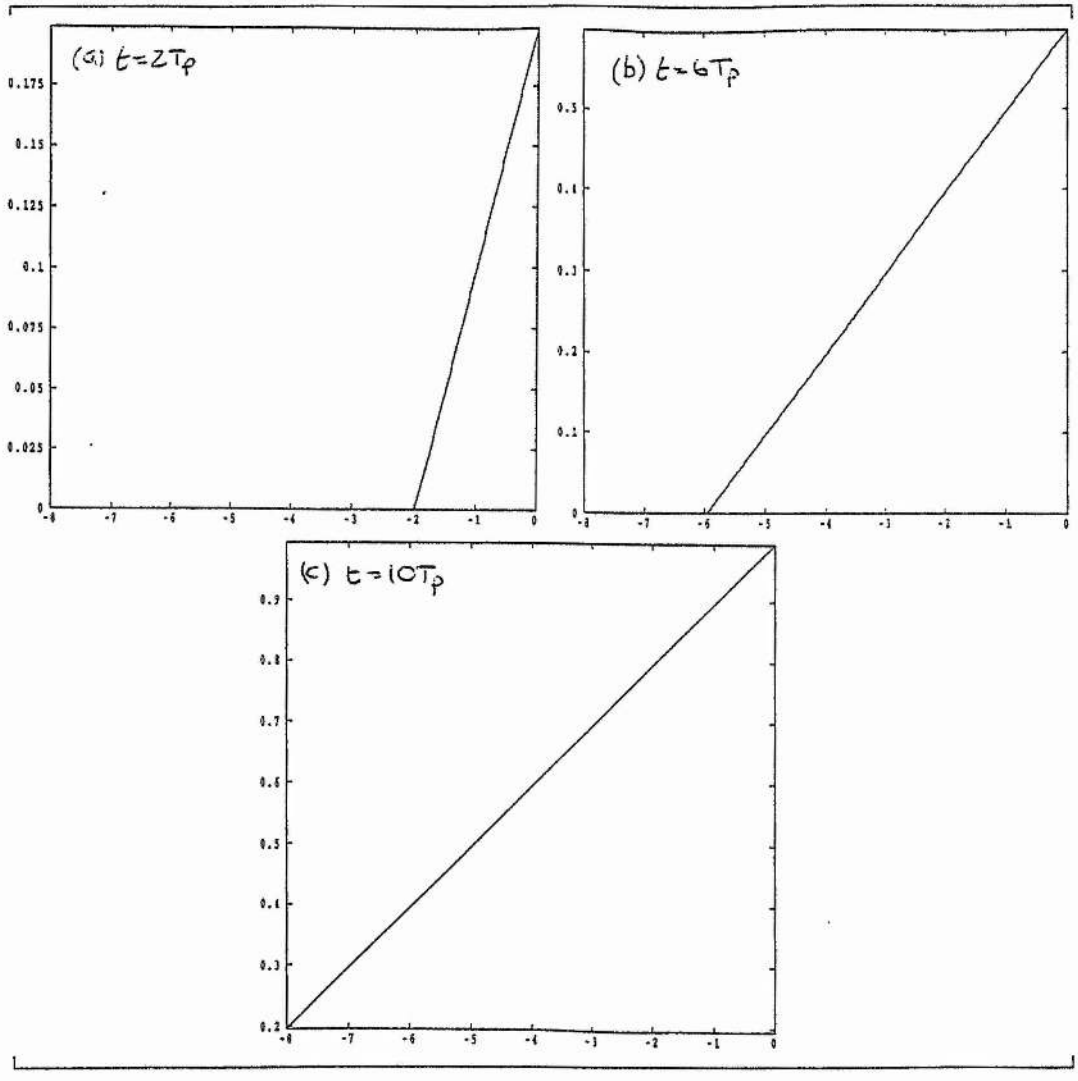

Figure 4.4: The evolution of the background density, held in the array D, in time.

Chapter 5

Summary and Conclusions

In Part I of this thesis, we have reviewed the three main schemes for plasma-based particle acceleration. These are the Plasma Beat Wave Accelerator[62], the Plasma Wakefield Accelerator[14] and the Laser Wakefield Accelerator[62]. The Plasma Beat Wave Accelerator has received the most attention in research literature, but a recent proof-of-principle experiment[42] has demonstrated that the Laser Wakefield Accelerator scheme is viable and avoids the difficulties associated with the beat-wave scheme. More experiments on the Laser Wakefield scheme are sure to be performed as more powerful laser systems become available in the future.

We have then concentrated our attention on a 1-Dimensional model for the generation of the wake structure by the laser pulse in the Laser Wakefield Accelerator. This model is based on the cold, relativistic fluid equations for the plasma description and Maxwell's equations to describe the laser pulse. It employs some approximations to reduce these equations to a coupled set of two equations for the laser vector potential and the plasma scalar potential. A computer program, Sunfad, is described and we have presented results to demonstrate the wake generation by a single laser pulse.

In Chapter 3 we have extended this single pulse model to investigate a multiple pulse scheme for wakefield generation. The modified theory and computer program give results which indicate the effectiveness of this new scheme. We find that, if

the energy in the leading pulse is sufficient to excite a nonlinear wake oscillation, the trailing pulse(s) in a pulse train may exploit this nonlinearity to excite a larger wake oscillation than a single pulse with the same total energy. The trailing pulses are most effective when they are positioned in the optimum phase of the plasma wave. This optimum phase moves from the linear position, $E_z = E_{z(\max)}$ towards the local minimum of the plasma scalar potential as the wake oscillation becomes more nonlinear. The results from our 1-Dimensional model indicate that this process of wake enhancement may continue until the wake oscillation amplitude reaches the cold plasma wave-breaking limit. The 1-Dimensional analysis, however, omits the behaviour in the radial direction. At the high pulse intensities considered in Chapter 3, 2-Dimensional effects may de-stabilise the wake structure so that it breaks at a lower amplitude. In the 1-D model we find that the plasma wave only breaks in the first period of the oscillation, it is suggested[6], however, that in a 2-D analysis the plasma wave may break at any point in the oscillation. The investigation of the multiple pulse scheme in a 2-Dimensional model to look at these effects would therefore be an interesting area for further study. In Chapter 3 we have also briefly illustrated the phenomenon of 'Photon Acceleration'. This occurs when a laser pulse is phased to lie in the accelerating region of the electrostatic plasma wave. The light pulse is 'accelerated' via an up-shifting of the frequency spread in the pulse as the photons associated with it gain energy.

Finally, we have considered a method for controlling the phase slippage which occurs between the accelerated particles and the plasma wave in laser plasma-based accelerators. This method attempts to modify the phase velocity of the plasma wave by altering the local plasma density as the laser pulse propagates through the plasma. We have formulated and presented a 1-Dimensional model for the laser wakefield generation in this inhomogeneous plasma. This model is based on a Lagrangian approach to the solution of the plasma cold, relativistic fluid equations, whilst retaining the pulse frame of the homogeneous plasma model. We have presented a numerical scheme

for the solution of the model equations, but a complete computer program implementation is not yet available. The development of this computer program would be an interesting task for future work, since this model may then be used to investigate the extent to which modification of the plasma density can increase the de-phasing distance in the Laser Wakefield Accelerator scheme.

End of Part I

Part II

Nonlinear Resonance Absorption

Chapter 6

Introduction to Part II

In Part II of this thesis we investigate the possible application of high power laser pulses in laser-matter interactions where a preformed plasma exists with a linear density gradient. The interaction at lower intensities is described by the theory of linear 'Resonance Absorption'. However, as the intensity of the laser pulses under consideration is increased, the absorption mechanism shows increasing evidence of nonlinear processes.

In this chapter we give a brief description of the relevant linear theory and set out the scheme for our investigation of the nonlinear regime.

6.1 Theory of Linear Resonance Absorption

We consider a plane electromagnetic wave (ω, k) propagating in the $y-z$ plane at an angle θ to the z-axis incident onto a plasma slab with an inhomogeneous electron density n_e(z) which increases with z. The vacuum-plasma interface is taken to be at z=0 and there are no variations in the x direction. As the light wave propagates into the plasma, the plasma density reaches a value such that at some value of z, defining the critical surface, the local plasma frequency becomes equal to the frequency of the incident wave. The dispersion relation for the electromagnetic wave and the definition

of the y-component of the wavenumber lead to the expression,

$$k_z^2 = \frac{\omega^2 \cos^2(\theta) - \omega_p^2}{c^2} \tag{6.1}$$

for the z-component of the wavenumber. This gives a cut-off (zero wavenumber) when $\omega_p = \omega \cos(\theta)$ so that in the WKB approximation, which assumes that the plasma does not vary much over the length scales of the order of a wavelength, we expect the light to be totally reflected at some point on the low density side of the critical surface. The point of reflection moves outwards from the critical surface as θ increases. However, if the electromagnetic wave is polarised in the plane of incidence, there will be a component along the density gradient at the turning point. This causes the plasma electrons to oscillate along the z-direction and the charge imbalance may allow the field to tunnel through to the critical surface. Here, the oscillation may act as a driving force and couple to the electrostatic longitudinal oscillation mode with angular frequency ω_p. This leads to a transfer of energy from the incident light wave to the electrostatic electron plasma wave under the phenomenon of 'Resonance Absorption'. The amplitude of the plasma wave increases resonantly and in order to achieve a steady state we require some damping on the motion. This damping may be due to dissipation by electron-ion collisions, linear or nonlinear wave-particle interactions, or even propagation of the wave out of the resonant region around the critical surface.

To determine the energy transfer to the excited plasma wave, we need to determine the size of the electric field along the z-axis near the critical surface. In order to evaluate E_z, it is convenient to work in terms of the magnetic field, B, which is purely in the $\hat{z}$-direction. If we assume that the density profile around the critical surface may be represented by a linear density gradient, the equation governing the magnetic field at the critical surface is [10],

$$\frac{\mathrm{d}^2 B}{\mathrm{d}z^2} - \frac{1}{z - i\nu\frac{L}{\omega}} \frac{\mathrm{d}B}{\mathrm{d}z} + \mid k \mid^2 \left[\frac{z}{L} - \sin^2(\theta)\right] B = 0\,. \tag{6.2}$$

where ν is the damping coefficient and L is the density scale length. This equation may be solved either numerically or analytically and the absorbed fraction of the incident wave is found to be as illustrated in Figure 6.1. This curve shows how the absorption coefficient varies as a function of the vacuum wavenumber, the density scale length and the angle of incidence θ via $q = (k_0 L)^{2/3} \sin^2(\theta)$. The shape of the curve can be explained as follows. At normal incidence there is no field component along the z-direction and so no coupling to the plasma wave. As the angle of incidence increases the component along z increases and absorption by coupling to the electrostatic mode increases. However, for large angles the turning point defined by $\omega_p = \omega \cos(\theta)$ moves away from the critical surface and the incident field has to tunnel further to reach the critical surface. This causes the absorption to decrease as θ increases. In laser-plasma interactions the strong electromagnetic field intensity near the critical surface makes resonance absorption effective over a wide range of angles and an important process. The linear theory describes the absorption process for long scale-length plasmas or moderate laser intensities very well. However, in ultra-steep density profiles or a ultra-high laser intensities the electron electrostatic oscillation excited extends over a large part of the density profile. When this occurs, the assumptions made in the linear theory, regarding the validity of local homogeneous plasma solutions, break down and the absorption process becomes nonlinear.

At the extreme of the steepening of the density profile, the Brunel model [8] describes the phenomenon of vacuum heating for a vacuum/solid interface. In this case, plasma electrons are dragged into the vacuum by the intense electromagnetic wave field and sent back into the plasma with velocities of the order of the vacuum quiver velocity. Gibbon and Bell [31] have reported some results for these 'sharp-edged' plasmas which were obtained using a particle simulation code. They found that the vacuum heating process dominates over resonance absorption for scale lengths $L/\lambda < 0.1$.

In this thesis, we investigate the behaviour in the regime between linear resonance

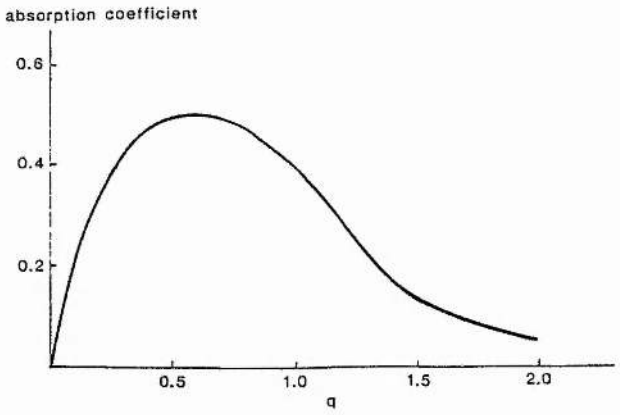

Figure 6.1: The absorption curve for resonant absorption. After Cairns[10]

absorption and the vacuum heating regime. Here the laser intensities are high and the density profiles are steepening so that the resonance absorption process becomes increasingly nonlinear.

In Chapter 7 we present a simple forced-oscillator model to investigate the consequences of this transition to nonlinear Resonance Absorption. In Chapter 8 we attempt to verify the results obtained from this simple model using a particle simulation code. In Chapter 9 we provide a brief summary to Part II of this thesis.

Chapter 7

A Simple Forced Oscillator Model For Resonance Absorption

In this chapter we present a simple, non-relativistic 1-D model for the response of the electrons in a plasma density gradient to an electrostatic pump wave in the direction of the density gradient. This electrostatic forcing field may be associated with an obliquely incident p-polarised laser pulse. We investigate this interaction by considering the oscillations of one of the electrons at a given position in the density profile, driven by the applied field.

7.1 The Model Equation

The model assumes a simple linear density profile in the plasma which extends from zero density (vacuum) to two hundred times the critical density. The model also assumes that the plasma consists purely of electrons and singly charged ions in equal numbers and that due to their relatively high inertia the ions may be considered to be immobile. Figure 7.1 illustrates the construction of a simple model for a density gradient with scale-length L. The density profile gives 'solid density' for negative values of the position variable, x. To the right of the origin, the density decreases linearly to zero over a scale-length L. In order to construct a model for the oscillation

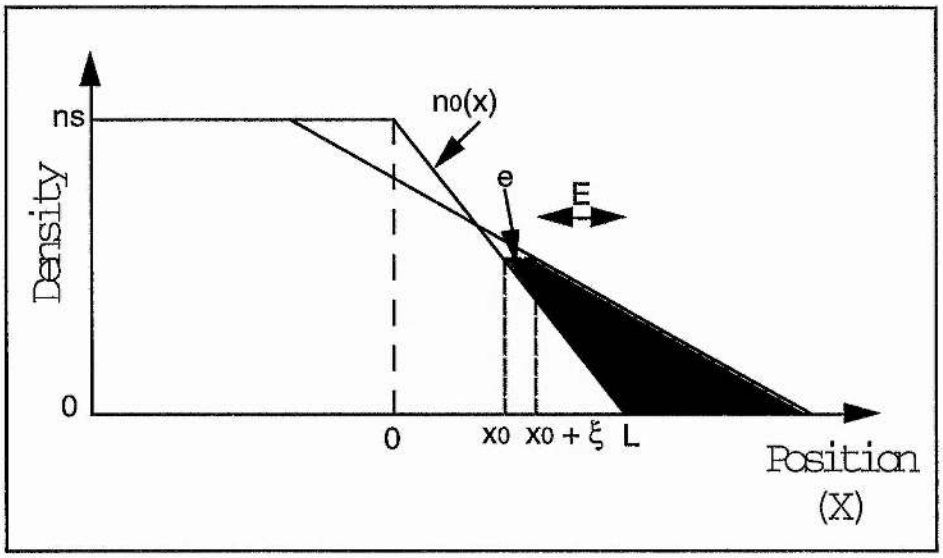

Figure 7.1: A schematic of a linear density gradient.

of the electrons in this profile, driven by the applied electrostatic field E, we have to represent the following:

1. The driving force - due to the pump wave at oblique incidence.

2. The restoring force - provided by charge separation.

3. The damping effect caused by collisions with local ions.

In our simple model, we represent the electrostatic driving field as the real part of $E_0 e^{i\omega_f t}$ where E_0 is the amplitude of the oscillating field. The restoring force for the oscillation of the electrons comes from the force due to the charge separation induced by the oscillation. If we consider an electron whose equilibrium position is x_0 $(0 \leq x_0 \leq L)$ and let the displacement from this position be ξ', then the restoring field at the point $x_0 + \xi'$ may be found from Gauss' Law,

$$\frac{\mathrm{d}E_r}{\mathrm{d}x} = \frac{e}{\varepsilon_0}(n_e - n_i) \ , \tag{7.1}$$

where E_r is the restoring field and n_e and n_i are the electron and ion numbers. We integrate to find $E_r(x_0 + \xi')$,

$$E_r(x_0 + \xi') = \frac{e}{\epsilon_0} \int_{x_0}^{x_0+\xi'} n_0(x)\, \mathrm{d}x\,, \tag{7.2}$$

where $n_0(x)$ is the piecewise linear density function. This integral expression for the restoring force assumes that the electron orbits do not cross.

Finally, we model the collisional damping of the electrons via a term proportional to the velocity of the electrons with the constant of proportionality chosen to be representative of typical electron-ion collision rates in laser-plasma interactions[43].

Before we write down the equation governing the motion of an electron in this model we perform a normalisation of the length and time units. We normalise the time unit to the characteristic period of the driving oscillation via $\tau = \omega_f t$ and normalise the length unit to the scale length of the density gradient by setting $\xi = \xi'/L$. With these normalisations, the equation of motion of an electron in the plasma is,

$$\ddot{\xi} + \frac{\nu}{\omega_f}\dot{\xi} = -\frac{\omega_{0p}^2}{\omega_f^2} F(\xi) + \frac{eE_0}{m\omega_f^2 L}\cos(\tau)\,, \tag{7.3}$$

where ν is the constant damping coefficient, ω_{0p}^2 is the local plasma frequency at the 'solid' density defined by $\omega_{0p}^2 = n_s e^2/\epsilon_0 m$ and the function $F(\xi)$ is defined in a piecewise manner by,

$$F(\xi) = \begin{cases} \xi + \frac{1}{2}\left(\frac{x_0}{L}\right)^2 & \xi + \frac{x_0}{L} < 0 \\ \xi\left(1 - \frac{x_0}{L}\right) - \frac{1}{2}\xi^2 & 0 \le \xi + \frac{x_0}{L} \le 1 \\ \frac{1}{2}\left(1 - \frac{x_0}{L}\right)^2 & \xi + \frac{x_0}{L} > 1 \end{cases} \tag{7.4}$$

The model is intended to represent the interaction of radiation from, for example, an Nd:YAG laser ($\lambda = 1.064\mu$m) with a target of solid density $n_s = 2 \times 10^{23}\mathrm{cm}^{-3}$. A constant collision frequency of $2 \times 10^{13}\mathrm{s}^{-1}$ is assumed as a suitable value for these

interactions. These values fix the values of two of the parameters in equation (7.3). We have,

$$\begin{aligned} \frac{\nu}{\omega_f} &\simeq 1.13 \times 10^{-2} \\ \frac{\omega_{0p}^2}{\omega_f^2} &\simeq 2.011 \times 10^2 \end{aligned} \tag{7.5}$$

The third parameter in equation (7.3) governs the ratio of the pump field amplitude to the density scale length in the plasma. Equation (7.3) may be solved numerically by writing it as the system of two first order equations in the variables $z_1(=\xi)$ and $z_2(=\dot{\xi})$,

$$\begin{aligned} \dot{z_1} &= z_2 \\ \dot{z_2} &= -\alpha z_2 - \beta F(z_1) + \Omega \cos(\tau) \end{aligned} \tag{7.6}$$

where $\alpha = \nu/\omega_f$, $\beta = \omega_{0p}^2/\omega_f^2$, $\Omega = eE_0/m\omega_f^2 L$ and initially $z_1 = z_2 = 0$. A simple program may be written to solve the system (7.6) using a Runge-Kutta-Merson method [32]. The program, called gen2000, inputs the values of the initial position, x_0/L, and the parameter Ω. It then solves system (7.6) with the initial conditions $z_1 = z_2 = 0$ over two thousand periods of the pump oscillation to allow transients in the electron response to decay. This decay time sets a lower limit on the duration of the laser pulses that may be modelled. For example, laser radiation of wavelength $\sim 1\mu$m requires a pulse length of $\sim$ 6ps to include 2000 periods. The program then continues to solve the system and writes the values of z_1 and z_2 to a data file for further analysis.

7.2 Data Analysis

The data on the motion of the test electron may be analysed in a number of ways. From linear theory we expect the electrons in the plasma to respond to the driving field by oscillating at the frequency of the driver. We also expect that this response will vary in amplitude depending on the resonant coupling between the driver and local plasma frequencies. As the field strength of the driver is increased, however, we expect to enter a nonlinear regime where the oscillation frequency of the electrons may differ from the frequency of the driver. We therefore require data analysis methods to investigate both the resonant response at different points in the density profile and the nature of the oscillation at each point.

The response across the density profile may be investigated graphically on a plot of the maximum displacement amplitude vs initial position and since the position in the profile and the local plasma frequency are related by,

$$\omega_p^2 = \omega_{0p}^2 \left(1 - \frac{x_0}{L}\right) \tag{7.7}$$

this data may also be used to plot the response amplitude vs local plasma frequency.

In the analysis of the nature of the oscillation at each point, we are interested in any departure from the oscillation at the frequency of the driver. We use $(\xi,\dot{\xi})$phase portraits to illustrate the cycle of the electron motion and, by sampling this data stroboscopically at intervals of the period of the driving field, we construct Poincaré maps. This mapping technique reduces the 3-Dimensional data $(\xi,\dot{\xi},\tau)$ to a 2-Dimensional plane $(\xi,\dot{\xi})$and allows us to compare the period of the electron oscillation with that of the driving field. If the two oscillate with the same period, then the map shows a single point in the phase plane. If, however, the electron oscillates with a period, say, twice that of the driver, then the Poincaré map contains two points in the phase plane. A third technique for analysing the motion of the electrons is to Fourier decompose the data. This gives an indication of the exact frequencies present in the

motion and their relative strengths.

Each of the above manipulations of the raw data are performed by specialised computer programs. We now briefly outline the operation of each program.

The program to generate the data for the Poincaré maps is straight forward. It simply integrates the system (7.6) for 2000 periods of the driving field, to allow the transients in the electron motion to decay, and then proceeds with a timestep equal to the period of the driving field. In this way it generates a data point in $(\xi,\dot{\xi})$space at the same phase of the driving oscillation each time. The program to generate the data for the phase trajectories in the $(\xi,\dot{\xi})$space integrates the system (7.6) until the transients in the electron response decay. Then it attempts to identify any periodicity in the data sampled from the next 10 timesteps. If the program is successful in this, it generates more data over a single cycle of the system, using 200 timesteps per period of the driving field. If the program detects no periodicity in the 10 samples, it proceeds with a default value of 10 periods of the driving field per cycle of the electron motion. In either case, the program writes the $(\xi,\dot{\xi})$data to a file for use in a graphing application. Finally, we describe the program to generate the data for the Fourier spectrum plots. This program again integrates for 2000 periods of the driving field before it saves any data. To obtain data suitable for Fourier decomposition, we need to choose a sampling rate and the number of samples. If we assume that the electron motion is frequency band-limited, the sampling theorem gives the relationship between the sampling rate, Δ, and the maximum frequency that may be distinguished as,

$$f\text{max} = \frac{1}{2\Delta}. \tag{7.8}$$

We arbitrarily choose $\Delta = \frac{\pi}{6}$, which allows frequencies up to 6 times that of the driving field to be included in the power spectra. In the choice of the number of samples we have two main concerns. We require a sufficient number of points to resolve each power spectrum adequately. On the other hand, too many samples is

inefficient in computational terms. The sampling theorem again reminds us that the range of frequencies explicitly decomposed by the Fourier analysis is $\frac{1}{N\Delta}, \frac{1}{(N-1)\Delta}, \ldots, \frac{1}{2\Delta}$ where N is the number of samples. The computer program dynamically assigns the number of samples, N, by analysing the periodicity of the last 10 of the 2000 initial sets of data and using this value in the algorithm,

$$N\Delta = 2\pi \times \text{periodicity number} \times 100 \tag{7.9}$$

where the 2π represents the time of a single period of the driver and the factor of 100 is an enhancement factor to boost the resolution of the spectrum. The program then generates the required number of samples and takes the Fourier transform of this data using a routine from the Numerical Algorithms Group (NAG) Fortran Library. The program then takes the log of each power value and employs a 'cut-off' value of 10^{-15}. The data file written by the program contains the resolved frequencies, normalised to the frequency of the driving field, and the log of the power value at each frequency.

We now use the methods mentioned above to investigate the Ω parameter space. We begin with very small values of Ω and compare our model with the linearised form. Then we slowly increase the value of Ω and identify the nonlinear effects which begin to occur.

7.3 The Linear Parameter Regime

If Ω is small, so that the amplitude of the forced electron oscillation is small, the restoring force integral in equation (7.2) may be approximated by,

$$\int_{x_0}^{x_0+\xi} n_0(x)\,\mathrm{d}x \approx n_0(x_0)\xi' \,. \tag{7.10}$$

This linearisation reduces the equation of motion in the normalised variables to,

$$\ddot{\xi} + \alpha\dot{\xi} + \left(\frac{\omega_p}{\omega_f}\right)^2 \xi = \Omega\cos(\tau)\,, \tag{7.11}$$

which may be integrated analytically. The general solution of the linearised equation is of the form,

$$\xi(\tau) = q_1\exp(r_1\tau) + q_2\exp(r_2\tau) + \frac{\Omega}{\sqrt{\left(\frac{\omega_p^2}{\omega_f^2}-1\right)^2+\alpha^2}}\cos(\tau-\delta)\,, \tag{7.12}$$

where q_1 & q_2 are constants, r_1 & r_2 are the roots of the characteristic equation for the complimentary function and δ represents a phase difference between the driving and driven oscillations. The roots r_1 & r_2 are complex and each have a negative real part, so that the first two terms on the right hand side of equation (7.12) represent transient solutions which decay in time. The steady-state solution may therefore be written in the equivalent form,

$$\xi(\tau) = \Re\left\{\frac{\Omega\exp(i\tau)}{\left(\frac{\omega_p^2}{\omega_f^2}-1\right)+i\alpha}\right\}. \tag{7.13}$$

In this linearised case, the average dissipation of energy over a period of the

oscillation contains the dependence,

$$\langle eE\dot{\xi}\rangle \propto \frac{\alpha}{\left(\frac{\omega_p^2}{\omega_f^2}-1\right)^2+\alpha^2}. \tag{7.14}$$

We now seek a limit on the magnitude of Ω for the above linearised form to remain valid. We consider the definition of $F(\xi)$ in the region of the density gradient,

$$F(\xi) = \left(1-\frac{x_0}{L}\right)\xi - \frac{1}{2}\xi^2. \tag{7.15}$$

The linearisation process requires that we neglect the term in ξ^2 in this definition and this is valid only if $\frac{1}{2}\xi^2 \ll \xi\left(1-\frac{x_0}{L}\right)$. This gives the condition on the displacement, ξ, for the linearised form as,

$$\xi \ll 2\left(1-\frac{x_0}{L}\right). \tag{7.16}$$

The steady-state solution, equation (7.13), contains a resonant term, since $\frac{\omega_p^2}{\omega_f^2} = \beta\left(1-\frac{x_0}{L}\right)$. The amplitude of the oscillation in equation (7.13) is largest at the resonance point, which occurs when $\frac{x_0}{L} = 1-\frac{1}{\beta}$. With the value of β given previously, this locates the resonance point (the critical surface) at $\frac{x_0}{L} = \frac{199}{200}$. If we consider the condition (7.16) at this point, we require,

$$\left(\frac{\Omega}{\alpha}\right)_{\max} \ll 0.01 \tag{7.17}$$

For the model with $\alpha = 1.13\times10^{-2}$ this gives a condition on Ω for the linearised form of the equation of motion to be valid. We therefore have the condition,

$$\Omega < 1\times10^{-4}. \tag{7.18}$$

For values of the parameter Ω which satisfy this condition, we expect the linearised form of the equation of motion to be valid. To illustrate this, Figure 7.3 shows the response of the system for $\Omega = 1\times10^{-5}$ with amplitude of displacement plotted against

the position in the system. In this figure, the circular markers indicate the results from the numerical solution of the system (7.6) and the dots represent the values predicted by the analytical solution of the linearised equation. We see that the two sets of data are in excellent agreement. This suggests that the electrons in the density profile oscillate according to the linear theory at lower driver strengths. To analyse the details of the oscillation, we employ the data analysis methods described in the previous section. Figure 7.4 shows the phase portrait, the Poincaré map and the Fourier power spectrum for the electron motion at the critical surface for a driver strength $\Omega = 1 \times 10^{-5}$. The phase portrait shows that the phase trajectories are slightly distorted from a linear, circular, orbit, but the electron oscillation has the same period as the driver field. The Poincaré map also shows that, once the transients decay, the electron oscillation generates a single point in the mapping. Finally, the Fourier power spectrum shows that the only frequencies present in the electron oscillation are the fundamental at $\omega = \omega_f$ and the two harmonics $\omega = 2\omega_f$ & $\omega = 3\omega_f$. The power spectrum also shows that the energy in the fundamental oscillation mode is approximately 4 orders of magnitude greater than that in the first harmonic mode. This explains why the motion is isoperiodic with the driving field and the presence of the harmonics is responsible for the distortion of the phase trajectories away from the circular orbit.

The agreement between the nonlinear model equation and the linearised form in the parameter regime $\Omega < 10^{-4}$ serves to verify the results from the model equation. We have obtained the expected linear behaviour for the electron oscillation and the well-known 'bell-shaped' response curve characteristic of linear resonance absorption.

We now seek to investigate the nonlinear regime in the Ω parameter space and in the next section we present some numerical results.

7.4 Nonlinear Regime

In the previous section we defined the linear parameter regime for $\Omega < 10^{-4}$. By this token, we must take the nonlinear regime in Ω to be all points in the Ω-space greater than $\sim 10^{-4}$. If we consider the definition of Ω, we have,

$$\Omega = \frac{eE_0}{m\omega_f^2 L} = \frac{v_{\rm osc}}{c}.\frac{\lambda_f}{2\pi L}, \tag{7.19}$$

where v_{osc} is the electron quiver velocity in the vacuum field and λ_f is the wavelength of the driving oscillation. For radiation from an Nd:YAG laser system and a density scale length $\sim 10^{-8}$m,

$$\Omega \simeq 10 \times \frac{v_{\rm osc}}{c} \ . \tag{7.20}$$

In order to avoid relativistic effects we require $v_{osc}/c \leq 10\%$ and this gives an upper bound on Ω of $\Omega \simeq 1$. We therefore investigate the parameter space from $\Omega = 1 \times 10^{-4}$ to $\Omega \sim 1$. We also notice that the driver strengths which correspond to the laser intensity regime where the growth rates for plasma instabilities are high (10^{14} W/cm^2 < I < 10^{18}W/cm^2), lie in the range $1 \times 10^{-1} \leq \Omega \leq 1 \times 10^{1}$. We may expect to find significant nonlinear effects in the electron dynamics as we approach the upper end of the range of Ω values we intend to study.

We begin our investigation by considering the electron behaviour for $\Omega = 1 \times 10^{-4}$. Figure 7.5 shows the phase portrait, Poincaré map and the Fourier power spectrum for oscillations centred on the critical point. The plot of the (ξ,$\dot{\xi}$)phase space shows that the electron oscillation is again at the same frequency as the driving field, but the amplitude of the oscillation is higher than the case with $\Omega = 10^{-5}$. The Fourier spectrum also shows a stronger component at the fundamental frequency and the further growth of harmonics. This behaviour is typical of the response at all positions in the density profile at this value of Ω. The electron oscillations are all still at the driving frequency, although the phase trajectories show that the orbits are further

distorted from the linear circular paths. The amplitude of the response across the density profile closely follows the linear theory as Figure 7.6 illustrates.

When we increase the value of Ω by an order of magnitude, we find a further growth in the number of harmonics present in the electron oscillation. Figure 7.7 shows the analysis of the electron oscillation at the critical surface for $\Omega = 1 \times 10^{-3}$. The phase portrait shows that the trajectories are egg-shaped and the amplitude of the oscillation has doubled from Figure 7.5 in the direction of positive displacement, but remains almost unchanged in the direction of negative displacement. This indicates that the motion of the electrons is becoming asymmetric with a larger amplitude in the direction of decreasing density. The Fourier spectrum shows the continuation in the trend of harmonic generation, with components now present at up to 6 times the frequency of the pump wave. Unlike the case at $\Omega = 10^{-4}$, however, this behaviour is not repeated throughout the density profile. In the underdense plasma, the electron oscillation varies markedly in its nature. The nonlinearity of system (7.6) allows a number of attractors to form in the parameter space of the model. Figure 7.8 shows the analysis of electron oscillations centred on $x_0/L = 0.996$. Now, the Poincaré map shows 4 points for the steady state oscillation which indicates that the period of the electron oscillation is 4 times that of the pump wave. The phase portrait also shows how this period $\times 4$ attractor distorts the phase trajectories showing that one cycle now takes 4 periods of the pump wave and the electron oscillation amplitude is asymmetric about the zero point. The Fourier spectrum confirms the existence of subharmonic components at $\omega_p/\omega_f = \frac{1}{4}, \frac{1}{2}, \frac{3}{4}, 1$. Figure 7.9 shows the situation at the position $x_0/L = 0.997$ for the same strength of pump wave. This time, we see that the oscillation falls into the domain of a period $\times 3$ attractor. The phase portrait again illustrates how the trajectories are distorted to make one period of the electron oscillation last three periods of the pump wave. The Fourier spectrum in this case shows strong components for the subharmonics at $\omega_p/\omega_f = \frac{1}{3}, \frac{2}{3}$.

In the range of positions between the critical surface and the vacuum we have

successfully identified electron oscillations with periods $2, 3, 4$ &6 times that of the pump wave. The pattern of attractor domains is extremely complex repeating itself on an infinitely fine scale so that a difference of one part in 10^{16} in the initial position places the system in the domain of a different attractor. A large amount of data has been collected about the domain of the attractors in the parameter space $(x_0/L, \Omega)$, but since it cannot be exhaustive we present only some examples of the electron dynamics here. Interspersed with these bifurcations to longer period oscillations are the domains of chaotic attractors. Such an attractor exists at the position $x_0/L = 0.9985$ for $\Omega = 1 \times 10^{-3}$ and Figure 7.10 shows the analysis of the electron dynamics at this point in the parameter space. The phase portrait shows that in this case there is no 'period' for the oscillation as the phase trajectories never join to form a closed orbit. However, one can see that there is a definite structure to the phase portrait. The Poincaré map further illustrates the structure of the chaotic attractor. The mapping consists of nine 'fingers' with a well defined structure within each one. As is characteristic of chaotic attractors however, although there is a discernible structure, given a particular point in a Poincaré map it is impossible to predict which point in the attractor will be mapped by the next sample. The Fourier power spectrum shows the characteristic broad-band noise of a chaotic motion. There are relatively strong components present at all subharmonic frequencies, and a spike in the spectrum indicates a strong component at the fundamental frequency, ω_f. With such a rich distribution of attractors in the parameter space for $\Omega = 10^{-3}$, it becomes difficult to generate data for the response of the electrons throughout the density gradient. This is because different attractors give varying oscillation amplitudes and periods. Figure 7.12 shows the oscillation amplitudes recorded by the gen2000 program for $\Omega = 10^{-3}$ across the density profile. The behaviour for positions > 0.995 illustrates the difficulty mentioned above. Figure 7.12 also shows an enhancement to the oscillation amplitude at the position $x_0/L = 0.9805$. The local plasma frequency

normalised to the driving frequency is given by,

$$\frac{\omega_p}{\omega_f} = \sqrt{\beta}\left(1 - \frac{x_0}{L}\right)^{\frac{1}{2}}, \tag{7.21}$$

and therefore at $x_0/L = 0.9805$ we have $\omega_p/\omega_f = 2$ so that the enhanced oscillation amplitude may be seen to be a resonance with the second harmonic of the forcing frequency. This enhanced oscillation is therefore not due to a difference in the nature of the attractor at $x_0/L = 0.9805$, but purely a resonant effect.

It is worth noting here that these dramatic nonlinear effects occur at a value of the parameter Ω much lower than we expect from earlier considerations. If we take the density scale length $L = 10^{-8}$m, then the value of Ω under consideration here corresponds to a laser intensity $\sim 10^9 \mathrm{W/cm}^2$.

If we continue to increase the value of Ω, we find that the domains of the chaotic attractors become larger in the parameter space. When $\Omega \sim 10^{-2}$ we find that nearly all the points in the underdense plasma fall into the domain of attraction of a chaotic attractor. As the value of Ω is increased further, the structure of the attractor, as shown in the Poincaré maps, changes. We find that the number of 'fingers' increases with new fingers being 'generated' at the left hand edge of the map and the existing fingers rotate clockwise. With the increase in pump strength, we also see a large increase in the asymmetric oscillation towards the vacuum region. Figure 7.11 shows the analysis of the electron dynamics for $x_0/L = 0.995$ and $\Omega = 1 \times 10^{-1}$. All three diagnostic plots show that the motion of the electrons, at this point in the parameter space, is chaotic. The Poincaré map shows how the structure of the attractor has changed compared with that in Figure 7.10. The Poincaré map and the phase portrait also illustrate the large asymmetry in the electron oscillation. The electron has a positive excursion amplitude $\sim 10 \times L$ compared to a minimal negative excursion amplitude.

As mentioned earlier, the domains of the attractors in the parameter space are

extremely complex and sensitive to the finest changes in either Ω or x_0/L. The same is true of the space of initial values $(\xi,\dot{\xi})$. To illustrate this, we consider the motion centred on $x_0/L = 0.996$ for $\Omega = 1 \times 10^{-3}$. This point in the parameter space lies in the domain of attraction of a period×4 attractor when the model equation is solved with the initial values $\xi = \dot{\xi} = 0$. To investigate the sensitivity of the final motion to the initial values, we solve the same point in the parameter space over an 11×11 mesh in the space of initial values. The step sizes are arbitrarily chosen so that $\Delta\xi_0 = 2 \times 10^{-3}$ and $\Delta\dot{\xi}_0 = 2 \times 10^{-1}$. Figure 7.13 illustrates the periodicity of the final steady state motion on this grid of starting values. Attractors of different periodicity are represented by different markers on the mesh. We see here that attractors of period $1, 2, 3\&4$ exist in the area of the space of starting values explored. We also note that two previously unseen attractors were discovered in this analysis and are labelled 3a and 4a in the figure. These attractors are of period 3 and 4 respectively, but differ from the previous attractors in the location of the stable points on the Poincaré map. This study of one small part of the space of starting values therefore serves to illustrate the complexity of the domains of attraction located within it.

From our analysis of the electron dynamics in this simple model we have seen that at pump strengths represented by $\Omega \geq 10^{-3}$ the electron motion is complicated and increasingly asymmetric. The question now arises whether the nonlinear nature of the electron oscillation may have an effect on the absorption of the energy in the pump wave by the plasma electrons. In the next section, therefore, we present some simple considerations on the absorption of the energy in the pump wave.

7.5 Absorption of Pump Energy

For the purposes of this investigation we define the average absorption of energy over a period of the electron oscillation at any point in the density profile by,

$$\langle abs \rangle_{T_e} = \frac{1}{T_e} \int_0^{T_e} \left(\dot{\xi} \times \Omega \cos(t) \right) \, \mathrm{d}t \; . \tag{7.22}$$

where T_e is the period of the electron motion. For values of Ω in the linear regime ($< 10^{-4}$) this should agree with the linearised calculation of the dissipation of energy from equation (7.14) which gives,

$$\langle abs \rangle_{T_e} = \frac{1}{2} \left(\frac{\alpha \Omega^2}{\left(\frac{\omega_p^2}{\omega_f^2} - 1 \right)^2 + \alpha^2} \right) \; . \tag{7.23}$$

We set out, therefore, to investigate the values for absorption across the density profile for the whole range of Ω space considered previously. Since, however, there are two parameters which we vary in the parameter space, namely Ω and x_0/L, we have two possible courses for our investigations. We may choose a value of Ω and look at the variation in the absorption throughout the density profile, or we may choose a fixed position in the profile and consider the changes to the absorption level as the value of Ω is varied. We present some results from each of these approaches here. We begin with the investigation at particular values of Ω and with $\Omega = \times 10^{-5}$. Figure 7.14 shows the numerical absorption calculated from equation (7.22) and the theoretical absorption value across the density gradient for $\Omega = 1 \times 10^{-5}$. For convenience, we actually plot the logarithm of the absorption value to compress the range on the y-axis. We see that the numerical and theoretical results show excellent agreement and we have a linear resonance absorption type curve. As we increase the value of Ω we begin to see a divergence between the linear theory and the nonlinear results. Figure 7.15 shows the absorption profile for $\Omega = 5 \times 10^{-4}$. In the overdense plasma,

the response still shows good agreement with the linear theory. Around the critical surface, however, we see that the peak in the absorption is reduced in magnitude and has moved towards the overdense body of the plasma, compared with the prediction of the linear theory. In addition, towards the right hand end of the density ramp we see a second peak in the absorption. This is clearly a nonlinear effect. As we increase the strength of the driver further, we see increasing evidence of nonlinear behaviour affecting the absorption mechanism. Figure 7.16 illustrates the absorption profiles for $\Omega = 1 \times 10^{-3}$. The linear theory again predicts a profile with a single peak at the critical surface. The nonlinear results, however, differ markedly from this predicted form. Once again, at this value of Ω, we see an effect due to the second harmonic which resonates with the plasma electrons at $x_0/L = 0.9805$. This resonance leads to an enhanced absorption value at this point in the density profile. The results from the nonlinear calculation around the region of the critical surface show a considerable departure from the prediction of the linear theory. As in the previous case, the peak value of absorption is significantly reduced, here by two orders of magnitude, when compared with the linear value. The location of the peak absorption has also moved further into the body of the plasma when compared with the case $\Omega = 5 \times 10^{-4}$. Finally in this analysis, Figure 7.17 illustrates the absorption behaviour through the density profile for $\Omega = 1 \times 10^{-2}$. We again see the contribution from the second harmonic and the trend of depressed peak value and shifting of the location of the peak are continued.

We now briefly present some results from the alternative approach to the study of $(\Omega, x_0/L)$ parameter space. In this approach we consider only the electron motion at the critical surface (x_0/L) and study the changes in the absorption values as the value of Ω is increased. For convenience, we arrange the results in groups of orders of magnitude of Ω. Figure 7.18 illustrates the absorption behaviour across a range of values in Ω that lies well within the regime of the linear theory. We see that as the value of Ω increases from 1×10^{-7} towards 1×10^{-6} the absorption increases

monotonically and in excellent agreement with the prediction of the linear theory. At $\Omega \sim 10^{-5}$, Figure 7.19, the values for the absorption from the nonlinear calculation begin to diverge from the predictions of the linear theory. We see that for values of Ω above $\simeq 1.5 \times 10^{-5}$, the nonlinear absorption values are increasingly depressed when compared with the linear theory. By the time Ω reaches 1×10^{-4}, the discrepancy between the two values has reached one order of magnitude. Finally, Figure 7.20 illustrates the behaviour at the critical surface for $\Omega \sim 10^{-3}$. We see here that the trend of reduced absorption continues and the difference between the linear and nonlinear results reaches over two orders of magnitude. We also observe that the nonlinear absorption profile is no longer a monotonic function of Ω and indeed shows a great deal of fluctuation for $\Omega > 2.5 \times 10^{-3}$. This coincides with the growth of period altering attractors for the point $x_0/L = 0.995$ in the parameter space and is another clear indication of the nonlinear effects on the electron dynamics causing a significant departure from linear behaviour.

7.5.1 Computational Considerations

The computer program to generate the nonlinear absorption data was initially written to implement the calculation given in equation (7.22) using the calculated values of instantaneous force and particle velocity. However, in the course of running this program it became apparent that this calculation is extremely sensitive to errors in the calculated values. This sensitivity sets unacceptably high requirements on the accuracy of the values of force and velocity (error $< 1 \times 10^{-14}$). The reason for this sensitivity, and a solution to the problem are illustrated by considering as an example, the linearised equation of motion in the form,

$$\ddot{x} + \nu\dot{x} + \omega_p^2 x = \Omega \exp(i\omega t) \; . \tag{7.24}$$

The solutions of such an equation take the form,

$$x \propto \Re\left\{\frac{\exp(i\omega t)}{(\omega_p^2 - \omega^2) + i\nu}\right\}, \tag{7.25}$$

so that,

$$\langle \dot{x} \times \Omega \cos(\omega t)\rangle \propto \langle \cos^2(\omega t) - \cos(\omega t)\sin(\omega t)\rangle . \tag{7.26}$$

The term in $\cos^2(\omega t)$ on the right hand side of the above is positive definite. The mixed trigonometric term however, has an oscillation in its sign, although it gives zero contribution when averaged over a complete cycle. Figure 7.2 illustrates the behaviour of the two terms over a single linear period. It becomes obvious, that in calculating

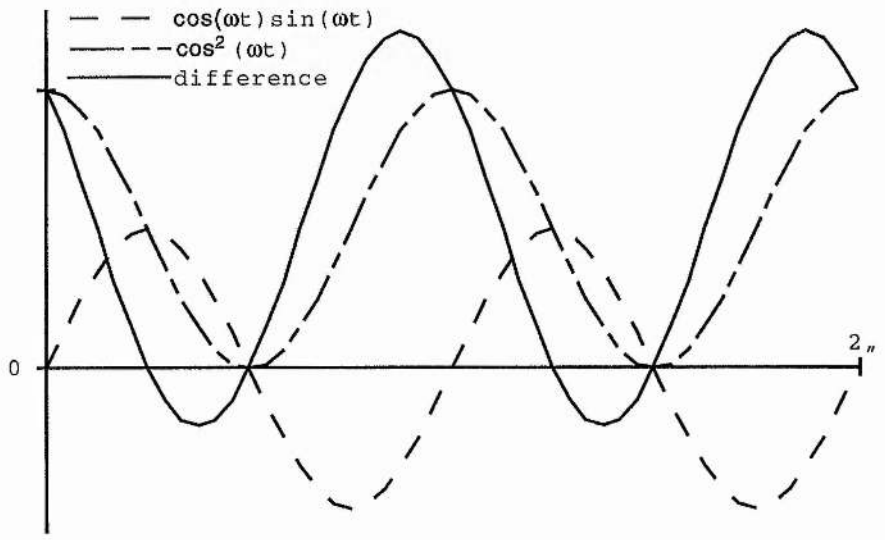

Figure 7.2: The oscillatory behaviour of the trigonometric terms in equation (7.26) over a single linear period.

the right hand side of equation (7.26) we are seeking a small remainder from a large oscillation which should cancel over a period. This scheme is vulnerable to numerical errors. An alternative treatment of the equation is to consider the restoring force as a conservative force derivable from a potential, V. Then we may write the equation

of motion as,

$$\ddot{x} + \nu\dot{x} + \frac{\mathrm{d}V}{\mathrm{d}x} = \Omega\cos(\omega t)\,. \tag{7.27}$$

If we multiply this equation through by $\dot{x}$ and take the average of the whole equation over a period of the oscillation, we get,

$$\langle \nu\dot{x}^2 \rangle = \langle \dot{x}\Omega\cos(\omega t) \rangle \tag{7.28}$$

The term on the left hand side above is the average dissipation, and we see that it balances the work done by the pump wave. Instead of calculating the average value of $\dot{\xi}\Omega\exp(i\tau)$, we may therefore use $\alpha\dot{\xi}^2$ to represent the absorption in the nonlinear model.

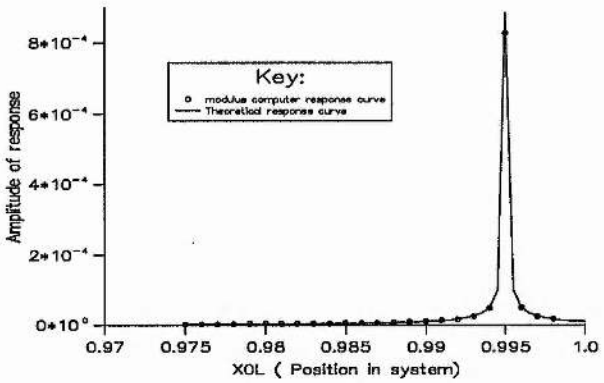

Figure 7.3: The amplitude of electron oscillations vs the position in the density profile for $\Omega = 1 \times 10^{-5}$. We see the linear 'bell-shaped' response.

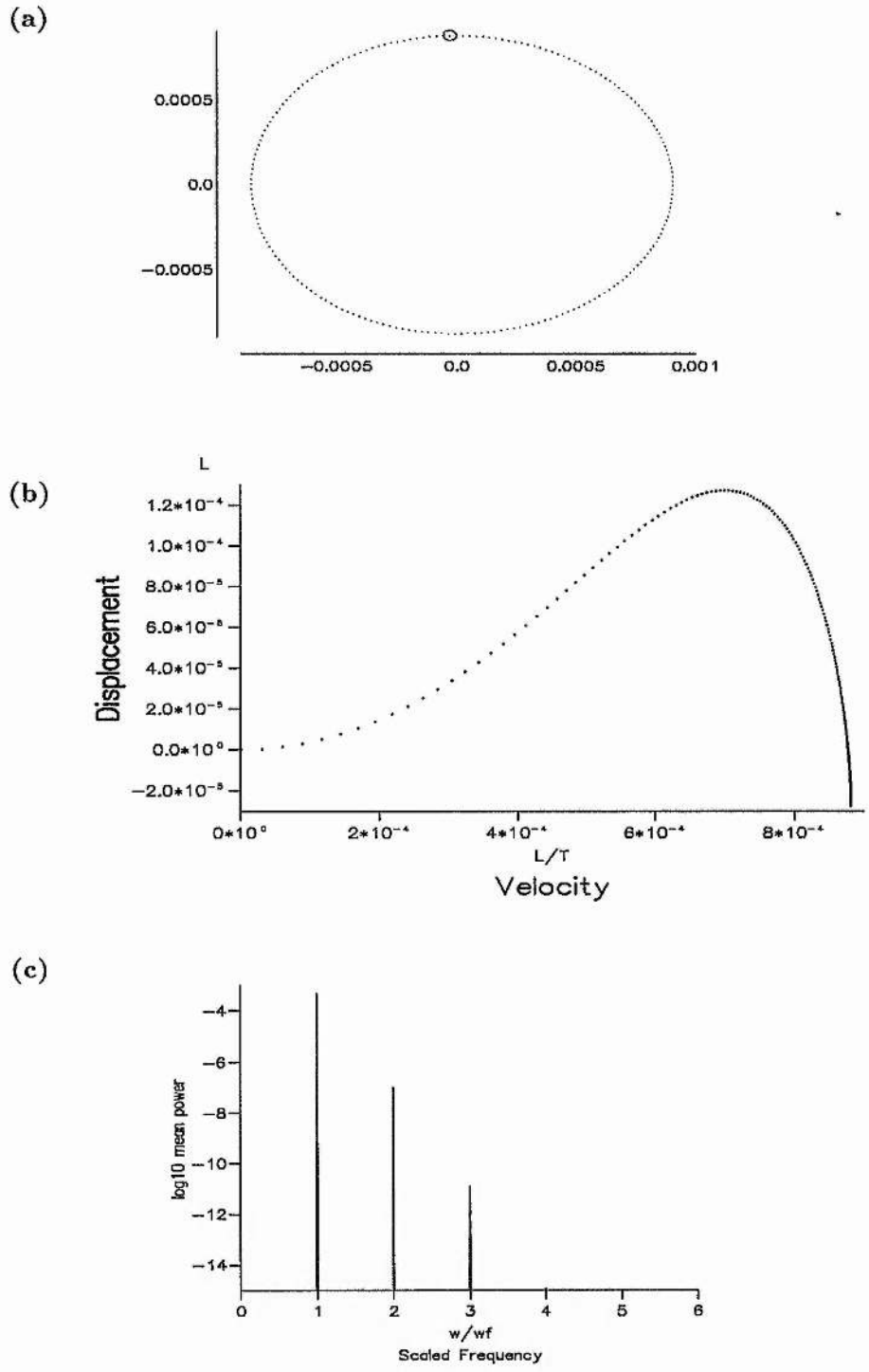

Figure 7.4: The analysis of the motion of an electron at the critical surface with driver strength $\Omega = 1 \times 10^{-5}$ **(a)** - The phase portrait in the displacement/velocity space; **(b)** - The poincaré map and **(c)** - The Fourier decomposition spectrum of the motion.

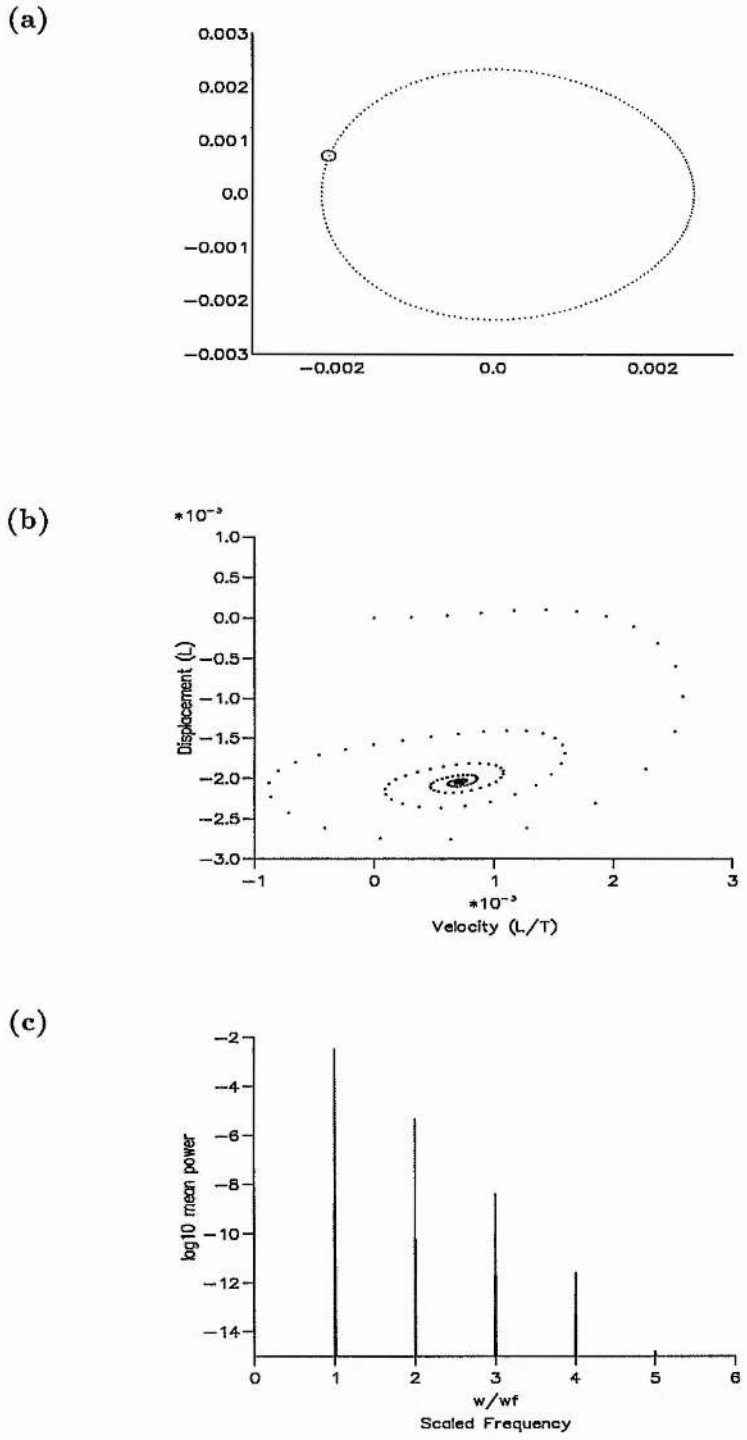

Figure 7.5: The analysis of the motion of an electron at the critical surface with driver strength $\Omega = 1 \times 10^{-4}$ **(a)** - The phase portrait in the displacement/velocity space; **(b)** - The poincaré map and **(c)** - The Fourier decomposition spectrum of the motion.

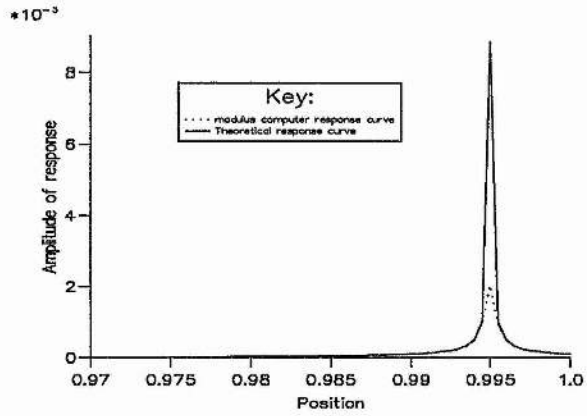

Figure 7.6: The amplitude of electron oscillations vs the position in the density profile for $\Omega = 1 \times 10^{-4}$.

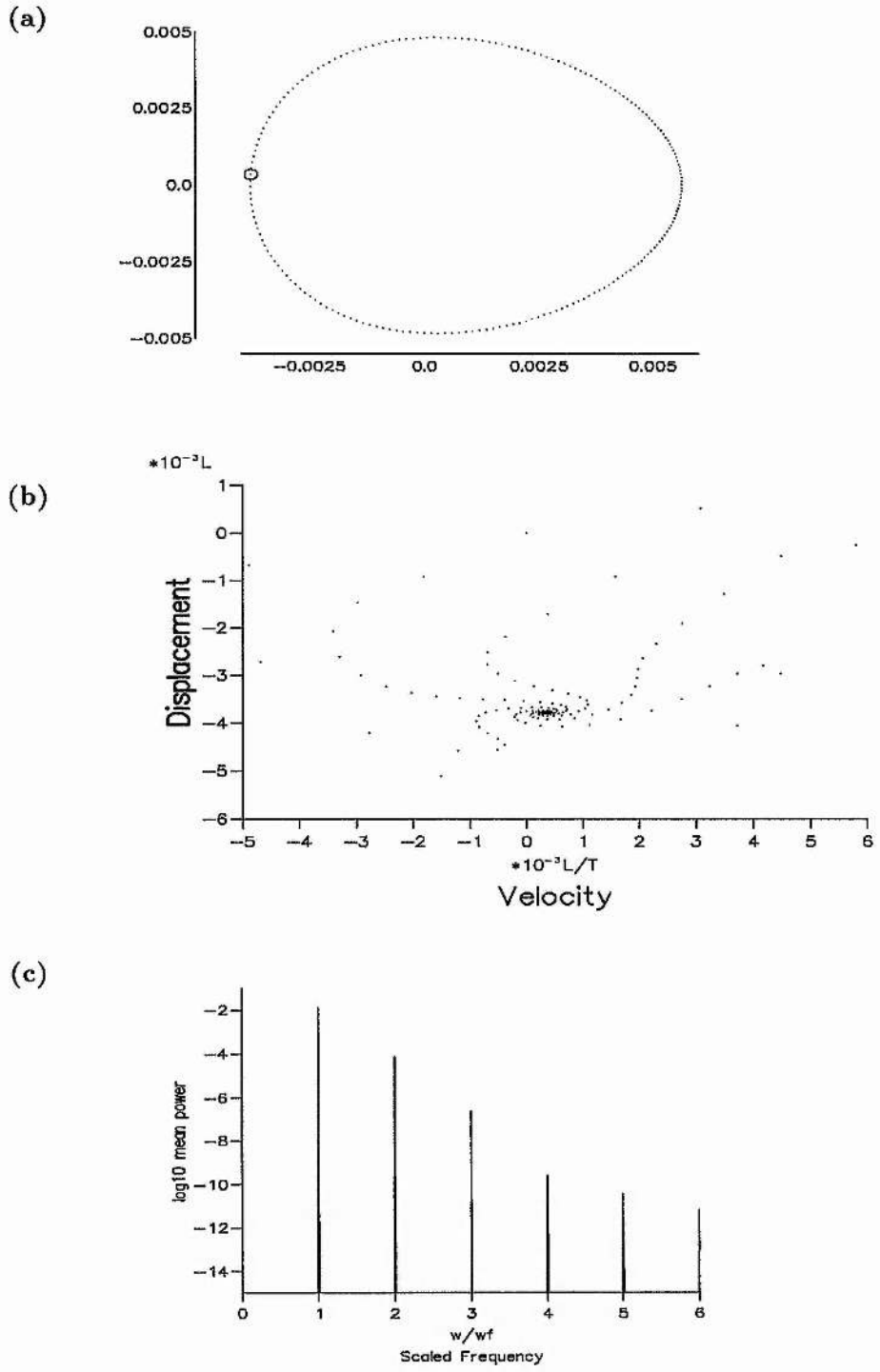

Figure 7.7: The analysis of the motion of an electron at the critical surface with driver strength $\Omega = 1 \times 10^{-3}$ **(a)** - The phase portrait in the displacement/velocity space; **(b)** - The poincaré map and **(c)** - The Fourier decomposition spectrum of the motion.

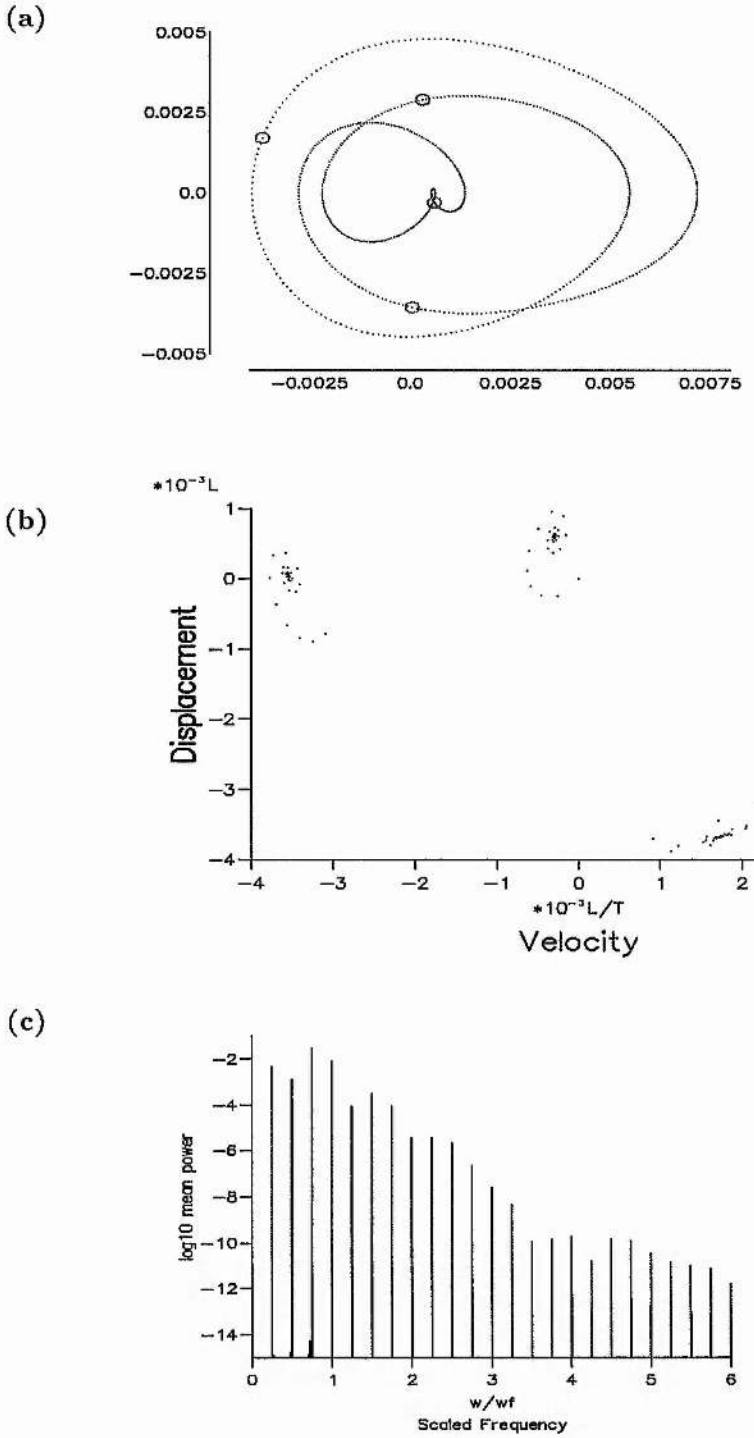

Figure 7.8: The analysis of the motion of an electron at the position $\frac{z_0}{L} = 0.996$ with driver strength $\Omega = 1 \times 10^{-5}$ **(a)** - The phase portrait in the displacement/velocity space; **(b)** - The poincaré map and **(c)** - The Fourier decomposition spectrum of the motion.

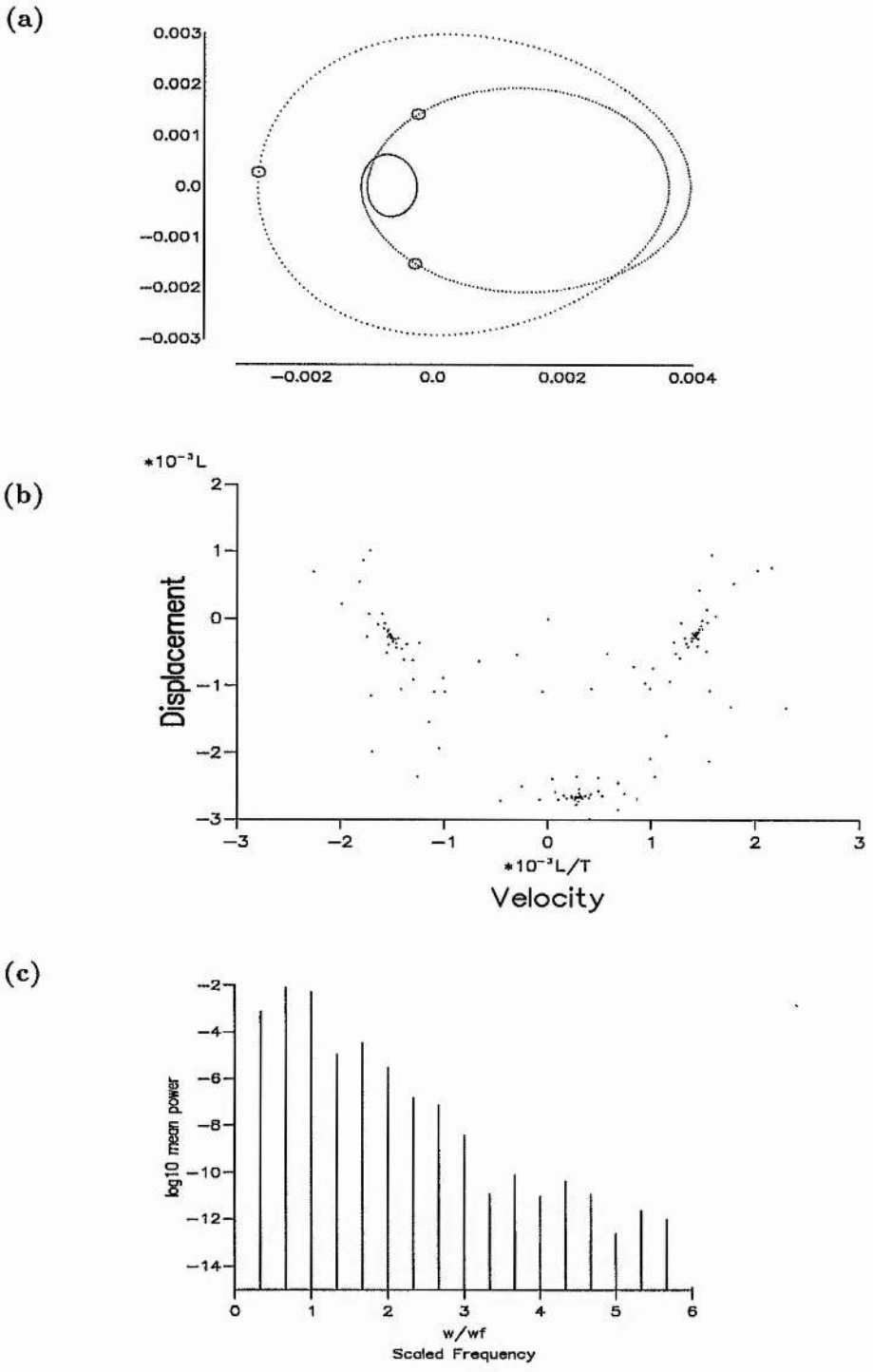

Figure 7.9: The analysis of the motion of an electron at the position $\frac{x_0}{L} = 0.997$ with driver strength $\Omega = 1 \times 10^{-3}$ **(a)** - The phase portrait in the displacement/velocity space; **(b)** - The poincaré map and **(c)** - The Fourier decomposition spectrum of the motion.

(a)

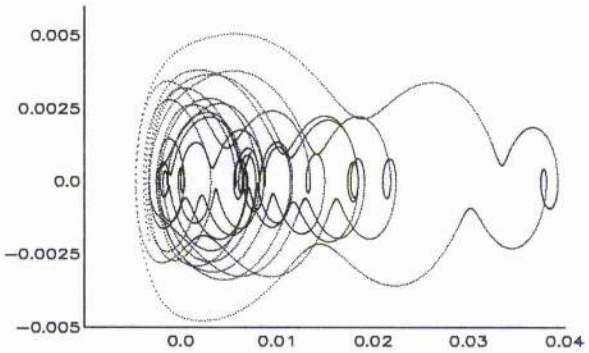

(b)

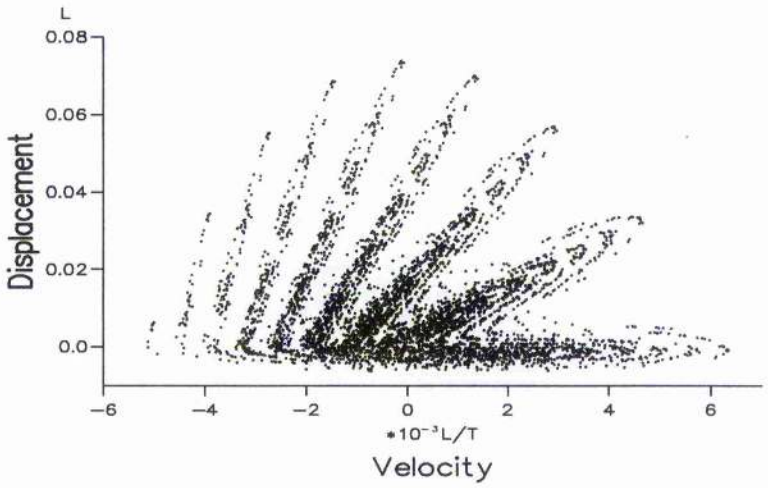

(c)

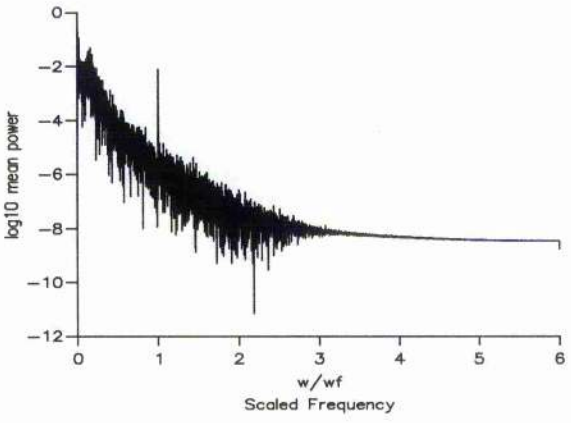

Figure 7.10: The analysis of the motion of an electron at the position $\frac{x_0}{L} = 0.9985$ with driver strength $\Omega = 1 \times 10^{-3}$ **(a)** - The phase portrait in the displacement/velocity space; **(b)** - The poincaré map and **(c)** - The Fourier decomposition spectrum of the motion.

(a)

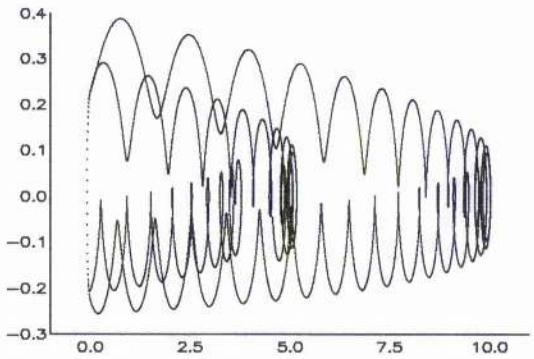

(b)

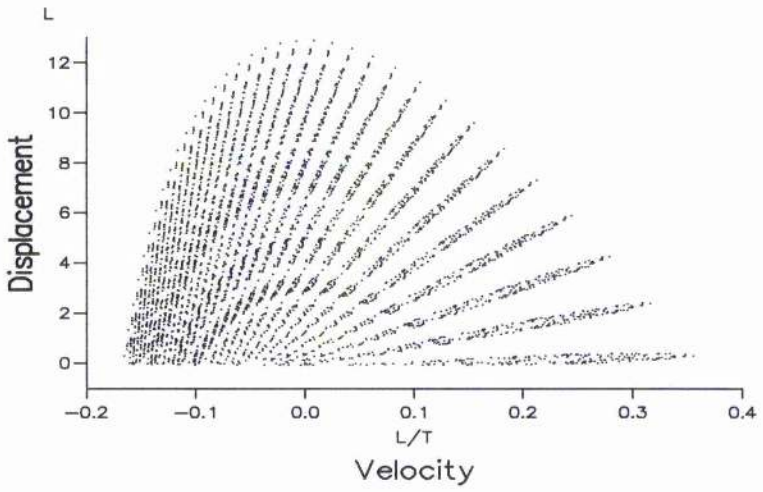

(c)

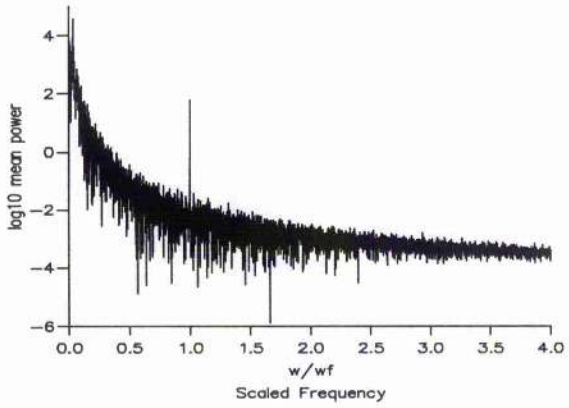

Figure 7.11: The analysis of the motion of an electron at the critical surface with driver strength $\Omega = 1 \times 10^{-1}$ **(a)** - The phase portrait in the displacement/velocity space; **(b)** - The poincaré map and **(c)** - The Fourier decomposition spectrum of the motion.

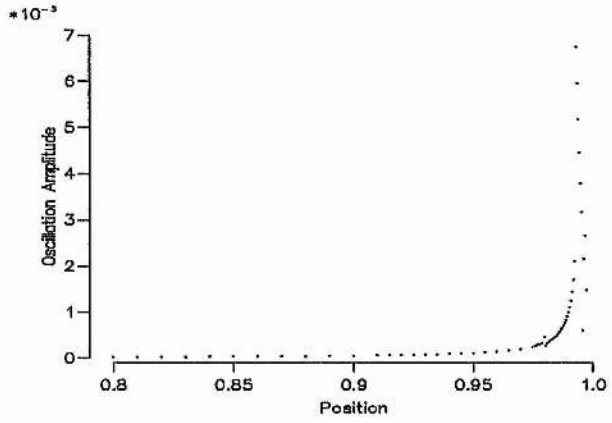

Figure 7.12: The amplitude of electron oscillations vs the position in the density profile for $\Omega = 1 \times 10^{-3}$.

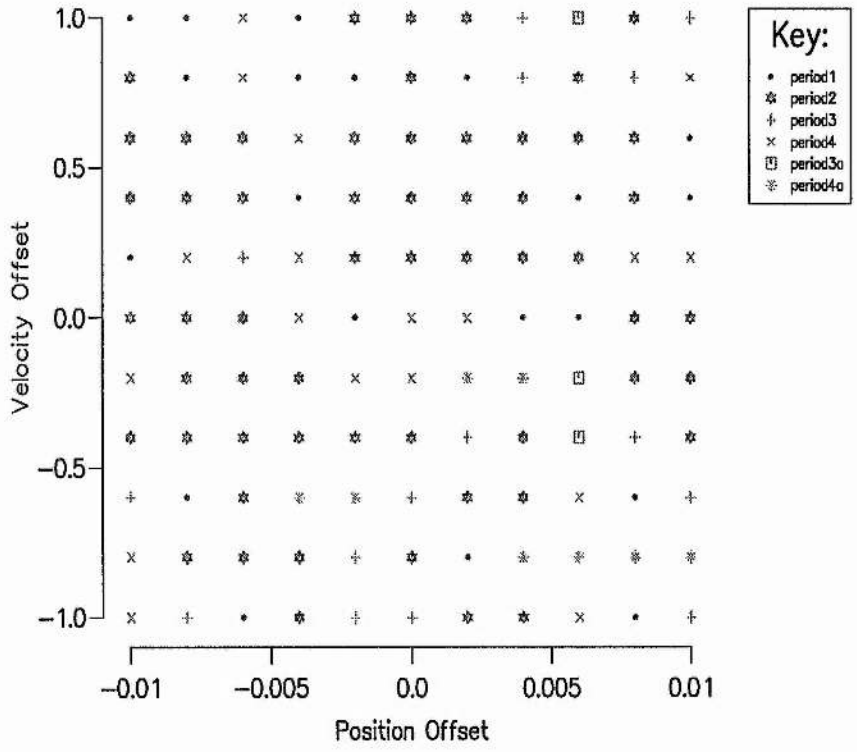

Figure 7.13: The periodicity of the final electron motion at $\frac{x_0}{L} = 0.996$ over a mesh of initial displacement and velocity values.

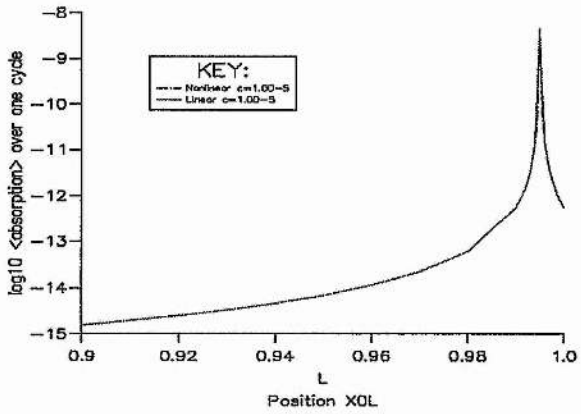

Figure 7.14: The plot of the calculated absorption value vs position in the profile for $\Omega = 1 \times 10^{-5}$.

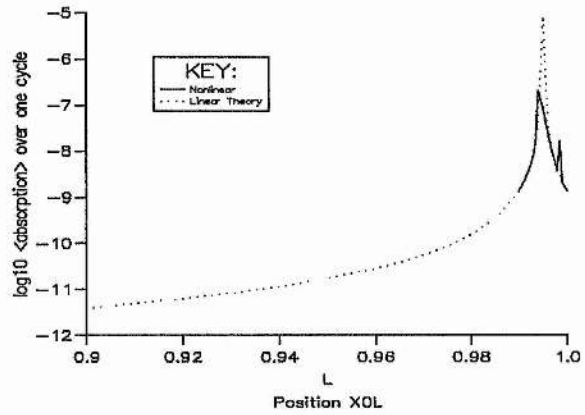

Figure 7.15: The plot of the calculated absorption value vs position in the profile for $\Omega = 5 \times 10^{-4}$.

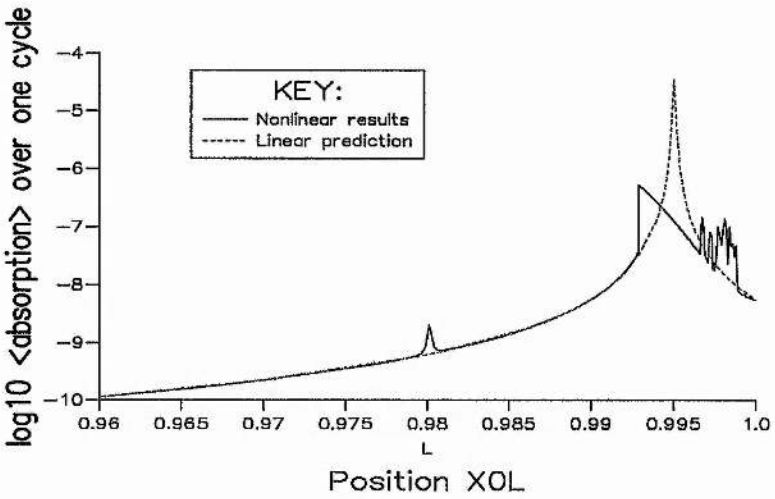

Figure 7.16: The plot of the calculated absorption value vs position in the profile for $\Omega = 1 \times 10^{-3}$.

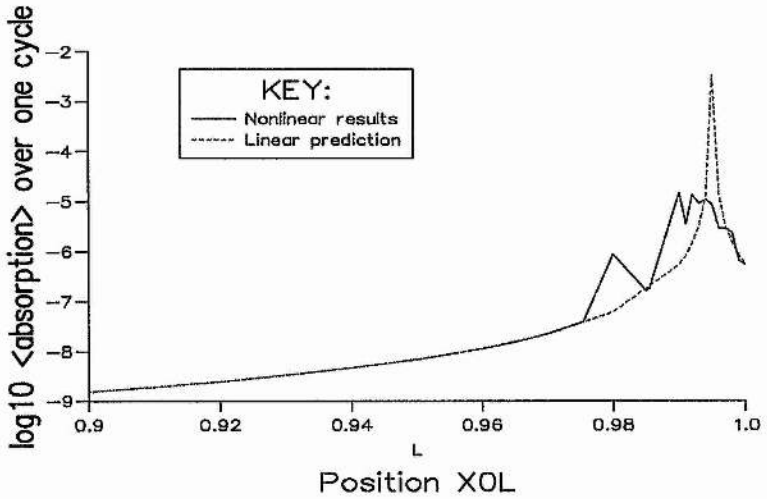

Figure 7.17: The plot of the calculated absorption value vs position in the profile for $\Omega = 1 \times 10^{-2}$.

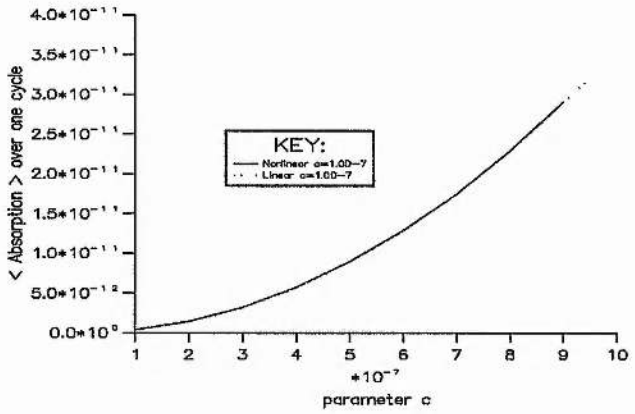

Figure 7.18: The plot of the calculated absorption value at the critical surface vs intensity of the driving field for $1 \times 10^{-7} \leq \Omega \leq 1 \times 10^{-6}$.

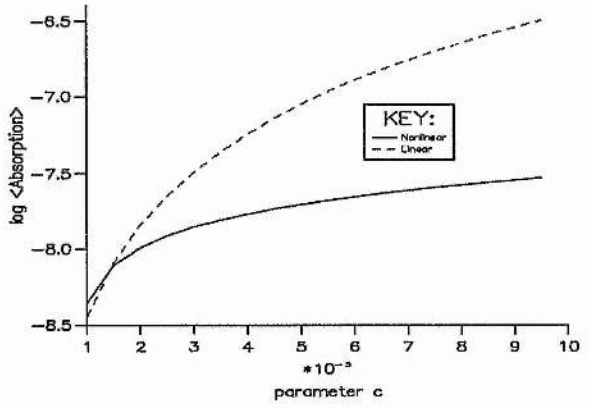

Figure 7.19: The plot of the calculated absorption value at the critical surface vs intensity of the driving field for $\Omega \sim 1 \times 10^{-5}$.

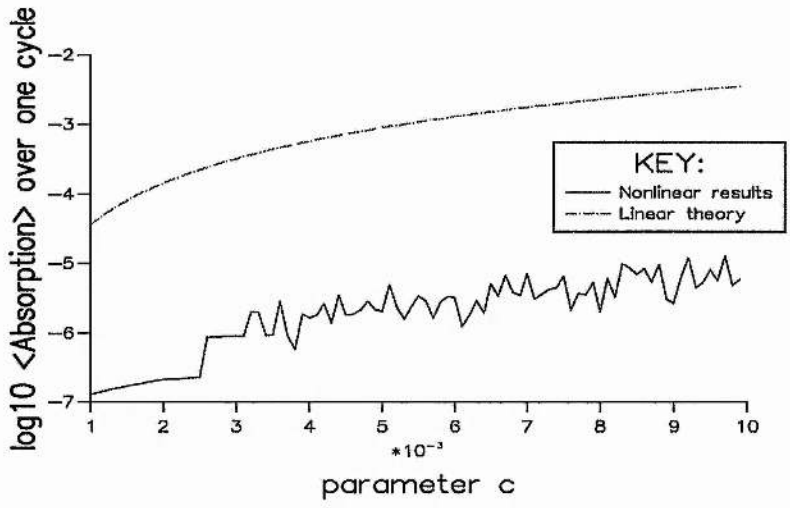

Figure 7.20: The plot of the calculated absorption value at the critical surface vs intensity of the driving field for $\Omega \sim 1 \times 10^{-3}$.

Chapter 8

Particle-In-Cell Simulations

In this chapter we discuss the application of a 1-Dimensional electrostatic particle-in-cell (PIC) simulation code to investigate the response of plasma electrons in a density gradient to an applied electric field. In particular we hope to confirm the electron dynamics reported in chapter 7. A particle-in-cell code solves the basic equations governing the motion of each particle in the simulation using finite-difference techniques and calculates the field at points on a computational mesh. It then applies the field to each of the particles and moves them accordingly. The particular code used here was obtained from the plasma physics group at Imperial College, London and is essentially the electrostatic code ES1 described in the book by Birdsall and Langdon [5]. We begin this chapter with a description of the various modifications made to the basic code for our purposes. Then we present an account of the way in which the various versions of the code were employed in our investigations and the results obtained.

8.1 Modifications to the PIC code

The basic PIC code as supplied by the plasma group at Imperial College, London required some modification to suit our specific application. Some of the changes to the code are to enhance its useability, whilst others are required to investigate the

electron dynamics of the electrostatic system. The useability enhancements include periodically dumping the values of the variables to a disk file, changing the program to read its input from a structured data file and introducing a confidence check on the value of the electron thermal velocity used for the simulation. As we shall see later, the electron thermal drift velocity can have a marked effect on the electron dynamics in response to the electrostatic driver field. The original version of the particle code sets the thermal drift velocity as a function of the number of grid points in the spatial mesh to avoid numerical diffusive effects [5]. However, this leads to differing thermal velocities for individual code runs, so the program was modified to read the value of the thermal electron drift velocity from the input data file and check it against the original formula to retain the suppression of numerical diffusion.

More substantial changes are made to tune the code to our application. The first of these changes is to introduce a test-particle amongst the electrons. This particle behaves like an electron in the fields present in the plasma, but without affecting the fields in any way. This allows us to follow the dynamics (position and velocity) of a single particle to construct phase trajectories for comparison with the results of our simple model. The test-particle is initially positioned at the critical surface in the plasma density gradient and has zero velocity. Data on the position and velocity of the test-particle is stored at regular time intervals so that a phase space trajectory plot may be constructed. The program is also modified to write output data in three discrete files. The first file contains data for the bulk motion of the plasma in the simulation. From this data a separate program produces the graphic representation of the $v_x - x$ phase space, the electrostatic field across the computational mesh and the electron density fluctuations across the mesh. The second data file contains more detailed time history data on the electrostatic field and from this we construct a three dimensional plot showing the evolution of the field in the $t - x$ plane. The final output file contains the test-particle data and from this we construct the phase trajectories in the $v_x - x$ space and Fourier decompose the motion to look for the presence of

sub-harmonic frequency components.

Output from early test runs (see next section) shows that there is a small oscillation in the test-particle data which is due to the thermal electron drift velocity and a small field induced by the initial positioning of the electrons relative to the ion ramp in the simulation. The linear electron and ion ramps are initially coincident causing a residual field which the electrons counteract by moving position slightly. In order to observe the fine scale behaviour of the previous chapter in the test-particle motion, we must attempt to reduce the 'zero driver' oscillation to a minimum. We therefore set out to modify the initial positioning of the electrons, relative to the fixed ion ramp, so that there is zero initial charge separation field in the plasma.

In the initialisation subroutine of the code, the particles are initially placed to give a uniform density, n_0, across the computational mesh $(0, z_0)$. We now define a mapping to reposition these electrons in a self-consistent manner across the linear ion ramp. If we denote the new density distribution by $\acute{n}(\acute{z})$, then we may define the mapping via,

$$\frac{\mathrm{d}\acute{z}}{\mathrm{d}z} = \frac{N_0}{\acute{n}(\acute{z})}, \tag{8.1}$$

where N_0 is the uniform density required to construct the self-consistent profile in the computational box. This is not quite equal to the n_0 defined in the PIC code since we will not include the entire profile in the range of the mesh. To force the right most point of the computational mesh, z_0, to map to itself we require,

$$z_0 = \frac{1}{N_0} \int_0^{z_0} \acute{n}(\tilde{z})\, \mathrm{d}\tilde{z}, \tag{8.2}$$

which fixes the value of N_0 required for the given density function $\acute{n}(\acute{z})$. We may then integrate equation (8.1) to obtain the mapping for $\acute{z} \rightarrow z$ as,

$$z = \frac{1}{N_0} \int_0^{\acute{z}} \acute{n}(\tilde{z})\, \mathrm{d}\tilde{z}. \tag{8.3}$$

This may then be used to invert the mapping by interpolating back from the z values of the particles' initial positions to the corresponding $\acute{z}$ values. In this way, we may position the electrons to give the required density profile according to the function $\acute{n}(\acute{z})$. We now require the form of the particular density function for the self-consistent profile. This may be calculated via the electrostatic potential, ϕ, using Poisson's equation,

$$\frac{\mathrm{d}^2\phi}{\mathrm{d}z^2} = -\frac{e}{\varepsilon_0}(n_i - n_e) \ , \tag{8.4}$$

where n_i and n_e are the ion and electron densities respectively. We require the electron density, n_e, consistent with the linear ion density initialised in the PIC code. We relate the electron density to the electrostatic energy and the thermal energy of the electrons via the Maxwell-Boltzmann distribution,

$$n_e = 2n_0 \exp\left(\frac{e\phi}{K_B T_e}\right) \ , \tag{8.5}$$

where $2n_0$ is the maximum density of the ion ramp. If we normalise $\Phi = e\phi/k_B T_e$ and $r = \frac{1}{2\pi}\frac{z}{L}$ where L is the scale length of the density gradient, we may rewrite Poisson's equation,

$$\frac{\mathrm{d}^2\Phi}{\mathrm{d}r^2} = -8\pi^2\left(\frac{L}{\lambda_D}\right)^2\left(\frac{n_i}{2n_0} - \exp(\Phi)\right) \ , \tag{8.6}$$

where $\lambda_D^2 = \frac{\varepsilon_0 K_B T_e}{n_0 e^2}$ is the Debye length and we have to solve this equation numerically across the ion ramp.

We solve this equation as a boundary value problem and we now define the boundary conditions at the left and right hand sides of the ion ramp. To the left of the ion ramp, the ion density is zero and equation (8.6) becomes,

$$\frac{\mathrm{d}^2\Phi}{\mathrm{d}r^2} = 8\pi^2\left(\frac{L}{\lambda_D}\right)^2\exp(\Phi) \tag{8.7}$$

which we may integrate to get the condition,

$$\frac{\mathrm{d}\Phi}{\mathrm{d}r} = 4\pi \left(\frac{L}{\lambda_D}\right) \exp\left(\frac{\Phi}{2}\right) . \tag{8.8}$$

Indeed, we may integrate again to obtain the analytic from of the solution to the left of the ion ramp,

$$\Phi = -2\ln\left[2\pi \left(\frac{L}{\lambda_D}\right)(r_0 - r)\right] , \tag{8.9}$$

where r_0 is the constant of integration which may be determined by matching to the numerical solution at the boundary.

To the right of the ion ramp, we assume a constant ion density of $2n_0$ so that equation (8.6) becomes,

$$\frac{\mathrm{d}^2\Phi}{\mathrm{d}r^2} = -8\pi^2 \left(\frac{L}{\lambda_D}\right)^2 (1 - \exp(\Phi)) , \tag{8.10}$$

and the boundary condition on the gradient of Φ is then,

$$\frac{\mathrm{d}\Phi}{\mathrm{d}r} = 4\pi \left(\frac{L}{\lambda_D}\right) \sqrt{(\exp(\Phi) - \Phi - 1)} . \tag{8.11}$$

We notice from the boundary conditions at the left and right hand edges of the ion ramp that they contain a dependence on the ratio of the density scale length to the plasma Debye length. Since the Debye length is equal to the ratio of the electron thermal drift velocity to the natural plasma frequency, with $v_{\text{thermal}} = \sqrt{\frac{K_B T_e}{m}}$, we see that a warm plasma will have a shallower gradient at the boundaries than a cold plasma and hence the electron density profile will not follow the ion profile as closely.

The numerical procedure to obtain the self-consistent electron density profile consists of solving equation (8.6) across the ion ramp, subject to the boundary conditions (8.9) and (8.11). To the left of the ion ramp we obtain an analytic solution, determining the value of r_0 in equation (8.9) at the matching point. We solve equation (8.6)

by defining the family of equations,

$$\frac{\mathrm{d}^2\Phi}{\mathrm{d}r^2} = -8\pi^2\left(1+\epsilon K\right)^2\left(\frac{n_i}{2n_0} - \exp(\Phi)\right), \tag{8.12}$$

where $K = L/\lambda_D - 1$ and ϵ is a parameter which we vary between 0 and 1. We begin by solving the equation with $\epsilon = 0$ and use this solution as the estimate to the solution of the next equation in the family and so on until we have the solution of the equation with $\epsilon = 1$. To solve each of the equations in the family, we split the second order differential equation into a system of two first order equations. However, a linear decomposition results in a system which is very sensitive to perturbations as the following analysis will show. If we consider an equation of the type (8.12) and suppose that it has a solution Φ_0, then consider a small perturbation on the solution $\delta\Phi$ so that,

$$\Phi = \Phi_0 + \delta\Phi \tag{8.13}$$

we find,

$$\frac{\mathrm{d}^2\left(\delta\Phi\right)}{\mathrm{d}r^2} = 8\pi^2\left(1+\epsilon K\right)^2\exp(\Phi_0)\,\delta\Phi\ . \tag{8.14}$$

This shows that the behaviour of the perturbation is governed by a term which is proportional to the square of the ratio L/λ_D. Therefore, as we increase this ratio the solution at the right hand boundary, where Φ is small and negative, becomes increasingly sensitive to perturbations in the solution. This sensitivity limits the value of the parameter K for which a numerical solution of the equations (8.12) may be found. In this case, the maximum value of K was found to be 6 which still corresponds to a warm plasma ($K_B T_e > 8$KeV for $L = c/\omega$). However, the sensitivity of the system may be reduced if we anticipate the experimental component in the splitting of the second order equation into two first order equations. That is, we use

the relationships,

$$y_1 = \Phi \quad , \quad y_2 = \exp(\Phi)\frac{\mathrm{d}\Phi}{\mathrm{d}r} \tag{8.15}$$

to obtain the system,

$$\begin{aligned} \acute{y_1} &= \exp(-y_1)\, y_2 \\ \acute{y_2} &= \exp(-y_1)\, y_2^2 - \exp(y_1)\left(8\pi^2 (1+\epsilon K)^2 \left(\frac{n_i}{2n_0} - \exp(y_1)\right)\right) . \end{aligned} \tag{8.16}$$

The new boundary conditions are then,

$$\begin{aligned} \text{left:} \qquad & \exp(-y_1)\, y_2 - 4\pi(1+\epsilon K)\exp\left(\frac{y_1}{2}\right) = 0 \\ \text{right:} \qquad & \exp(y_1)\, y_2 - 4\pi(1+\epsilon K)\sqrt{\exp(y_1) - y_1 - 1} = 0 \end{aligned} \tag{8.17}$$

This scheme turns out in practice to be more stable than the previous decomposition. The practical limit on the value of K is now 12 which corresponds to a cooler plasma ($k_B T_e \sim 3$ KeV). We use this scheme, therefore to calculate the self-consistent electron density at a temperature of 3KeV and use the numerical solution in the initialisation routine of the code to position the particles accordingly.

The final significant modification that we make to the PIC code affects the treatment of particles approaching the boundaries of the cell. In its original form, the code simply reflects these particles by changing the sign of their velocities. However, this creates an artificial source of high energy particles in the simulations, so we modify the boundary conditions to achieve a more realistic treatment. Instead of reflecting particles when they reach the right hand boundary, we allow them to escape into the dense plasma and replace them with new particles at the boundary point with velocities assigned according to a half Maxwellian distribution. The velocity for each particle is assigned in the following way. First, we generate a random number n_1, in

the interval [0,1]. Then we use the mapping

$$P(v) = \frac{\mathrm{d}n}{\mathrm{d}v} \tag{8.18}$$

where $P(v)$ is the Maxwellian Distribution function and v is the velocity of the particle normalised to the electron thermal drift velocity. Integrating this relationship we obtain,

$$v = \sqrt{-2\ln(1-n)}\,. \tag{8.19}$$

Finally, we project this velocity onto the axis of the electron motion by multiplying by $\cos\left(\frac{\pi}{2} + n_2\pi\right)$, where n_2 is a second random number in [0,1] and the $\pi/2$ in the argument of the cosine function ensures that the velocity of the new particle is negative (since it enters the cell from the right).

8.2 Parameter Identification

In order to use the particle code to study the interaction described by our simple model in the previous chapter, we must identify the correspondence between the parameters in the two systems. We recall that the critical parameter in our simple model is the coefficient of the forcing term on the right hand side of the equation of motion. This is defined,

$$\langle \gamma \rangle = \frac{eE}{m\omega^2 L} .$$

In the particle code, we have the parameters e-capacitor and z-ramp defined by,

$$\text{e-capacitor} = \frac{eE}{m\omega c}$$

$$\text{z-ramp} = \frac{L\omega}{c},$$

so that,

$$\gamma = \frac{\text{e-capacitor}}{\text{z-ramp}} .$$

We conclude from this reconciliation of parameters that investigating the γ parameter space in our simple model should be equivalent to looking at the space of values of the ratio of e-capacitor to z-ramp in the particle code. We therefore begin our investigations using the PIC code by examining the effect of this ratio on the behaviour of the particles.

8.3 Results

We now present the results obtained with the various versions of the program. We begin with the code with the test-particle inserted, a linear electron density profile and no other modifications. Our original intention was to use this code to generate the numerical phase trajectories of the test-particle for comparison with our simple model in the similar parameter regime. In the previous section we have identified the correspondence between the parameters of the two models and so we start by considering a fixed ratio for e-capacitor/z-ramp in the code. Since our simple model shows (almost) linear behaviour for this ratio at $1 : 10^4$ we ran three cases for this value in the PIC code. Figure 8.1 shows the output at time $t = 5T_l$ for parameter values e-capacitor $= 2\pi \times 10^{-4}$ and z-ramp $= 2\pi$. This figure shows the bulk behaviour of the plasma via the phase plot of (v_z, z), the final electric field across the simulation grid and the density profile. We can see from these graphics that an electrostatic oscillation is excited around the critical surface as expected. Figure 8.1 also shows the phase trajectories of the test-particle. These suggest that the test-particle oscillates in the field at the critical surface with a drift into the body of the plasma due to the thermal drift velocity. This drift appears to prevent the particle oscillating on a closed trajectory. Figure 8.2 shows the output for the parameter values e-capacitor $= 4\pi \times 10^{-4}$ and z-ramp $= 4\pi$ at time $t = 10T_l$. The bulk quantities show that the plasma electrons around the critical surface oscillate resonantly with the electrostatic during field to produce a large localised field. The density profile now begins to show signs of modification around the critical surface. The phase trajectories, however, appear to show further evidence that the test-particle has a drift velocity. Figure 8.3 illustrates the behaviour at the later time $t = 20T_l$ for the parameters e-capacitor $= 8\pi \times 10^{-4}$ and z-ramp $= 8\pi$. Now the bulk quantities show that the resonant oscillation of the electrons has modified the density profile significantly producing a density spike in front of the critical surface. We also notice that the electrostatic

field across the density ramp is becoming asymmetric about the critical surface. This suggests that we might expect to see a nonlinear effect on the phase trajectories of the test-particle. However, the phase trajectories show that the test-particle drifts further into the body of the plasma, away from the critical surface, with no apparent nonlinear effect on the frequency of its motion. We note here that if we allow for a guiding centre moving into the plasma with some drift velocity, the motion of the test-particle becomes close to periodic as the simulation reaches its end. Figure 8.3 includes a surface plot of the electric field giving a time-history to the development of the field across the computational grid. We note here that as time progresses the peak of the field becomes more localised as the plasma electrons respond to the driving field and oscillate more energetically. From this first set of results we can see that the expected resonant response of the electrons is present and that after ~ 20 plasma periods the electrostatic field becomes asymmetric about the critical surface, which we would expect to have an effect on the electron dynamics around that point. However, the test-particle phase trajectories do not show the closed orbits we would like to observe. This is due, in part, to the drift velocity which is defined in this version of the code as a function of the length of the density ramp. The true single particle motion may also be masked by the 'zero-field' oscillation present when no electrostatic driving force is applied. This is due to the initial positioning of the linear electron density profile, which is not done in a self-consistent way, so that there is a residual electrostatic field. The modification to calculate a self-consistent electron density profile to match the linear ion ramp is intended to reduce the 'zero-field' oscillation. However, as we have seen in a previous section, the self-consistent profiles may only be calculated for electron temperatures $>$ 3KeV. Figure 8.4–8.7 show the effect of differing code and drift velocities on the test-particle phase trajectories. In each of the these figures, the values of e-capacitor and z-ramp are the same and the output is at time $t = 10T_l$. The difference between then lies in the number of mesh points across the simulation space, which also affects the definition of the thermal drift

velocity in the PIC code. We can see from these figures that the phase trajectories are completely different in each case. The behaviour in Figure 8.6 shows that the electron appears to be thrown out into the vacuum region.

If we continue our investigation of the behaviour at a fixed ratio of driver strength to ramp length of $1 : 10^3$ with differing defined thermal velocities in the code, we again obtain broadly consistent bulk behaviour but the phase trajectories are again unhelpful. Figure 8.8 shows the bulk properties for the simulation with e-capacitor $= 2\pi \times 10^{-3}$ and z-ramp$= 2\pi$ at time $t = 5T_l$. We can see that with the stronger relative driver the plasma oscillation is more energetic and we can already see evidence of density profile modification. Figure 8.9 shows the output for some ratio at time $t = 10T_l$. Now, the (v_z, z) phase plot shows the formation of high energy 'tails' of electrons with velocities directed towards the vacuum at the left hand side of the simulation cell. The phase plot in Figure 8.10, which illustrates the behaviour at time $t = 20T_l$, shows the formation of several high energy beams of electrons although some of these are artefacts produced by the reflecting boundary conditions in this version of the PIC code. Figure 8.10 also shows the time history of the electric field for the simulation and we can again see the resonant rise in the amplitude of the field at the critical surface. By the end of the simulation at time $t = 20T_l$ we can also see that the electrostatic field has become markedly asymmetric about the critical surface. This, again, suggests that some nonlinear electron dynamics may be expected, but due to the problems with the test-particle data we are unable to observe this directly. We recall from the previous chapter that the electron dynamics at different positions in the density profile may be markedly different. With this in mind, we present some Fourier decomposition spectra for the motion at various points in the profile. Figure 8.11 shows the decomposition for the motion excited with e-capacitor $= 2\pi \times 10^{-4}$ and z-ramp $= 2\pi$. The frequency components are normalised to the frequency of the driving field and the spectra are produced at positions $\frac{z}{\text{z-ramp}} = 1/over4, \frac{3}{8}, \frac{1}{2}, \frac{5}{8}, \frac{3}{4}$. We can see that each decomposition shows the

strongest component at the fundamental frequency and it is impossible to distinguish the presence of any sub harmonics due to the high noise level in the spectra. It is possible to identify harmonics at the critical surface. The high noise level in these spectra is a general feature of PIC codes [5]. Figure 8.12 shows the spectra generated for the ratio e-capacitor/z-ramp $= 1 \times 10^{-3}$. Again, harmonics may be observed at the critical surface but fine scale effects are swamped by the high level of noise.

In an attempt to obtain comparable results for the test-particle behaviour, we modify the PIC code to accept a given electron drift velocity, subject to a lower limit for numerical reasons [5], so that we can run each case under the same conditions. We now choose to set the electron temperature to 1KeV and we repeat our investigation for e-capacitor/z-ramp $=10^{-3}$. Figure 8.13 shows a representative output from the many simulation runs, at time $t = 100T_l$. The bulk properties are broadly similar to those presented previously and are not repeated here. The test-particle data however, shows some notable differences. The phase trajectories resemble those obtained in the previous chapter for chaotic particle motion, with the particle traversing a large part of the simulation region. Secondly, it is possible to generate a Fourier decomposition spectrum of the test-particle's motion over the time of the simulation. This spectrum shows the expected peak at the fundamental frequency and also a significant power in all the sub-harmonic frequencies. This type of spectrum is commonly associated with chaotic motion and may support the results in Chapter 7.

Self-Consistent Density Profiles

The results presented so far in this chapter use the original code's linear density profile for the plasma electrons. We now present some of the results obtained using a self-consistent electron density profile and compare them with those obtained using the linear ramp. In order to examine the behaviour of the system more closely, the output in the results that follow has been generated at eight equally-spaced intervals over a single period of the driving field. These snap-shot results allow us to see exactly

how the plasma electrons oscillate during the period of the laser field. A total of 30 sets of results have been generated for varying values of the parameters e-capacitor and z-ramp with the ratio of the two parameters in the range 1×10^{-3}–1×10^{-2}. As mentioned earlier, the numerical limitation on the routine to solve for the self-consistent electron density profile means that the lowest electron temperature for which we may generate results is 3KeV. The results generated for the 30 different combinations of input parameters show similar bulk plasma behaviour for the same ratio of the parameters. To avoid repetition therefore, we will present just two sets of results here.

The first set of results that we present are for the parameter ratio $\frac{\text{e-capacitor}}{\text{z-ramp}} = 1 \times 10^{-3}$ with an electron temperature $T_e = 3\text{KeV}$. For comparison with the results from the self-consistent profile simulations, Figures 8.14–8.16 show the bulk quantities and the time history of the electric field at times $t = 10T_l, 10.5T_l$ and $11T_l$ respectively. We notice that these results indicate that the plasma oscillation has the same period as the driving field, since the output in Figures 8.14 and 8.16 is very similar and the output in Figure 8.15 shows the electric field across the density profile to be 180° out of phase with the fields shown in Figures 8.14 and 8.16. We also notice in the phase space analysis that some electrons which should escape into the vacuum are reflected by the artificial left hand boundary condition to produce spurious high energy electron beams in the simulation. Figures 8.17–8.19 show the bulk behaviour obtained using the self-consistent electron density profile and Maxwellian boundary conditions mentioned earlier in this chapter. It is immediately obvious that these results are markedly different from those obtained with the linear profile. The phase space plots show an incredibly detailed structure with roughly equal numbers of electrons having large positive and negative velocities. The application of the Maxwellian boundary conditions has eliminated the artificial electron beams produced in Figures 8.14–8.16. It is a great deal more difficult to attempt to identify any periodicity from the output in Figures 8.17–8.19. The difference between the two sets of results

is also shown in the Fourier decomposition of the long time runs. Figures 8.20 and 8.21 show the Fourier decomposition of the electron dynamics at various positions in the linear and self-consistent density profiles respectively for data sampled over 1ps of interaction time. In Figure 8.20 the motion is strongly periodic at all points in the profile and is more strongly periodic around the critical surface ($z/z - ramp = 0.5$). Figure 8.21 shows a strong component at the fundamental frequency, but the noise level is around four orders of magnitude higher than in Figure 8.20. We may also distinguish higher harmonics in the second Fourier decomposition. The two sets of output suggest rather different electron dynamics. The linear ramp results suggest a periodic electron oscillation due to the behaviour of the electric field over time. However, the results generated using the self-consistent electron profile suggest that the electron motion is chaotic due to the highly structured phase plot and the broad-band noise frequency spectrum.

The second set of results we present are for the ratio $\frac{\text{e-capacitor}}{\text{z-ramp}} = 1 \times 10^{-2}$, again with an electron temperature of 3KeV. Figures 8.22–8.24 show the bulk quantities and the time history of the electric field at times $t = 10T_l, 10.5T_l$ and $11T_l$. As in the previous case, the results in Figures 8.22 and 8.24 share many similarities. In particular, the electric field across the density profile is in the same phase in each of these figures. The electric field in Figure 8.23 again appears to be 180° out of phase with the field in the two other figures. This suggests that the bulk behaviour of the plasma electrons is periodic with a period equal to the period of the driving field. Snap-shots of the bulk quantities at times $t = 10.25T_l$ and $t = 10.75T_l$ for the same parameter values are given in Figures 8.25 and 8.26 and, together with Figures 8.22–8.24, they allow the reader to construct an idea of the dynamics of the system over a period. Next, we present the results obtained for the same values of e-capacitor, z-ramp and vthermal using a linear electron density profile with the Maxwellian boundary conditions. The results shown in Figures 8.27–8.29 show the effect of changing the boundary condition. The bulk phase plot shows that there

are electrons present in the system with a wider distribution of velocities. This is due to the random 1/2-Maxwellian velocity distribution of the electrons which are 'injected' at the right hand boundary to replace the escaping electrons. The majority of the particles in the simulation, however, do not cross the right hand cell boundary and they form similar momentum distributions to the observed in Figures 8.22–8.24. We notice also that the periodicity in the bulk quantities evident in Figures 8.22–8.23 is not as clear in Figures 8.27–8.29. This time, the structure of the phase plots at times $t = 10T_l$ and $t = 11T_l$ show a similar distribution of particles. The electric field across the cell and the electron density profile are also almost identical at the two times. However, the electric field at time $t = 10.5T_l$ is not 180° out of phase with the field at the earlier and later times. A further study over two periods of the driving field with eight snap-shot samples per period failed to identify any field in antiphase with that shown in Figures 8.27–8.29. The results generated for the bulk quantities using a self-consistent electron density gradient are given in Figures 8.30–8.32 at times $t = 10T_l, 10.5T_l$ and $t = 11T_l$. These results are similar to those in Figures 8.27–8.29, the main difference being the distribution of the lower energy electrons as demonstrated in the phase plots. In an attempt to identify the character of the electron dynamics in these results, the electron motion at equally spaced intervals in the density profile was Fourier analysed over 1ps. Figures 8.33 and 8.34 show the resulting spectra for the linear and self-consistent profiles respectively. In each case, we see that the strongest component in the electron motion is at the fundamental frequency and a number of harmonic frequency components may be observed in the electron oscillation in the underdense plasma. In each spectrum at the critical surface, we may detect a small component at one half the fundamental frequency. However, the power in this mode of oscillation is only slightly above the background noise level and we are therefore unable to confirm a subharmonic observation.

8.4 Summary

In this chapter we have presented an account of the modifications made to a simple one dimensional electrostatic particle-in-cell simulation code to enable the study of the response of the plasma electrons in a density gradient to an electrostatic field. We have also presented the results obtained from the various versions of this computer code. The results from our simulations remain inconclusive. We have observed behaviour in the bulk plasma quantities which suggests that the electron motion is periodic in the parameter regime $1 \times 10^{-3} \leq \frac{\text{e-capacitor}}{\text{z-ramp}} \leq 1 \times 10^{-2}$. However, the particle simulation generates too much numerical noise to allow a reliable Fourier decomposition of the motion of a test particle at the critical surface. In the case of the self-consistent electron density profile, a numerical limitation in the method used to calculate the profiles places a lower limit of 3KeV on the electron temperature. We are therefore unable to study interactions with electron temperatures of the order 1KeV with these profiles. The thermal effects on the Maxwellian boundary condition for the self-consistent profiles introduce a high degree of thermalisation in the simulations which may destroy any periodicity.

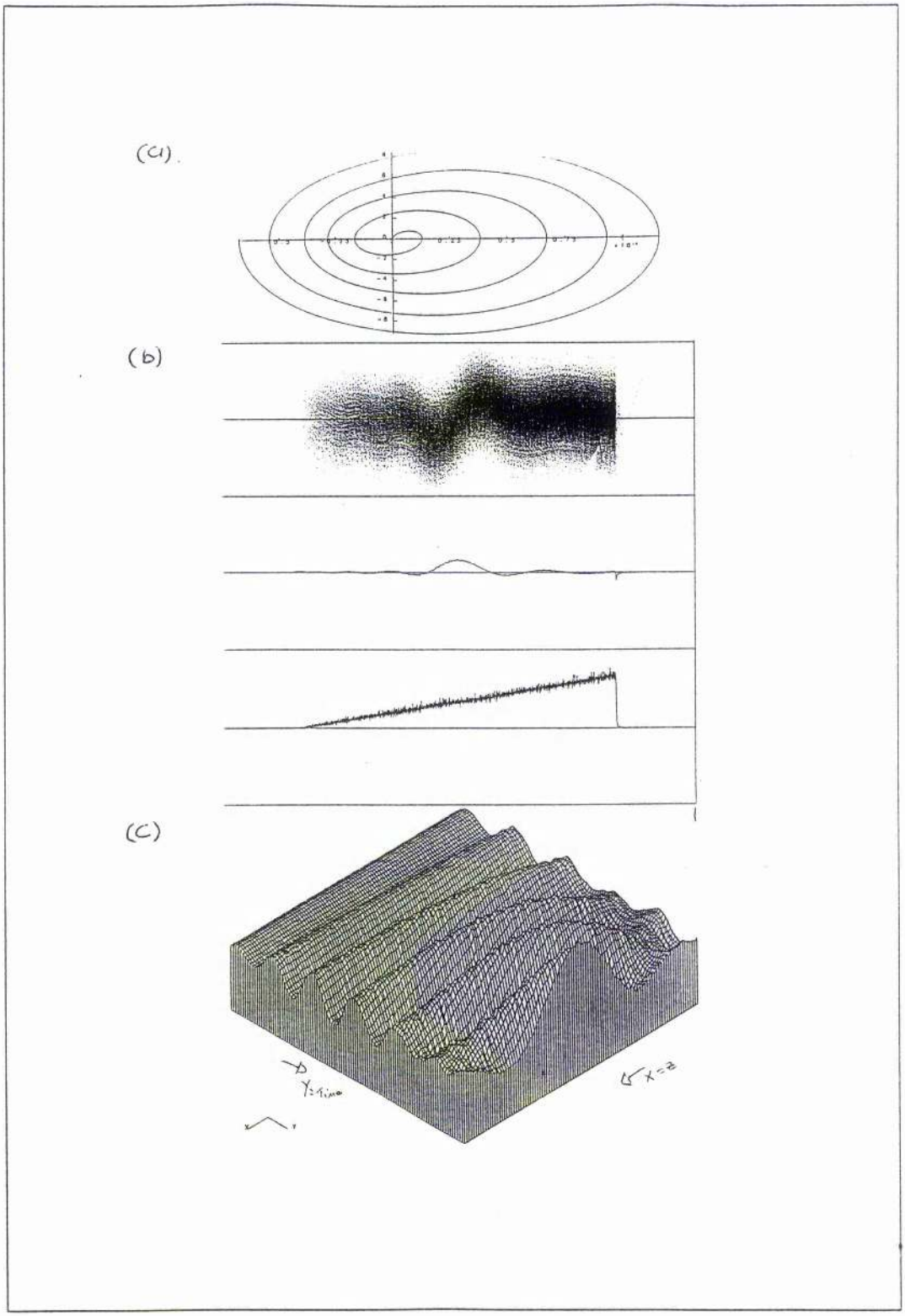

Figure 8.1: The test particle trajectories, bulk plasma quantities and electric field time history for the values e-capacitor $= 2\pi \times 10^{-4}$ and z-ramp $= 2\pi$ at time $t = 5T_l$. (a) shows the test particle trajectories; (b) shows the bulk plasma quantities - the (z, v_z) phase space, the electric field across the simulation grid and the electron density profile respectively; (c) shows the electric field time history with time increasing to the right and position increasing out of the page.

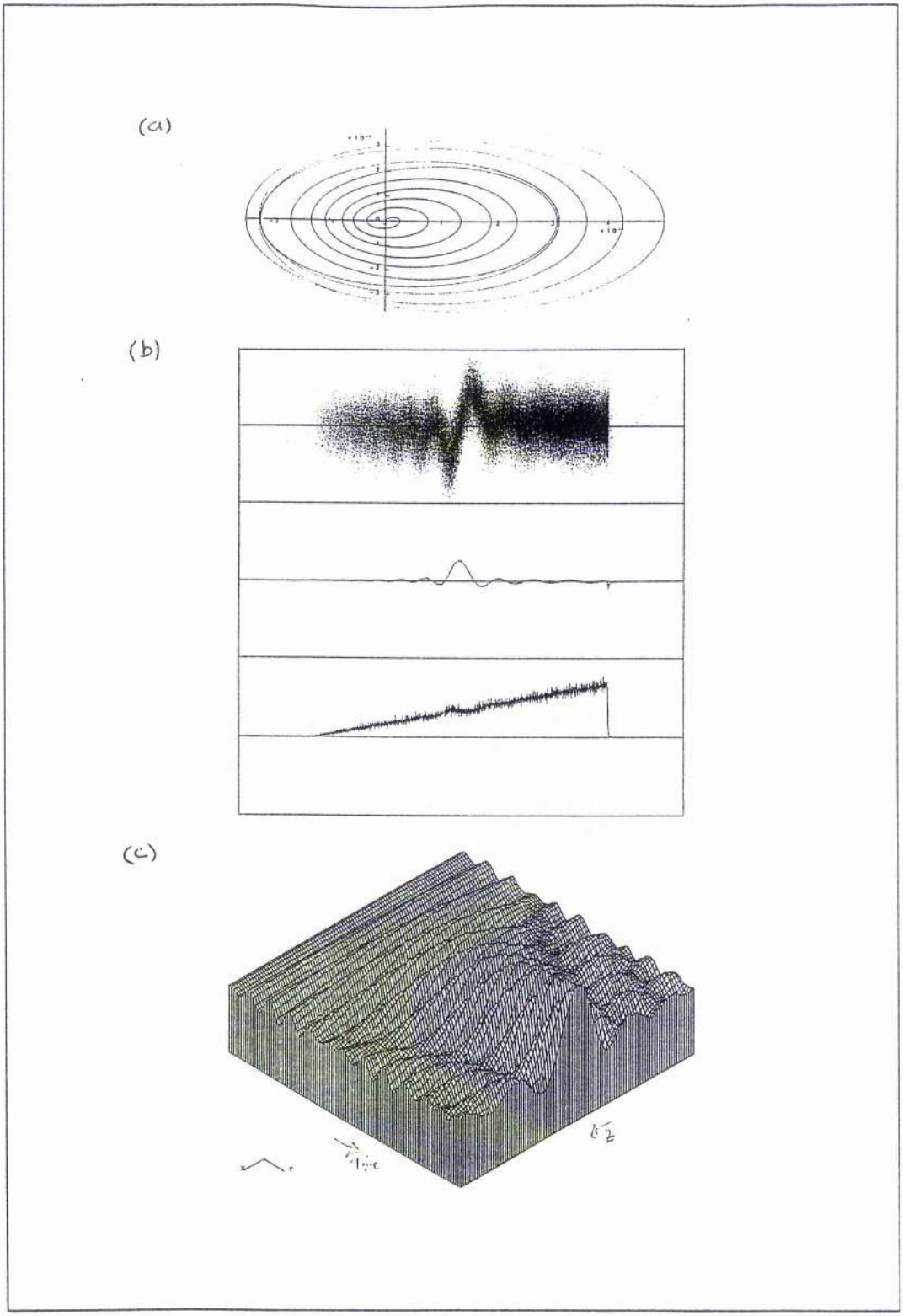

Figure 8.2: The test particle trajectories, bulk plasma quantities and electric field time history for the values e-capacitor $= 4\pi \times 10^{-4}$ and z-ramp $= 4\pi$ at time $t = 10T_l$. (a) shows the test particle trajectories; (b) shows the bulk plasma quantities - the (z, v_z) phase space, the electric field across the simulation grid and the electron density profile respectively; (c) shows the electric field time history with time increasing to the right and position increasing out of the page.

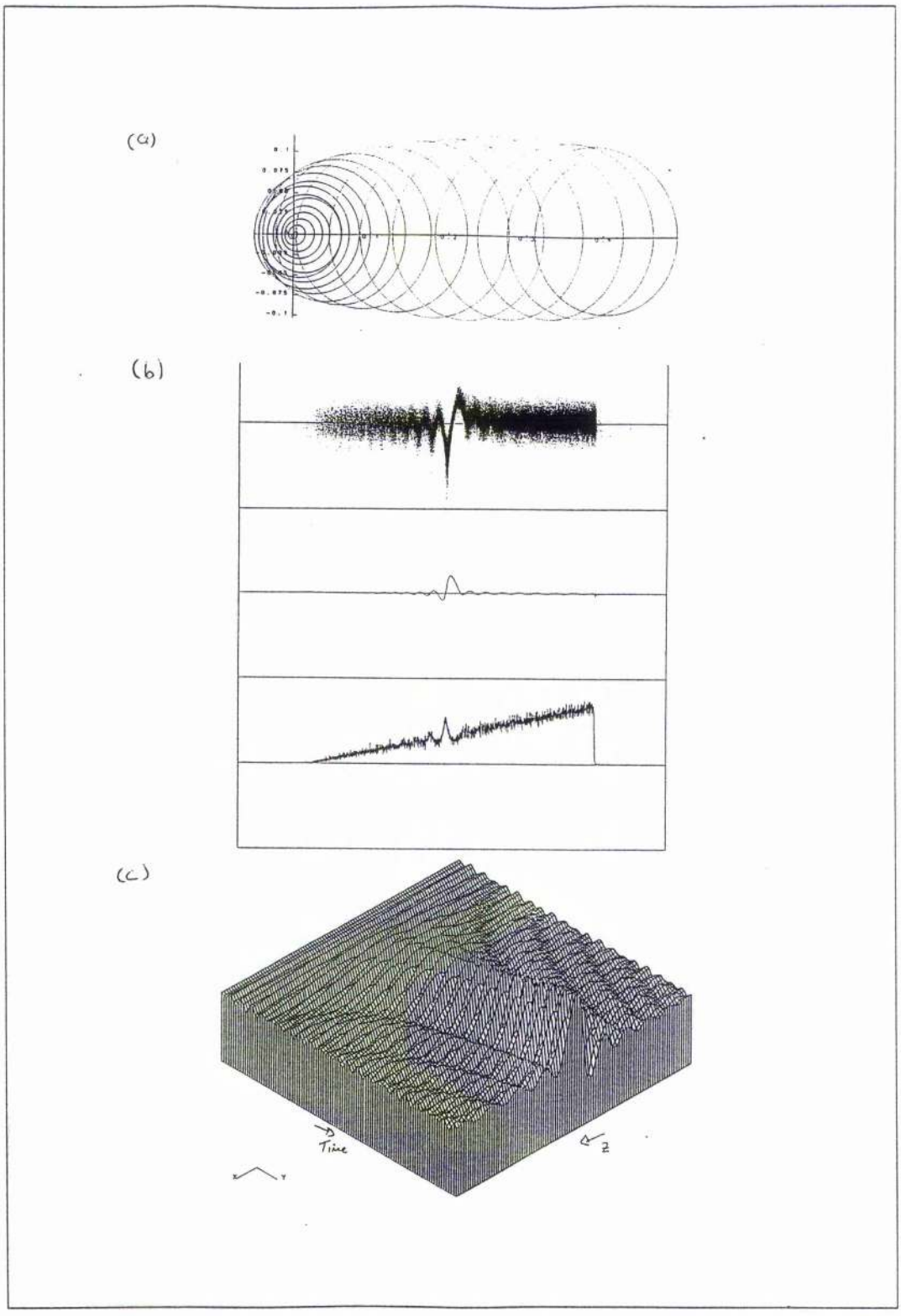

Figure 8.3: The test particle trajectories, bulk plasma quantities and electric field time history for the values e-capacitor = $8\pi \times 10^{-4}$ and z-ramp = 8π at time $t = 20T_l$. (a) shows the test particle trajectories; (b) shows the bulk plasma quantities - the (z, v_z) phase space, the electric field across the simulation grid and the electron density profile respectively; (c) shows the electric field time history with time increasing to the right and position increasing out of the page.

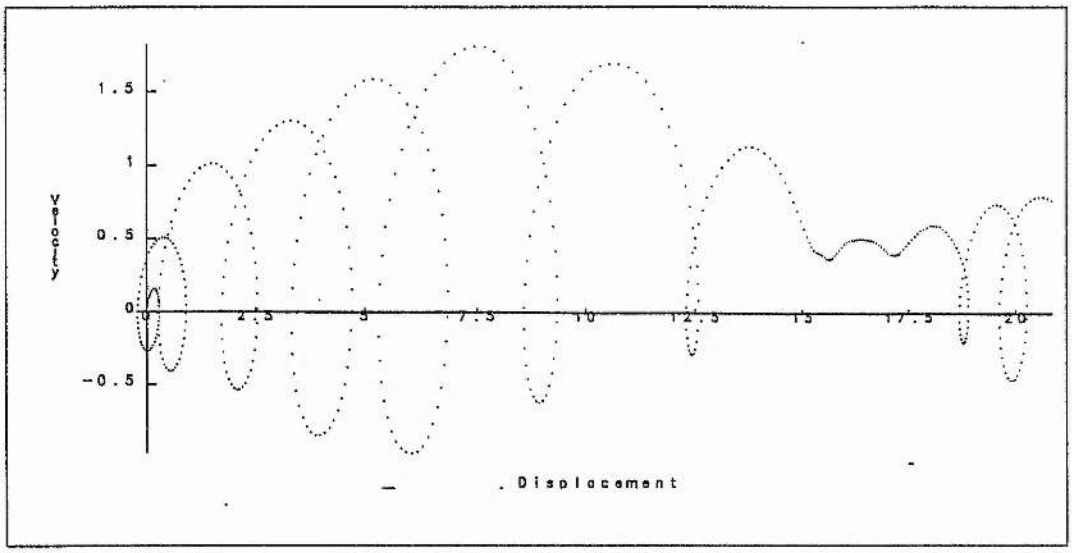

Figure 8.4: The test particle phase trajectories generated for the parameter values e-capacitor = 0.1 and z-ramp = 40π with 1500 grid points over the computational box.

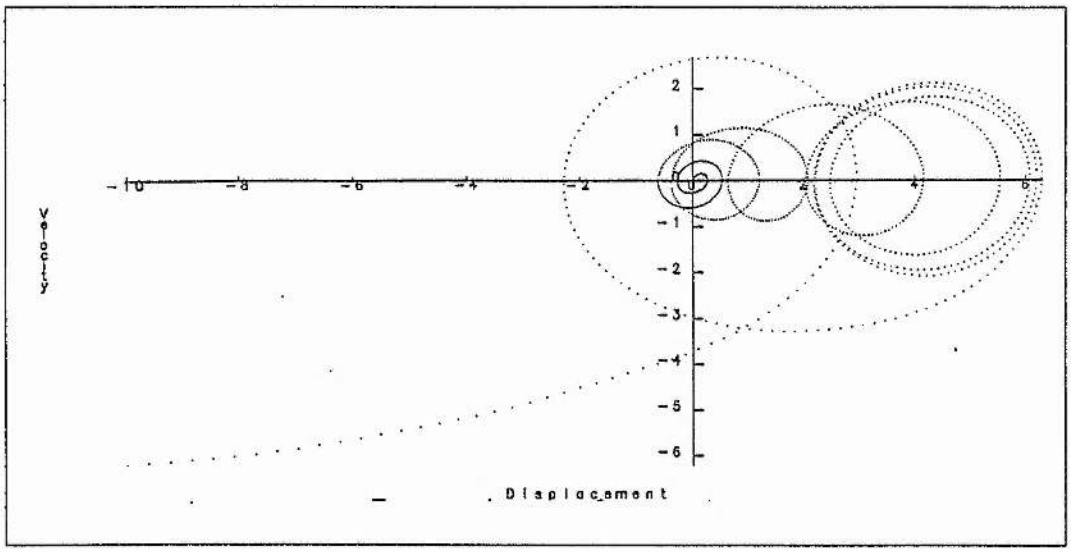

Figure 8.5: The test particle phase trajectories generated for the parameter values e-capacitor = 0.1 and z-ramp = 40π with 3000 grid points over the computational box at time $t = 10T_l$.

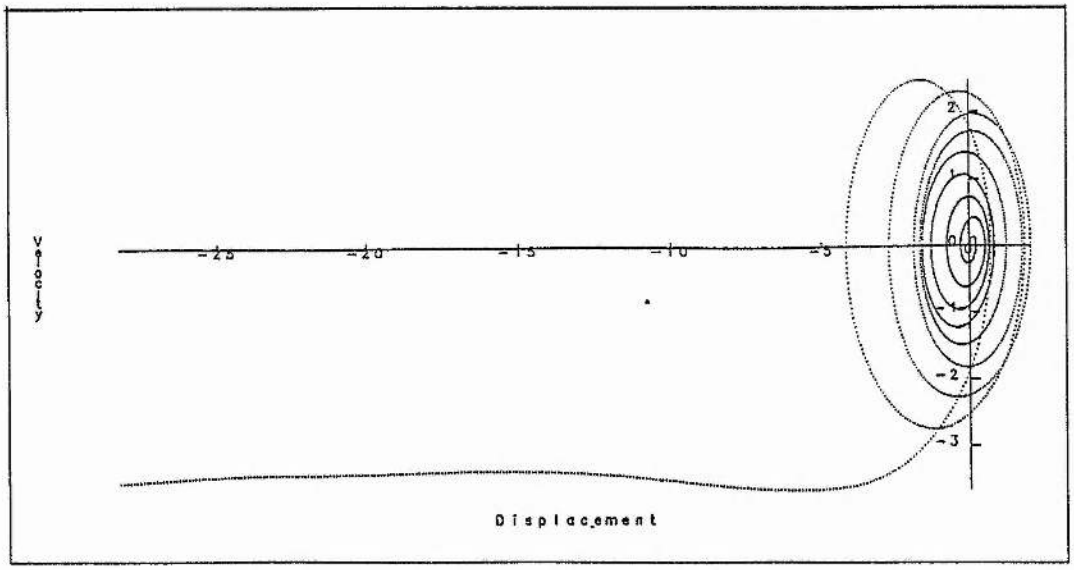

Figure 8.6: The test particle phase trajectories generated for the parameter values e-capacitor $= 0.1$ and z-ramp $= 40\pi$ with 6000 grid points over the computational box at time $t = 10T_l$.

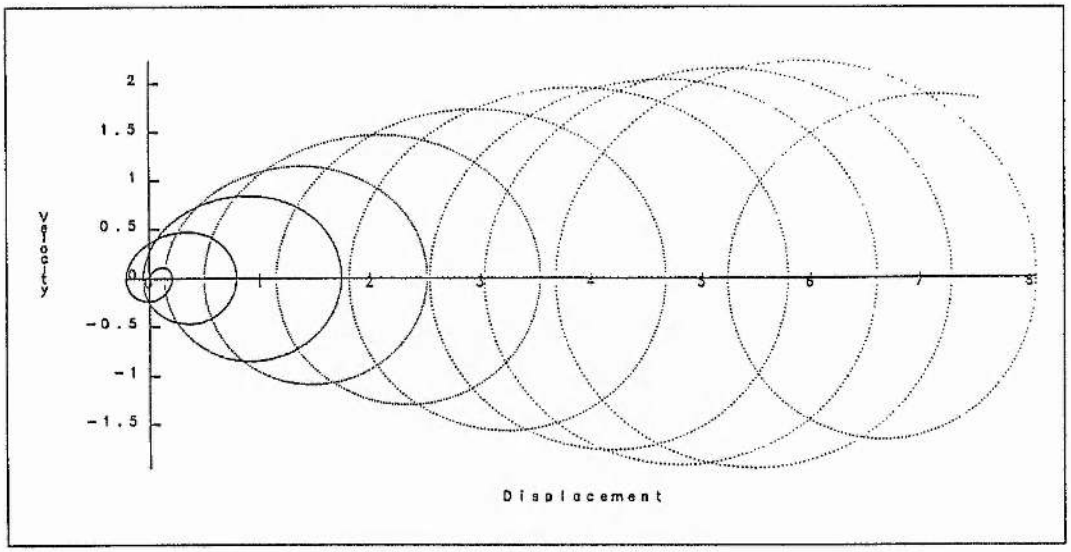

Figure 8.7: The test particle phase trajectories generated for the parameter values e-capacitor = 0.1 and z-ramp = 40π with 9000 grid points over the computational box at time $t = 10T_l$.

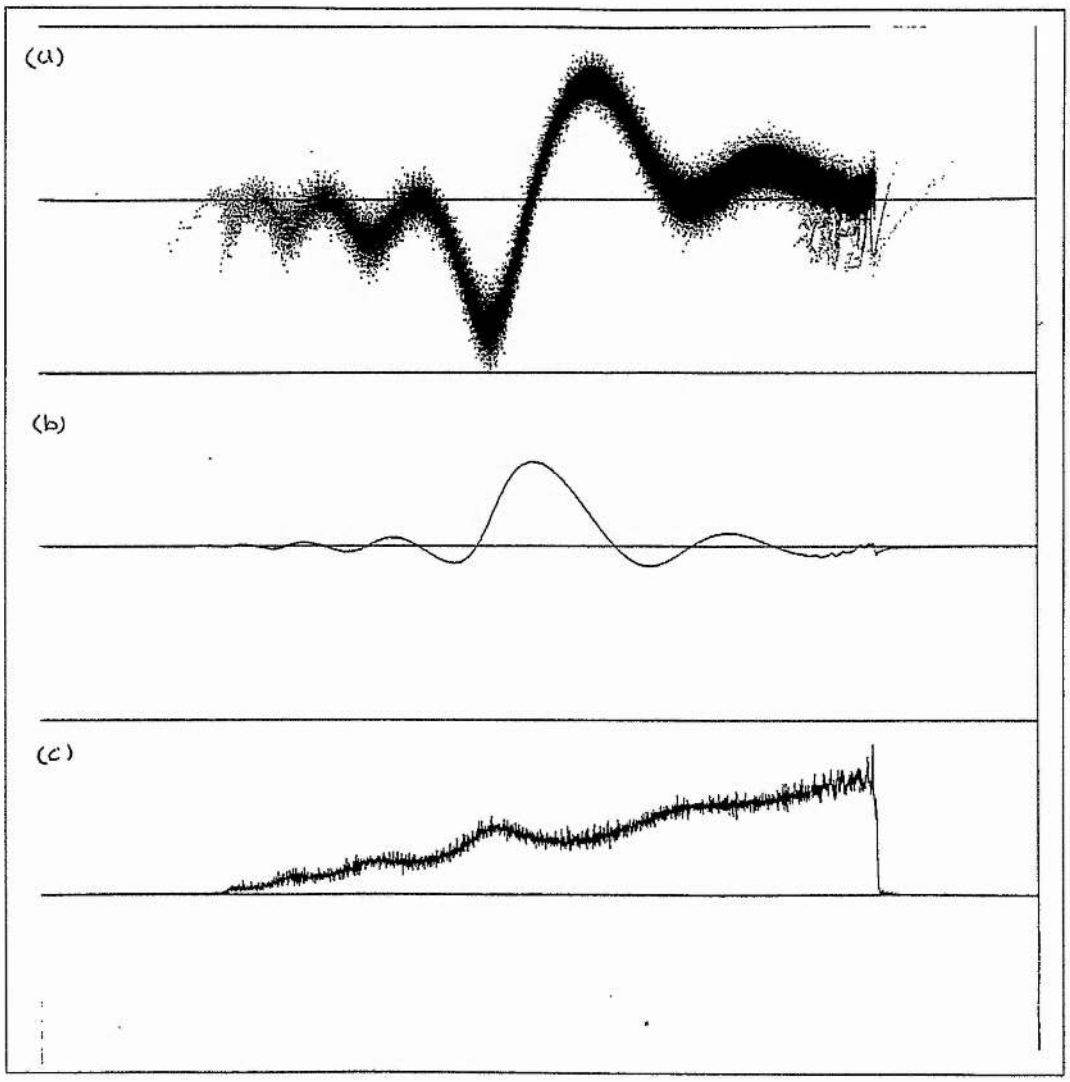

Figure 8.8: The bulk plasma quantities for the parameter values e-capacitor $= 2\pi \times 10^{-3}$ and z-ramp $= 2\pi$ at time $t = 5T_l$. (a) shows the (z, v_z) phase space; (b) shows the electric field across the simulation grid and (c) shows the electron density profile.

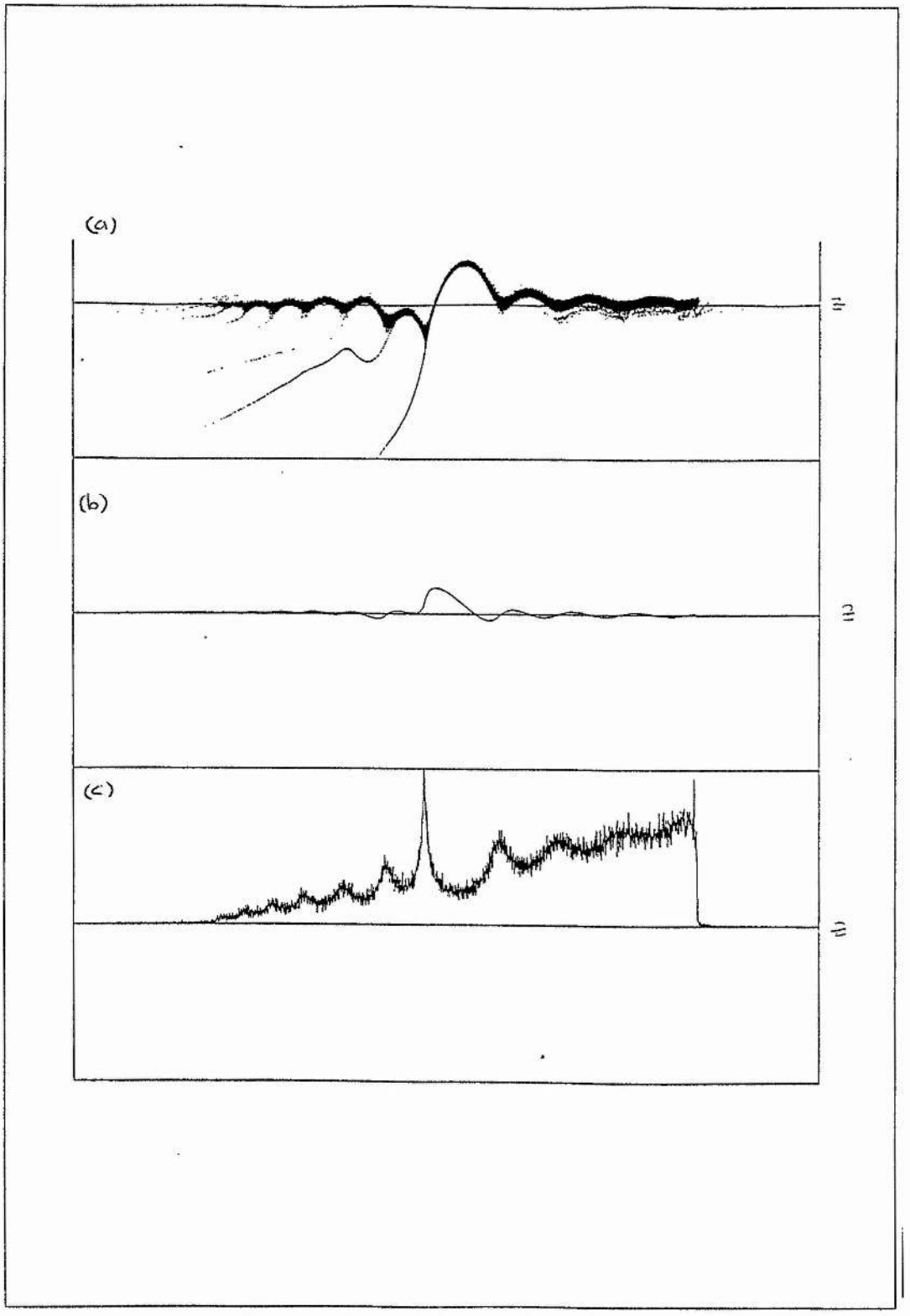

Figure 8.9: The bulk plasma quantities for the parameter values e-capacitor $= 4\pi \times 10^{-3}$ and z-ramp $= 4\pi$ at time $t = 10T_i$. (a) shows the (z, v_z) phase space; (b) shows the electric field across the simulation grid and (c) shows the electron density profile.

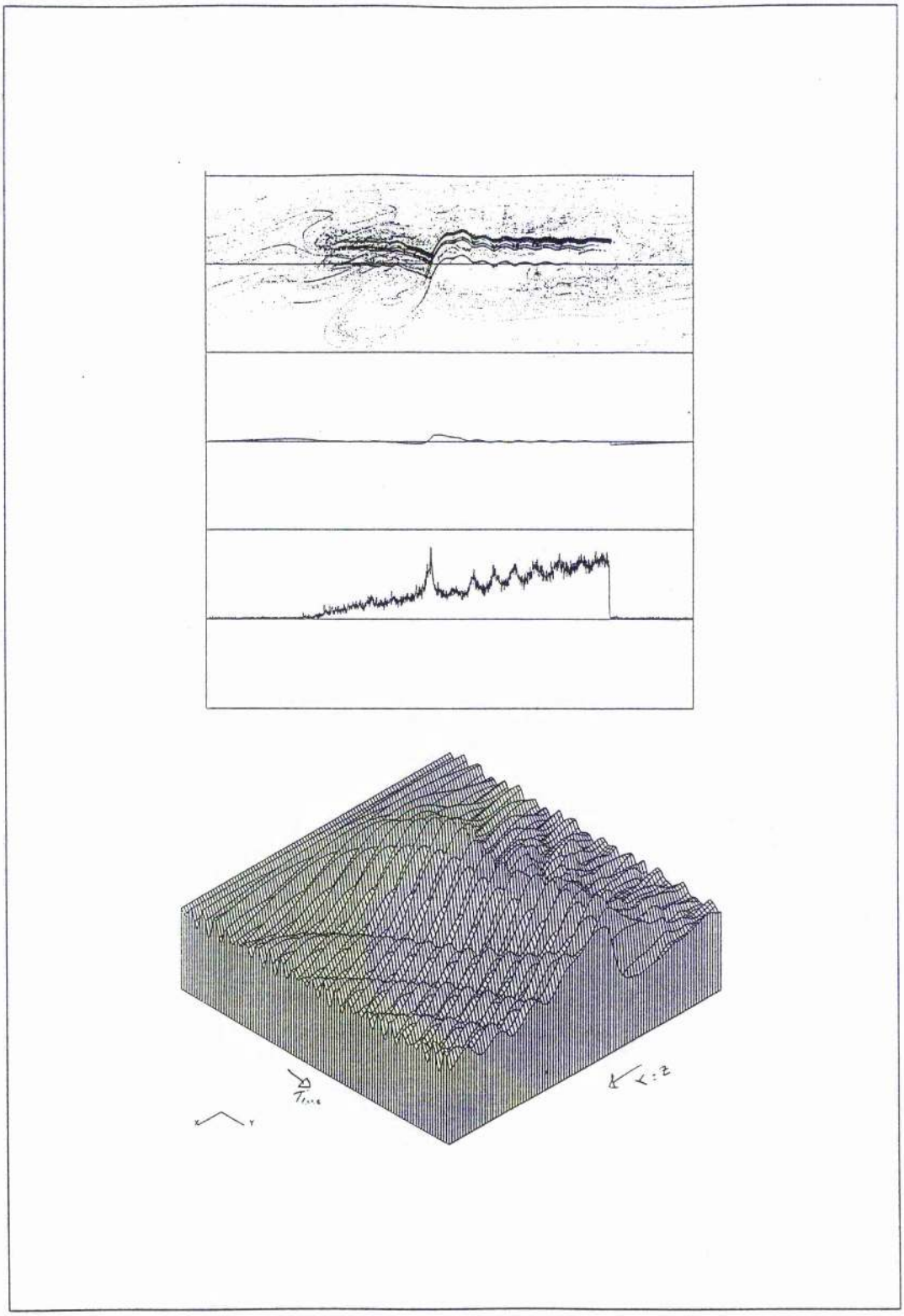

Figure 8.10: The bulk plasma quantities and the time history of the electric field for the parameter values e-capacitor $= 8\pi \times 10^{-3}$ and z-ramp $= 8\pi$ at time $t = 20T_l$. (a) shows the bulk plasma quantities - the (z, v_z) phase space, the electric field across the simulation grid and the electron density profile respectively; (b) shows the electric field time history with time increasing to the right and position increasing out of the page.

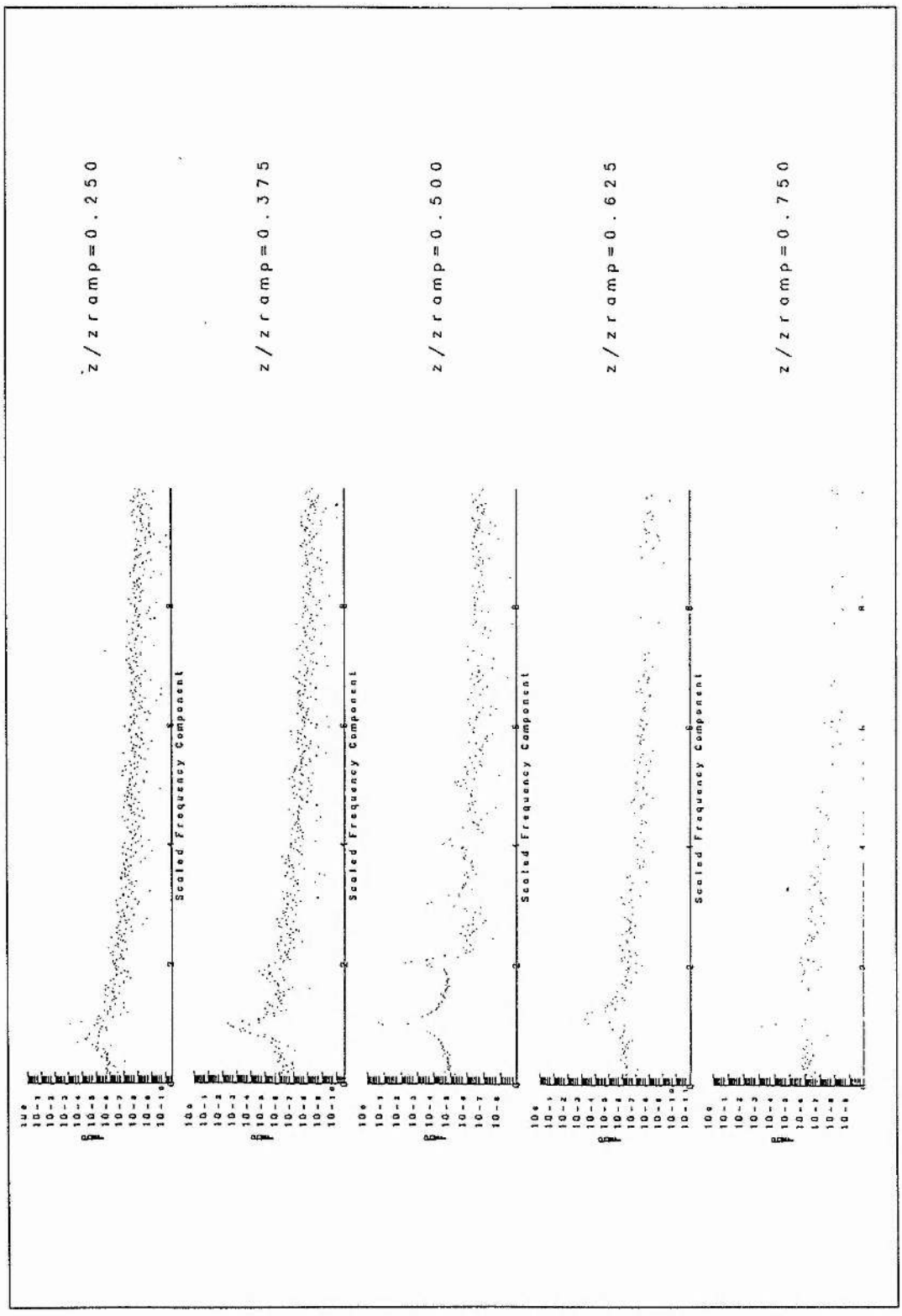

Figure 8.11: The Fourier decomposition of the electron motion at equally spaced intervals in the density profile for parameter values e-capacitor $= 2\pi \times 10^{-4}$ and z-ramp $= 2\pi$.

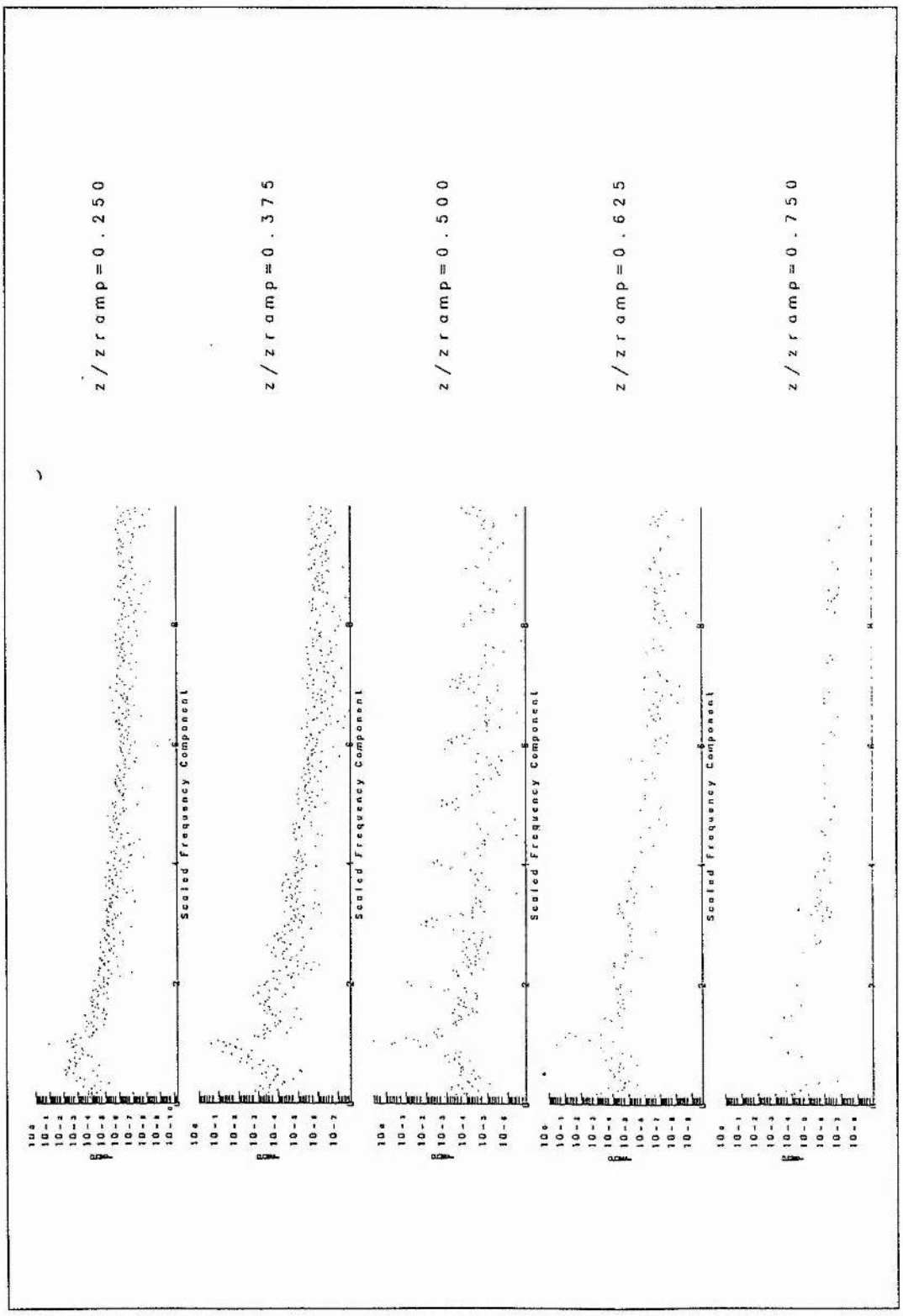

Figure 8.12: The Fourier decomposition of the electron motion at equally spaced intervals in the density profile for the parameter ratio $\frac{\text{e-capacitor}}{\text{z-ramp}} = 1 \times 10^{-3}$.

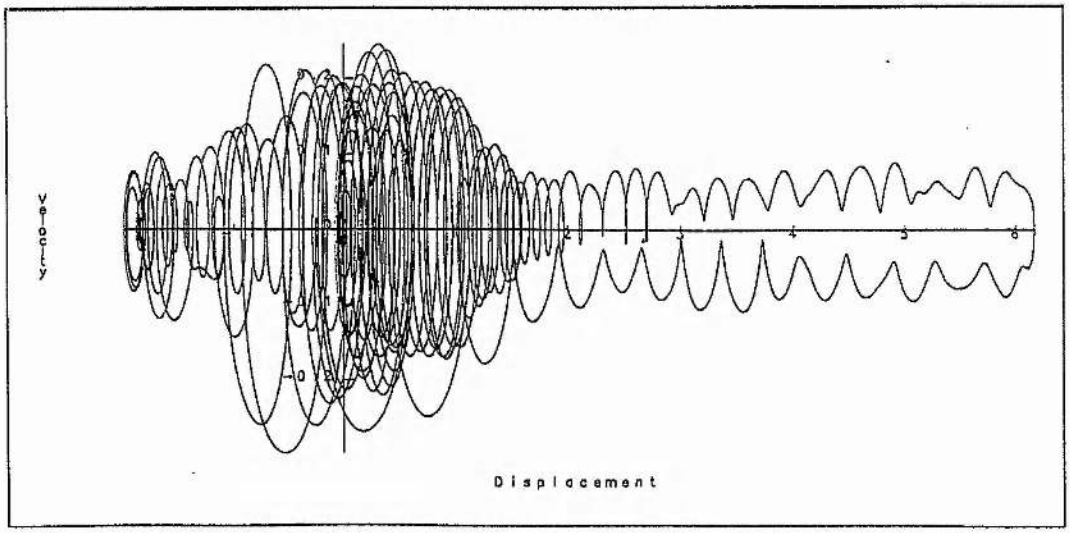

Figure 8.13: The test particle phase trajectories generated for the parameter values e-capacitor $= 4\pi \times 10^{-3}$ and z-ramp $= 4\pi$ at time $t = 100T_i$.

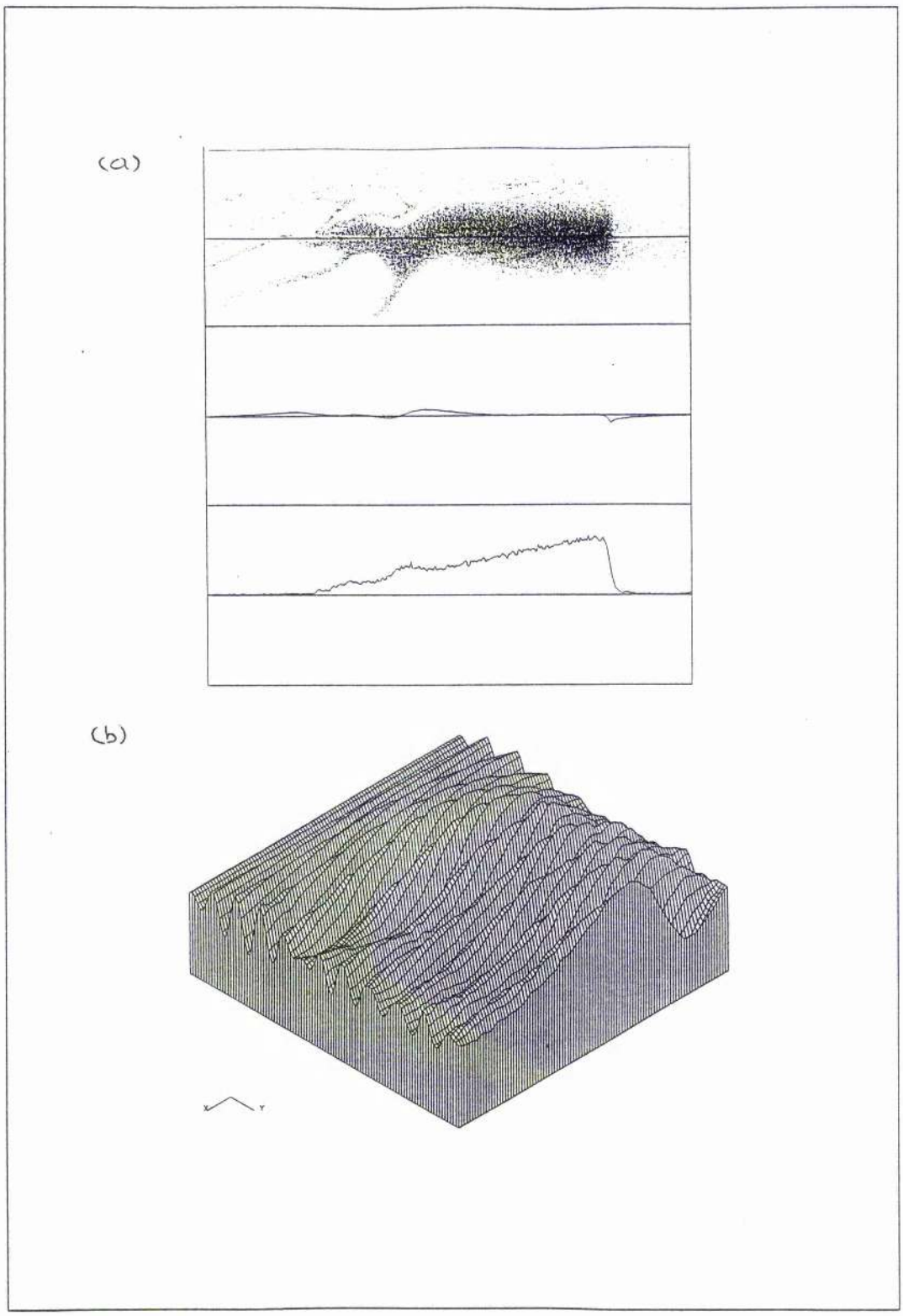

Figure 8.14: Results generated using a linear electron density profile for the parameter values e-capacitor $= 2\pi \times 10^{-3}$ and z-ramp $= 2\pi$ at time $t = 10T_l$. (a) shows the bulk plasma quantities - the (z, v_z) phase space, the electric field across the simulation grid and the electron density profile respectively; (b) shows the electric field time history with time increasing to the right and position increasing out of the page.

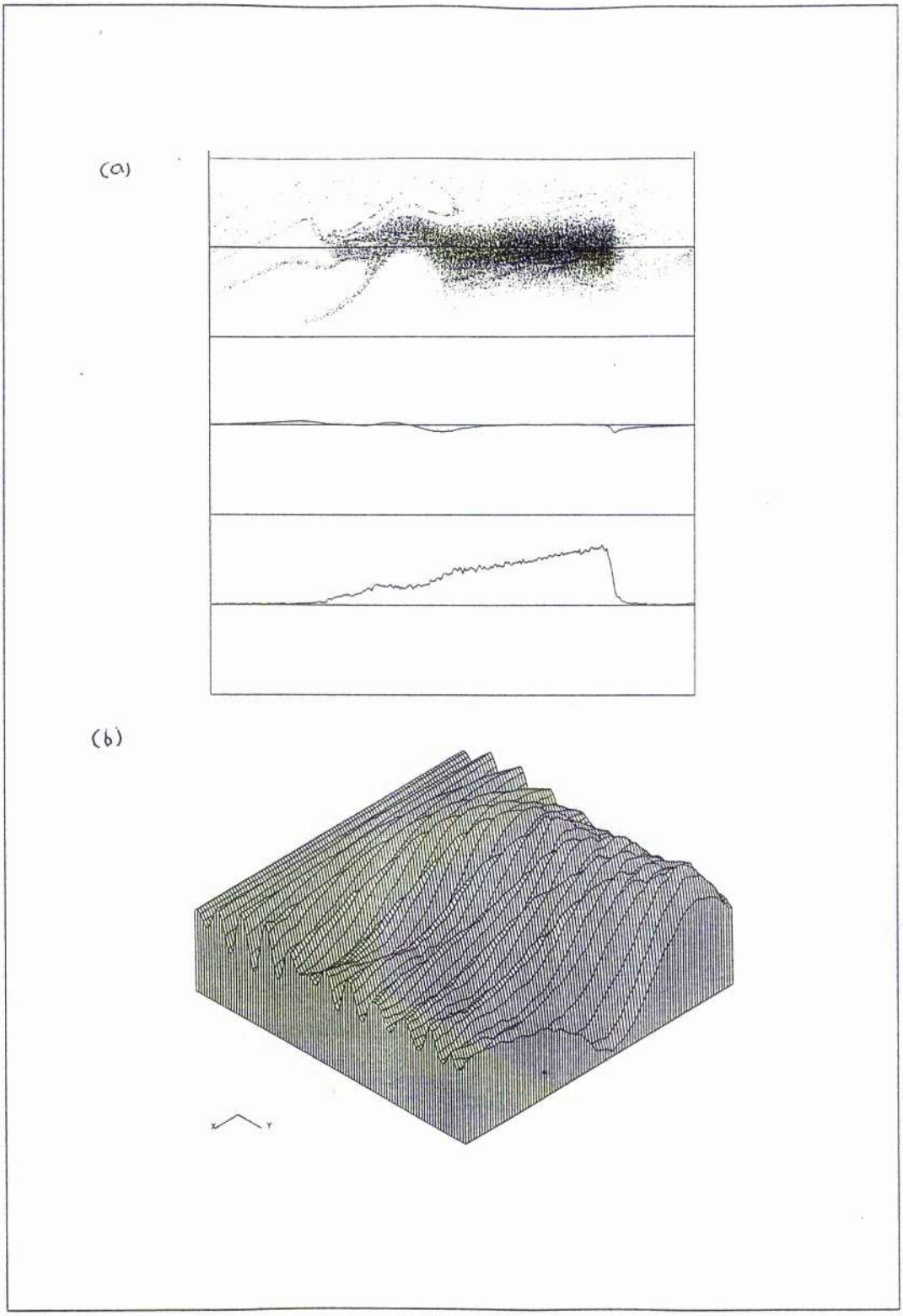

Figure 8.15: Results generated using a linear electron density profile for the parameter values e-capacitor $= 2\pi \times 10^{-3}$ and z-ramp $= 2\pi$ at time $t = 10.5T_l$. (a) shows the bulk plasma quantities - the (z, v_z) phase space, the electric field across the simulation grid and the electron density profile respectively; (b) shows the electric field time history with time increasing to the right and position increasing out of the page.

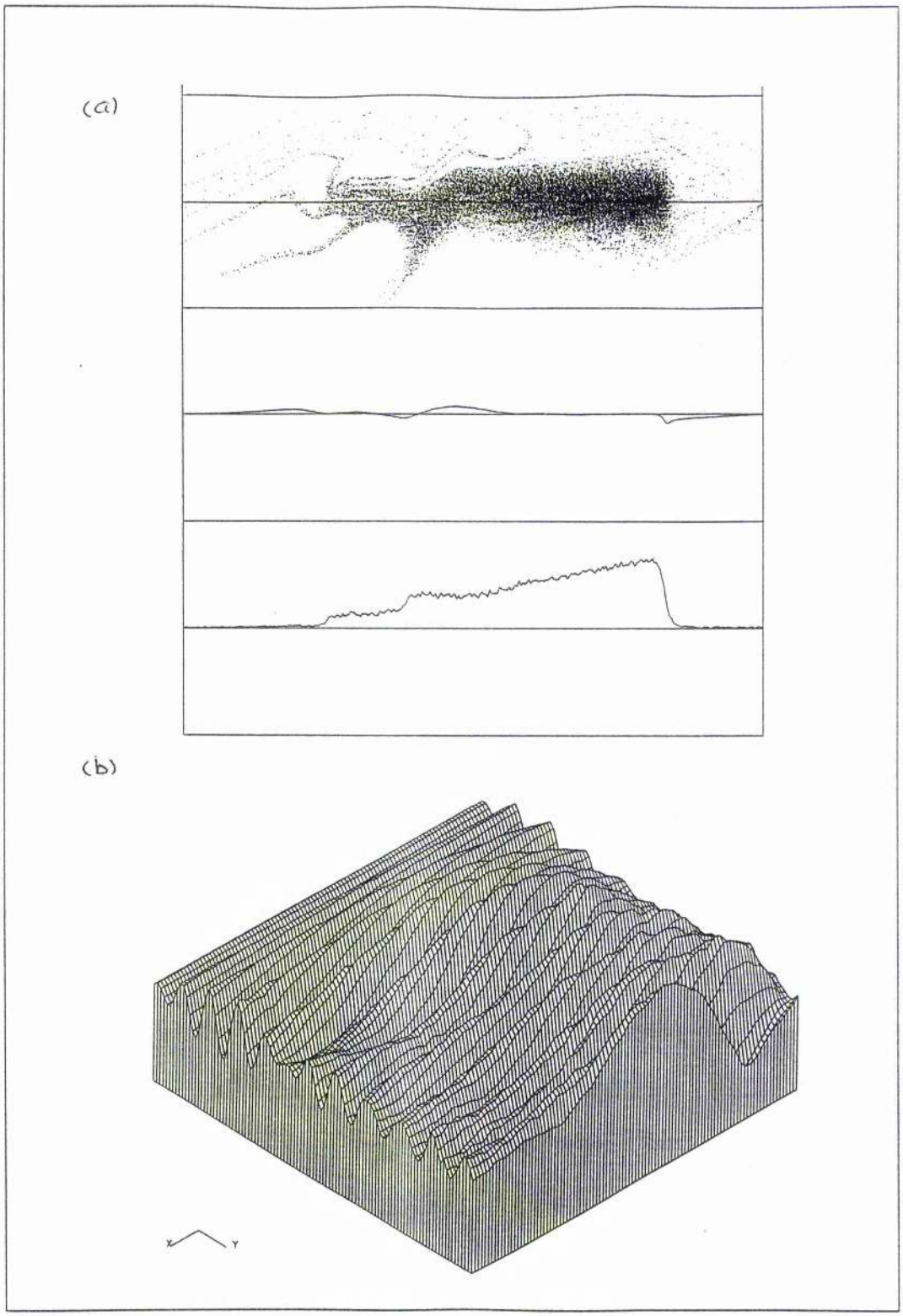

Figure 8.16: Results generated using a linear electron density profile for the parameter values e-capacitor $= 2\pi \times 10^{-3}$ and z-ramp $= 2\pi$ at time $t = 11T_l$. (a) shows the bulk plasma quantities - the (z, v_z) phase space, the electric field across the simulation grid and the electron density profile respectively; (b) shows the electric field time history with time increasing to the right and position increasing out of the page.

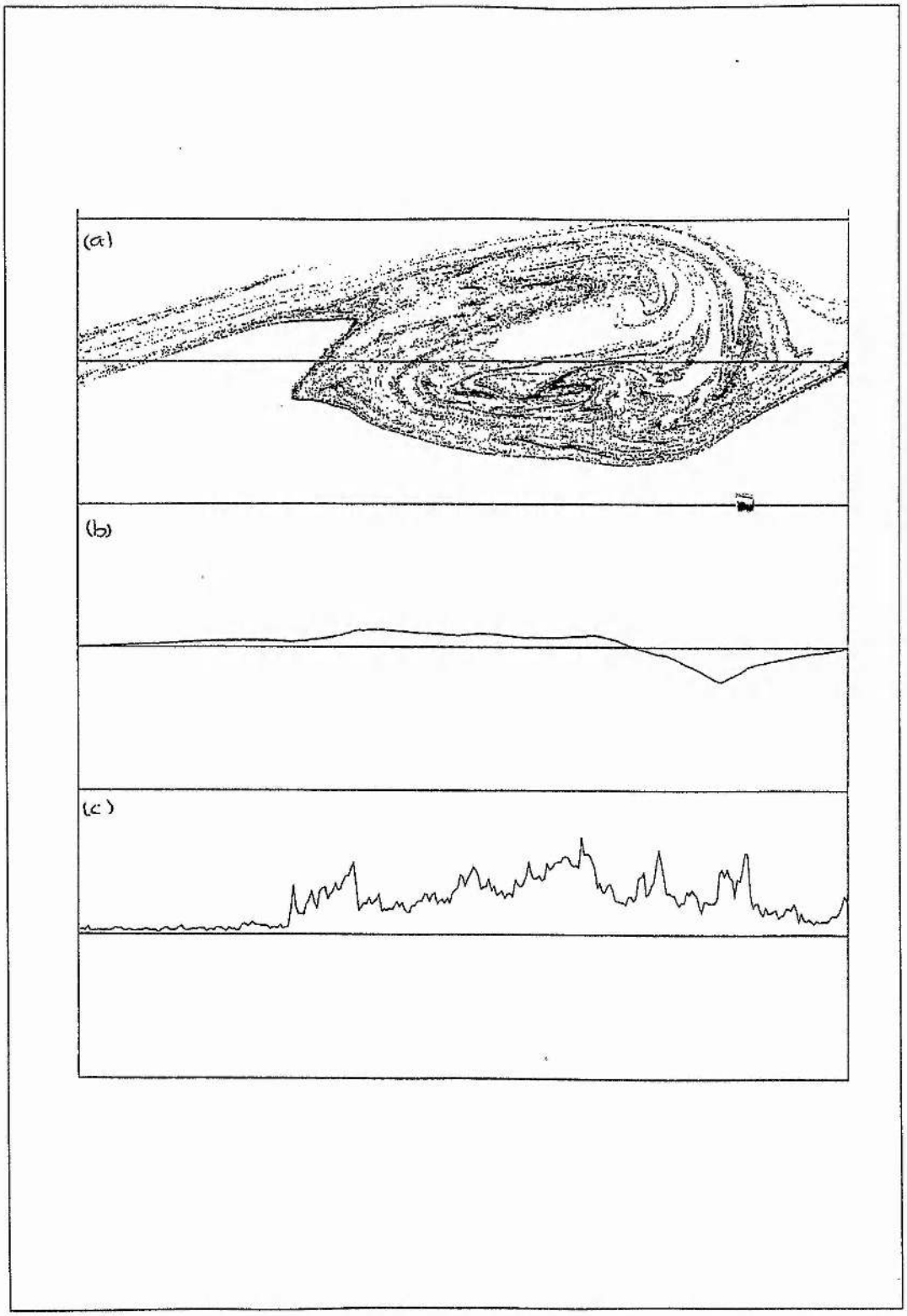

Figure 8.17: Results generated using the self-consistent electron density profile and the Maxwellian boundary condition for the parameter values e-capacitor $= 2\pi \times 10^{-3}$ and z-ramp $= 2\pi$ at time $t = 10T_l$. (a) shows the (z, v_z) phase space; (b) shows the electric field across the simulation grid and (c) shows the electron density profile.

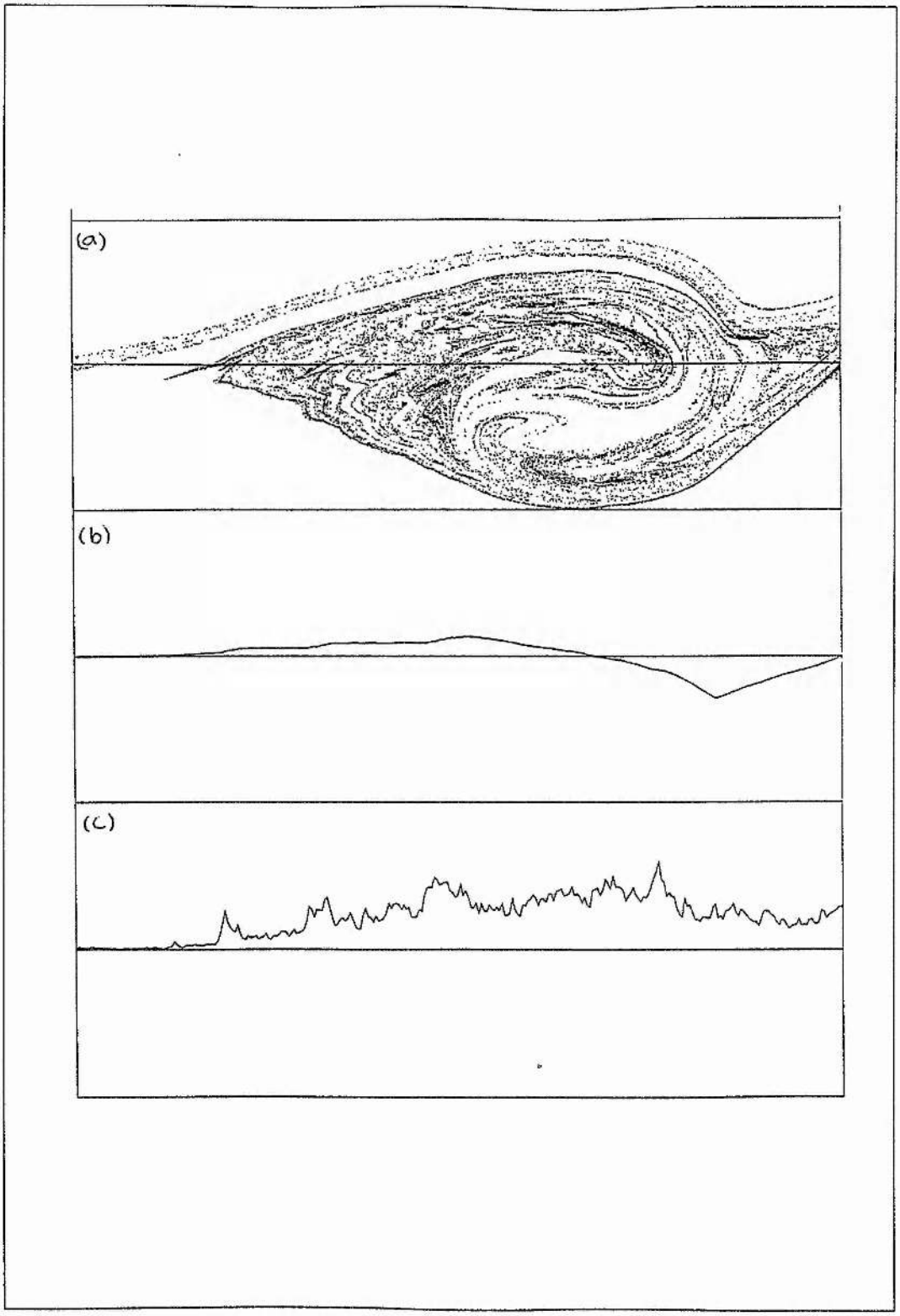

Figure 8.18: Results generated using the self-consistent electron density profile and the Maxwellian boundary condition for the parameter values e-capacitor $= 2\pi \times 10^{-3}$ and z-ramp $= 2\pi$ at time $t = 10.5T_l$. (a) shows the (z, v_z) phase space; (b) shows the electric field across the simulation grid and (c) shows the electron density profile.

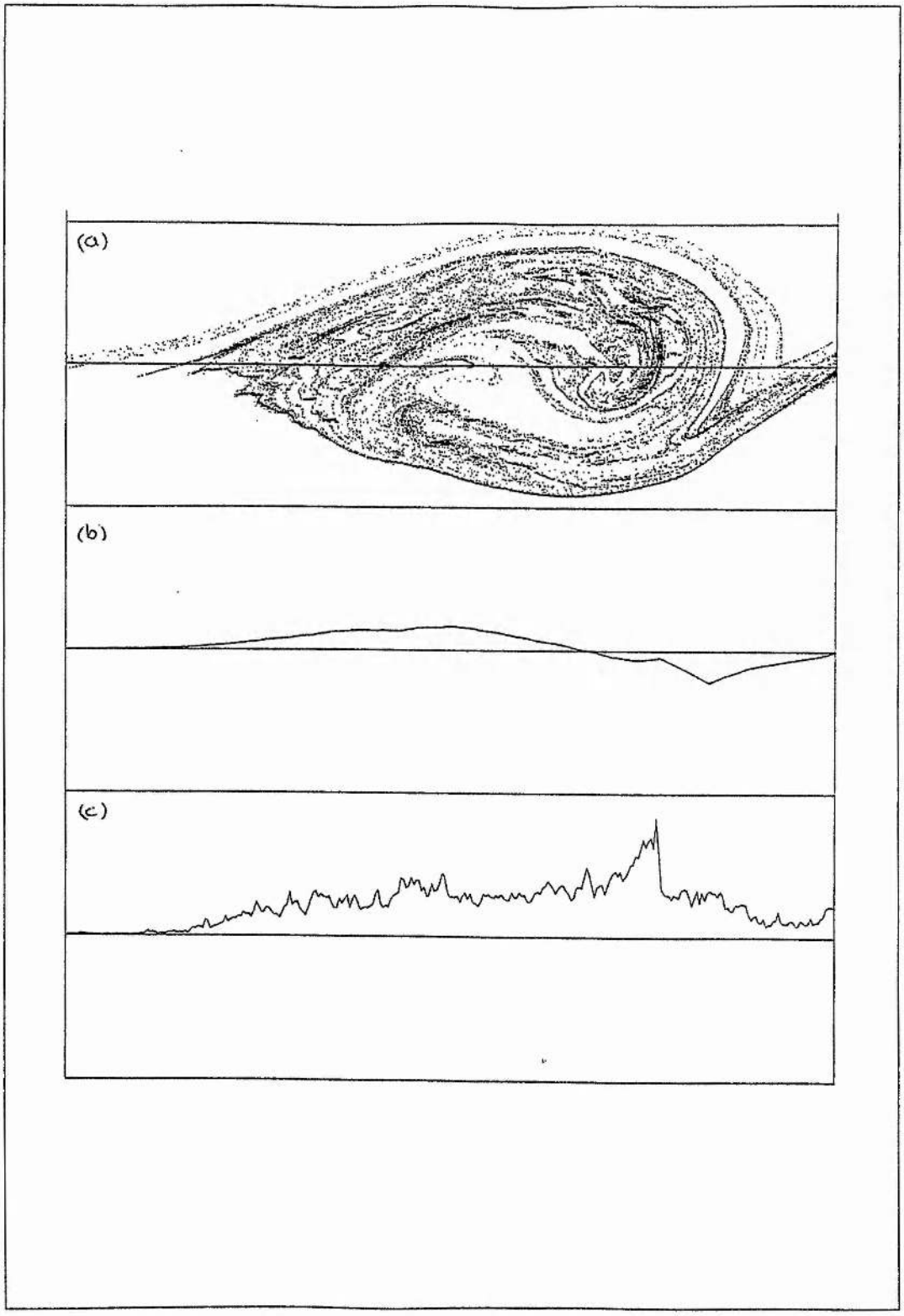

Figure 8.19: Results generated using the self-consistent electron density profile and the Maxwellian boundary condition for the parameter values e-capacitor $= 2\pi \times 10^{-3}$ and z-ramp $= 2\pi$ at time $t = 11T_l$. (a) shows the (z, v_z) phase space; (b) shows the electric field across the simulation grid and (c) shows the electron density profile.

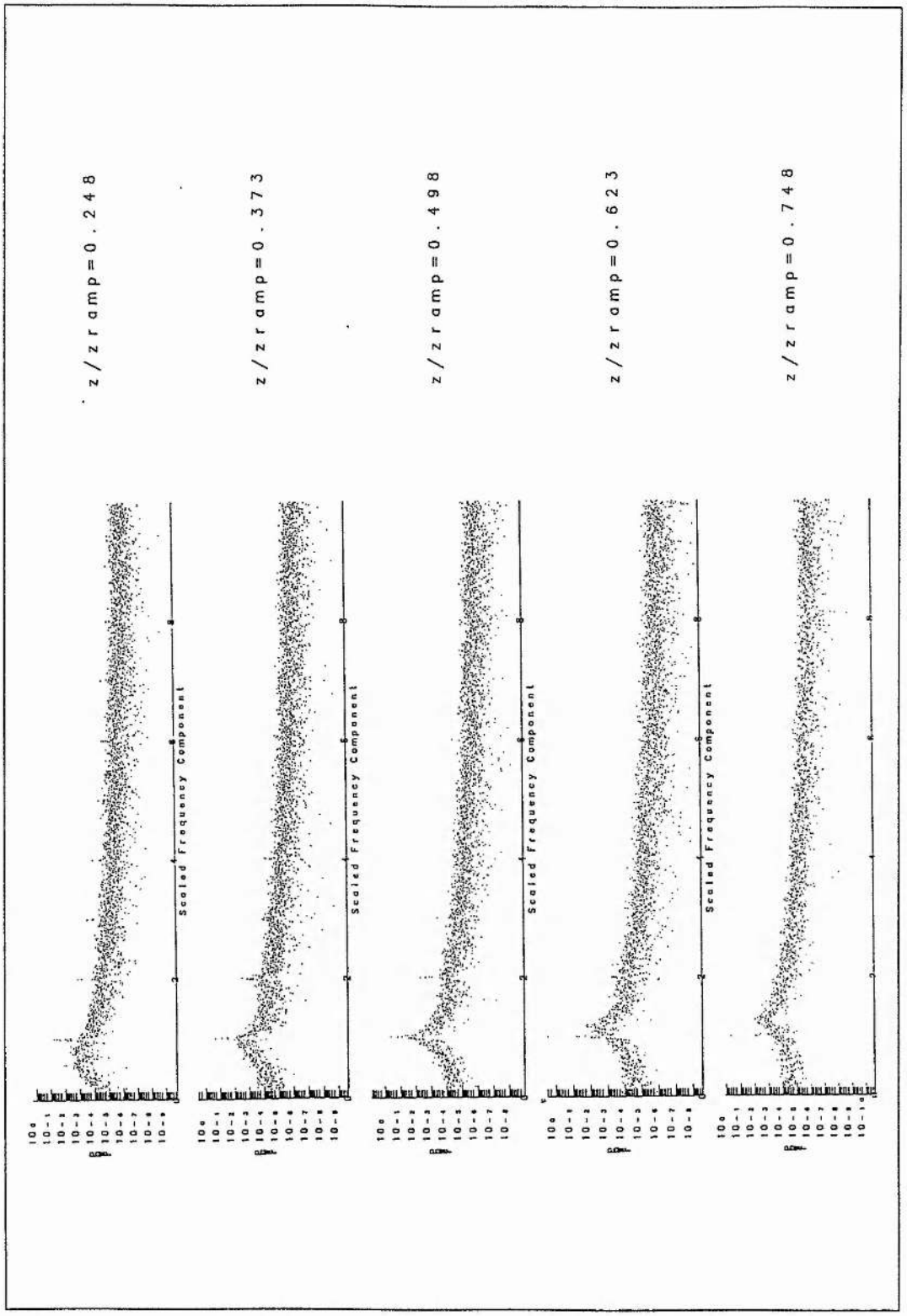

Figure 8.20: The Fourier decomposition spectra for the electron motion at equally spaced intervals in the linear density profile for the parameter values e-capacitor = $2\pi \times 10^{-3}$ and z-ramp = 2π.

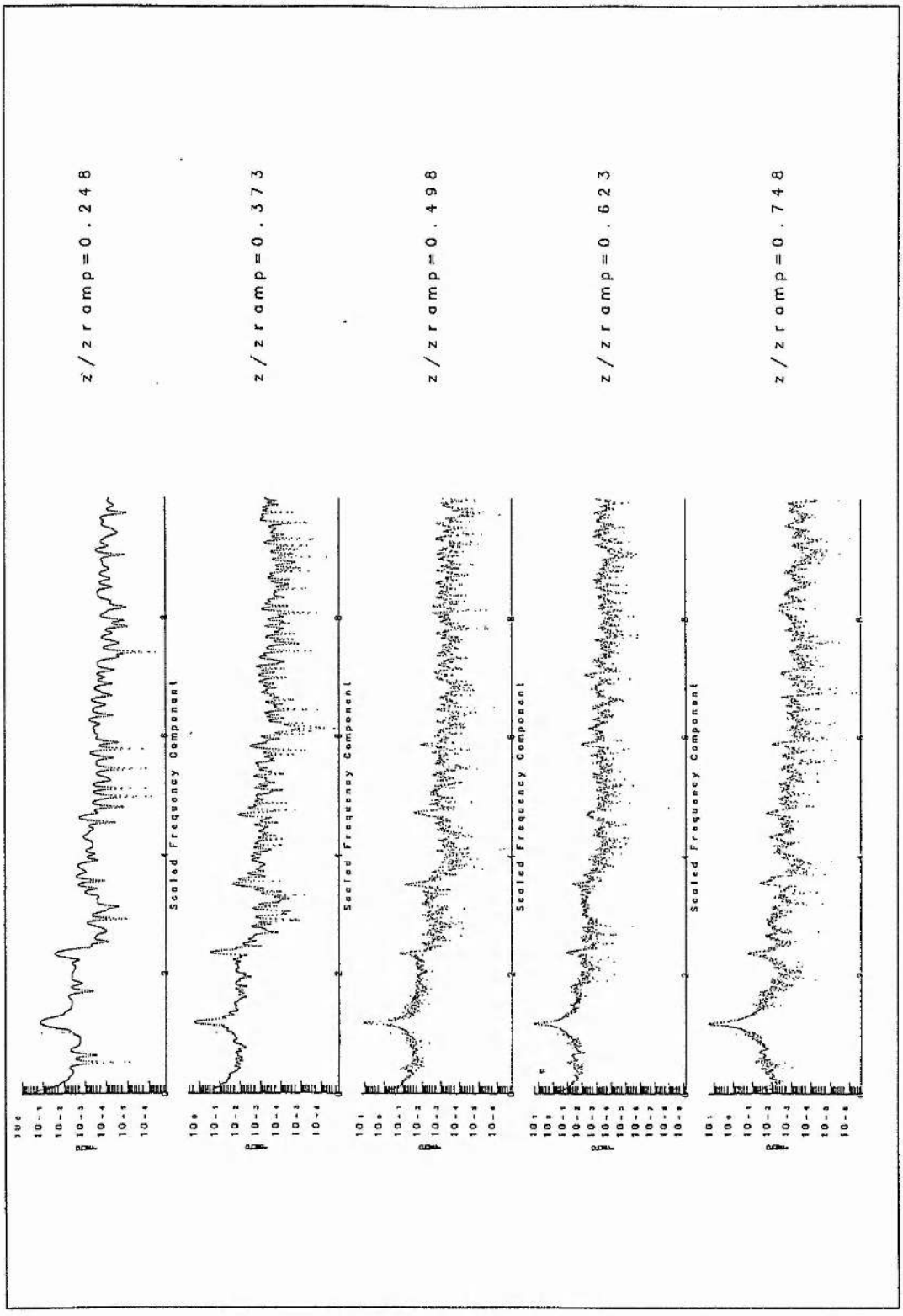

Figure 8.21: The Fourier decomposition spectra for the electron motion at equally spaced intervals in the self-consistent density profile for the parameter values e-capacitor $= 2\pi \times 10^{-3}$ and z-ramp $= 2\pi$.

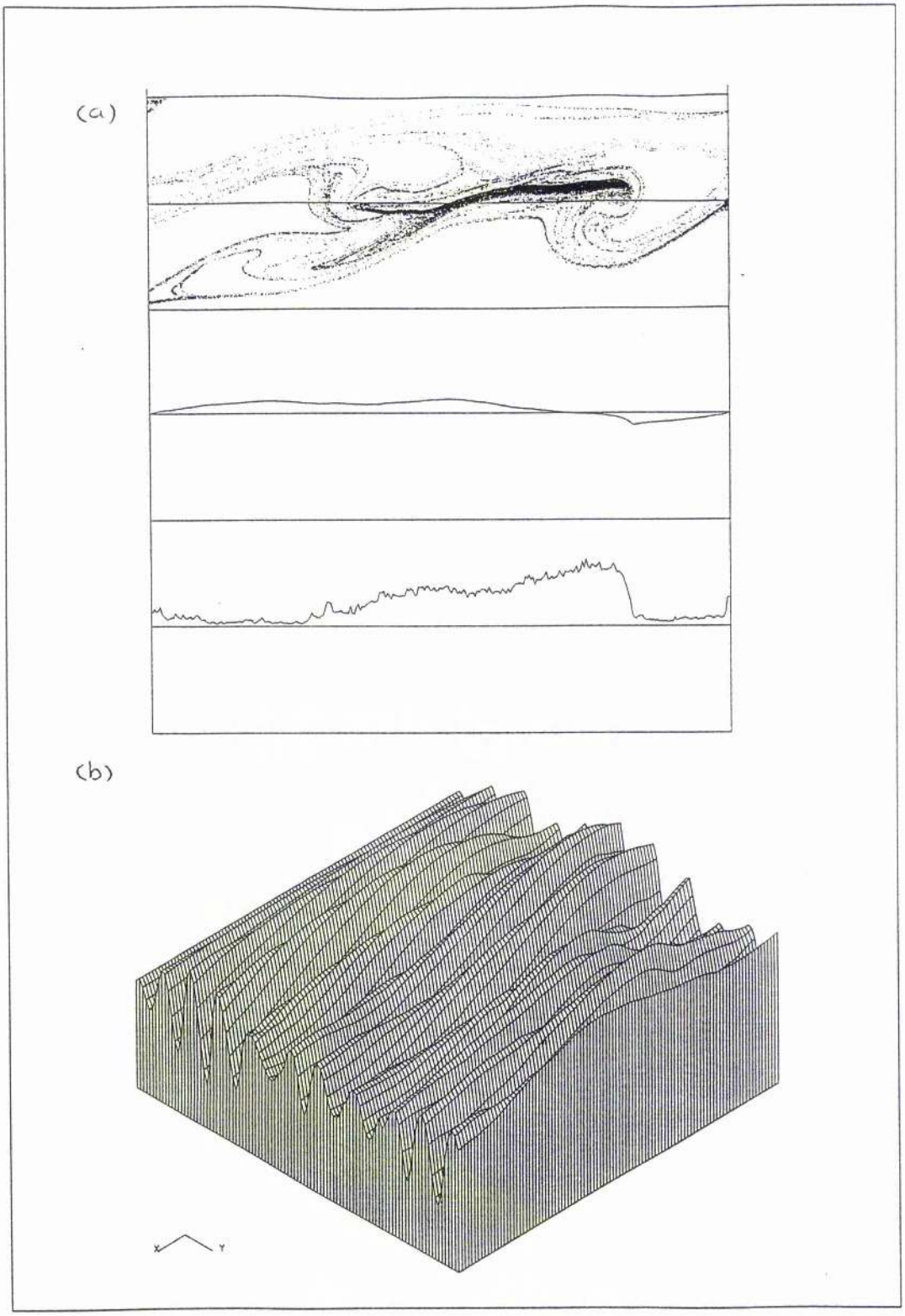

Figure 8.22: Results generated using a linear electron density profile for the parameter values e-capacitor $= 2\pi \times 10^{-2}$ and z-ramp $= 2\pi$ at time $t = 10T_l$. (a) shows the bulk plasma quantities - the (z, v_z) phase space, the electric field across the simulation grid and the electron density profile respectively; (b) shows the electric field time history with time increasing to the right and position increasing out of the page.

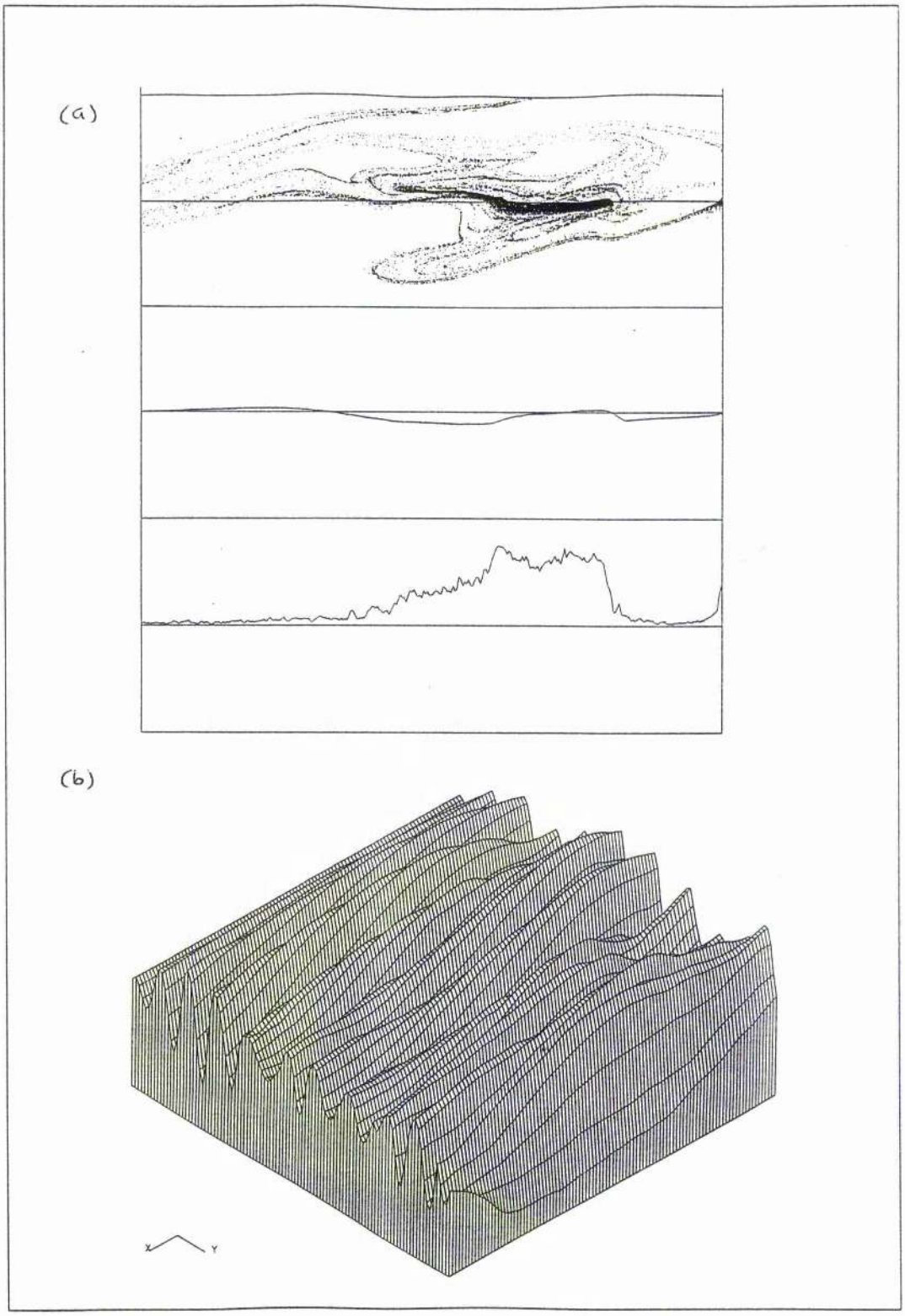

Figure 8.23: Results generated using a linear electron density profile for the parameter values e-capacitor $= 2\pi \times 10^{-2}$ and z-ramp $= 2\pi$ at time $t = 10.5T_l$. (a) shows the bulk plasma quantities - the (z, v_z) phase space, the electric field across the simulation grid and the electron density profile respectively; (b) shows the electric field time history with time increasing to the right and position increasing out of the page.

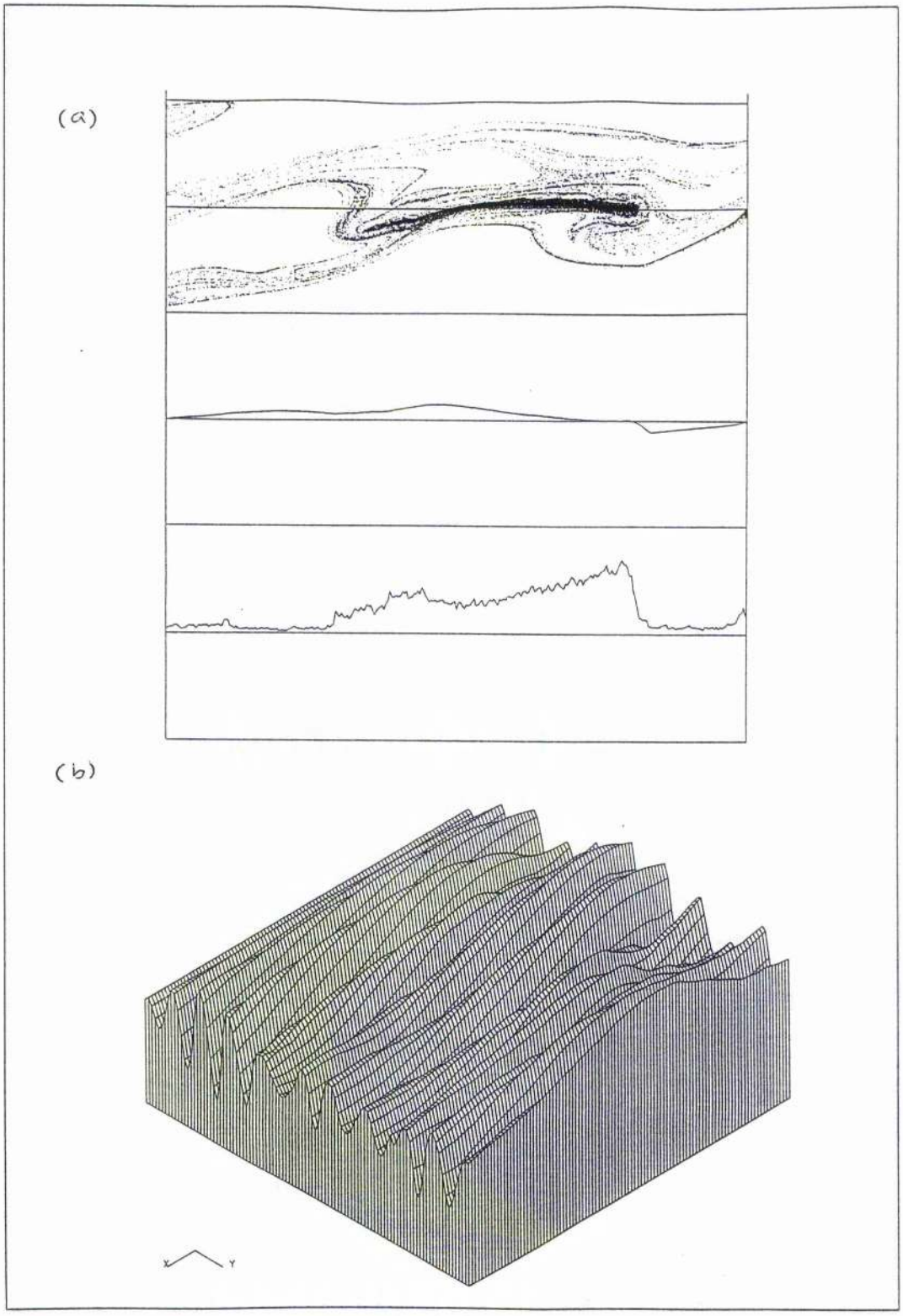

Figure 8.24: Results generated using a linear electron density profile for the parameter values e-capacitor $= 2\pi \times 10^{-2}$ and z-ramp $= 2\pi$ at time $t = 11T_i$. (a) shows the bulk plasma quantities - the (z, v_z) phase space, the electric field across the simulation grid and the electron density profile respectively; (b) shows the electric field time history with time increasing to the right and position increasing out of the page.

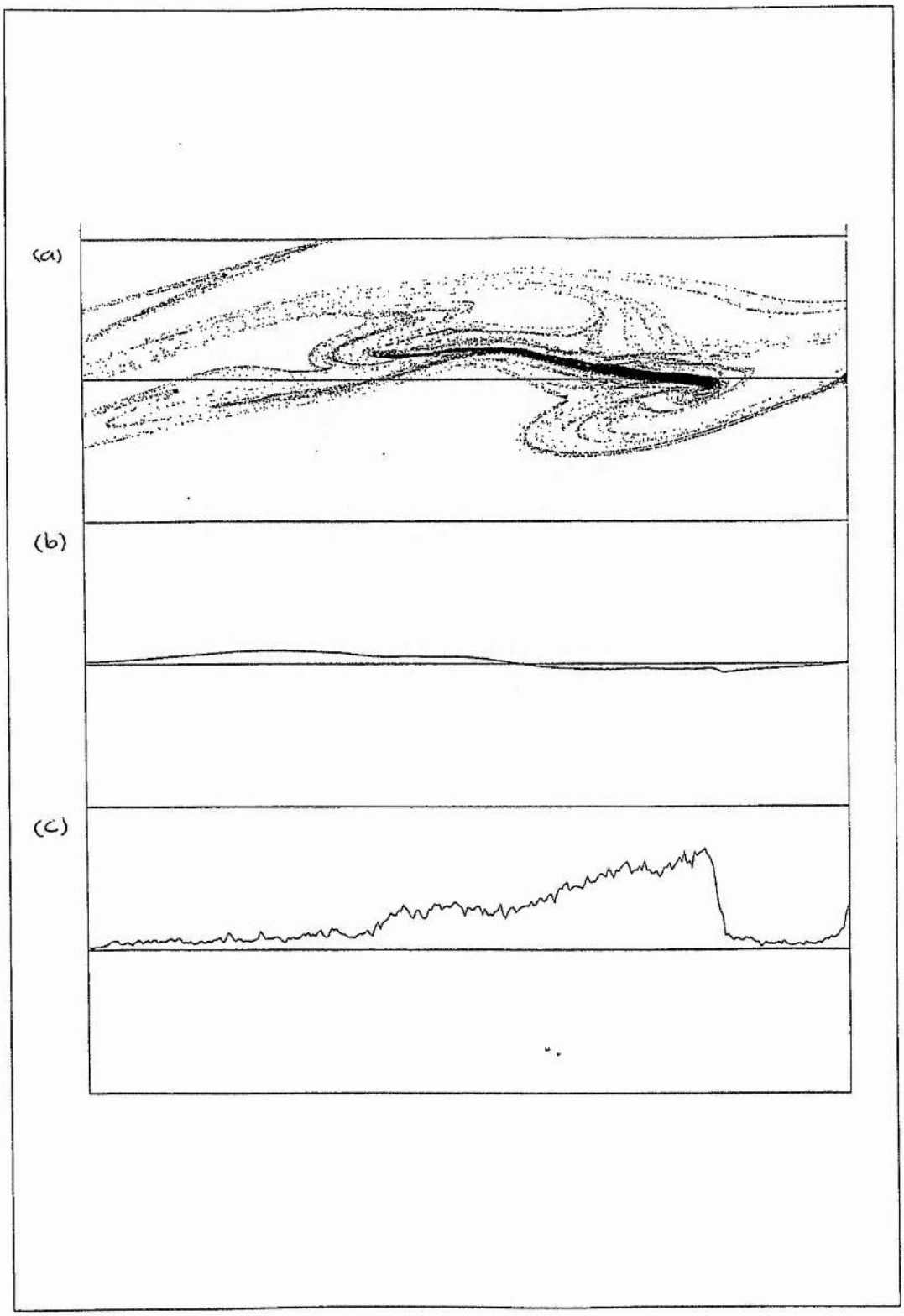

Figure 8.25: Results generated using a linear electron density profile for the parameter values e-capacitor $= 2\pi \times 10^{-2}$ and z-ramp $= 2\pi$ at time $t = 10.25T_l$. (a) shows the (z, v_z) phase space; (b) shows the electric field across the simulation grid and (c) shows the electron density profile.

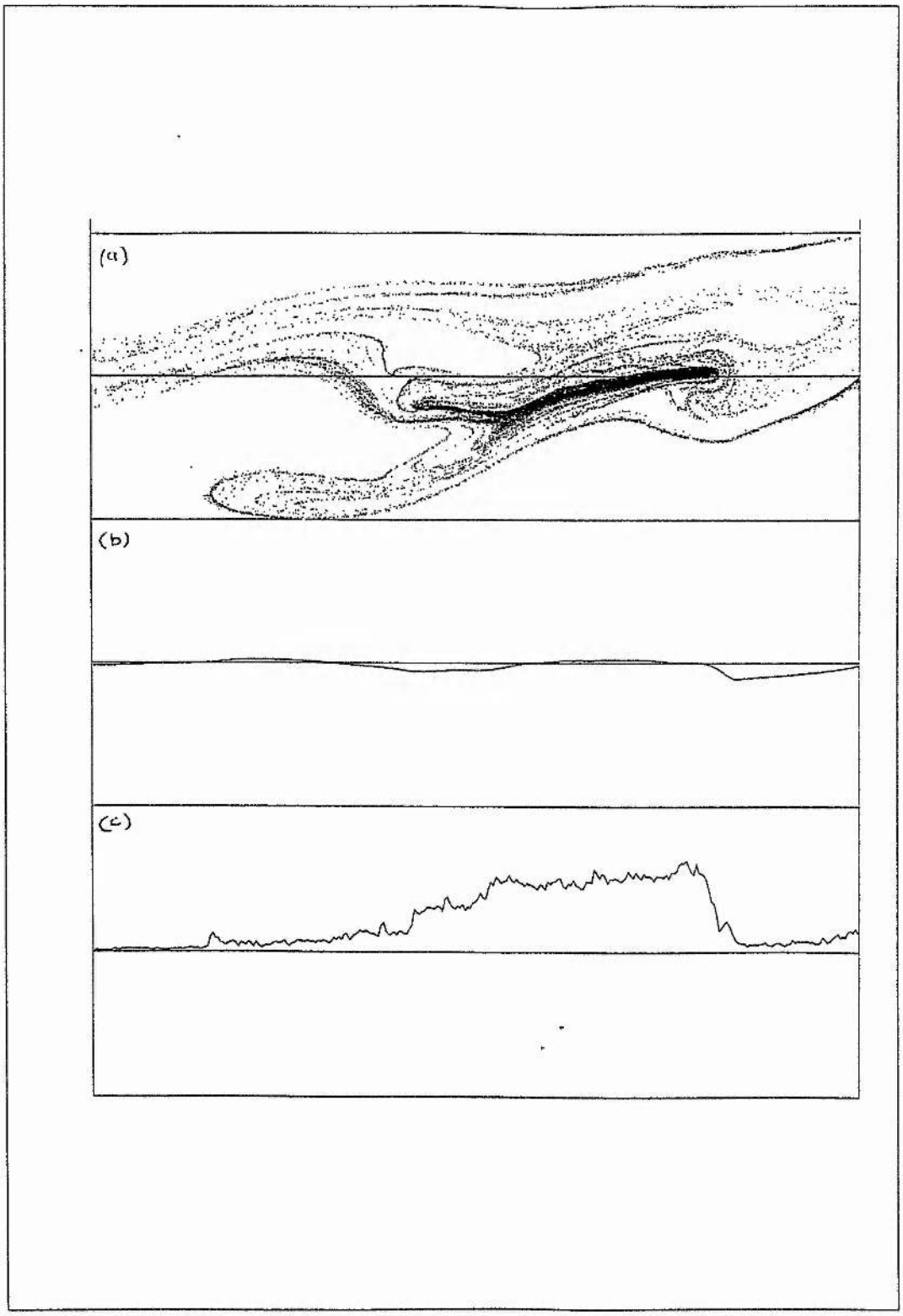

Figure 8.26: Results generated using a linear electron density profile for the parameter values e-capacitor $= 2\pi \times 10^{-2}$ and z-ramp $= 2\pi$ at time $t = 10.75T_l$. (a) shows the (z, v_z) phase space; (b) shows the electric field across the simulation grid and (c) shows the electron density profile.

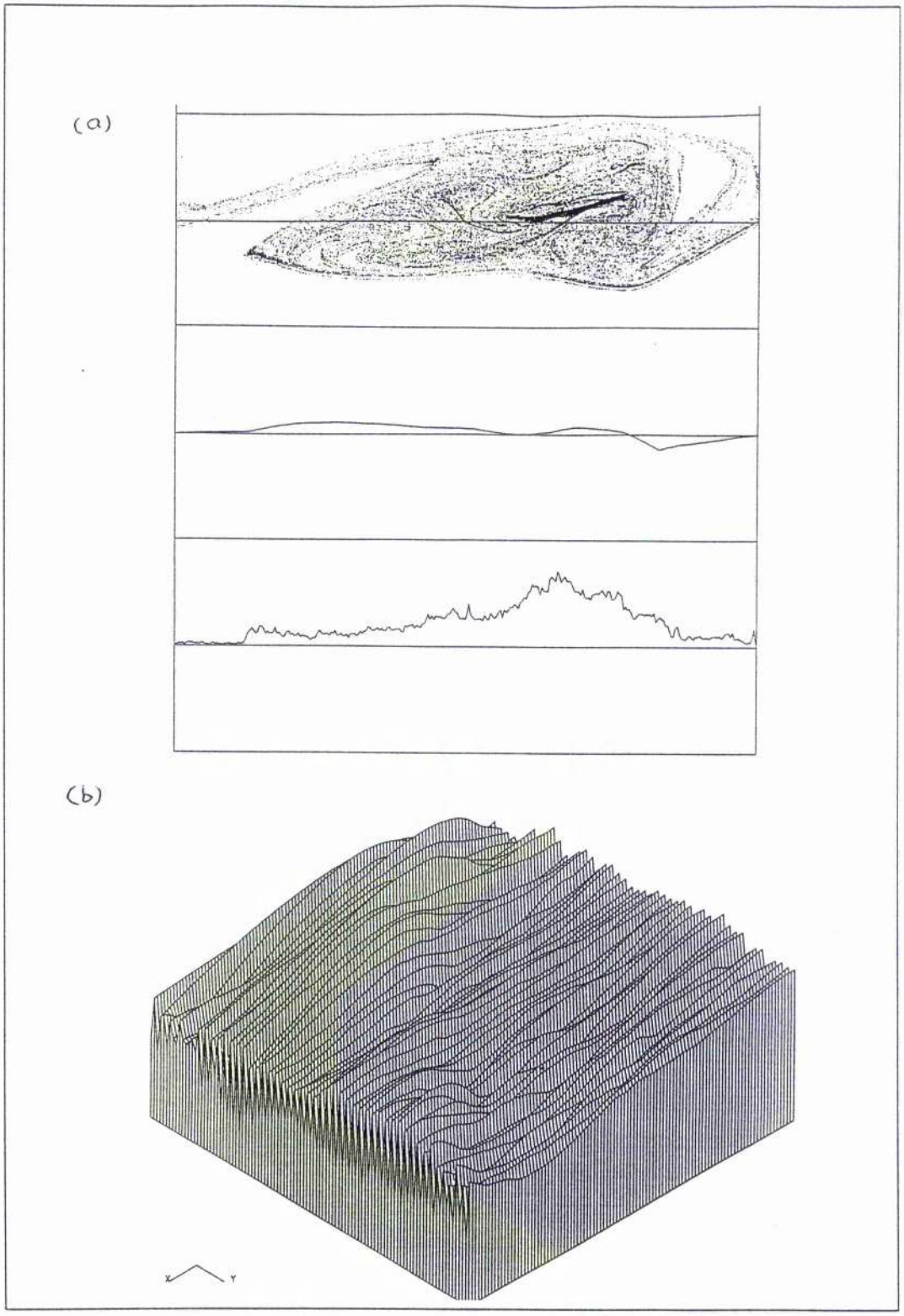

Figure 8.27: Results generated using a linear electron density profile with Maxwellian boundary conditions for the parameter values e-capacitor $= 2\pi \times 10^{-2}$ and z-ramp $= 2\pi$ at time $t = 10T_l$. (a) shows the bulk plasma quantities - the (z, v_z) phase space, the electric field across the simulation grid and the electron density profile respectively; (b) shows the electric field time history with time increasing to the right and position increasing out of the page.

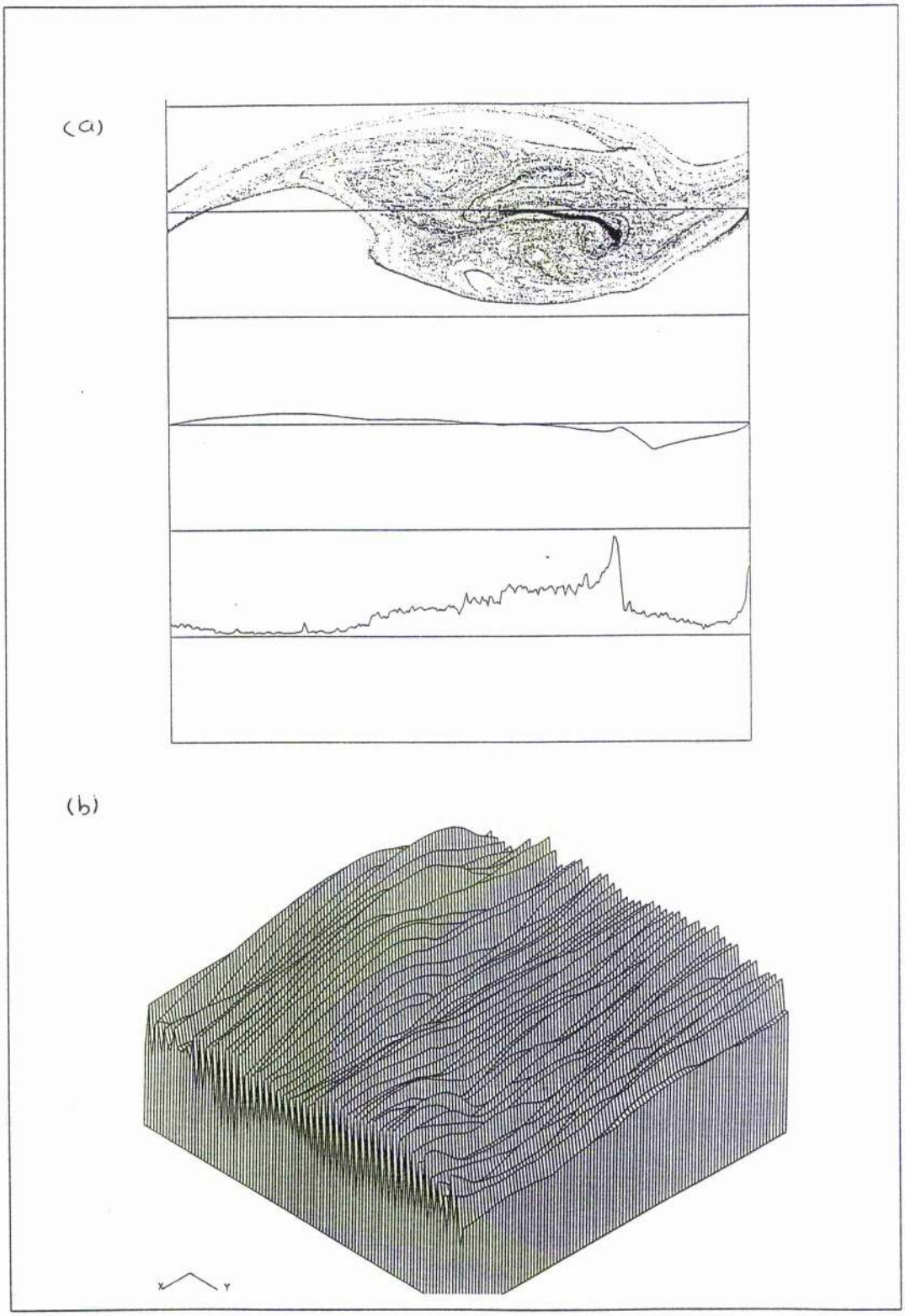

Figure 8.28: Results generated using a linear electron density profile with Maxwellian boundary conditions for the parameter values e-capacitor $= 2\pi \times 10^{-2}$ and z-ramp $= 2\pi$ at time $t = 10.5T_l$. (a) shows the bulk plasma quantities - the (z, v_z) phase space, the electric field across the simulation grid and the electron density profile respectively; (b) shows the electric field time history with time increasing to the right and position increasing out of the page.

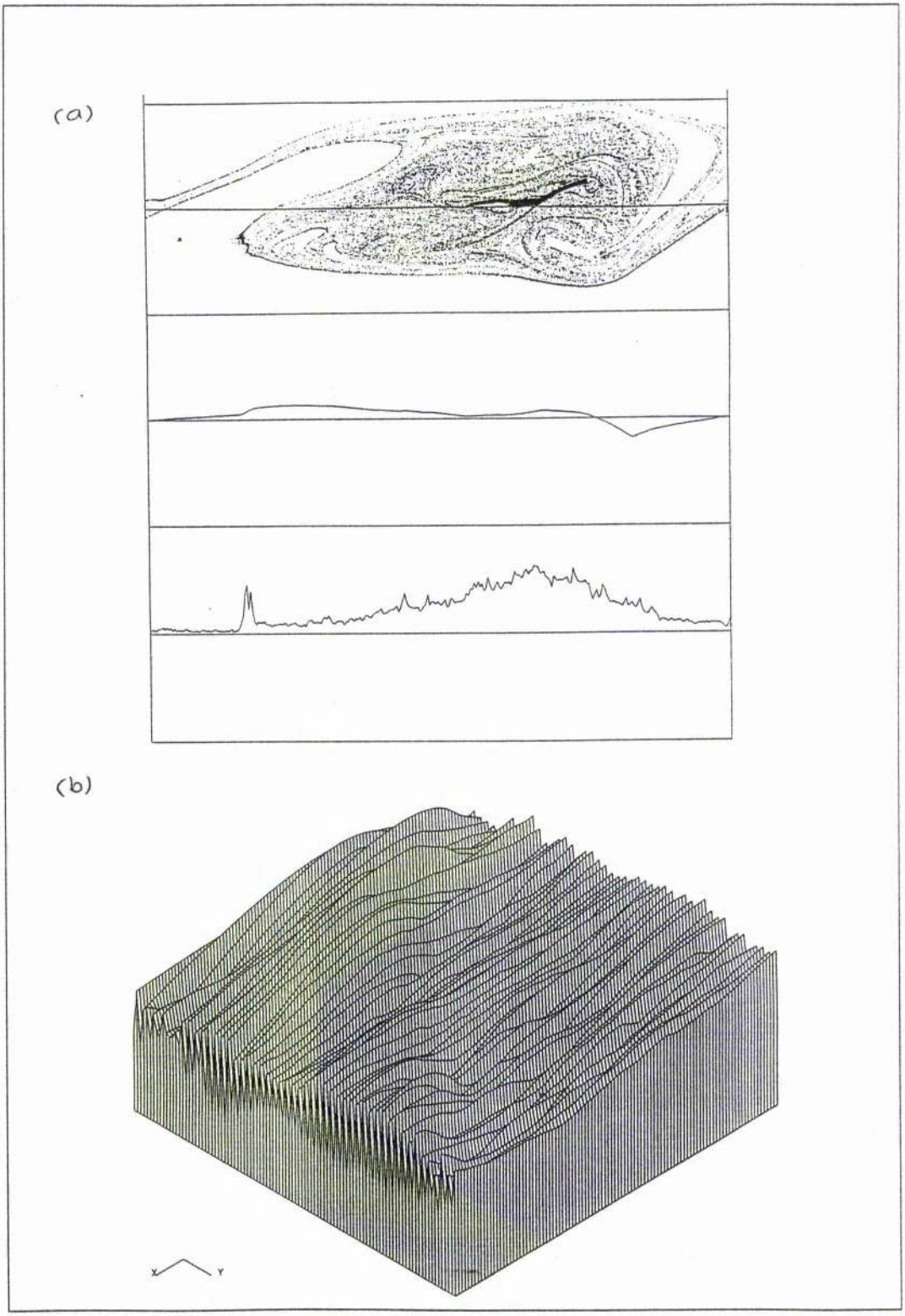

Figure 8.29: Results generated using a linear electron density profile with Maxwellian boundary conditions for the parameter values e-capacitor $= 2\pi \times 10^{-2}$ and z-ramp $= 2\pi$ at time $t = 11T_l$. (a) shows the bulk plasma quantities - the (z, v_z) phase space, the electric field across the simulation grid and the electron density profile respectively; (b) shows the electric field time history with time increasing to the right and position increasing out of the page.

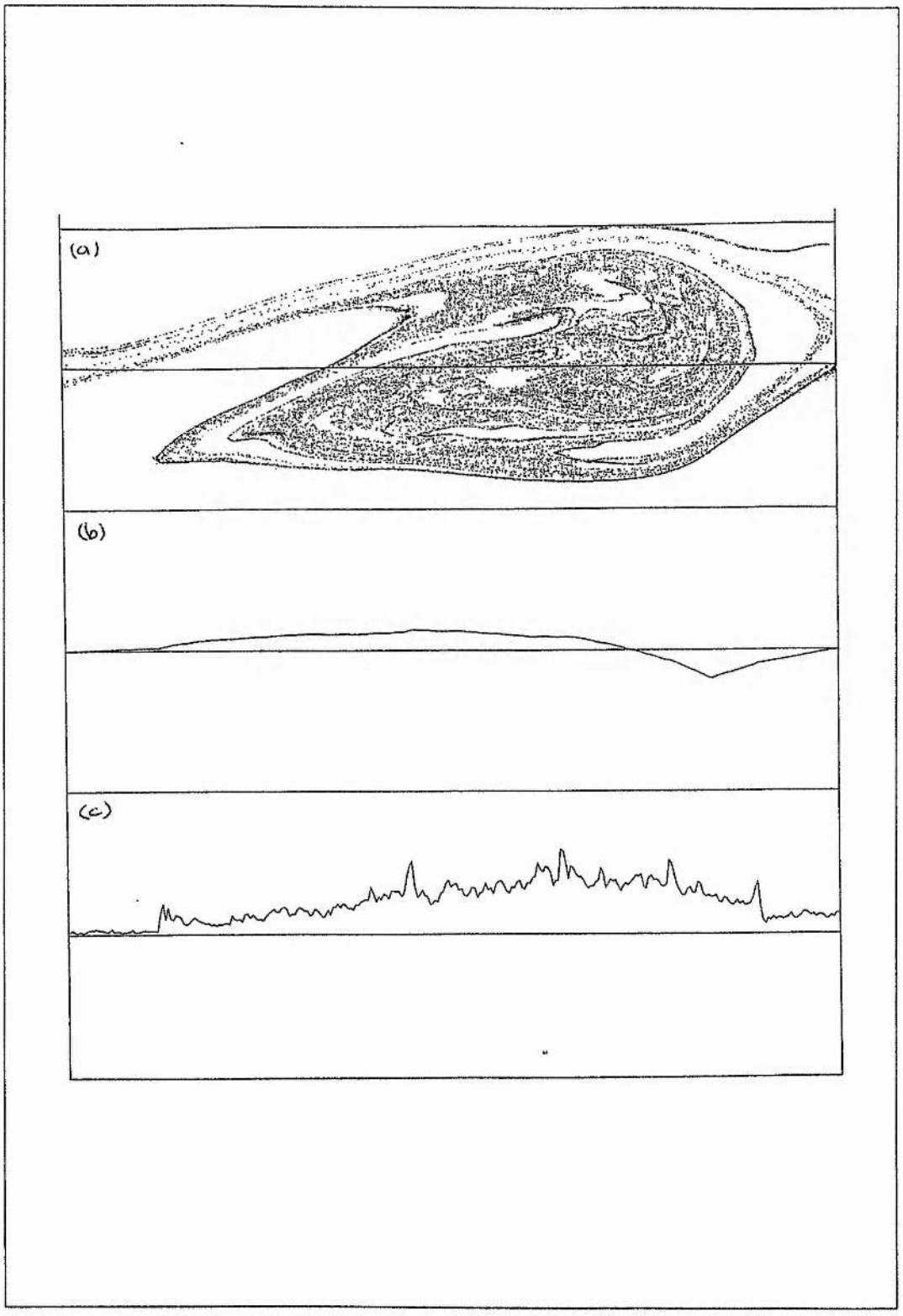

Figure 8.30: The bulk plasma results obtained using the self-consistent electron density profile with the Maxwellian boundary conditions for the parameter values e-capacitor $= 2\pi \times 10^{-2}$ and z-ramp $= 2\pi$ at time $t = 10T_l$. (a) shows the (z, v_z) phase space; (b) shows the electric field across the simulation grid and (c) shows the electron density profile.

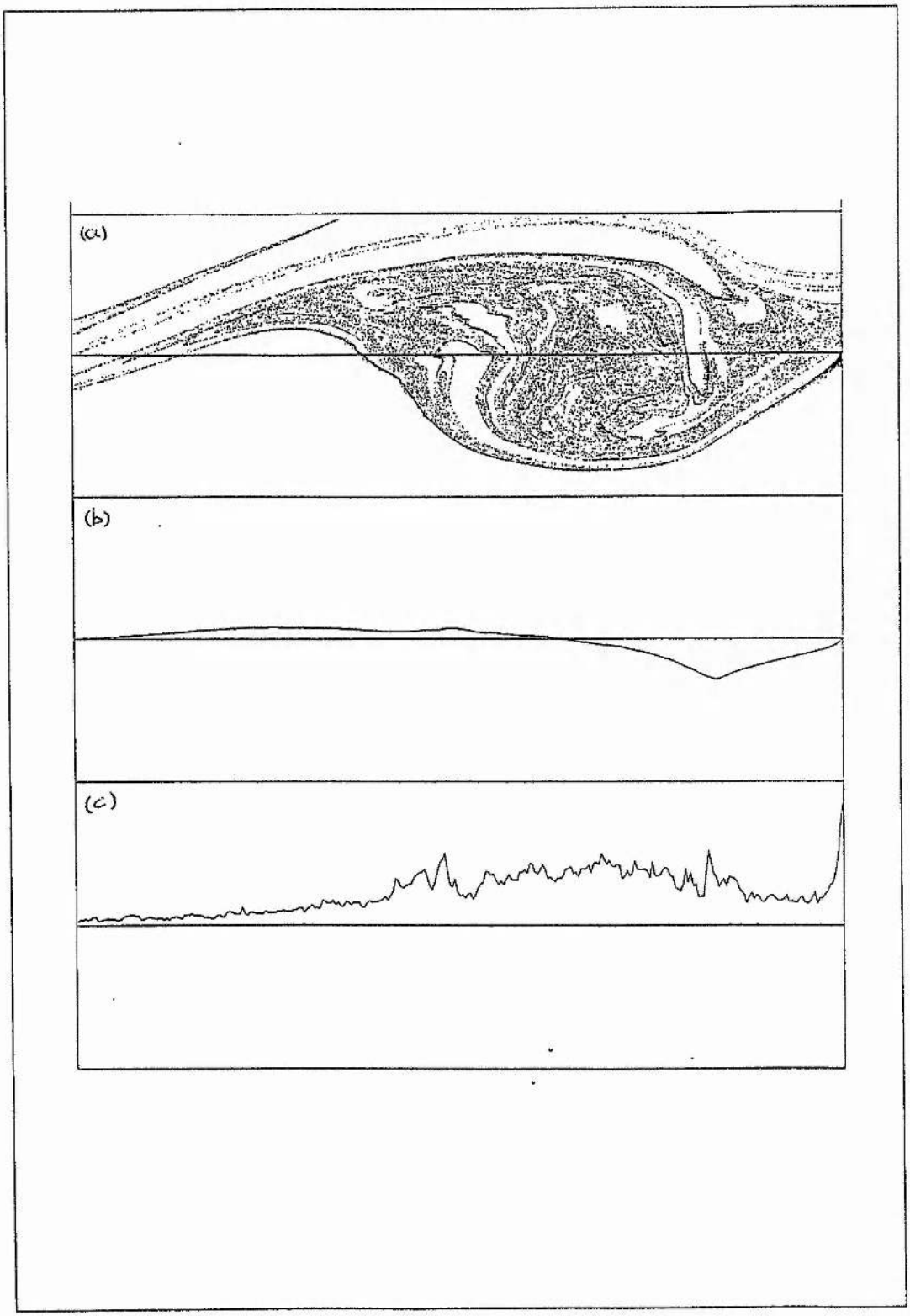

Figure 8.31: The bulk plasma results obtained using the self-consistent electron density profile with the Maxwellian boundary conditions for the parameter values e-capacitor $= 2\pi \times 10^{-2}$ and z-ramp $= 2\pi$ at time $t = 10.5T_i$. (a) shows the (z, v_z) phase space; (b) shows the electric field across the simulation grid and (c) shows the electron density profile.

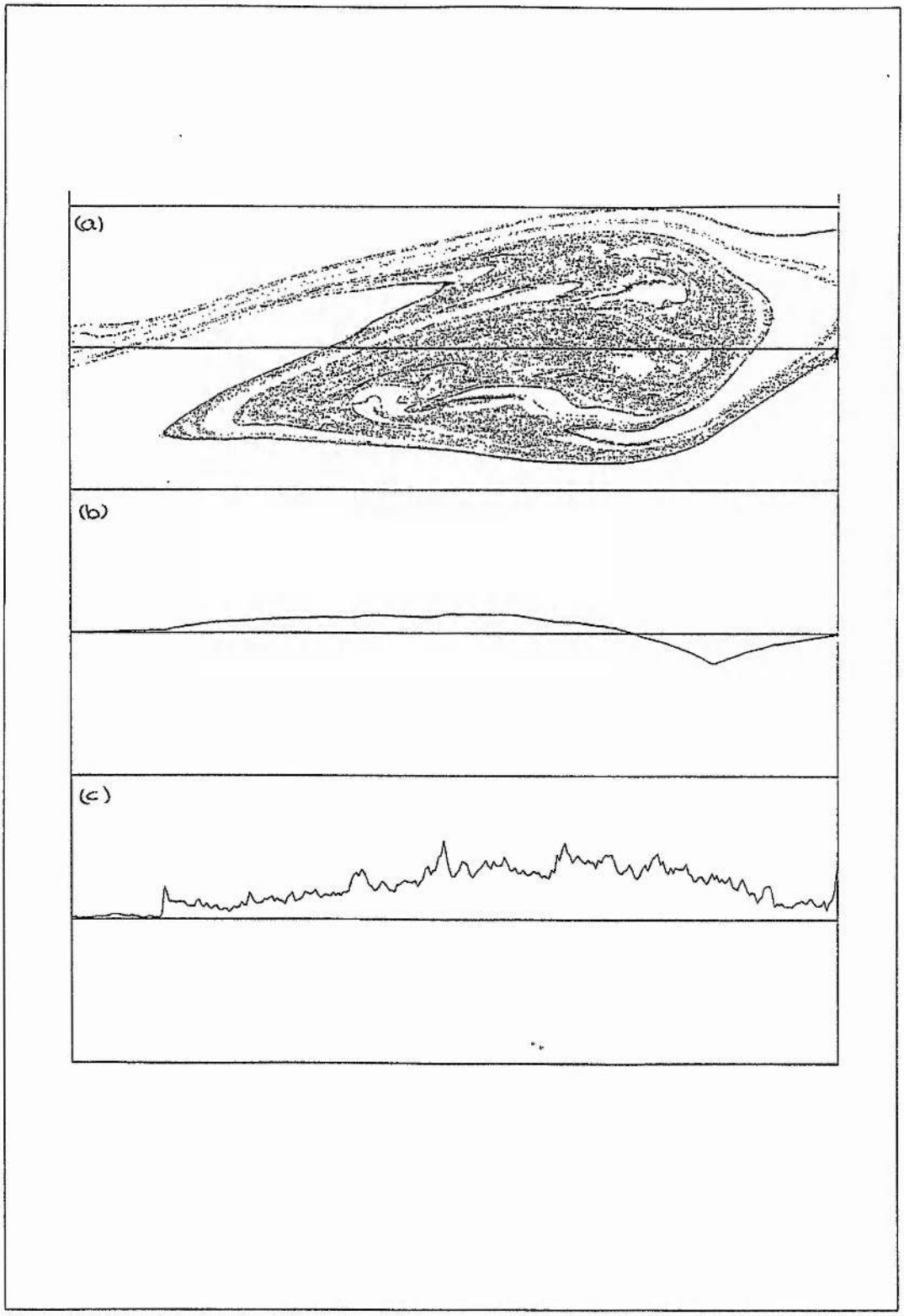

Figure 8.32: The bulk plasma results obtained using the self-consistent electron density profile with the Maxwellian boundary conditions for the parameter values e-capacitor $= 2\pi \times 10^{-2}$ and z-ramp $= 2\pi$ at time $t = 11T_l$. (a) shows the (z, v_z) phase space; (b) shows the electric field across the simulation grid and (c) shows the electron density profile.

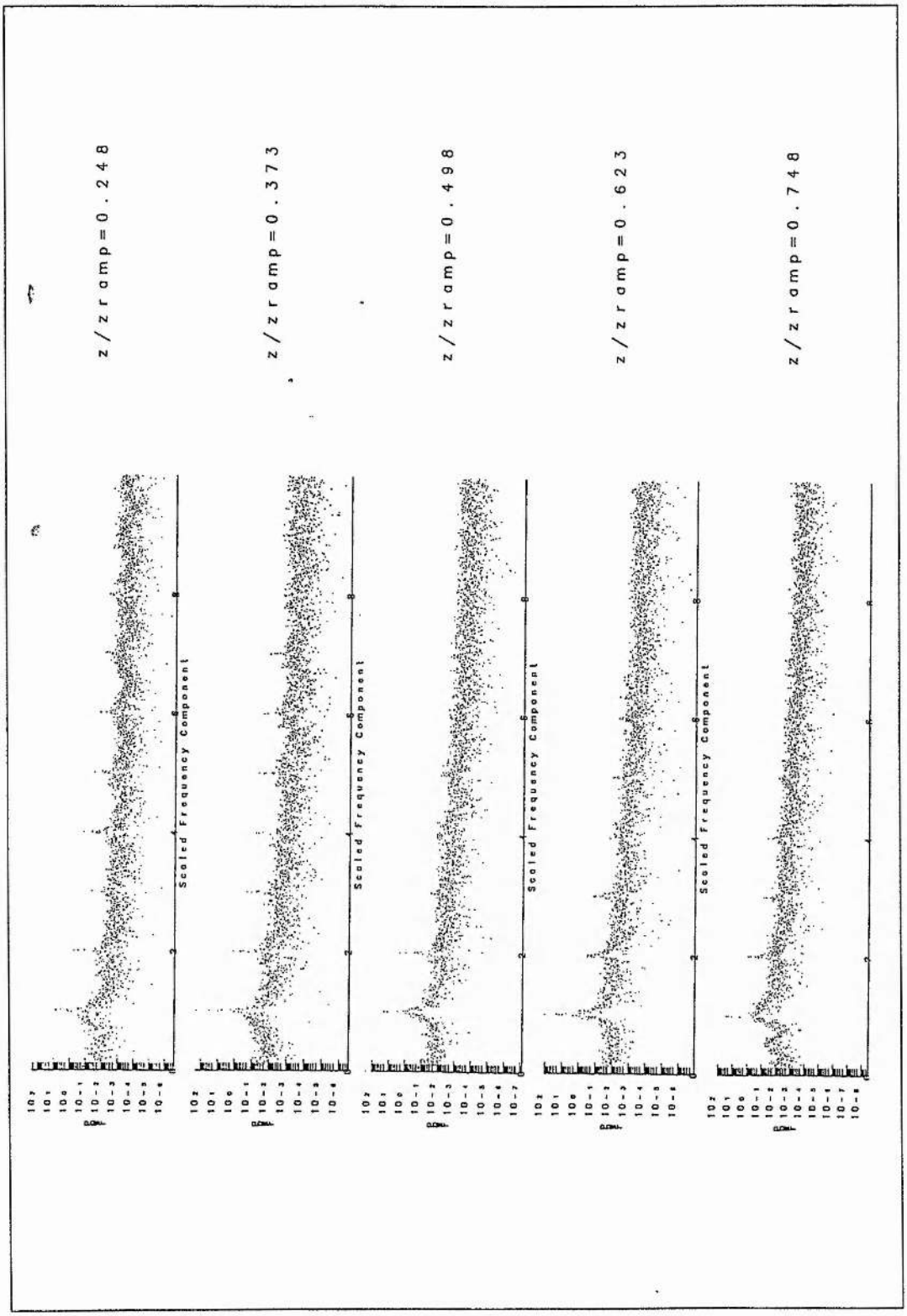

Figure 8.33: The Fourier decomposition spectra for the electron motion at equally spaced intervals in the linear density profile for the parameter values e-capacitor = $2\pi \times 10^{-2}$ and z-ramp = 2π.

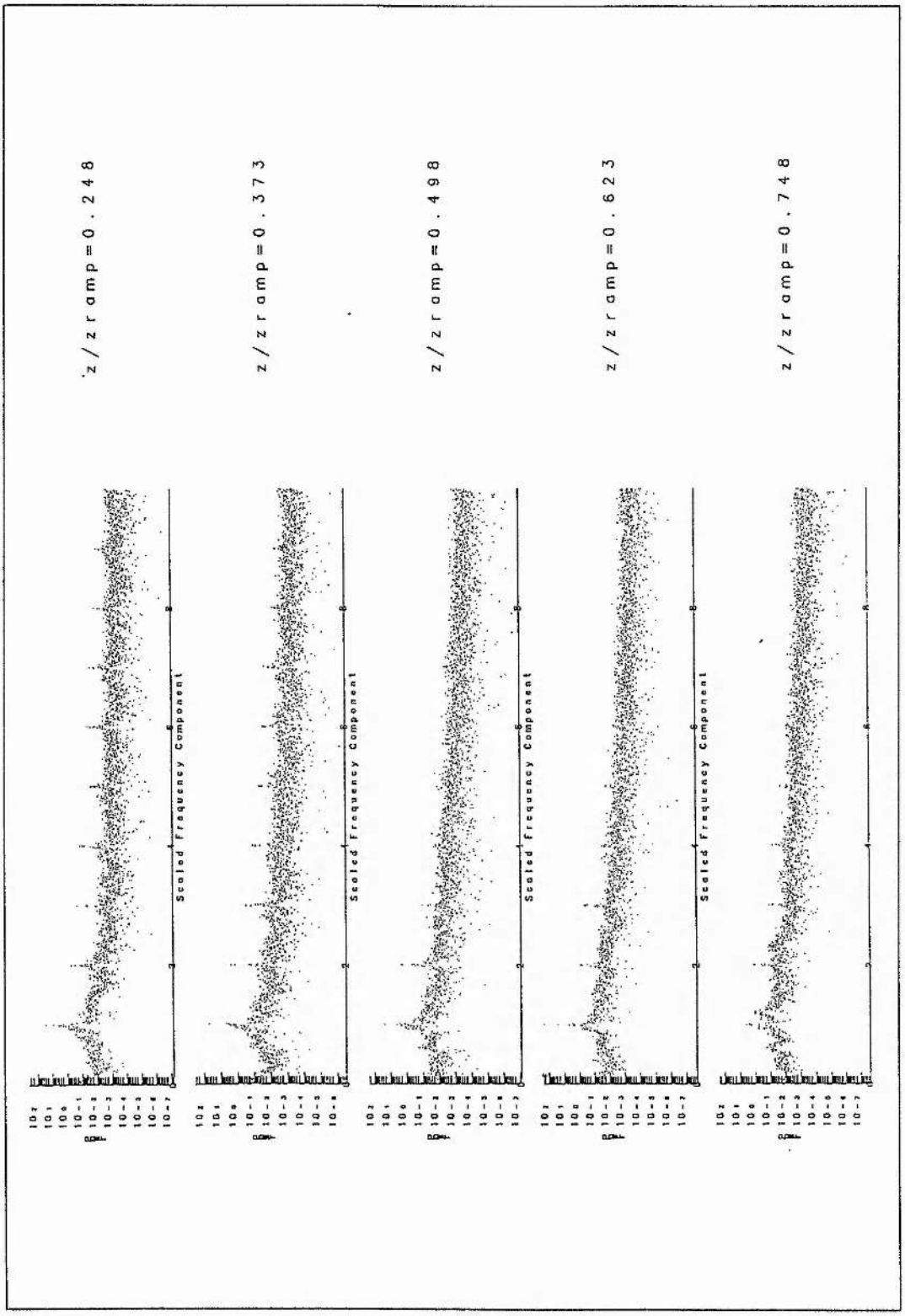

Figure 8.34: The Fourier decomposition spectra for the electron motion at equally spaced intervals in the self-consistent density profile for the parameter values e-capacitor $= 2\pi \times 10^{-2}$ and z-ramp $= 2\pi$.

Chapter 9

Summary to Part II

In the second part of this thesis, we have studied the response of plasma electrons in a density gradient to an applied oscillating electrostatic field. At the outset, we expected to find evidence of some nonlinear behaviour when the electrostatic field strength becomes such that the vacuum quiver velocity of the electrons in the field becomes relativistic. This parameter regime corresponds to an applied laser intensity of the order of $10^{18}\mathrm{W/cm}^2$. The simple model of Chapter 7 is aimed at studying the response of the plasma electrons as forced oscillators by including a basic description of the physical processes involved. The results of this forced oscillator study may be analysed by numerical techniques to reveal any periodicity in the electron dynamics. We find that significant nonlinear behaviour occurs in the dynamics at field strengths three orders of magnitude lower than expected from our initial considerations. The results reveal an extremely complicated dynamics as the electron oscillations distort from linear isoperiodic motion to period doubled, tripled, quadrupled, and chaotic motion. The effects of this change in the character of the electron motion on the absorption process have also been considered. We find some interesting effects on the absorption process in the region of the critical surface in the plasma density profile. As the strength of the forcing field is increased, the peak of the absorption curve becomes depressed and moves back towards the body of the more dense plasma.

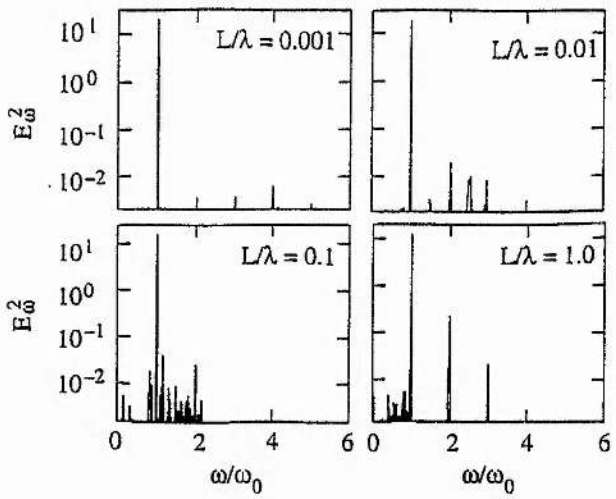

Figure 9.1: Power spectrum of the reflected light for the interaction of A 100fs Gaussian laser pulse of irradiance $I_0\lambda^2 = 10^{16}\mathrm{W/cm}^2\,\mu\mathrm{m}^2$ with a linear density profile. After [37]

In Chapter 8 we have presented the results of some PIC simulations of the interactions under investigation in our simple model. However, the general noise level in particle codes together with a numerical limitation on the electron temperatures we may model restricted the scope of our investigations. However, by considering the bulk plasma quantities (the momentum/displacement phase space, the electric field across the simulation grid and the plasma electron density), we have observed some behaviour which suggests that the delicate structures of Chapter 7 may indeed exist. In particular analysis of the time history of the electric field across the simulation grid has shown that the field is asymmetric about the critical surface and shows a periodic nature. Fourier spectra may also be generated for the oscillations at various points within the density gradient. These show the strong frequency components present at the fundamental and harmonic frequencies, although we have not obtained a result which illustrates the presence of subharmonic frequencies apart from the chaotic spectra produced at higher driver strengths. The results of the particle-in-cell investigations therefore remain inconclusive in determining the electron dynamics in the laser plasma interaction studied here.

In conclusion, the results presented in Part IIof this thesis serve to illustrate the fact that the electron dynamics in the laser plasma interactions we have studied is extremely complicated. Our simple model has demonstrated that effects such as period doubling and transitions to chaotic motion may be encountered without coupling to other wave modes or other fluid effects. Recent studies with particle-in-cell codes [37] have revealed that the characteristics of laser matter interactions in a given intensity regime, such as the generation of harmonics, depends strongly on the scale length of the density profile. For a 100fs p-polarised Gaussian pulse with an irradiance of $10^{16}\mathrm{W/cm^2}\,\mu\mathrm{m}^2$ incident at 30 degrees onto a linear density profile, the power spectrum of the reflected light is shown in Figure 9.1 for various density scale lengths. We notice that for the longer density scale lengths considered in this study, subharmonic frequency components are detected. This is the type of behaviour predicted by our simple model in Chapter 7 and results such as these are sure to bring renewed interest in this area for future work.

References

[1] M. R. Amin. *Nonlinear Plasma Waves and their Applications.* PhD thesis, University of St. Andrews, 1990.

[2] K. Bane, T. Weiland, and P. Silson. . In M. Month, P. F. Dahl, and M. Dienes, editors, *Physics of High Energy Particle Accelerators*, number 127 in AIP Conference Proceedings, page 875, 1985.

[3] K. L. F. Bane, P. Chen, and P. B. Wilson. . *IEEE Transactions in Nuclear Science*, NS-32:3524, 1985.

[4] V. I. Berezhiani and I. G. Murusidze, 1992. Physica Scripta **45**(2):87–90.

[5] C. K. Birdsall and A. B. Langdon*Plasma Physics via Computer Simulation.* Adam Hilger (IOP Publishing), 1991.

[6] B. Breizman. Institute for Fusion Studies, University of Texas.
Private Communication.

[7] G. Brianti. Accelerator technology from SC to LHC. *Physics Reports*, 225(1–3):79–87, 1993.

[8] F. Brunel. Not-So-Resonant, Resonant Absorption. *Phys. Rev. Lett.*, 59(1):52–55, 1987.

[9] S. V. Bulanov, V. I. Kirsanov, and A. S. Sakharov. Excitation of Ultra-Relativistic Langmuir Waves by Electromagnetic Pulses. *Physica Scripta*, T30:208–209, 1990.

[10] R. A. Cairns*Plasma Physics.* Blackie (Glasgow), 1985. pp 84–91.

[11] *The Generation of High Fields for Particle Acceleration to Very High Energies, Proceedings of the CAS-ECFA-INFN workshop*, Frascati, 1984.

[12] A. W. Chao. . In *Physics of High Energy Particle Accelerators*, number 105 in AIP Conference Proceedings, page 353, 1982.

[13] F. F. Chen. Excitation of Large Amplitude Plasma Waves. *Physica Scripta*, T30:14–23, 1990.

[14] P. Chen, J. M. Dawson, R. W. Huff, and T. Katsouleas. Acceleration of Electrons by the Interaction of a Bunched Electron Beam with a Plasma. *Phys. Rev. Lett.*, 54(7):693–696, 1985.

[15] P. Chen, J. J. Su, J. M. Dawson, K. L. F. Bane, and P. B. Wilson. Energy Transfer in the Plasma Wake-Field Acclerator. *Phys. Rev. Lett.*, 56(12):1252–1255, 1986.

[16] C. E. Clayton and C. Joshi. Relativistic Plasma-Wave Excitation by Collinear Optical Mixing. *Phys. Rev. Lett.*, 54:2343, 1985.

[17] C. E. Clayton, K. A. Marsh, A. Dyson, M. Everett, A. Lal, W. P. Leemans, R. Williams, and C. Joshi. Ultrahigh-Gradient Acceleration of Injected Electrons by Laser-Excited Relativistic Electron Plasma Waves. *Phys. Rev. Lett.*, 70(1):37–40, 1993.

[18] R. Courant, K. O. Friedrichs, and H. Lewy. *Math. Ann.*, 100:32, 1928.

[19] J. Crank and P. Nicholson. *Proc. Camb. Phil. Soc.*, 43:50, 1947.

[20] A. E. Dangor, A. K. L. Dymoke-Bradshaw, and A. E. Dyson. Observation of Relativistic Plasma Waves Generated by the Beat–Wave with 1 μm Lasers. *Physica Scripta*, T30:107–109, 1990.

[21] C. Darrow, D. Umstadter, T. Katsouleas, W. B. Mori, C. E. Clayton, and C. Joshi. Saturation of Beat–Excited Plasma Waves by Electrostatic Mode Coupling. *Phys. Rev. Lett.*, 56(24):2629–2632, 1986.

[22] U. de Angelis. Excitation of a Large Amplitude Plasma Wave by a Short Laser Pulse. *Physica Scripta*, T30:210–214, 1990.

[23] C. D. Decker and W. B. Mori. Group Velocity of Large Amplitude Electromagnetic Waves in a Plasma. *Phys. Rev. Lett.*, 72(4):490–493, 1994.

[24] A. Dyson and A. E. Dangor. Laser beat wave acceleration of particles. *Laser and Particle Beams*, 9(2):619–631, 1991.

[25] *The Challenge of Ultra-High Energies. Proceedings of ECFA-RAL meeting*, Oxford, September 1982.

[26] E. Esarey and A. Ting, 1990. Physical Review Letters **65**:1961.

[27] E. Esarey, A. Ting, P. Sprangle, and G. Joyce. The Laser Wakefield Accelerator. *Comments on Plasma Physics and Controlled Fusion*, 12(4):191–205, 1988.

[28] J. F. Drake et al. Parametric Instabilities of Electromagnetic Waves in Plasmas. *Physics of Fluids*, 17:778, 1974.

[29] R. G. Evans. Plasma simulation using fluid and particle models. In M. B. Hooper, editor, *Laser-Plasma Interactions 3*, pages 247–278, 1985.

[30] J. R. Fontana and R. H. Pantell. A high-energy laser accelerator for electrons using the inverse Cherenkov effect. *Journal of Applied Physics*, 54(8):4285–4288, August 1983.

[31] P. Gibbon and A. R. Bell. Collisionless Absorption in Sharp-Edged Plasmas. *Phys. Rev. Lett.*, 68(10):1535–1538, 1992.

[32] G. Hall and J. M. Watt*Modern Numerical Methods for Ordinary Differential Equations.* Clarendon Press (Oxford), 1976. p59.

[33] T. Katsouleas et al. Plasma Accelerators. In *Laser Acceleration of Particles*, number 130 in AIP Conference Proceedings, page 63, 1985.

[34] Y. Kitagawa, T. Minamihata, K. Sawai, K. Matsuo, K. Mima, K. Nishihara, H. Azechi, K. A. Tanaka, H. Takabe, and S. Nakai. Beat–Wave Excitation of Plasma Wave and Observation of Accelerated Electrons. *Phys. Rev. Lett.*, 68(1):48–51, 1992.

[35] J. Krall, G. Joyce, and E. Esarey. Vlasov simulations of very-large-amplitude-wave generation in the plasma wake-field accelerator . *Phys. Rev. A*, 44(10):6854–6861, 1991.

[36] J. D. Lawson. The physics of particle acceleration. In ECFA1 [25], pages 9–44.

[37] Particle-in-Cell Simulations of the Interaction of Gaussian Ultrashort Laser Pulses with Targets of Varying Initial Scale Lengths. *LLE Review*, 58:76–82, 1994.

[38] P. Maine, D. Strickland, et al. Generation of ultrahigh peak power pulses by chirped pulse amplification. *IEEE Journal of Quantum Electronics*, 24(2):398–403, February 1988.

[39] O. E. Martinez, 1987. SCIENCE **23**:1385.

[40] P. Mora, D. Pesme, A. Héron, G. Laval, and N. Silvestre. Modulational Instability and Its Consequences for the Beat-Wave Accelerator. *Phys. Rev. Lett.*, 61(14):1611–1614, 1988.

[41] K. Nakajima. Plasma-wave resonator for particle-beam acceleration. *Phys. Rev. A*, 45(2):1149–1156, 1992.

[42] K. Nakajima, 1993. Poster presented at International Workshop on Acceleration and Radiation Generation in Space and Laboratory Plasmas, Kardamyli, Greece.

[43] Naval Research Laboratory Plasma Formulary (1987 Revised Edition).

[44] A library of computer software for Numerical Analysis ditributed freely from the University of Kent at Canterbury's archive site. Email - netlib@uk.ac.ukc.

[45] R. D. Richtmyer and K. W. Morton.*Difference Methods for Initial-Value Problems.* Interscience (New york), 1967. A. R. Mitchell.*Computational Methods in Partial Differential Equations.* Wiley, 1969. C. E. Fröberg.*Introduction to Numerical Analysis.* Addison-Wesley, 1970.

[46] R. B. Palmer et al. Report of Near Field Group. In *Laser Acceleration of Particles*, number 130 in AIP Conference Proceedings, page 234. AIP, 1985.

[47] C. Pellegrini. A High Energy $e^+ - e^-$ Collider using an Inverse Free Electron Laser Accelerator. In ECFA1 [25], pages 249–266.

[48] M. D. Perry and Gerard Mourou. Terawatt to petawatt subpicosecond lasers. *SCIENCE*, 264(5161):917–924, 13 May 1994.

[49] M. Pessot et al., 1987. Optics Communications **62**:419.

[50] J.-M. Rax and N. J. Fisch. Ultrahigh Intensity Laser-Plasma Interaction: A Lagrangian Approach. *Physics of Fluids B*, 5(7):2578–2583, 1993.

[51] M. N. Rosenbluth and C. S. Liu. Excitation of Plasma Waves by Two Laser Beams. *Phys. Rev. Lett.*, 29(11):701–705, 1972.

[52] J. B. Rosenzweig, B. Cole, C. Ho, W. Gai, R. Konecny, S. Mtingwa, J. Norem, M. Rosing, P. Schoessow, and J. Simpson. Experimental Studies of Plasma Wake-Field Acceleration and Focusing. *Physica Scripta*, T30:110–121, 1990.

[53] J. B. Rosenzweig, P. Schoessow, B. Cole, W. Gai, R. Konecny, J. Norem, and J. Simpson. Experimental measurement of nonlinear plasma wake fields. *Phys. Rev. A*, 39(3):1586–1589, 1989.

[54] J. T. Seeman. . *IEEE Transactions in Nuclear Science*, NS-30:3180, 1983.

[55] P. Sprangle and E. Esarey. Interaction of ultrahigh laser fields with beams and plasmas. *Physics of Fluids B*, 4(7):2241–2248, 1992.

[56] P. Sprangle, E. Esarey, J. Krall, and G. Joyce. Propagation and Guiding of Intense Laser Pulses in Plasmas. *Phys. Rev. Lett.*, 69(15):2200–2203, 1992.

[57] P. Sprangle, E. Esarey, and A. Ting. Nonlinear interaction of intense laser pulses in plasmas. *Phys. Rev. A*, 41(8):4463–4469, 1990.

[58] P. Sprangle, E. Esarey, and A. Ting. Nonlinear Theory of Intense Laser-Plasma Interactions. *Phys. Rev. Lett.*, 64(17):2011–2014, 1990.

[59] P. Sprangle, E. Esarey, A. Ting, and G. Joyce. Laser wakefield acceleration and relativistic optical guiding. *Applied Physics Letters*, 53(22):2146–2148, 1988.

[60] P. Sprangle and C. M. Tang. Evolution of the Laser Beam Envelope in the Beat Wave Accelerator. In *Laser Acceleration of Particles*, number 130 in AIP Conference Proceedings, page 156. AIP, 1985.

[61] D. Strickland and G. Mourou, 1985. Optics Communications **56**:219.

[62] T. Tajima and J. M. Dawson. Laser Electron Accelerator. *Phys. Rev. Lett.*, 43(4):267–270, 1979.

[63] N. L. Tsintsadze. Effects of Electron Mass Variations in a Strong Electromagnetic Wave. *Physica Scripta*, T30:41–49, 1990.

[64] S. C. Wilks. *Theory and Simulations of Novel Plasma-Based Accelerators and Light Sources.* PhD thesis, University of California at Los Angeles, 1989.

[65] S. C. Wilks et al. Photon Accelerator. *Phys. Rev. Lett.*, 62(22):2600–2603, 1989.

Appendix A

MacWaket Program Listing

```
program macwaket
implicit none
C     .. Parameters ..
      INTEGER           NEQ, LENWRK, METHOD
      PARAMETER         (NEQ=2,LENWRK=32*NEQ,METHOD=2)
      DOUBLE PRECISION  ZERO, ONE, TWO, FOUR
      PARAMETER         (ZERO=0.0D0,ONE=1.0D0,TWO=2.0D0,FOUR=4.0D0)
C     .. Local Scalars ..
      DOUBLE PRECISION  HNEXT, HSTART, PI, T, TEND, TINC,
     &                  TLAST, TOL, TSTART, TWANT, WASTE
      DOUBLE PRECISION a0,sigma
      DOUBLE PRECISION TSTORE, TINCS, Y2OLD, GTOL
      INTEGER           L, NOUT, STPCST, STPSOK, TOTF, UFLAG
      LOGICAL           ERRASS, MESAGE
      character dummy*1
C     .. Local Arrays ..
      DOUBLE PRECISION  THRES(NEQ), WORK(LENWRK), Y(NEQ), YMAX(NEQ),
     &                  YP(NEQ), YSTART(NEQ)
C     .. External Subroutines ..
  DOUBLE PRECISION F, SETUP, STAT, UT
      EXTERNAL          F, SETUP, STAT, UT
C     .. Intrinsic Functions ..
      INTRINSIC         ATAN, COS, SIN, exp
      COMMON/PASS/a0,pi,sigma
C     .. Executable Statements ..
C
C  Set the initial conditions.
C
      TSTART = ZERO
      YSTART(1) = ZERO
```

```
      YSTART(2) = ZERO
      PI = FOUR*ATAN(ONE)
      TLAST = FOUR*TWO*PI
      TEND = TLAST + PI
Y2OLD=0.0D0

C
C  Set default values
C
GTOL=1.0D-2
NOUT=250
C
C  Input required info
C
print *,'Enter a0'
read *,a0
print *,'and the value of sigma'
read *,sigma
print *,'the number of data points'
read *,NOUT
PRINT *,'Finally, the gradient tolerance'
READ *,GTOL

C
C  Set error control parameters.
C
      TOL = 5.0D-5
      DO 20 L = 1, NEQ
         THRES(L) = 1.0D-10
   20 CONTINUE
C
C  Call the setup routine.
C
      MESAGE = .TRUE.
      ERRASS = .FALSE.
      HSTART = ZERO
      CALL SETUP(NEQ,TSTART,YSTART,TEND,TOL,THRES,METHOD,'Usual Task',
     &           ERRASS,HSTART,WORK,LENWRK,MESAGE)
C
C  Compute answers at NOUT equally spaced output points. We
C   code the calculation of TWANT so that the last value
C  is exactly TLAST.
C

      TINC = (TLAST-TSTART)/NOUT
open(15,file='macwaket.data')
rewind(15)
```

```
write(15,*) 'Position, Phi, Pulse'
print *,'Calculating Wakefield ...'
C
C  Enter the loop to solve the eqns
C

      DO 40 L = 1, NOUT
         TWANT = TLAST + (L-NOUT)*TINC
         CALL UT(F,TWANT,T,Y,YP,YMAX,WORK,UFLAG)
C
         IF (UFLAG.GT.2) GO TO 60
C
write(15,'(e9.3,a,e14.2,a,e14.2)') T/(two*pi),',',Y(1),',',
     1 a0*exp(-1.0d0*((T-2.0d0*pi)/(2.0d0*pi*sigma))**2)
C
C  If the last two values straddle a minimum in Phi, home in...
C
      IF((Y2OLD.LT.0.0D0).AND.(Y(2).GT.0.0D0)) THEN
      WRITE(*,*)'Finding Minimum of Wake Potential ...'
      TSTORE=TWANT
      TINCS=TINC
      TWANT=TWANT-TINC
   31 TINC=TINC*5.0D-1
    CALL SETUP(NEQ,TSTART,YSTART,TEND,TOL,THRES,METHOD,
     & 'Usual Task',ERRASS,HSTART,WORK,LENWRK,MESAGE)
   32 TWANT=TWANT+TINC
    CALL UT(F,TWANT,T,Y,YP,YMAX,WORK,UFLAG)
    IF (UFLAG.GT.2) GO TO 60

      IF (Y(2).GT.GTOL) THEN
      TWANT=TWANT-TINC
      GO TO 31
      ELSE IF (Y(2).LT.0.0D0) THEN
      GO TO 32
      END IF

      WRITE(9,99991) T/(two*pi)-1.0d0,Y(2)
      TWANT=TSTORE
      TINC=TINCS
      CALL SETUP(NEQ,TSTART,YSTART,TEND,TOL,THRES,METHOD,
     & 'Usual Task',ERRASS,HSTART,WORK,LENWRK,MESAGE)
      CALL UT(F,TWANT,T,Y,YP,YMAX,WORK,UFLAG)
    IF (UFLAG.GT.2) GO TO 60
    PRINT *,'Calculating Wakefield ...'
      END IF
      Y2OLD=Y(2)
   40 CONTINUE
```

```
C
C  The integration is complete or has failed in a way reported in a
C  message to the standard output channel.
   60 CONTINUE
close(15)

C  Pause so the user can read the screen output, then quit...

print *,'Press <RETURN> to quit'
read *,dummy
      STOP
99991 format(1x,'Stationary point near displacement ',f6.3,
     1 ' Gradient= ',f7.4)
      END

      SUBROUTINE F(T,Y,YP)
C     .. Scalar Arguments ..
      DOUBLE PRECISION  T
C     .. Array Arguments ..
      DOUBLE PRECISION  Y(*), YP(*)
      DOUBLE PRECISION a,a0,pi,sigma,ts,gamma2
      COMMON/PASS/a0,pi,sigma
      INTRINSIC exp
C     .. Executable Statements ..

ts=(T-2.0d0*pi)/(2.0d0*pi)
a=a0*exp(-1.0d0*(ts/sigma)**2)
gamma2=(1.0d0+0.5d0*a**2)
      YP(1) =  Y(2)
      YP(2) = 5.0D-1*(gamma2/(1.0d0+Y(1))**2-1.0d0)
      RETURN
      END
```